METHODS FOR ATOMISTIC INPUT INTO THE INITIAL YIELD AND PLASTIC FLOW CRITERIA FOR NANOCRYSTALLINE MATERIALS

A Thesis
Presented to
The Academic Faculty

by

Shreevant Tiwari

In Partial Fulfillment
of the Requirements for the Degree
Doctor of Philosophy in the
School of Materials Science and Engineering

Georgia Institute of Technology
December 2014

METHODS FOR ATOMISTIC INPUT INTO THE INITIAL YIELD AND PLASTIC FLOW CRITERIA FOR NANOCRYSTALLINE MATERIALS

Approved by:

David L. McDowell, Advisor
GWW School of Mechanical Engineering,
School of Materials Science and Engineering
Georgia Institute of Technology

Ting Zhu
GWW School of Mechanical Engineering
Georgia Institute of Technology

Naresh Thadhani
School of Materials Science and Engineering
Georgia Institute of Technology

Seung Soon Jang
School of Materials Science and Engineering
Georgia Institute of Technology

Richard W. Neu
GWW School of Mechanical Engineering
Georgia Institute of Technology

Date Approved: October 31, 2014

To my parents, Uma and Vijai, who inspired me to seek excellence at every step.

ACKNOWLEDGEMENTS

The present work would not have been possible without the support of some key people. I would like to thank my thesis advisor, Dr. David McDowell, for his excellent guidance, constant support, and encouragement over the past five years. Our numerous discussions regarding coursework, research, and career and have contributed immensely to my educational and professional development.

I would also like to thank my thesis reading committee: Dr. Thadhani, Dr. Neu, Dr. Zhu, and Dr. Jang, for their comments and insights that have been instrumental in providing direction to this research effort.

This thesis was supported primarily by the US National Science Foundation grant CMMI-1030103 on Methods for atomistic input into the initial yield and plastic flow criteria for nanocrystalline materials. Additional support from the Carter N. Paden, Jr. Chair in Metals processing is also acknowledged.

I take this opportunity to thank my colleagues at Georgia Tech: Garritt, Jagan, Shuozhi, Anirban, Matthew, Sam, Bill, Jason, Jeff, Brett, and Luke, for sharing their valuable ideas, experiences and advice, regarding not just research, but life in general.

I want to thank my family: Uma, Vijai, Shruti and Raj, whose care and concern I felt all this time, despite being half-way around the world. Most of all, I thank Abhi, my fiancée, for her patience and unwavering support through all the highs and lows of our lives during these past five years.

TABLE OF CONTENTS

LIST OF TABLES

LIST OF FIGURES

LIST OF SYMBOLS OR ABBREVIATIONS

ART	Activation-Relaxation Technique.
CG	Coarse-grained.
CNA	Common Neighbor Analysis.
CSL	Coincident Site Lattice.
DFT	Density Functional Theory.
DNH	Discrete Nosé-Hoover.
EAM	Embedded Atom Method.
ECAE	Equi-channel Angular Extrusion.
ED	Electrodeposition.
GB	Grain Boundary.
GBAZ	Grain Boundary-Affected Zone.
GBE	Grain Boundary Engineering.
HPT	High Pressure Torsion.
IGC	Inert Gas Condensation.
MD	Molecular Dynamics.
MEAM	Modified Embedded Atom Method.
MEP	Minimum-Energy Path.
MRE	Microstructure Rearrangement Event.
MS	Molecular Statics.
NC	Nanocrystalline.
NH	Nosé-Hoover.
NHC	Nosé-Hoover Chain.
NN	Nearest Neighbor.
NS	Nanostructured.
PBM	Phase Boundary Migration.
PC	Polycrystalline.
PES	Potential Energy Surface.

PR Parinello-Rahman.

SFE Stacking Fault Energy.

SPD Severe Plastic Deformation.

STGB Symmetric Tilt Grain Boundary.

STZ Shear Transformation Zone.

SU Structural Unit.

TEM Transmission Electron Miroscopy.

TF Thin Film.

USFE Unstable Stacking Fault Energy.

SUMMARY

Nanocrystalline (NC) metals and alloys are known to possess superior mechanical properties, e.g., strength, hardness, and wear-resistance, as compared to conventional microcrystalline materials. NC metals are characterized by a mean grain size <100 nm; in this grain size regime, inelastic deformation can occur via a combination of interface-mediated mechanisms viz., grain boundary sliding/migration, and dislocation nucleation from grain boundary sources. Recent studies have suggested that these interface-mediated inelastic deformation mechanisms in fcc metals are influenced by non-glide stresses and interfacial free volume, unlike dislocation glide mechanisms that operate in microcrystalline fcc metals. Further, observations of tension-compression strength asymmetry in NC metals raise the possibility that yield and inelastic flow in these materials may not be adequately described by solely the deviatoric stress. Unfortunately, most literature concerning the mechanical testing of NC metals is limited to uniaxial deformation or nanoindentation techniques, and the multiaxial deformation behavior is often predicted assuming initially isotropic yield and subsequent flow normal to the yield surface.

The primary objective of this thesis is to obtain a better understanding of the nature of inelasticity in NC metals by simulating multiaxial deformation at the atomistic resolution, and developing methods to interpret the results in ways that would be useful from a continuum constitutive modeling viewpoint. First, we have presented a novel, statistical mechanics-based approach to unambiguously resolve the elastic-plastic transition as an avalanche in the proliferation of mobile defects. This approach is applied to nanocrystalline Cu to explore the influence of pressure and multiaxial stress states on the inelastic deformation behavior. The results suggest that initial yield in nanocrystalline Cu under biaxial loading is only weakly anisotropic in the $\sim$ 5 nm grain size regime, and that plastic flow evolves in a direction normal to the von Mises yield surface. However, triaxial deformation

simulations reveal a significant effect of the superimposed hydrostatic stress on yielding under shear. These results are analyzed in detail in order to assess the influence of pre-existing internal stresses and interfacial excess volume on the inelastic deformation behavior.

Further, we have studied the effects of imposed hydrostatic pressure on the shear deformation behavior of Cu bicrystals containing symmetric tilt interfaces, as well as Cu nanocrystals of different grain sizes. Most interfaces exhibit an increase in shear strength with imposed compressive hydrostatic pressure. However, for some interfaces, this trend is reversed. Neither the sign nor the magnitude of the pressure-induced elevation in shear strength appears to correlate with interface structure or particular deformation mechanism(s). In Cu nanocrystals, we observe that imposed compressive pressure leads to strengthening under shear deformation, and the effect of imposed pressure on the shear strength becomes stronger with increase in grain size or temperature. Activation parameters for shear deformation have been computed for these nanocrystals, and computed values seem to agree with existing experimental and theoretical estimates. Finally, we have proposed some modifications to conventional isothermal molecular dynamics algorithms, in order to isolate dislocation nucleation events from interfacial sources, and thereby permit explicit computation of the activation parameters for such events.

CHAPTER I

INTRODUCTION

1.1 Motivation

Understanding the effects of a material's microstructure on its emergent properties is of central importance to the field of Materials Science and Engineering. In recent decades, advanced material characterization techniques have permitted a closer investigation of the structure of engineering materials at the scales of microns and lower, and have helped established relations between chemical composition, material processing routes, microstructure, and resultant properties. The influence of material microstructure on bulk properties is a multi-scale phenomenon; properties that are manifested at the macroscale are inextricably linked to a complex interplay of evolving microstructural elements and interacting defect structures at several finer length scales [195]. In the latter half of the past century, major advances have been made towards understanding the polycrystalline structure of metals, the dynamics of lattice dislocations in crystalline materials, and the role of interfaces such as grain boundaries (GBs). This knowledge has helped accelerate the development of high-performance alloys, via strengthening/toughening mechanisms [7], and grain boundary engineering (GBE) [262, 171, 170] approaches. Awareness of the static and dynamic aspects of microstructure is not only helpful towards predicting the behavior of existing materials, but also encourages the notion that engineering materials could be *designed* [158, 159, 135] in a bottom-up manner with specific properties in mind, in contrast to traditional approaches of material selection [12] to meet performance objectives.

Recent decades have seen the development of nanocrystalline (NC) metals [71, 208, 60, 242], which are characterized by a very fine mean grain size of 100 nm or lower. This grain size regime represents a refinement by 2-3 orders of magnitude over conventional coarse-grained (CG) metals, where the mean grain size is on the order of microns. Compared to CG metals, NC metals exhibit several improved mechanical properties such as strength

[280, 43, 75, 97, 101, 110, 103], wear resistance [285, 203, 258], fatigue life [160, 81, 113, 248], and superplasticity [127, 148, 138, 131]. It is now known that these improvements stem from the refinement of characteristic microstructural length scale down to the scale of nanometers, leading to the suppression of classical plastic deformation mechanisms. Deformation mechanisms that typically operate in CG metals and their alloys, e.g., the nucleation, migration, interaction, and annihilation of lattice dislocations in crystalline grains, are severely limited in NC metals; instead, interface-mediated mechanisms such as GB sliding/migration, dislocation nucleation from GB sources, and twinning tend to dominate. Figure 1(a) schematically shows various transitions in deformation mechanism encountered as the grain size is reduced from microns (Traditional) down to extremely fine-grained (Nano-1). In the CG grain size regime, a decrease in grain size is associated with an increase in strength (the Hall-Petch relation [80, 162]). In the NC regime, the onset of GB-sliding processes at grain sizes below $\approx$ 20 nm leads to weakening, also known as the inverse Hall-Petch effect [45, 185, 219, 22, 183].

The transition to non-classical, interface-mediated deformation mechanisms at NC grain sizes has profound implications regarding the predictive modeling of plastic deformation in these materials. First, traditional theories of crystal plasticity [9, 10] do not apply at nanoscale grain sizes, since these do not account for GB-mediated processes. Second, in the regime of sub-micron grain sizes, experimental [37, 281, 187] and computational [129, 149, 128, 230, 56] studies have reported strength asymmetry in tension vs. compression (also see Figure 1(b)). These observations question several core assumptions of classical plasticity theories, namely, that initial inelastic yield in metals is driven only by deviatoric stress, and that subsequent flow occurs normal to the yield surface. Third, plastic deformation of NC grains is limited by the interface-mediated nucleation and pinning of dislocations [245]; therefore, classical strengthening mechanisms that are based on dislocation multiplication+storage and dislocation-obstacle interactions in the lattice may not apply to NC metals. Clearly, there is a need for constitutive theories for NC plasticity to incorporate these non-classical effects, especially with respect to scaling of material strength with microstructural length scale(s), and plastic yield and flow behavior.

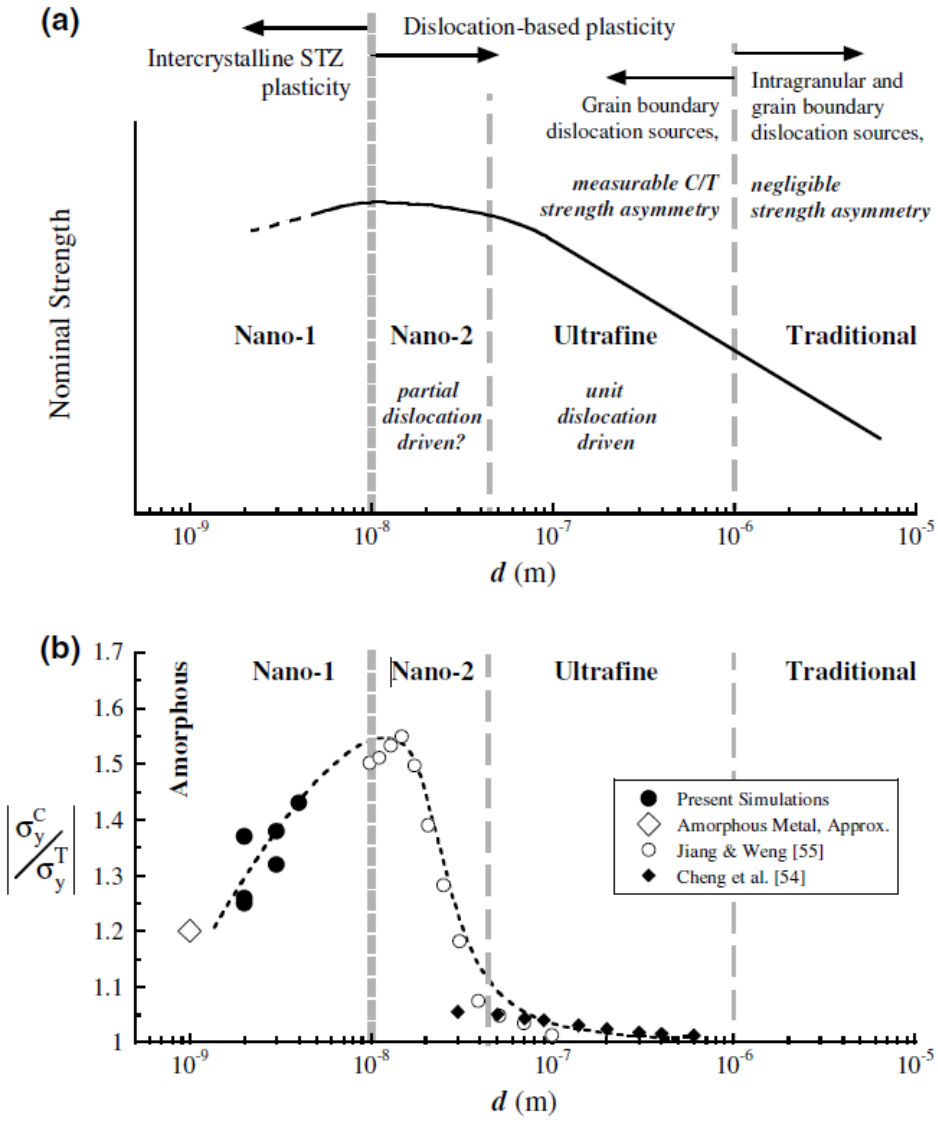

Figure 1: (a) Schematic showing the scaling of nominal strength with grain size d in metallic materials. Various scaling regimes (Nano-1, Ultrafine, etc.), along with expected deformation mechanisms that primarily operate in those regimes, have been marked. (b) Schematic showing the scaling of tension-compression strength asymmetry (shown on the vertical axis) with grain size d [128].

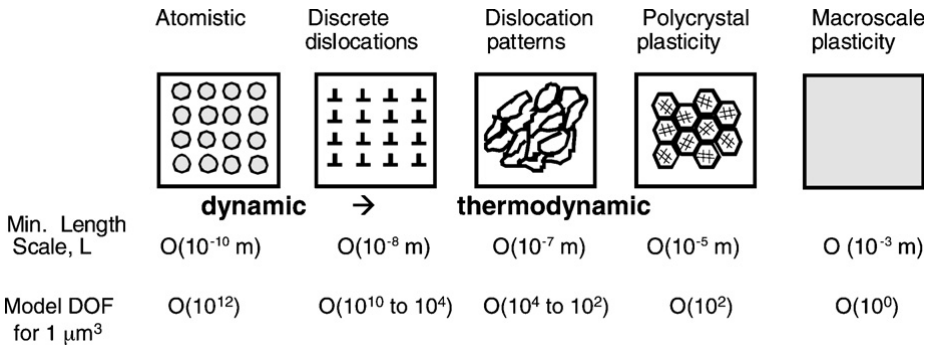

Figure 2: Schematic showing the hierarchy of plasticity models used for polycrystalline CG metals. While going from left to right, the size of the "window of observation" increases, and the degrees of freedom (DOF) associated with the model decrease [136].

Mechanical testing practice for NC metals, and nanostructured (NS) materials in general, is still evolving, and experimental exploration of general, multiaxial deformation behavior is time-consuming and expensive. However, with the increasing power (and decreasing cost) of computing resources in recent times, direct numerical simulation of such material phenomena has become feasible. Computational efforts can provide a supplement to experimental studies, and can potentially accelerate the development of NC materials with tailored properties. Atomistic techniques, e.g., Molecular dynamics (MD) offer one class of computational methods to estimate the material response (and more importantly, the microstructural origins of such a response) [27]. Atomistic simulations are naturally suited for the study of physical processes that occur at the scale of nanograins, and several past studies [183, 243, 244, 246, 245, 51, 237, 61] have made critical contributions towards the current understanding of plasticity in NC metals. While these studies do reveal important qualitative aspects of defect dynamics in NC metals, predicting bulk properties in a bottom-up manner using knowledge of fine-scale material physics is often a tough challenge [136]. Even if the behavior of individual material defects (vacancies, dislocations etc.) is well-understood, directly modeling a microstructure containing a large population (often on the order of Avogadro's number) of such defects is computationally infeasible. Therefore, for the purpose of predictive modeling of plasticity in large material volumes (having dimensions on the order of microns and larger), it is necessary to adopt various *reduced-order*

models of material behavior. As an example, Figure 2 shows a multi-scale hierarchy of several models used to describe dislocation-mediated plasticity in CG metal polycrystals [136], where each model pertains to a different range of length scales, and a model applicable to a particular length scale can be parameterized based on information from both higher (top-down) and lower (bottom-up) length scales. A similar hierarchy can be envisioned for NC metals. Here, bottom-up approaches based on atomistic simulations have even greater utility, due to the smaller length scale-separation between the atomic scale and the scale of NC polycrystalline aggregates.

1.2 Problem definition

The primary question that motivates the present research is this: *how is the elasto-plastic deformation behavior of NC microstructures and bicrystal interfaces affected by the stress state?* In particular, what is the role of non-deviatoric stress components (e.g., hydrostatic stress, stress normal to crystallographic slip planes), grain size, and temperature on the kinetics and kinematics of non-classical, interface-mediated deformation processes that operate in NC metals? The aim of the present work is to develop and test a suite of tools (simulation strategies, analytics and algorithms) that can be applied within the framework of atomistic simulation techniques to computationally probe the yield/flow surface(s) of NC microstructures, as well as resolve the evolution of continuum fields such as stress, strain and curvature in different microstructure elements such as crystalline grains and interface, where distinct deformation mechanisms operate.

Specific questions addressed in this thesis are enumerated below:

1. *How can deformation behavior under combined multiaxial stress/strain states be explored by atomistic simulations?* In the literature, the vast majority of atomistic simulation studies of elasto-plastic deformation in nanocrystals and bicrystals in the literature have been performed under uniaxial loading, which is insufficient to assess the appropriate mathematical form for plasticity theories of a full multiaxial nature. Therefore, there is a need to design methodologies with the framework of molecular dynamics that can impose deformation along specific paths in the stress/strain space

via the prescription of evolving boundary conditions. Preferably, these methodologies should also permit explicit control over components of the stress or strain that directly affect the motion of mobile defects.

2. *How can the onset of inelastic yield be demarcated for an arbitrary deformation path?* A variety of inter-granular and intra-granular deformation mechanisms are known to operate in NC metals in different regimes of grain size (see Figure 1). These mechanisms are known to lead to non-linear, partially-recoverable deformation [168, 26, 24, 25], making it difficult to demarcate the onset of plastic deformation (i.e., the yield point) via conventional approaches e.g., strain offsets on the stress-strain curve. To address this problem, more nuanced methods to resolve the yield transition are needed, which take the underlying microstructure evolution into account.

3. *How can atomistic simulations be used to quantify the kinetics and kinematics of initial yield and plastic flow in NC metals?* Atomistic simulations of material deformation provide high-resolution information regarding the evolution of microstructure, down to precise atomic trajectories. However, interpreting this information to create a reduced-order description of material behavior is often not straightforward. In the context of the elasto-plasticity of NC metals, outstanding issues are (a) the distribution of the inelastic strain between different interface-mediated deformation mechanisms, (b) appropriate constitutive laws for structural transitions that occur via such mechanisms, and (c), the role of stress components/invariants other than the resolved shear stress in the mathematical formulation of these constitutive laws. Obtaining such information from atomistic simulations requires a combination of computational tools, e.g., metrics of structural/topological analysis, methods to quantify the energy barriers to deformation (activation parameters), and algorithms to directly compute the evolution of key microstructural quantities (interfacial free volume, for instance).

4. *How is stress-driven interface motion affected by the interface structure*? Interfaces are arguably the most important microstructural components in NC metals. Besides

serving as dislocation sources and subsequent pinning sites for dislocation loops, interfaces can also directly contribute to the inelastic strain via stress-driven motion (sliding/migration/dissociation). The mechanics of such interface motion, especially the role of interface structure (structural unit/free volume content) is not well-understood as yet.

1.3 Thesis Objectives

The objectives of this thesis are to:

1. Classify microstructural rearrangements associated with the deformation of NC structures, based on separate intergranular and intragranular deformation mechanisms.

2. Study the elastic-plastic response of NC structures under a variety of multiaxial stress states and temperatures, and analyze domain–wide statistics of microstructure rearrangement to resolve cooperative kinetics of deformation.

3. Using information from 2, demarcate the elastic-plastic transition in NC metals and compare yield loci based upon criteria of both strain and dissipation.

4. Extend previous work on bicrystals [201, 197, 230, 225, 234] to explore the effects of imposed hydrostatic pressure on the shear deformation response of such bicrystal .

5. Determine the partitioning of the inelastic strain rate among competing deformation mechanisms and assess the degree of non-associativity of the flow potential with the yield surface.

6. Estimate activation parameters for intergranular vs. intragranular deformation mechanisms, by observing the effect of temperature on the partitioning of microstructural rearrangement caused due to each mechanism.

7. Explore methods to control the activation of interfacial dislocation sources in atomistic ensembles, with the purpose of obtaining atomic trajectories associated with single dislocation sources. These trajectories can then be used as input to optimization

methods such as Nudged Elastic Band [84] to obtained energy barriers to nucleation for various source(s).

While this thesis focuses primarily on the properties of NC metals and the nature of interface-mediated deformation mechanisms, the approaches and methods developed in this thesis could potentially be applied to any atomistically-modeled material microstructure in which the effect of general multiaxial stress states/loading path is of interest.

1.4 Significance of Research

This thesis investigates the role of non-classical, interface-mediated deformation mechanisms viz., GB-assisted dislocation activity in the grain interior, and features of yield and flow behavior arising due to these mechanisms. The present work has addressed critical aspects of the understanding of plastic deformation pathways in NC metals, from the perspectives of GB structure, interfacial internal stress/free volume, and thermal activation.

Atomistic simulations offer the advantage of directly modeling NC ensembles. For engineering applications, however, more broad-spectrum descriptors of material behavior at the bulk scale are desired. In structural components, for example, changes in temperature and loading rate are obvious factors to be considered in material selection. So is the role of combined stress states involving hydrostatic, shear, and normal stresses. The trends observed in the deformation behavior of atomistic NC ensembles and extracted statistics of nanoscale defect cascades can inform higher length-scale continuum constitutive models, which are essential for predictive stress and failure analysis of structural components. At present, no physically-faithful and robust constitutive models suitable for multiaxial loading conditions are available for NC metals. This thesis describes a set of simulation strategies and analytic tools which provides the necessary machinery to explore and interpret multiaxial deformation behavior of any material microstructure accessible to simulation via MD.

1.5 Thesis structure

This thesis is organized as follows. In Chapter 2, first, an overview of several key concepts of metal plasticity and atomistic simulation techniques such as molecular statics, molecular

dynamics, interatomic potentials, and statistical ensembles is presented. The chapter then provides a background of the structure and properties of NC metals, with a focus on mechanical properties, the role of interfaces, and unusual mechanistic aspects that distinguish these materials from CG metals. In later sections of Chapter 2, the methodology for the construction and simulated deformation of atomistic models of NC microstructure(s) has been described. Lastly, analytic methods that are used to interpret the results of these atomistic simulations have been discussed, including metrics of local crystalline class, and atomic-scale metrics of strain, rotation, and material spin.

In Chapter 3, a statistical mechanics-based approach is introduced to demarcate the elastic-plastic transition in deforming atomistic ensembles. The approach relies upon ensemble-scale thermometry, whereby dissipation due to inelastic rearrangement events is indirectly resolved by the evolution of a thermostat variable. This approach reveals cascades of atomic rearrangement that unambiguously correspond to the onset of plasticity, and permit the quantification of yield surface(s) without prior knowledge of either the prevalent deformation mechanisms, or the stress-state dependence of the activation of these mechanisms. The thermostat-based yield criterion is tested for the uniaxial deformation of a Cu nanocrystal.

In Chapters 4-6, several approaches have been employed to simulate the deformation of periodic atomic ensembles under a variety of complex combinations of applied stress- and displacement-type boundary conditions. These approaches are based on the framework of Parinello-Rahman [161] dynamics, and provide selective control of all six applied stress and strain components. Particularly, they permit deformation via ramped-stress or ramped-strain schemes, thereby allowing exploration of the spaces of stress/strain components in which yield/flow surfaces are formulated.

In Chapter 4, loading-unloading simulations have been performed on a NC Cu ensemble along several plane-stress biaxial and full multiaxial deformation paths. These simulations are used to estimate the effect of imposed hydrostatic pressure on the onset of inelasticity, and the extent of normality of the inelastic strain rate with the von Mises yield surface. Additionally, the evolution of strain fields within the microstructure has been investigated for possible correlations with atomic-scale measures of unrelaxed internal stress and interfacial

excess volume.

Chapters 5 and 6 are concerned with assessing effects of imposed hydrostatic pressure on shear-driven, interface-mediated deformation mechanisms. In chapter 5, the shear deformation response of several Cu symmetric tilt grain boundaries (STGBs) has been investigated under conditions of an imposed hydrostatic pressure. Chapter 6 extends these investigations to Cu nanocrystals, where effects of grain size, temperature, and superimposed pressure on the shear deformation behavior have been analyzed, and associated activation parameters computed. The computed values are compared with existing theoretical models of dislocation nucleation as well as recent experimental results where similar deformation mechanisms have been reported. However, it should be noted that activation parameters computed from the deformation response of an ensemble of NC grains represent mean values, and may not pertain to individual defect activation events. To address this limitation, a modification to isothermal MD is proposed in Chapter 7. The modified dynamics algorithm permits the prescription of a spatially-discretized temperature field, which can potentially be employed to selectively activate and suppress dislocation nucleation in different regions of the microstructure, and obtain atomic trajectories that correspond to isolated inelastic events.

Chapter 8 summarizes major findings of this work, and lists various methods that have been developed to probe and interpret the multiaxial deformation behavior of various atomistically-modeled material systems, not just nanocrystals. Finally, some outstanding issues, limitations of the present work, and avenues for future research have been discussed.

CHAPTER II

BACKGROUND AND METHODOLOGY

2.1 Plastic deformation of metallic materials

Plastic deformation plays a key role in the thermomechanics of engineering metals and alloys. Plasticity is of central concern in the ductile failure, surface wear, and deformation processing of metals. Additionally, mechanisms of fracture, fatigue, and damage typically involve plastic deformation (e.g., the blunting of cracks). As novel engineering materials are developed with demanding next-generation applications in mind, a better understanding of the nature of plastic deformation in these materials is desired, not only from a fundamental scientific viewpoint, but also to help predict structural failure and tailor material microstructure for better performance.

At the atomic scale, plastic deformation in metals is the result of stress-driven irreversible rearrangement of atoms, i.e., bond-switching (this should be contrasted with bond-breaking, which leads to brittle fracture). Constitutive descriptions of plasticity attempt to establish relations between the kinetics (force-like quantities, e.g., stress) and kinematics (displacement-like quantities, e.g., strain) that emerge from such rearrangement events. To that end, many (but not all) models of metal plasticity invoke the concepts of a *yield surface* and *flow potential*. As a ductile material is deformed, its stress-strain response is characterized by an initial linear elastic deformation regime (Hooke's law), where the deformation is completely reversible. Upon further deformation, the onset of irreversible deformation, called *yield*, is usually indicated by deviation from linearity. For a material volume deformed under the influence of a general, multiaxial stress tensor $\boldsymbol{\sigma}$, yield is modeled by a scalar function $F(\boldsymbol{\sigma})$, called the yield function. Deformation is elastic for stresses that result in $F < 0$, and the yield point is reached when $F = 0$. The surface defined by $F = 0$ is called the yield surface. The plastic strain $\boldsymbol{\epsilon}^{\mathrm{P}}$ evolves in a direction given by the flow potential function Φ , i.e., $d\boldsymbol{\epsilon}^{\mathrm{P}} = d\lambda(d\Phi/d\boldsymbol{\sigma})$.

Irrecoverable deformation in metals occurs via permanent distortion (shape change), which is driven primarily by shear stresses. This behavior was incorporated in early models of metal plasticty, such as those by Tresca [221] and von Mises [252]. The von Mises yield function is given by:

$$J_2 - K = 0 \tag{1}$$

where J_2 is the second invariant of the stress deviator tensor and K is directly proportional to the yield strength under pure shear deformation. Note that Equation 1 implies isotropic yield with no dependence on hydrostatic stress. Phenomena in the post yield behavior were identified in cyclic loading-unloading experiments, which revealed strain hardening and the Bauschinger effect (lowering of the yield stress for reversed loading). Consequently, various isotropic and kinematic hardening theories [156, 164, 292] were formulated to account for these effects. These theories incorporate the effects of deformation history via the expansion and translation of the yield surface, respectively. Despite the simplicity of the von Mises yield criterion (also called the J_2 criterion), it continues to be used extensively in engineering design and analysis to predict initial yield, especially for isotropic polycrystalline metallic materials.

The aforementioned models of plasticity are *phenomenological*, i.e., they are postulated simply based on empirical evidence obtained from 'macroscopic' indicators such as stress-strain behavior, with no consideration of material microstructure or its evolution. As a result, phenomenological models often cannot effectively predict changes in the material response due to deformation-induced changes in microstructure. Furthermore, the choice of parameters and the mathematical form of phenomenological models is based on empirical evidence, and therefore it is difficult to ascribe the predicted material response to specific physical processes. Therefore, in recent decades, there has been a surge of interest towards improving existing plasticity models by explicitly incorporating knowledge of micro- and nano-scale mechanics obtained from material science [136, 137]. This pursuit of physically-accurate models has also been motivated by advances in dislocation theory [85, 92], and improvements in techniques of material characterization. Examples of plasticity theories that incorporate some information of material microstructure and/or defects include strain

gradient plasticity [64, 65], crystal plasticity models [9, 10], and discrete dislocation models [282, 30]. These theories are geared towards cases where von Mises plasticity is ill-suited, e.g., to model finite size effects in plasticity, or to correctly reproduce texture evolution in polycrystals as a result of complex deformation history.

Regardless of their precise formulation, most constitutive theories of metal plasticity share some common features. First, it is assumed that the glide of dislocations on slip system is driven by the resolved shear stress, and the influence of non-deviatoric stress components is negligible. This assumption is reflected in Schmid's law [184] of crystallographic slip in single crystals, and leads to the von Mises yield criterion at the scale of an untextured bulk polycrystal. The other assumption is the normality of flow; whereby the same function is used as the yield function F and the flow potential Φ. Since the direction of flow (increment of the plastic strain tensor) is along the gradient of Φ with respect to stress, it is also normal to the yield surface. The von Mises yield criterion and flow normality are valid assumptions in the case of the vast majority of ductile metals and alloys. However, significant deviations are observed in the case of pressure-sensitive materials where dislocation activity is not the primary deformation mechanism, e.g., soil [58, 294], or metallic glasses [57, 186]. Even in materials where plastic deformation occurs via dislocation glide, some body centered cubic (bcc) metallic systems deviate from Schmid's law due to the spreading of dislocation cores on multiple slip systems [249, 250, 165].

2.2 Nanocrystalline materials

The growing field of nanotechnology is characterized by a sustained effort to better understand the physics of material behavior due to the reduction of characteristic dimensions of an object down to the scale of nanometers. Interest in this field can be traced back to the seminal lecture by Feynman [63], who envisioned the manipulation of matter at the atomic scale to achieve novel functionality. Since then, the development of several advanced material fabrication techniques has facilitated the creation of both individual nanostructures e.g., nanoparticles [147, 83], nanowires [277, 272, 40, 121] and nanotubes [216, 239], as well as bulk nanostructured (NS) materials including nanocrystals [71, 208], multilayers

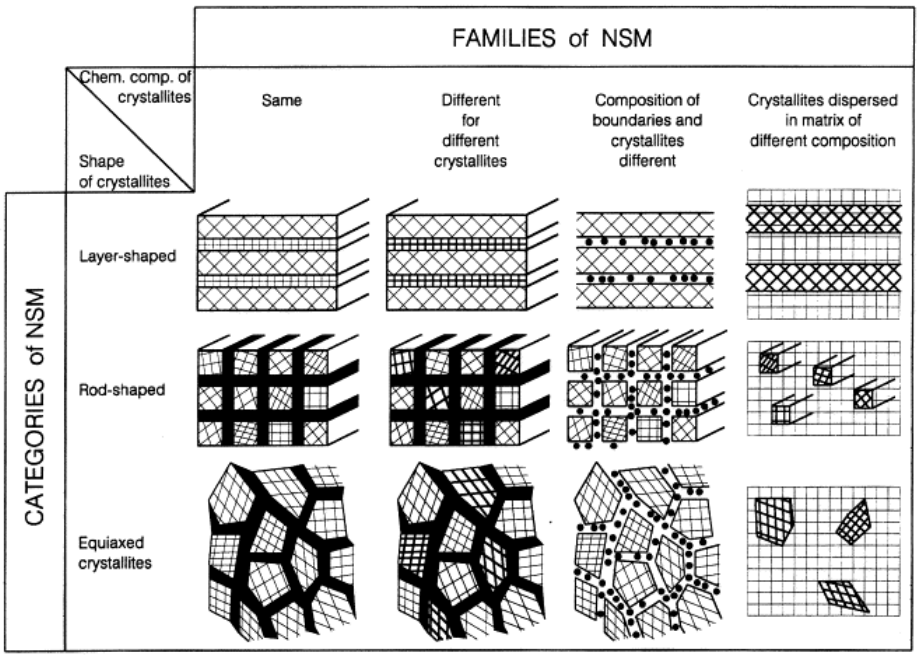

Figure 3: A schematic showing different classes of nanostructured (NS) materials, based on morphology (shape) of crystallites, and chemical composition [72].

[214, 70, 91], and nanotwinned [126, 86, 125] materials.

In NS materials, the internal length scale (defined as the size/spacing of oriented microstructural features) is typically on the order of 10^{-9} m. The schematic in Figure 3 shows different classes of microstructures encountered in NS materials, based on chemical composition and the distribution of different phases. A defining characteristic of NS materials is the enhanced influence of interfaces such as grain boundaries (GBs) and/or free surfaces on the physical properties. In conventional engineering materials, internal length scales are typically on the order of microns or higher, and therefore, physical properties are controlled by the behavior of bulk phases(s) that constitute the material. However, when these length scales are reduced to nanometers, as is the case in NS solids, the population of atoms that belong to the interfaces and/or free surfaces becomes comparable to the bulk atoms. Consequently, material properties are strongly affected by interfacial structure, surface tension forces, impurity segregation at interfaces, and the presence of disordered phases.

Nanocrystalline (NC) materials constitute a particular class of NS materials, whose microstructure consists of polyhedral grains similar to conventional engineering metals, but

with a mean grain size smaller than $\sim$ 100 nm. NC materials have received significant attention in recent years due to their unique physical, mechanical, and electromagnetic properties [71, 208, 60, 139, 13, 102, 169]. Compared to relatively coarse-grained (CG) microcrystalline metals, NC metals exhibit:

- improved strength [59, 75, 142, 97]
- improved wear resistance [210, 212]
- improved fatigue life [160, 81, 113, 248]
- increased potential for superplasticity [127, 148, 138, 131]
- higher diffusivity compared to GB diffusion in CG metals [89, 53, 179]
- enhanced strain rate sensitivity [260, 41, 188]

NC metals and alloys also exhibit other interesting properties not observed in CG metallic materials, such as tension–compression asymmetry [187] and time–recoverable deformation [168]. Unfortunately, several undesirable properties, e.g., low microstructural structural stability [284, 181], limited tensile ductility [103, 104, 177, 241], and propensity for room temperature creep [257, 278, 148] have also been reported in NC metals. While some of these properties are expected simply due to the NC microstructure (metastability of interfaces, lack of pre-existing dislocation sources), they were much more common in early experimental studies (notably, pre-2000s) due to fabrication-related defects in experimental samples. In recent years, fabrication techniques and alloying strategies have been improved to allay many such concerns [38, 124, 220, 46, 153].

2.2.1 Fabrication of nanocrystalline metals

Due to the extremely small size of crystalline grains in NC materials, several conventional fabrication and manufacturing methods that are routinely used for CG metals cannot be used. Instead, several specialized fabrication methods have been developed to restrict the size of grains and obtain a high volume fraction of interfaces. These methods can broadly categorized into two types: single-step methods where nanograins are formed in-situ, and

multi-step methods that rely on the creation and subsequent consolidation of nanometer-sized clusters. Electrodeposition (ED) [60] and Severe Plastic Deformation (SPD) [242] are two single-step methods that are commonly used to fabricate NC microstructures in metallic materials. In ED, metal ions are electrolytically deposited from a solution onto a substrate by applying pulses of current. Several factors such as current density, pulse frequency, nature of the substrate and pH of the solution determine the grain size of the deposited layer, and these factors are finely adjusted to yield a nanocrystalline grain size. In SPD, large deformations are repeatedly applied to a metal block with a CG microstructure, resulting in a cumulative shear strain of several hundred percent. The purpose of these deformation steps is to induce large amounts of plastic deformation and increase the dislocation density to a point that dislocations begin rearranging into low-energy configurations, and ultimately form high-angle grain boundaries. In practice, SPD is performed either by Equi-Channel Angular Extrusion (ECAE) [189], i.e., repeatedly extruding the initially-CG sample through an angular die, or by High Pressure Torsion (HPT) [286], where a disc of CG materials is placed under high pressure and deformed under torsion to large strains. A multi-step method commonly used for the fabrication of NC metal microstructures is Inert Gas Condensation (IGC) [152, 154]. In IGC, metal nanoclusters are first created by condensing metal vapor in an inert atmosphere onto a cold finger. The condensed clusters are then scraped off the finger and consolidated. Compaction and/or sintering may be used to obtain the final NC sample. Most NC metallic samples used for mechanical testing in the literature were fabricated via one of ED, SPD, or IGC methods. That said, several other methods exist for the synthesis of NC materials; a discussion of these can be found in Glieter [71].

The aforementioned NC synthesis methods differ greatly in terms of the accessible grain size, grain size distribution, the potential to introduce undesirable defects/impurities, and their suitability for different material systems. Figure 4 shows transmission electron micrographs of NC Cu microstructures fabricated via (a) SPD, and (b), via ED. Several differences between the microstructures in (a) and (b) are noted. First, the grains are larger in (a) than in (b); while the grain size is processing history-dependent, minimum grain sizes achievable

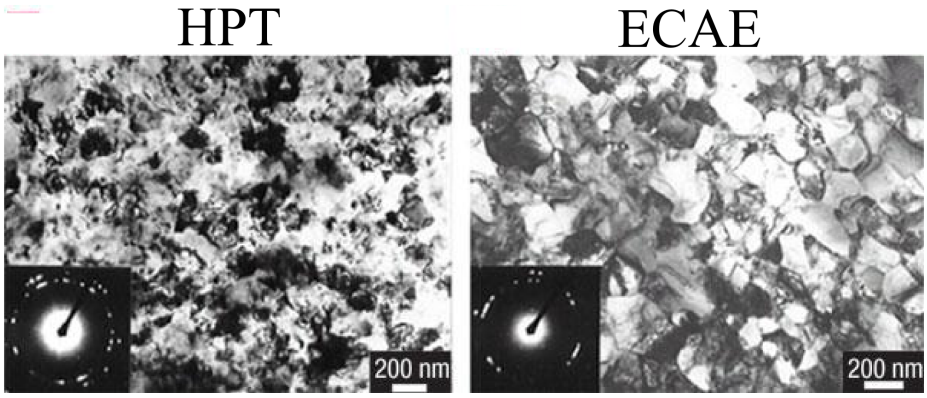

(a)

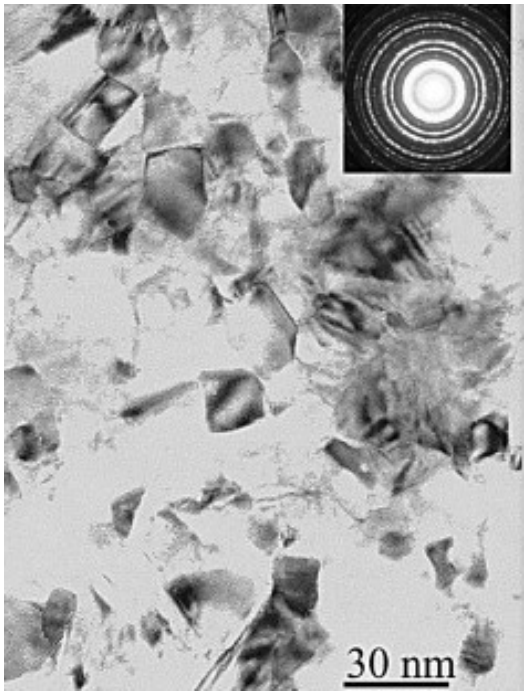

(b)

Figure 4: Transmission electron micrographs of NC microstructures prepared via (a) High-Pressure Torsion (HPT) [240], and (b) electrodeposition (ED) [109]. The material is Cu in (a) and Ni, in (b).

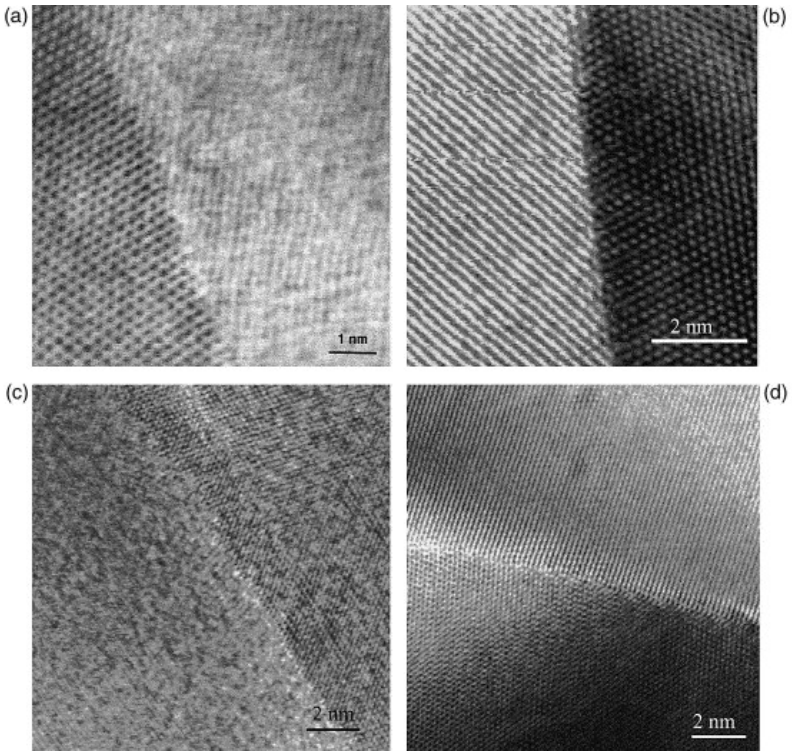

Figure 5: High Resolution Transmission Electron micrographs of interfaces in (a,b) electrodeposited NC Ni, and (c,d) NC Cu, obtained from gas-phase condensation. Notice that crystallinity is maintained right up to the interface, and no GB 'phase' of finite thickness is observed. [109]

via SPD are typically higher than those that can be reached via ED. Second, interfaces between grains are not as well-resolved in (a) as they are in (b). This is because GBs in SPD-processed microstructures are formed by the reorganization of dislocations from a highly-strained lattice. This implies that GBs in SPD materials are predominantly high-angle, non-equilibrium structures with both trapped Burgers content as well as high internal stress and strain [240]. In contrast, GBs in (b) were formed via deposition, which results in a GB structure that is closer to equilibrium. Third, the electron diffraction patterns in the inset of each image show that crystallographic texture is considerably stronger in the SPD samples. This is expected since the large plastic deformation of SPD encourages preferential reorientation of material volumes. While crystallographic texture can be developed in ED as well [59], it becomes less pronounced as the grain size of the deposited material decreases.

Since the early years of development of NC metals, the structure of interface regions was a matter of debate. Specifically, the existence of a distinct, structurally-disordered phase at and near the GBs was postulated (e.g., [71, 291]). While the degree of structural disorder near GBs obviously depends on the fabrication route, in several TEM-based studies [110, 263, 191] no such GB phase has been observed. Figure 5 shows high resolution electron micrographs of ED- and IGC-prepared samples that reveal crystallinity all the way up to the interfaces. Note, however, that the atomic misfit at GBs do produce short-range stress and strain fields near the interface. At very small grain sizes (approaching the amorphous regime), as the fraction of atoms belonging to GBs significantly increases, structural disorder increases as well [271, 52].

2.2.2 Deformation behavior

From the standpoint of elasto-plastic deformation, the significant differences between the CG microstructure and the compositionally-similar NC microstructure arise from the suppression of lattice dislocation activity in the confined crystalline volumes inherent to NC materials [51]. Unlike CG metals, NC metals do not have a significant concentration of either pre–existing dislocations [82], or dislocation sources [275]. Additionally, extended dislocation pileups are unlikely to form owing to the small grain size. Figures 6(a) and (b)

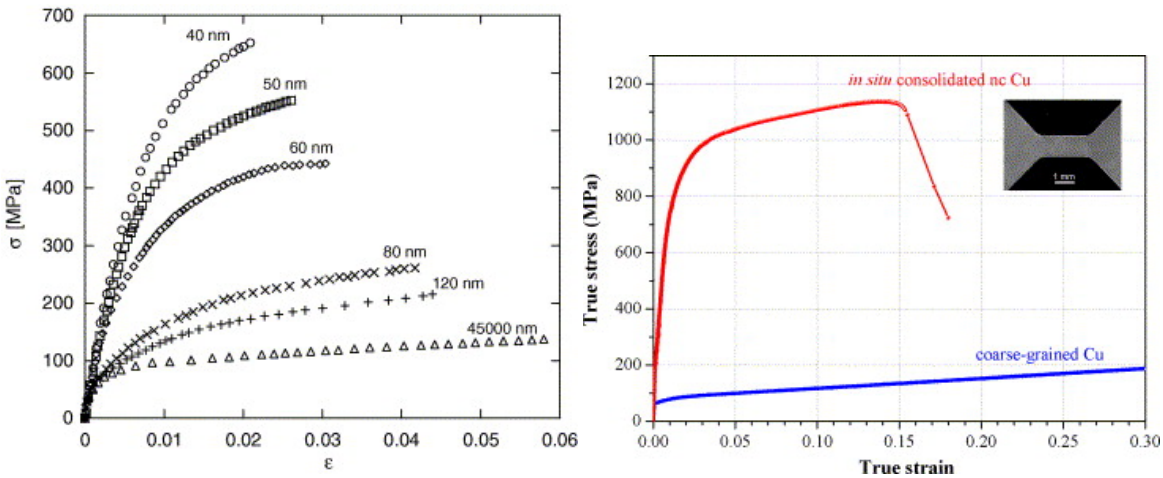

(a) (b)

Figure 6: Effect of mean grain size on the stress-strain response of various CG and NC material samples. Plots are for (a) Al, deformed under compression (Khan et al. [101]), and Cu, deformed under tension (Guduru et al. [75]). In (a), plot labels denote to mean grain size.

shows mechanical testing results from the literature, comparing uniaxial stress-strain curves for microstructures of various grain sizes in Al and Cu, respectively. In both (a) and (b), the increase in strength with decreasing grain size is evident.

Atomistic simulations [68, 180, 246, 228, 276, 245] have suggested that dislocations in NC metals nucleate from GB sources. A snapshot from such a simulation is shown in Figure 7. The snapshot was captured following the successive nucleation of two partial dislocations—a leading partial (LP), and a trailing partial (TP) separated by a stacking fault (red), from the GB network (blue atoms show GB atoms that lie in the dislocation slip plane). Due to the small size of grains in nanocrystalline materials, these GB sources tend to be small compared to Frank-Read sources in CG metals. Further, Figure 7 shows that the dislocations LP and TP nucleate from different sites on the GB network. This is the result of small scale stress-variations in the GB atoms, which influence not only the nucleation of dislocations, but also serves to pin dislocation loops as they thread through the grain [245].

At grain sizes on the lower end of the NC regime (below $\approx$ 20 nm), GBs can have a non-negligible contribution to strain in the form of several GB processes (GBPs), e.g.,

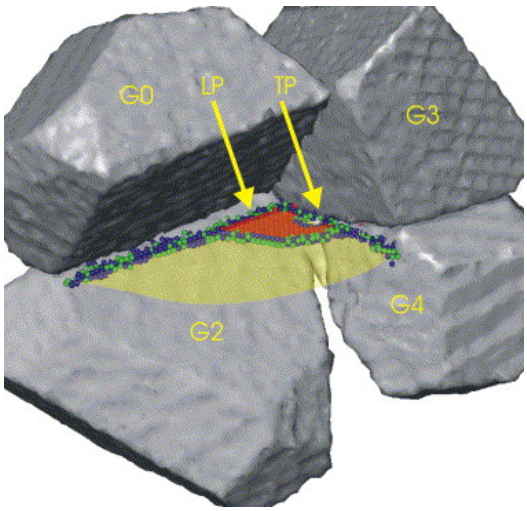

Figure 7: Snapshot from an MD simulation of NC Al, showing a pair of leading partial (LP) and trailing partial (TP) dislocations separated by a stacking {111} stacking fault (red). Arrows indicate locations on the interface where the LP and TP nucleated [245]. fcc atoms in the grain containing the dislocation have not been shown.

GB sliding [243], GB migration [270, 175] and grain rotation [130, 191]. As the grain size decreases below $\approx$ 5 nm, the material becomes nearly amorphous, and a transition to glass-like deformation mediated by shear transformation zones (STZs) is expected [8, 128]. These transitions have been cited as the reason behind the reversal of the Hall-Petch relationship [182, 279] for the scaling of yield strength in NC metals having grain size smaller than $\approx$ 20 nm. Besides the aforementioned mechanisms, the abundance of interfaces in NC metals increase the propensity of diffusive rearrangement in GB regions, and Coble creep could be a significant contributor to plasticity [45]. Recent experimental observations based on in-situ microscopy [190, 191, 42, 115] have confirmed several mechanisms suggested by prior atomistic simulation studies, namely the activation of GB dislocation sources and significant GB migration.

Since the 2000s, the knowledge of deformation mechanisms and mechanical behavior of NC metals has improved tremendously. However, the literature is largely silent on the issue of elasto-plastic deformation in NC metals under multiaxial stress states. Primarily, this is due to the lack of standardized mechanical testing apparatus for NC samples, which are often too small and inconveniently-shaped for conventional testing equipment. For instance, even for uniaxial tensile deformation of NC samples, complex, customized microsample testing

apparatus had to be developed [259, 114]. Testing of NC material samples under controlled multiaxial stress states is still more complex, and a dedicated experimental setup has been developed only recently [5].

An understanding of the deformation behavior of NC metals under the influence of multiaxial loading is important due to several reasons. First, combined stress states are routinely encountered in mechanical components, and effects of stress multiaxiality is fundamental to the understanding of not just ductile failure, but also in non-brittle fracture and fatigue mechanisms. Second, several observations in the mechanics of NC metals are not consistent with typical assumption made in classical theories of metal plasticity. The most prominent observation is strength asymmetry under tensile vs. compressive loading (T-C asymmetry) [187, 56, 218]. Atomistic simulations of dislocation nucleation from GBs in bicrystals [230] have revealed considerably higher yield strengths in compression vs. tension. Note that T-C asymmetry is a common feature of deformation in metallic glasses, and in that context, similarities between deformation mechanisms in nanocrystals and glassy phases are also worth exploring. Atomistic simulations have also revealed non-Schmid effects (influence of normal stresses) in dislocation nucleation from GB sources [201] or homogeneous [227].

Strength asymmetry in multiaxial plasticity of NC metals has been explored in some recent atomistic simulation-based studies [128, 55, 55]. Figure 8(a) and (b) shows simulated biaxial, plane-stress yield loci for NC Ni and Cu respectively. For the Ni nanocrystal (grain size of 2 nm) in (a), the compressive and tensile lobes of the yield loci are fit separately to the Tresca (top) and von Mises (bottom) criteria. The difference in fitted curves reveals the asymmetry of yielding. In contrast, in the NC Cu nanocrystal (grain size 6 nm), the yield loci appears to agree with the von Mises criterion. Figure 9 shows results of a subsequent atomistic-based work where the effect of grain size on the T-C strength asymmetry of NC Cu was quantified. In Figure 9(b), a non-monotonic variation in T-C asymmetry with grain size is noted, with a minimum around 4 nm. These results reveal a clear scaling of strength asymmetry in NC metals with grain size.

Another unique aspect of NC metals is the nature of the elastic-plastic transition. In CG fcc metals with little or no resistance to depinning of 'pre-existing' dislocation cores, such as

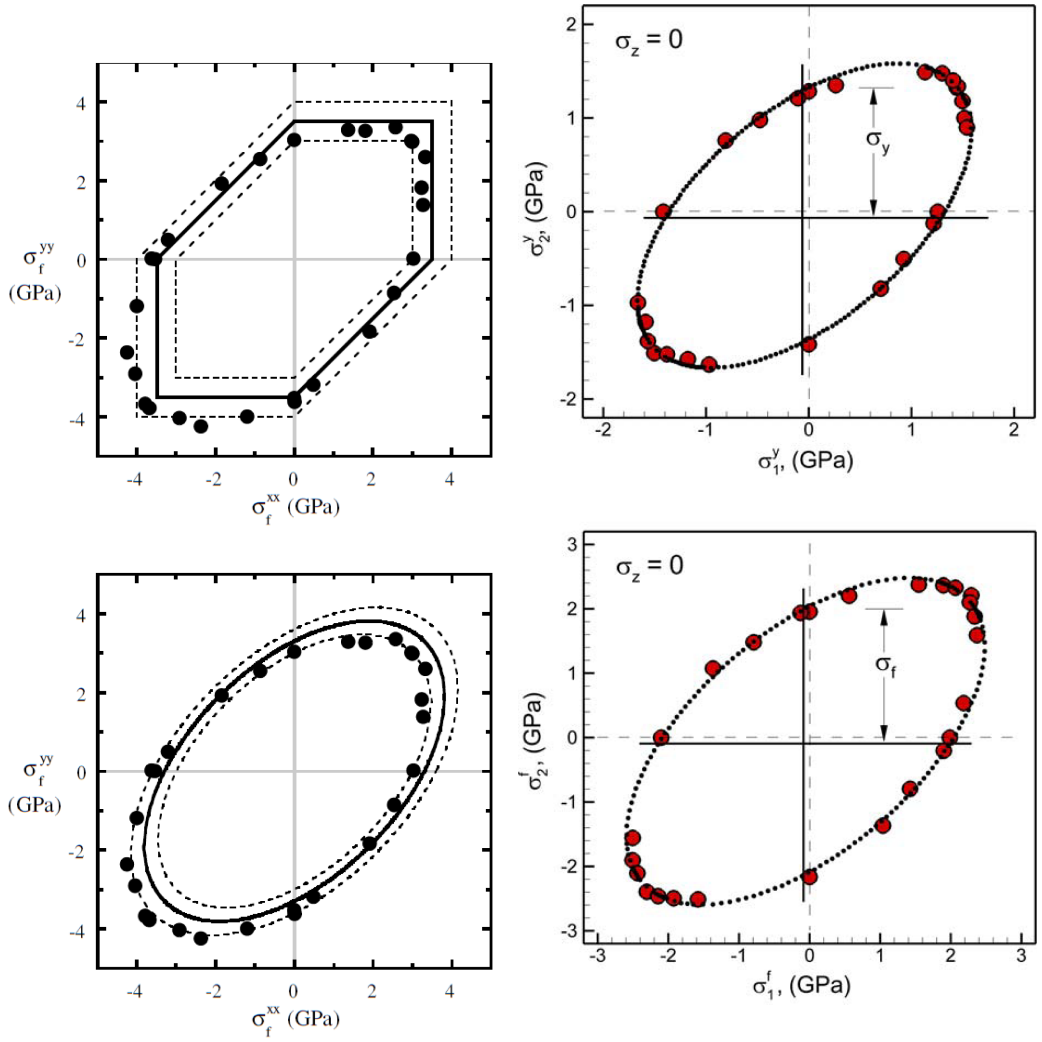

Figure 8: Biaxial yield surfaces of (a) NC Ni [128], and (b), NC Cu [55], computed using atomistic simulations. Simulated microstructures had mean grain size in the range 2-6 nm.

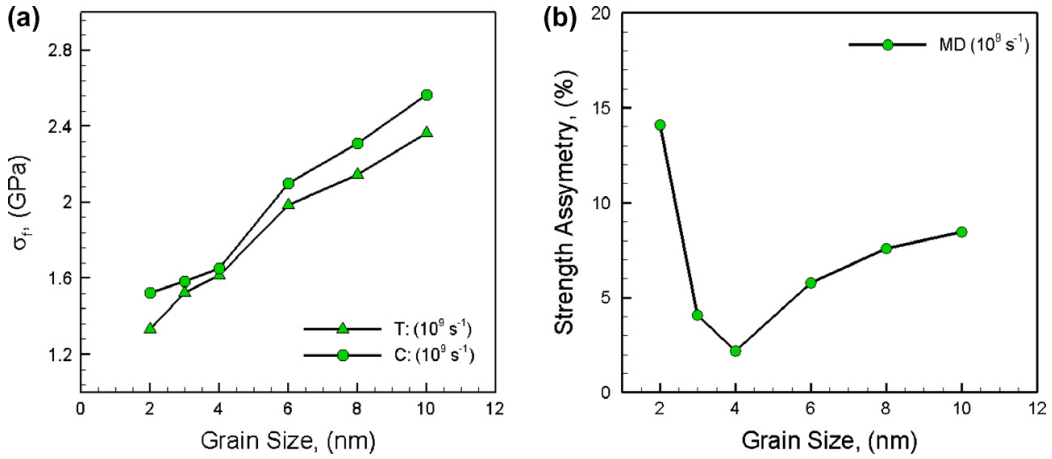

Figure 9: (a) A comparison of tensile (T) and compressive (C) yield strengths, computed using MD simulations, for several NC Cu microstructures of different mean grain size in the range 2-10 nm. (b) The asymmetry in yield strength computed using the values in (a) [56].

CG OFHC (oxygen-free high conductivity) Cu, a prominent yield point is indeed absent, and lattice dislocation glide dominates. In NC metals, however, there is both a frictional barrier (in the form of GB sliding resistance) as well as a dislocation nucleation/propagation barrier to inelastic deformation. Additionally, considerable strain recovery has been observed even after the onset of non-linearity the stress-strain curves for NC samples [25]. Hence, yield criteria based on simple measures such as deviation from proportionality or offset strain may fail to represent the extent of inelastic deformation suffered, in separate GB–dominated and dislocation–dominated deformation regimes [237]. The presence of multiple simultaneous deformation mechanisms also raises questions regarding the normality of flow. While classical plasticity theories tend to assume normality, the concept is not just a heuristic; for instance, normality is expected only when the (kinetic) driving forces and (kinematic) fluxes for different mechanisms of evolution of microstructure are not cross-coupled (this is the idea of generalized normality as formulated by Ziegler [293]). In fact, the dominance of a single force and associated flux pair has been shown to be the cause of flow normality in classical metal plasticity [173]. In the context of dislocation-based mechanisms competing with GB processes in a deforming NC microstructure, non-negligible influences of one mechanism on the other can lead to non-normal flow, e.g., if non-Schmid effects apply to dislocation nucleation, but not to further propagation. Similar arguments can be made for

GB processes, such as GB sliding/migration.

A number of continuum constitutive models have been formulated in recent years to model the experimental stress–strain behavior of NC metals. Composite micromechanical models [35, 36, 14] assume a distribution of 'inclusions' of hard crystalline phase embedded in a viscous GB 'phase', while specifying a different constitutive behavior for each phase. In the work by Wei et al. [265], the GBs were represented as a network of cohesive elements having a non-associated traction–separation behavior. Wei et al. [264], modeled stress–assisted diffusive mass transfer through the GB network and suggested a possible mechanism for the experimentally observed time–dependent strain recovery in NC Al thin films [168]. However, the aforementioned approaches model the microstructure top–down, and therefore, inherently depend on *assumed* deformation mechanisms, nucleation sites and barrier strengths or evolution profiles for internal variables. In these models, it is often open to question whether the assumed nanoscale kinematics is faithful to the physics of the deformation processes. Finally, the effect of combined stress states—particularly, the appropriate mathematical form for the yield function and flow potential suitable for a full 3-D, continuum constitutive theory of NC plasticity—has not been addressed.

2.3 Homophase interfaces in fcc metals

Interfaces such as grain boundaries (GBs) and/or twin boundaries (TBs) are planar defects present in polycrystalline materials such as CG and NC metals. From a mechanics standpoint, interface act as barriers to dislocations and can provide paths for the propagation of intergranular cracks. GBs are also associated with local enhancements in diffusivity, corrosion, and impurity segregation. While the role of GBs and TBs in influencing the kinetics of material processes has long been known, relatively little attention was directed towards investigations of interface *character*, i.e., the fine structure and associated properties of the interface. In recent decades, however, significant advances have been made in the understanding of interface character, motivated partly by the availability of characterization and computational tools, and partly by the recent development of nanostructured materials such as thin films, multilayers, nanowires and nanocrystals.

In a single-phase material, an interface is formed by the mutual impingement of crystals of different lattice orientations growing into each other. Compared to other material defects such as vacancies and dislocations, the structure of interfaces is considerably more complicated. A homophase interface has a total of five degrees of freedom, comprising the relative misorientation θ of the lattices on either side of the interface, and the orientation of the interface plane [171]. The misorientation affects the tilt/twist character[1] of the interface, while the GB plane orientation affect the degree of atomic misfit. These parameters can be expected to significantly influence dislocation slip transfer, corrosion, fracture, or diffusion properties of the interface.

2.4 Structure and mechanical properties of interfaces

There have been several attempts to establish models for the mechanical properties of GBs based on their structure. In early approaches based on dislocation theory, GB misorientation was accommodated through an array of dislocations, with spacing inversely proportional to the misorientation. For low-angle boundaries (misorientation angle $<15\ ^\circ$), these models often gave accurate estimates of GB energy [172]. However, in high-angle GBs, the individual dislocation cores are too close and linear elastic solutions for dislocation interaction energy (and thereby, the GB energy) are no longer applicable. Alternatively, disclination-based models were suggested [118] to account for the misfit of atoms at the interface.

Currently, no general theory relating the structure and mechanical properties of high-angle GBs exists. Considerable progress, however, has been made in the context of interfaces with a coincident site lattice (CSL) misorientation. The CSL is a lattice obtained by considering the hypothetical superimposition of two misoriented lattices that lie on either side of an interface. For some misorientiations, this superimposition results in a significant fraction of *coincident* lattice sites. The CSL is the lattice formed by these coincident sites. Figure 10 shows a 2-D schematic for such a misorientation, where the superimposed lattices result in coincidence of 1/7 of the lattice sites. By convention, both the misorientation as well as

[1] If the misorientation is expressed as a rotation, the tilt/twist character pertains to the orientation of the rotation axis with respect to the interface plane. Pure tilt interfaces contain the rotation axis in the interface plane, while in pure twist interfaces, the rotation axis is normal to the interface plane. The vast majority of misorientations correspond to mixed tilt/twist character

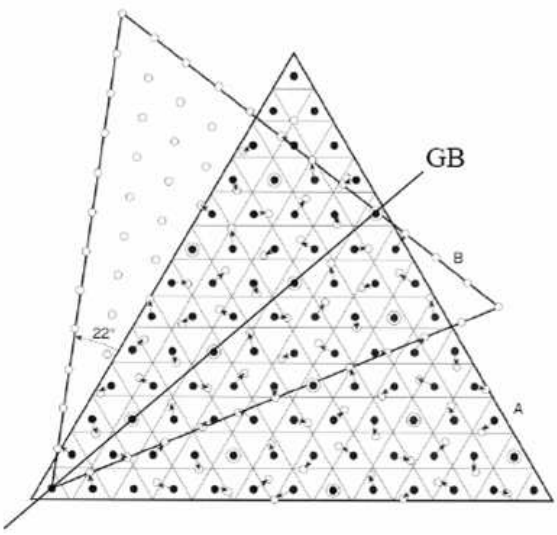

Figure 10: A schematic demonstrating the concept of the Coincident Site Lattice (CSL). Two misoriented lattices, with lattice points denoted by hollow and filled circles respectively, have been shown superimposed. The CSL is composed of points where hollow and filled circles coincide. The solid line 'GB' show the plane corresponding to a symmetric CSL boundary [171].

the interface(s) resulting from this orientation are denoted by the Greek letter Σ followed by the reciprocal of the fraction of coincident sites. Accordingly, the misorientation in Figure 10 is identified as $\Sigma 7$. It is important to note, however, that the CSL Σ-value pertains only to the relative misorientation of two lattices; the interface plane is not specified. Therefore, multiple interfaces can share the same Σ value. Of these, one particular interface plane (labeled 'GB') has been shown in Figure 10. This plane corresponds to a symmetric tilt grain boundary (STGB), named so because similar lattice planes on either side of the GB are equally inclined to the interface plane.

Figure 11 shows the structure of two low-Σ CSL GBs in Al, comparing images obtained from transmission electron microscopy (TEM), and structures generated via atomistic simulation. The boundaries have the same crystallographic tilt axis: $\langle 110 \rangle$. In both boundaries, periodically-repeating polyhedra composed of atoms in the GB plane have been shown. These polyhedra are identified based on the structural unit (SU) model of Sutton and Vitek [209]. In Figure 11, the direction of the GB plane is indicated in curly braces {}.

In fcc metals, several low-Σ STGBs have been found to exhibit special properties. For

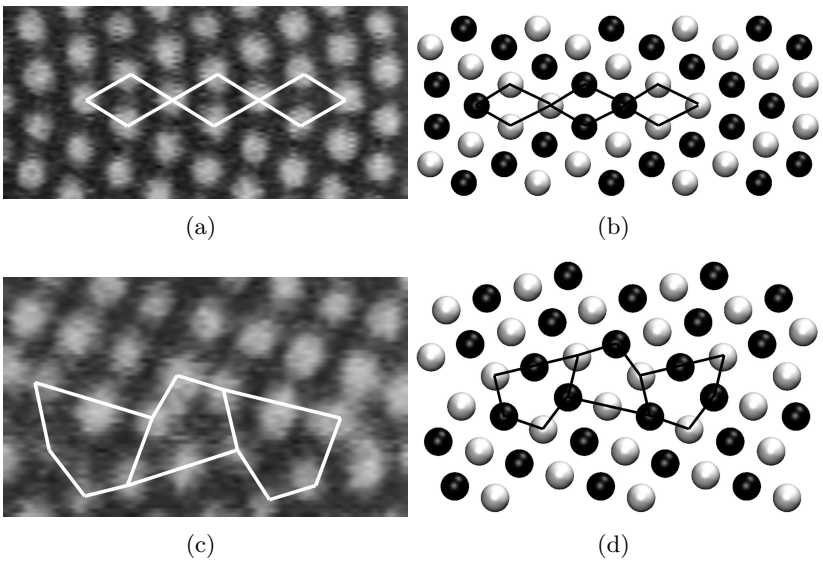

Figure 11: Structures of two coincident site lattice (CSL) symmetric tilt grain boundaries (STGBs), $\Sigma 11\{113\}$ (a,b), and $\Sigma 9\{221\}$ (c,d) in Al. Structures obtained from transmission electron microscopy TEM (a,c) [144], and atomistic simulations (b,d) [198] have been compared. The structural units in each interface are marked with solid lines.

example, the coherent twin boundary ($\Sigma 3$ STGB) is practically free of misfit strains, which leads to a low energy and high tensile strength. Low energy and high tensile strengths have also been observed in fcc $\Sigma 11$ boundaries [201]. To some extent, such behavior is intuitive, since good lattice coincidence across an interface (signified by the low Σ number) can be expected to result in a GB structure having a good atomic fit. However, not all low-Σ STGBs exhibit 'special' properties. Further, for the same misorientation, different orientations of the GB plane can significantly change the degree of atomic fit at the interface.

A better understanding of the deformation behavior of individual interface structures is desired for two reasons. First, interface-mediated processes (dislocation nucleation, pinning of dislocations at interface facets, and various interfacial sliding/migration mechanisms) are of first order importance in the deformation behavior of NC metals. Second, even in CG metals, grain boundary engineering (GBE)[170, 262] techniques preferentially modify the population of some types of GBs in the microstructure; in that case, nuances of the interaction of these GBs with dislocations/cracks is likely to be important.

Figure 12 shows snapshots from atomistic simulations showing details of the (a) tensile and (b), shear response of a $\Sigma 11\{113\}$ GB in Al. Strain is accommodated via dislocation

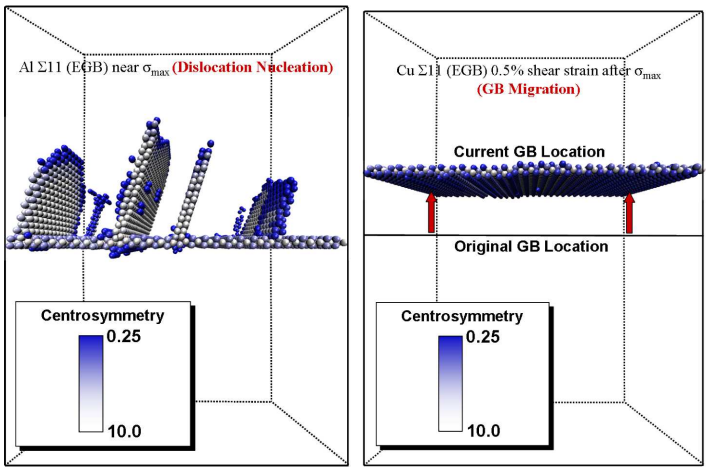

(a) (b)

Figure 12: Atomistic simulation of bicrystals containing a Σ11{113} interface deformed under (a) uniaxial tension normal to the interface plane, and (b) shear deformation in the plane of the interface.[236]. Only atoms that belong to defect structures (interfaces, dislocations, and stacking faults) have been shown.

nucleation under tensile loading, while shear deformation leads to the boundary migrating to a new position. The nucleation of dislocations from GB ledges was first proposed by J.C.M. Li [117] in the 1960s. In CG metals, with regard to plasticity, GBs tend to be treated mostly as barriers to dislocation glide. Over the past decade, however, mechanical properties of grain boundaries have been studied in great detail, and atomistic simulations have significantly accelerated progress in that direction. Atomistic simulations have been used to study dislocation nucleation from a variety of Cu and Al STGBs under uniaxial loading normal to the boundary plane [197, 201, 225, 235]. In these studies, the role of GB structure, interface plane orientation, free volume and non-equilibrium character have been assessed. Several interesting phenomena have been reported in these studies e.g., the weakening of interfaces with the E structural unit [201], and the significant effect of the GB plane orientation [225] and excess free volume [235] on the deformation response.

Other studies [230, 224] have revealed T-C strength asymmetry and non-Schmid effects on dislocation nucleation in both Cu bicrystals as well as single crystals (homogeneous nucleation). Figures 13 and 14 show atomistic simulation results that reveal difference in nucleation stress for dislocations. In Figure 13, nucleation stresses under compressive loading are substantially higher—by a factor of ≈ 3—than under tensile loading. Even

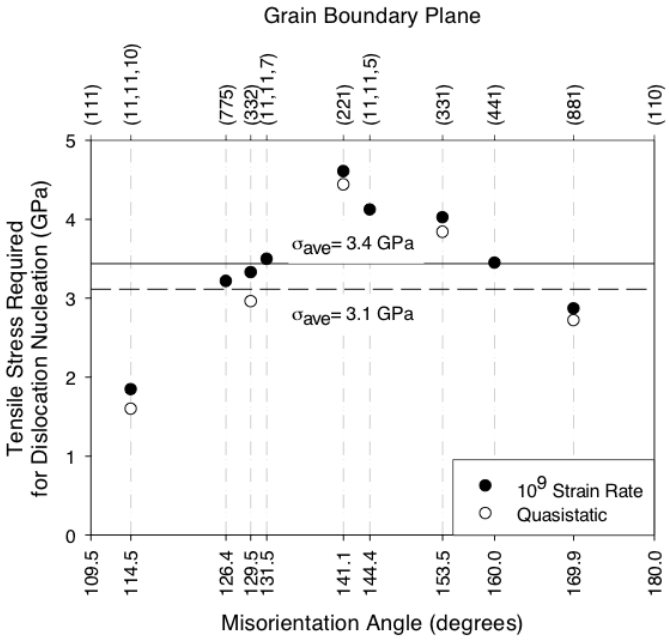

(a)

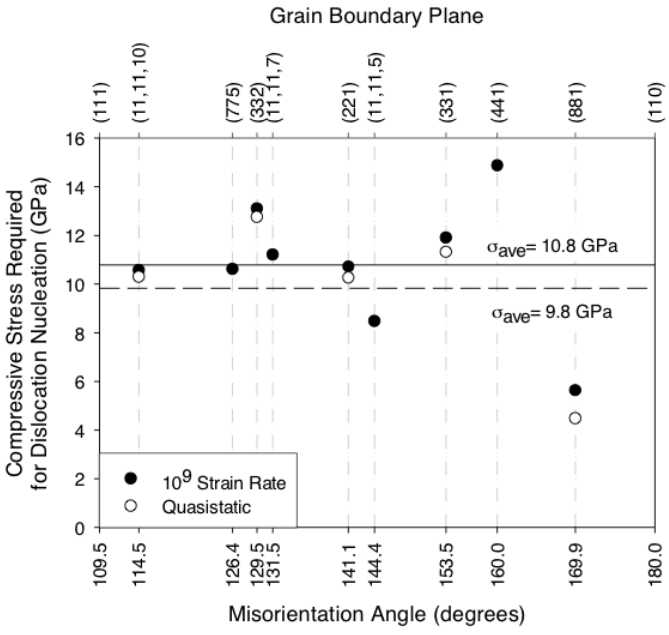

(b)

Figure 13: A comparison of uniaxial stresses required for dislocation nucleation from nine symmetric CSL bicrystal interfaces (characterized by the misorientation angle) in Cu, under (a) tension, and (b), compression [224].

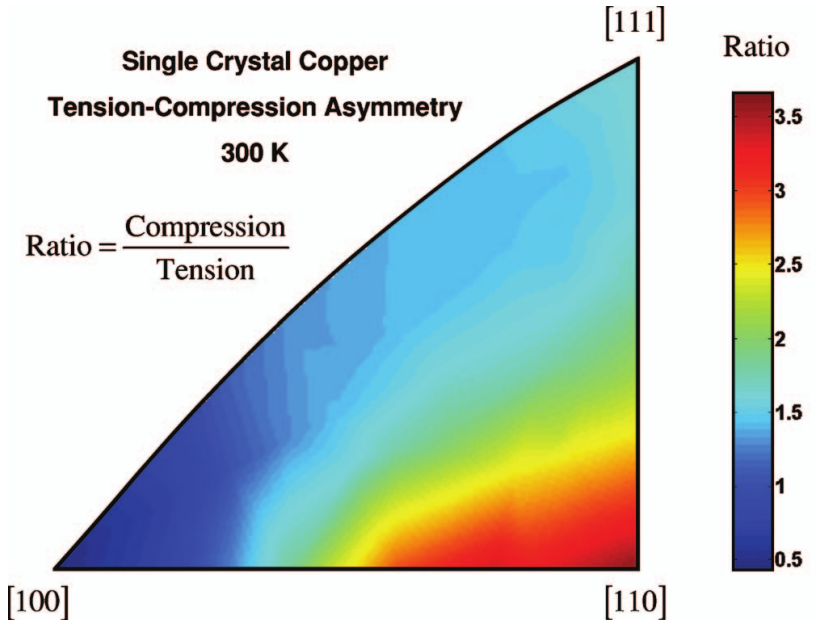

Figure 14: A stereographic heatmap shows the tension-compression asymmetry of dislocation nucleation stresses in single crystal Cu, for deformation along different crystallographic directions. The low-index directions [100], [110], and [111] are shown. [226]

in single crystals (Figure 14), the crystal orientation appears to significantly affect the stress required for dislocation nucleation. Furthermore, for some crystal orientations, the nucleation stress under compression was found to be lower than that under tension.

Stress-driven GB-migration has been observed in experiments [115, 190, 191, 175, 116, 270] involving both nanocrystals and bicrystals. Unlike tensile deformation, which always results in dislocation nucleation, the (computed) responses of various interfaces were quite varied under shear, ranging from sliding, migration, dissociation, and dislocation nucleation [234]. The activated mechanism has been found to depend not only on GB structure, but also its non-equilibrium character [235]. Studies based on the Quasi-continuum method [143] have observed GB sliding via shear suffling of GB atoms in some cases, and dislocation nucleation in others [178, 261]. Cahn, Mishin and coworkers [33, 32, 146] simulated the shear deformation behavior of several CSL boundaries in the $\langle 100 \rangle$ family of misorientations, and reported stress-driven shear-coupled migration with geometrically-expected coupling factors.

2.5 Atomistic simulations

The structure of matter at the scale of angstroms is inherently discrete, and can be modeled as atoms interacting via inter-atomic forces. The idea that physical phenomena could be predicted simply based on the knowledge of initial conditions comprising the positions and velocities of participating atoms and the laws of classical mechanics was theorized historically by Laplace [112]. However, it is only in recent decades that advances in computing technology and a better understanding of inter-atomic interactions have made such simulations practical. Since then, a variety of atomic and molecular systems have been studied using atomistic techniques, e.g., liquids, solids, interfaces, micelles, proteins and nanocrystals (e.g., [98, 134, 269, 167, 180, 197]).

In atomistic simulations, atoms are represented as point particles that interact via forces that are given by the spatial gradient of an interatomic potential field. The total force $\mathbf{F}$ acting on an atom i is obtained as:

$$\mathbf{F}_i = -\frac{\partial U(\mathbf{r_1}, \mathbf{r_2}, \mathbf{r_3} \ldots \mathbf{r_N})}{\partial \mathbf{r}_i} \tag{2}$$

where $\mathbf{r}_i$ is the position vector of atom i, and U is a scalar interatomic potential that is a state function of the atomic positions $\mathbf{r_1}, \mathbf{r_2}, \mathbf{r_3} \ldots \mathbf{r_N}$ in a system containing N atoms. The following sections discuss three necessary components of any atomistic modeling strategy: (i) a realistic model for the interatomic forces (Section 2.5.1), (ii) algorithms to update position(s) of atoms based on the influence of these interatomic forces (Section 2.5.2), and (iii) algorithms to implement constraints/boundary conditions to simulate the effect of external factors such as temperature, applied deformation and/or stress (Section 2.5.2).

2.5.1 Interatomic Potentials: The Embedded Atom Method

The interatomic potential (U in Equation 2) primarily determines the accuracy of the atomistic model in comparison to the real material. U is arguably the most important component of an atomistic simulation. While the nature of atomic bonding in most materials is best described using quantum electronic structure (accessible via Hartree-Fock [194] methods or Density Functional Theory (DFT) [106], U represents a purely classical potential that

attempts to reproduce the effects of interatomic bonding without explicit consideration of electronic interactions.

In past decades, several empirical potentials were formulated to simulate 'model' materials, such as the Lennard-Jones (LJ) potential [95] for liquids and the Morse potential [150] for bonded interactions. Both the LJ and Morse potentials consider only atom-pair interactions, and incorporate simple forms of van der Waals attraction at long ranges and Pauli repulsion at close range. Unfortunately, the utility of these simple potentials for many real materials is limited, since they fail to account for multi-atom interactions. For example, pair potentials incorrectly predict surface relaxation in metals [50], and cannot account for dissimilar elastic constants C_{11} and C_{44} in several crystals. Similarly, in covalent/molecular systems, the effects of bond-angle, bond torsion, and non-bonded interactions (e.g., van der Waals, electrostatic) necessitates a much more complex form of the scalar potential U. Since U cannot account for precise electronic phenomena, the appropriate mathematical form for U must be guessed based on the interactions present in the system. The parameterization of such a potential for a particular materials system is then achieved by 'fitting' to material properties obtained from more accurate (but also more computation-intensive) methods such as DFT. Potentials developed in this manner are often classified as semi-empirical.

The present work focuses on the mechanical deformation response of face centered cubic (fcc) metals, where the nature of atomic bonding permits several simplifications. Metallic bonding has weak directionality, with no explicit bonded interactions. Also, due to the effect of the core electrons in a metal, the long-range electrostatic forces are effectively screened. While these simplifying assumptions are not universal (body centered cubic (bcc) and hexagonal close packed (hcp) crystal structures show major deviations), for many fcc metals, the atomic bonding can be adequately described as metal ions interacting with an isotropic electron density background, in addition to pair interactions with neighboring ions (this electron density is the results of the delocalization of valence electrons that are loosely bound to their ions). This picture of metallic bonding motivated the development of the Embedded Atom Method (EAM) of Daw and Baskes [50, 49]. EAM is a multi-atom, effective medium approximation-based method where the potential energy of an atom is

determined by *embedding* it at a point in the neighborhood of other atoms. EAM assumes that the electron density $\rho(r_{ij})$ at a point A in space is given by the superposition of individual electron densities from all other atoms in the system. If an atom is added to the system at point A(r_{ij}) then its potential energy is composed of the pairwise interactions with neighboring atoms and additionally, an embedding energy which is a functional of the effective electron density at point A. In EAM, the total energy of a set of atoms is given by:

$$U = \sum_i G^i(\rho^j_{ave}(r_{ij})) + \frac{1}{2} \sum_{i,j(j\neq i)} \phi(r_{ij}) \tag{3}$$

where r_{ij} is the distance between atoms i and j, $\rho^j_{ave}(r_{ij})$ is the spherically averaged electron density contribution from all neighboring atoms (superscript j) at the position of atom i. G is the embedding energy, which is a functional of the electron density. $\phi(r_{ij})$ is the pair interaction function.

There are several advantages of the EAM approach. First, its computational cost is only marginally higher than pair potentials. Second, it can account for differences in behavior of atoms near vacancies, interstitials, or free surfaces. That said, EAM assumes an isotropic electron density distribution in the neighborhood of ions. While this assumption is reasonable for metals with full or nearly-full d-bands (e.g., Cu) where bond directionality is negligible, it is often insufficient for metallic systems where bond directionality is important due to partially-filled d-bands. To address this limitation, several modified EAM (MEAM) potentials [15, 17, 16] have been developed, which incorporate the angular dependence of the electron density.

The present research is concerned with the inelastic deformation behavior of Cu microstructures, and throughout this work, the EAM potential for Cu developed by Mishin and coworkers [145] has been used. Following the precedent of earlier EAM potentials, the Mishin potential has been fit to several materials properties obtained from DFT calculations, e.g., elastic constants, vacancy formation energy, phonon frequencies, and energies of different crystal structures. In addition, the Mishin potential is also fit to the intrinsic stacking fault energy (SFE), which pertains to the excess energy of the faulted hcp phase

left in the wake of partial dislocations, with respect to the perfect fcc crystal. The SFE determines the separation of dislocations into leading and trailing partial components, which makes the SFE important from the standpoint of metal plasticity. However, the process of partial crystallographic slip involves the crossing of a barrier, given by the Unstable Stacking Fault Energy (USFE), and the kinetics of dislocation nucleation and propagation is more closely linked to the USFE [174, 244]. Although the Mishin potential is not explicitly fit to the unstable stacking fault energy, a comparison of EAM potentials by Boyer et al. [20] revealed that the value of unstable stacking fault energy obtained using the Mishin potential shows good agreement with DFT computations.

2.5.2 Molecular Statics and Molecular Dynamics

Molecular Statics (MS) and Molecular Dynamics (MD) are two classes of numerical methods that can be used to prescribe the motion of atoms under the influence of interatomic forces. The methods differ in whether they affect only atomic positions (MS), or both atomic positions and velocities (MD). Depending upon the application, a MS or MD-based method may be appropriate. For example, MS methods are used for constrained structural optimization (e.g. finding structurally stable configurations or transient states) as well as for computing thermodynamic properties via statistical averaging (Monte Carlo methods).

One MS method: *geometry optimization* or *energy minimization*, has been frequently used throughout this work. Energy minimization is a structural optimization process that can be applied to relax an atomic configuration having excess potential energy into a more stable, lower-energy configuration. Energy minimization is an iterative process; for a system containing N atoms, each iteration involves a line search along a direction on the $3N$-dimensional potential energy surface, until a minimum in potential energy is found. The search direction can either be taken as the direction of steepest descent (SD), or selected using the method of conjugated gradients [192]. The latter leads to faster convergence and has been used in this work. Each iteration moves atoms closer to their equilibrium separation(s), thereby lowering the system's potential energy. The process continues until the energy of the system converges to a local minimum.

In contrast to MS, MD is predominantly used to model the *time-evolution* of a system via prescribed equations of atomic motion and subject to any external forces/fields. An MD method essentially consists of two parts: (i) a set of ordinary differential equations (ODEs) that prescribe the evolution of atomic positions and momenta, and (ii) a numerical integration algorithm to solve these ODEs and obtain atomic trajectories.

(i) Equations of motion: The simplest MD equations of motion are those of classical Newtonian dynamics, i.e.,

$$\dot{\mathbf{r}}_i = \frac{\mathbf{p}_i}{m_i}, \tag{4a}$$

$$\dot{\mathbf{p}}_i = \mathbf{F}_i \tag{4b}$$

Here, subscript i refers to an individual atom, whose position, momentum, and mass are $\mathbf{r_i}$, $\mathbf{p_i}$ and m_i, respectively. $\mathbf{F_i}$ denotes the total force acting on atom i, which equals $\dot{\mathbf{p}}_\mathbf{i}$, the time-derivative of the atom's momentum.

Note that Equations 4 can also be interpreted as a time-evolution law for the composite vector $\chi = \{\mathbf{r_1}, \mathbf{r_2}, \mathbf{r_3} \ldots \mathbf{r_N}, \mathbf{p_1}, \mathbf{p_2}, \mathbf{p_3} \ldots \mathbf{p_N}\}$. χ, which contains $6N$ components, corresponds to a point in the *phase space*. In statistical mechanics, the term 'ensemble' pertains to a distribution of points in the phase space, i.e., with every phase space point χ, a density $g(\chi)$ can be assigned, which specifies the probability of occurrence of points in the vicinity of χ in the ensemble. Since each phase space point relates to a specific *state* of the system, consisting of atom positions and momenta, physically, $g(\chi)$ quantifies the relative likelihood of finding the system in a particular state.

A thermodynamic ensemble is a specific type of statistical ensemble that applies to a system of particles (atoms, in this work) that are in thermodynamic equilibrium. For example, Newtonian dynamics (Equations 4) conserves the time-averaged total (potential+kinetic) energy E and volume V of the system, provided no external forces are applied to the system. Equations 4 therefore sample the microcanonical (NVE) ensemble, characterized by constancy of number of particles (N), volume (V), and total energy (E). The NVE ensemble simulates a thermally *isolated* system having rigid boundaries, and is therefore not equipped to model realistic conditions where exchange of heat and/or work with the surroundings is

allowed. Other thermodynamic ensembles can be used for these purposes. The *canonical* ensemble (NVT) corresponds to a system with rigid boundaries, but where heat exchange with an external bath (at temperature T) is allowed. Similarly, for a system with movable boundaries and external heat exchange, the *isothermal-isobaric* ensemble (NPT) applies, where P is the pressure.

It should be noted that while deterministic dynamics can be used to generate atomic trajectories, it is not necessary to sample the ensemble. Monte Carlo (MC) simulations, which use random numbers for generating configurations or selecting perturbations, as well as dynamics algorithms that include stochastic forces [6, 18], could be used equally well. However, deterministic dynamics is often preferable when precise atomic trajectories are desired. In the present work, the rearrangement of atoms under the influence of internal and external forces is of foremost importance, which necessitates the use of deterministic dynamics.

Several methods have been proposed to sample the NVT and NPT ensembles via deterministic dynamics. In the present work, these dynamics methods have been employed not just for controlling temperature/pressure in MD simulations, but also to derive metrics of inelastic criticality (Chapter 3) and to control defect nucleation (Chapter 7). Therefore, only a short overview of these methods has been presented here; more detailed explanations of concepts and the formulation of these methods can be found in the aforementioned chapters.

To sample the NVT ensemble, Nosé [155] introduced a temporal scaling factor s via which atomic speeds were adaptively increased or decreased, thereby controlling the temperature. Hoover [88] improved upon Nosé's concept by using the instantaneous excess micro-kinetic energy of atoms in an MD system to drive a (variable) drag factor η, i.e.,

$$\dot{\mathbf{r}}_i = \frac{\mathbf{p}_i}{m_i}, \tag{5a}$$

$$\dot{\mathbf{p}}_i = \mathbf{F}_i - \frac{p_\eta}{Q}\mathbf{p}_i, \tag{5b}$$

$$\dot{\eta} = \frac{p_\eta}{Q}, \tag{5c}$$

$$\dot{p}_\eta = \sum_{i=1}^{N} \frac{\mathbf{p}_i^2}{m_i} - dNk_{\mathrm{B}}T \tag{5d}$$

where the factor η modifies atomic velocities based on a negative feedback from the difference between the system's instantaneous microkinetic energy ($\sum_{i=1}^{N} \frac{\mathbf{p}_i^2}{m_i}$) and the target thermodynamic temperature ($dNk_{\mathrm{B}}T$), and therefore acts as a *thermostat*. A similar negative feedback loop can be also be used to impose pressure control. Constant-pressure molecular dynamics algorithms [141, 133] modify the boundaries of a MD simulation domain to match the system's internal pressure P_{int} with the prescribed target pressure P_{ext}, via another variable ω, i.e.,

$$\begin{aligned}
\dot{\mathbf{r}}_i &= \frac{\mathbf{p}_i}{m_i} + \frac{p_\omega}{W}\mathbf{r}_i, \\
\dot{\mathbf{p}}_i &= \mathbf{F}_i - \left(1 + \frac{d}{N_{\mathrm{f}}}\right)\frac{p_\omega}{W}\mathbf{p}_i - \frac{p_\eta}{Q}\mathbf{p}_i, \\
\dot{V} &= \frac{dVp_\omega}{W}, \\
\dot{\eta} &= \frac{p_\eta}{Q}, \\
\dot{p}_\omega &= dV(P_{\mathrm{int}} - P_{\mathrm{ext}}) + \frac{d}{N_{\mathrm{f}}}\sum_{i=1}^{N}\frac{\mathbf{p}_i^2}{m_i} - \frac{p_\eta}{Q}p_\omega, \\
\dot{p}_\eta &= \sum_{i=1}^{N}\frac{\mathbf{p}_i^2}{m_i} + \frac{p_\omega^2}{W} - (N_{\mathrm{f}}+1)k_{\mathrm{B}}T
\end{aligned} \tag{6}$$

here, ω is called the barostat, and serves to control fluctuations in the system volume V. The system's internal pressure P_{int} is obtained as:

$$P_{\mathrm{int}} = \frac{1}{dV}\left(\sum_{i=1}^{N}\frac{\mathbf{p}_i^2}{m_i} + \sum_{i=1}^{N}\mathbf{r}_i.\mathbf{F}_i. - (dV)\frac{\partial U}{\partial V}\right) \tag{7}$$

where two contributions: a kinetic contribution ($\sum_{i=1}^{N} \frac{\mathbf{p}_i^2}{m_i}$), and a virial term ($\sum_{i=1}^{N} \mathbf{r}_i.\mathbf{F}_i$) are included. Note that P_{int} represents a system-wide sum over atomic kinetic energies and virial terms. Also, Equations 6 pertain to a MD domain where only isotropic volume fluctuations are allowed. Such a domain precludes shape distortions, which are necessary to simulate plasticity. By introducing more barostat variables, each corresponding to a different component of the domain-level stress tensor $\boldsymbol{\sigma}$, the simulation domain can be placed under an arbitrary stress state. For this purpose, the Parinello-Rahman (PR) barostat [161], which permits the full triclinic distortion of a simulation domain, is employed in this work.

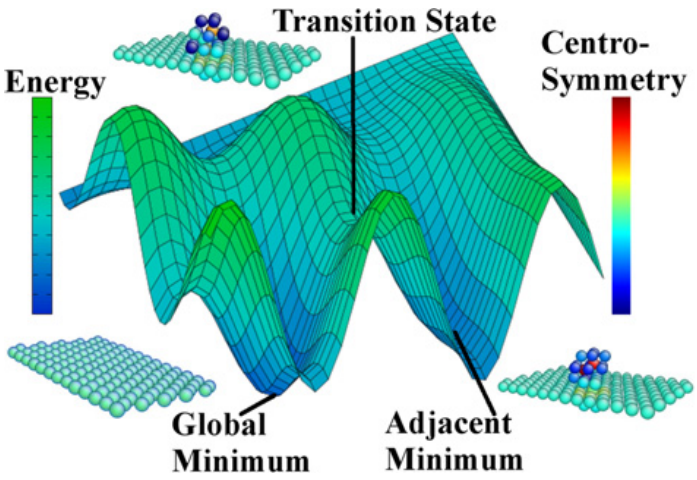

Figure 15: A schematic showing a two-dimensional simplified potential energy surface (PES), highlighting the position of locally stable configurations (troughs or minima) and transition states (saddle points). [2]

(ii) Integration algorithm: To integrate atomic positions and velocities over time, the Velocity Verlet algorithm [3] has been used:

$$\begin{aligned} \mathbf{r}(t+\Delta t) &= \mathbf{r}(t) + \mathbf{v}(t)\Delta t + \frac{1}{2}\mathbf{a}(t)(\Delta t)^2 \\ \mathbf{v}(t+\Delta t) &= \mathbf{v}(t) + \frac{\mathbf{a}(t)+\mathbf{a}(t+\Delta t)}{2}\Delta t \end{aligned} \tag{8}$$

where $\mathbf{r}$,$\mathbf{v}$ and $\mathbf{a}$ are respectively the instantaneous position, velocity and acceleration of an atom. The terms t and $t+\Delta t$ denote consecutive timesteps. Velocity verlet is a symplectic[2], second-order integration algorithm and has found application in various fields where numerical solutions to particle dynamics problems are needed.

Details regarding general concepts in MD simulations can be found in books by Allen and Tildesley [3] and Haile [79].

2.6 Energy landscapes and activation parameters

The method of energy minimization described in the previous section involves descent on a potential energy surface (PES). For materials modeled using the EAM potential, the PES is a scalar function of atomic positions $\{\mathbf{r_1}, \mathbf{r_2}, \mathbf{r_3} \ldots \mathbf{r_N}\}$ ($3N$ degrees of freedom). Such a surface is shown schematically for a system with only two degrees of freedom in Figure 15. The

[2] volume-conserving in phase space

PES is composed of peaks (unstable configurations), valleys (locally stable configurations), and saddle points (transition states) separating adjacent valleys. Structural transitions in solids involve atomic rearrangements; on the PES, these structural rearrangements are manifested as hops between adjacent valleys (local minima), after going through a transition state. Since the transition state is of higher potential energy than either minima, there is always an *energy barrier* to rearrangement. Further, several different rearrangements can be possible starting from a given stable configuration. This can be seen in Figure 15, where several adjacent minima are typically accessible, and the transition to each minimum could potentially involve a different transition state (and therefore, a different energy barrier). In practice, the rate at which different structural transitions occur is determined by the relative magnitudes of the energy barriers associated with different transitions.

Although the PES offers a generic way to interpret the kinetics of structural rearrangement in materials, the complexity of the PES rapidly increases with the number of atoms (N). For large N, information regarding local minima and saddle points in the space of $3N$ position coordinates becomes computationally intractable. Further, in phenomena involving stress-driven structural rearrangement, such as plastic deformation, the application of external stress tends to change the shape of the PES, reducing the activation energy barrier from some transitions. This stress-dependence is approximated to the first order using a linear approximation, i.e.,

$$Q = Q^* - \Omega\sigma \tag{9}$$

where σ is the applied stress, Q^* is the activation energy on the PES corresponding to $\sigma = 0$, and Q is the activation energy for the applied stress. The coefficient of stress-dependence, Ω has dimensions of volume and is therefore called the *activation volume*. Physically, Ω quantifies the number of atoms involved in the rearrangement at the saddle point.

Despite computational limitations in computing PESs, PES-based approaches are nevertheless useful for certain specific types of problems involving atomic rearrangement: (i) where the path of rearrangement (i.e, kinematics) is known, or (ii) where the PES is probed only locally, i.e., only in the vicinity of a known stable configuration. Different types of MS techniques are typically used to numerically compute the PES and activation barriers in

these cases. For known rearrangement mechanisms (aforementioned case (i)), energy pathway sampling via the Nudged Elastic Band (NEB) method [84] is commonly used in the literature. In NEB, several atomic configurations are generated by interpolating the positions of atoms between two stable configurations that correspond to adjacent minima on the PES. The interpolated configurations are then sequentially coupled via virtual spring forces (the "elastic band") with additional constraints (the "nudging"). In the extended system (interatomic potential+spring energy+constraints), an optimization of the potential energy yields a minimum energy path (MEP), whose maximum corresponds to the transition state (saddle point).

Figure 16 shows a particular application of the NEB method to compute the activation parameters for nucleation of a dislocation from the free surface of a Cu nanopillar under compression [290]. In (a), computed transition states/saddle point configurations are shown for the cases of nucleation from a face (left), and from a corner (right). For the case of corner nucleation, the variation of activation energy and volume with applied compressive stress is shown in Figure 16(b).

In cases where structural transitions are not precisely known (aforementioned case (ii)), the PES must be probed along several directions near a known minimum to search for saddle points. Naively, even a random sampling of the neighborhood of a minimum can be expected to resolve the local shape of the PES; this forms the basis of a variety of Monte-Carlo techniques where configurations are generated based on randomized atomic 'moves'. However, owing to the high dimensionality of the search space, and little knowledge of kinematics (i.e., which kind of 'moves' result in structural transition), these methods are of limited utility. In contrast, other MS methods attempt to traverse the PES quasi-deterministically, by 'ascending' the slopes of the PES in different directions until an adjacent minimum is reached. One examples of such a method is activation-relaxation technique (ART) [151], originally developed to probe the PES in glasses. Figure 15 shows atomic configurations corresponding to a thermally-activated rearrangement in a grain boundary, computed using ART.

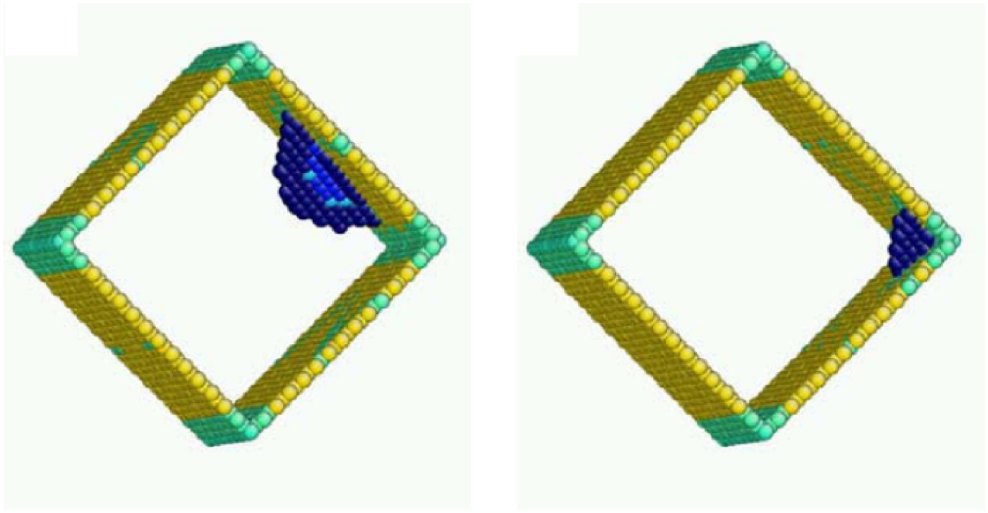

(a)

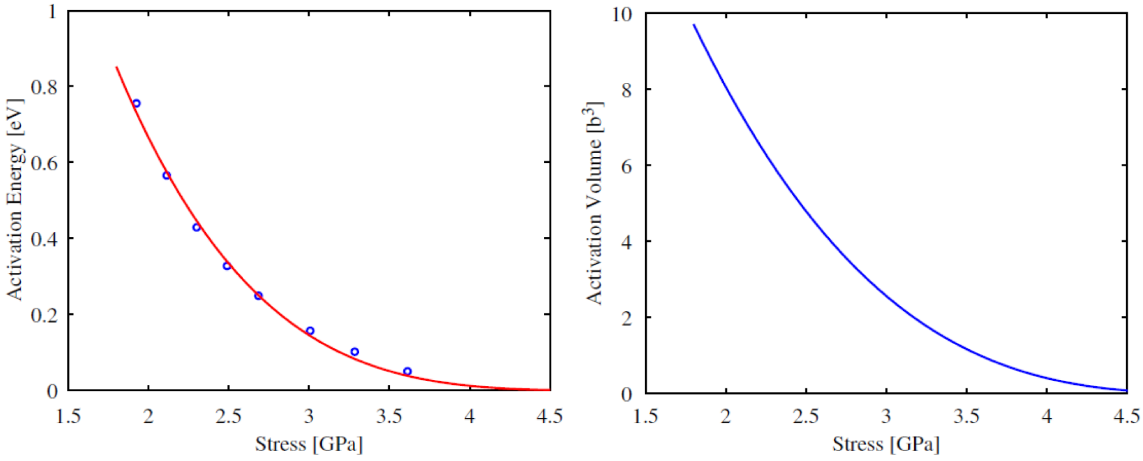

(b)

Figure 16: (a) Transition states (saddle-point configurations) for dislocation nucleation from the free surface of a Cu nanopillar, obtained using a Free End Nudged Elastic Band (FENEB) computation. Images on the left and right respectively show nucleation from a face and corner of the pillar. Only atoms with a non-fcc coordination are shown. (b) Activation Energy and activation volume for the corner nucleation event, shown as a function of stress [290].

The activation parameters for structural transitions can also be obtained via experimental means. If the effect of temperature and stress on some metric of structural rearrangement (e.g., flow stress, diffusivity) is quantified, activation parameters Q and Ω can be defined. Figure 17 shows activation parameters computed for plastic deformation in nanocrystalline Ni at several different temperatures, using strain rate jump tests and stress-relaxation tests. Note however, that in an experimental context, these parameters represent averaged values that may pertain to the activation of several different rearrangement mechanisms, and/or their mutual interaction. An example can be cited from crystal plasticity: the activation parameters for dislocation glide in a crystal with a low initial dislocation density can be expected to be similar to values obtained from PES-based computations over isolated dislocation sources. However, as dislocations multiply and interact elastically, cooperative rearrangements involving forest dislocation-cutting become more common. This is fundamental change in the nature of barriers, and activation parameters are likely to change accordingly. Although the microscopic (PES-based) and macroscopic (experimental) interpretations of thermally-assisted and stress-assisted activation are conceptually similar, one must be careful comparing the magnitudes of activation parameters obtained from these two approaches, since the phenomenology of a material behavior is often the result of processes occurring at several length scales.

2.7 Simulation methodology

2.7.1 Creating Cu nanostructures

Two types of Cu nanostructures have been studied in this work: (i) Cu bicrystals containing CSL STGBs, and (ii), Cu nanocrystals having a mean grain size in the range 5-20 nm. All microstructures were created inside an initially-orthogonal (cube-shaped) simulation domain.

Bicrystalline structures were created in a manner identical to previous work [198, 223], whereby two misoriented Cu lattices are constructed in each half of a simulation domain. These lattices have a common crystallographic tilt axis ($\langle 100 \rangle$ or $\langle 110 \rangle$) and a mutual misorientation angle that corresponds to a CSL. This is followed by a proximity-based

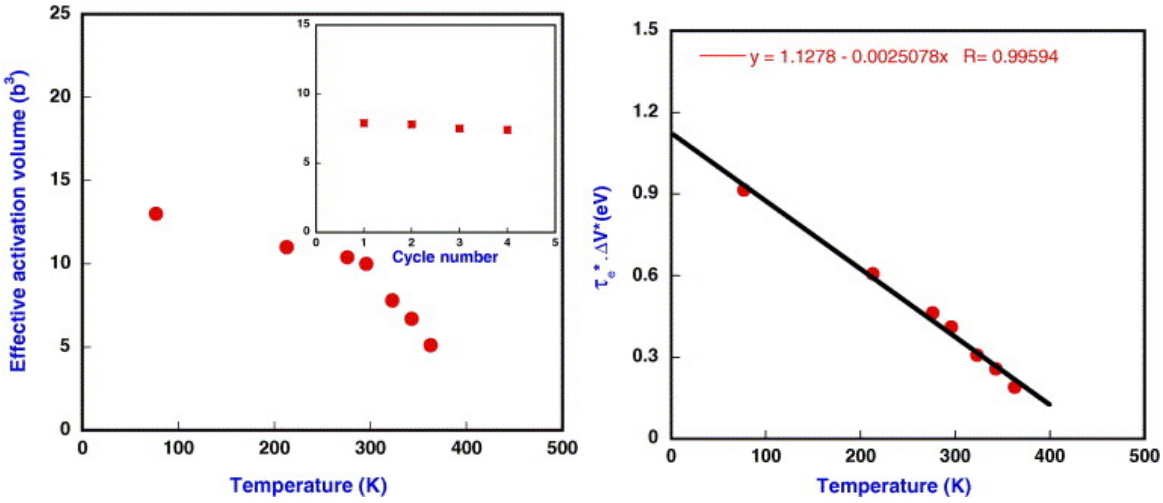

(a) (b)

Figure 17: Plots of (a) the activation volume, and (b), the activation energy (plotted on the vertical axis) with temperature, obtained for a NC Ni sample via strain rate-jump and stress-relaxation tests [260].

atom deletion step, in which one atom out of each pair of atoms that are closer than half the lattice parameter (for Cu, this distance is 1.8075 $\mathring{A}$) is randomly deleted. Subsequently, energy minimization is used to relax atoms into their equilibrium positions. In general, this step converges to local minimum of potential energy; therefore, one lattice is iteratively translated parallel to the other and energy minimization is applied to all such configurations until a global minimum energy is encountered.

To create a NC microstructure, first, the simulation domain is divided into several 'grains', based on a Voronoi tessellation [253, 176]. The seed points for the tessellation are chosen based on the grain morphology desired: a 3-D uniform random distribution of seed points results in polyhedral grains with a log-normal size distribution, while a 2-D tessellation can be used to generate a columnar grain structure. Similarly, to generate grains of similar shape and size, seed points can be chosen on a lattice (a small spatial perturbation can be applied to avoid identical grain shapes). While computing the Voronoi polyhedra, periodicity of the resulting tessellation is ensured by enforcing the minimum image convention. The convention is applied as follows: while constructing the polyhedron for seed point A, images of another seed point B are obtained by translating B by a length equal to the domain dimensions in one or more Cartesian directions, resulting in a total

of seven images (including B itself). The image of B that is closest to seed A is used to generate the tessellation around point A. The minimum image convention ensures that tessellated grains are continuous across periodic boundaries.

Following the tessellation, an fcc lattice of Cu atoms is created within each polyhedral grain. The lattice orientations are chosen randomly from the group of 3-D rotations, resulting in an untextured microstructure containing predominantly high-angle interfaces of mixed tilt-twist character. Like the bicrystal structures, proximity-based atom deletion is applied at this stage, followed by energy minimization to relax the microstructure into a local minimum of energy. Note, however, that unlike the bicrystal, the possible rotational/translational perturbations in each nanograin are too numerous to permit a simple iterative search for a global minimum.

At the end of the minimization step, residual stresses might still be present at the boundaries of the simulation domain. To relax these stresses, both the bicrystal and nanocrystals are equilibrated under $N\boldsymbol{\sigma}T$ conditions to a prescribed temperature and stress. In this work, temperatures of 10 K, 300 K, and 500 K have been used. The prescribed stress, if non-zero (i.e., initially stress-free microstructure), is primarily of a hydrostatic nature.

2.7.2 Deformation scheme and boundary conditions

The primary focus of this thesis is to study the elasto-plastic deformation behavior of Cu nanocrystals and bicrystals under general multiaxial stress state(s), via MD simulations. Therefore, we have explored methods to simulate the effect of complex stress states and deformation paths on plasticity in a nanoscale material volume that is embedded within the bulk.

The need to simulate complex deformations in a bulk-embedded volume places some specific restrictions on the simulation domain. First, free surfaces at the domain boundaries are undesirable since they can serve as sites for dislocation/crack nucleation, and can also introduce domain-level stress gradients, such that the simulation is not representative of

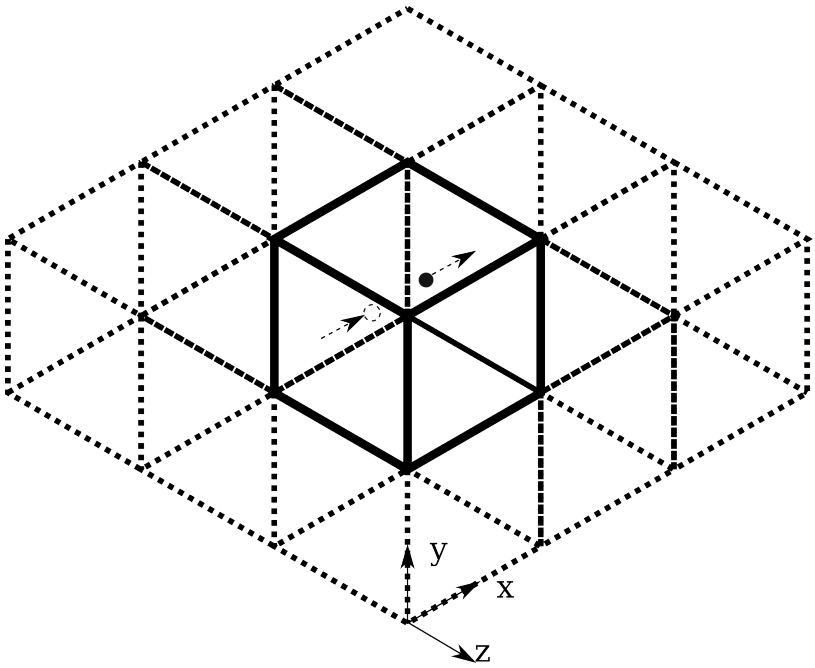

Figure 18: A schematic showing the effect of periodic boundary conditions on particle dynamics in a MD simulation domain. Solid lines show the real simulation domain; the surrounding periodic images (virtual domains) of the real domain are shown as dotted lines. Arrows indicate the continuous motion of a particle (filled circle), across the domain boundary. Note that domain-images could exist in all three Cartesian directions. For clarity, only domain-images lying in the x-z plane are shown.

plasticity in the bulk. Second, when the material volume is placed under a general, multiaxial stress state, it should be free to undergo any affine deformation[3]. Physically, this implies that boundary conditions imposed on an initially-orthogonal simulation domain should allow the domain to both expand volumetrically, as well as 'warp' into a parallelepiped shape of triclinic symmetry.

To eliminate free surfaces at the domain boundaries, periodic boundary conditions are used (they are, in fact, necessary if stresses at the domain boundaries are to be externally controlled, as is the case in the present work). Figure 18 shows a schematic of periodic boundary conditions applied to an initially-orthogonal simulation domain. Along with the real simulation domain (solid lines in Figure 18), several identical virtual copies of the domain are assumed to exist (dotted lines) at all times. All atoms in the real domain can interact not only with other real atoms, but also with nearby 'ghost' atoms that belong to virtual domains (the reader can verify that this is the same as the minimum image convention of the previous section applied to individual atoms). As shown in Figure 18, an atom that leaves the simulation domain by crossing a periodic boundary re-enters from the opposite side. In the present work, periodic boundaries have been used in all three dimensions.

All nanostructures studied in this work initially occupy orthogonal simulation domains. Figure 19 shows an MD simulation domain with various stress components marked (the strain components are identified by a similar convention). To study only the effects of deformation under normal stresses (i.e., a diagonal stress tensor), the domain need only have three deformation degrees of freedom (corresponding to strains ϵ_{xx}, ϵ_{yy} and ϵ_{zz}). However, if shear stresses (σ_{xy}, σ_{yz} or σ_{zx}) are also applied, six degrees of freedom are required. The former class of deformations can be applied using MD frameworks used in previous bicrystal simulations [201, 197, 230, 225] , e.g., those developed by Melchionna et al. [141]. For the latter however, the Parinello-Rahman [161] framework must be used. For simulation domains that are constrained to be orthogonal (i.e., three degrees of freedom), shear

[3]The deformation is affine/homogeneous only at the level of the overall domain. Fine-scale deformation heterogeneities may be present in the microstructure.

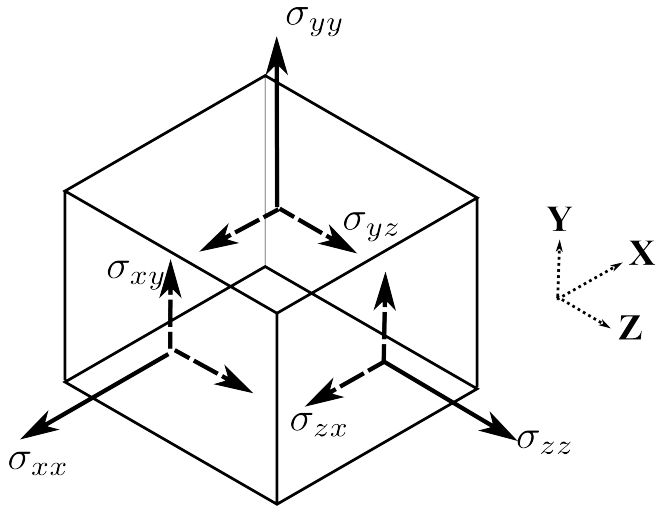

Figure 19: Schematic of an initially-orthogonal MD simulation domain, showing various normal and shear stress components acting at the domain boundaries.

stress/strain components cannot be prescribed. However, in non-constrained simulation domains with six degrees of freedom, all six stress and strain components can potentially be prescribed, with the obvious restriction that the same component of stress and strain cannot be prescribed simultaneously.

To impose deformation, the motion of the domain boundaries in Figure 19 can be prescribed in several ways. In a stress-controlled deformation scheme, the stress σ_{ij} (i,j are Cartesian components) evolves according to the following equation:

$$\sigma_{ij}(t) = \sigma_{ij}^0 + \sigma_{ij}^t(t) \tag{10}$$

where σ_{ij}^0 is constant stress that is applied prior to deformation ($t = 0$), and $\sigma_{ij}^t(t)$ is a 'ramped' stress that varies with time. As the applied stress is ramped, the domain boundaries deform so as to reach the prescribed stress component σ_{ij}. Alternatively, deformation can be imposed by prescribing specific strain components; usually, these are prescribed to simulate a constant strain rate ϵ_{ij}. Based on the stress/strain components prescribed, and the deformation degrees of freedom of the simulation domain, three types of multiaxial deformation schemes have been implemented:

- *Ramped principal stress:* The simulation domain is constrained to remain orthogonal. All three normal stress components are prescribed and ramped up at different rates

Table 1: A comparison of the capabilities of different stress- and strain-controlled deformation schemes employed in this work.

Deformation Method	*Proportional loading (in $\boldsymbol{\sigma}$ space) possible?*	*Stable flow possible?*	*Can impose confining pressure?*
Ramped principal stresses	Yes	No	Yes
Ramped principal strains	No	Yes	No
Direct shear	Yes	Yes	Yes

along different directions. No strains are prescribed.

- *Ramped principal strains:* The simulation domain is constrained to be orthogonal. No normal stresses are prescribed. Normal strains are ramped at different rates.

- *Direct shear:* The simulation domain is not constrained to remain orthogonal (i.e., it can warp). All normal stress components are prescribed, and two out of three shear stress components are prescribed as zero. Along the remaining shearing direction, either a ramped shear stress or a constant shear strain rate is applied.

The above schemes are chosen to simulate specific multiaxial deformation paths. For example, the ramped principal stress scheme is useful for exploring biaxial and triaxial loading paths in the space of principal stresses. Based on the choice of the time-invariant and ramped stresses (Equation 10) both proportional and non-proportional loading paths can be simulated. However, a drawback of the ramped principal stress scheme is that deformation beyond the yield point is not stable. This drawback is avoided in the ramped principle strain scheme, although the latter scheme comes with a trade-off that an imposed stress, e.g., a time-invariant confining pressure, cannot be applied. The direct shear scheme has neither of these limitations. However, it does require a fully flexible simulation domain, and therefore does not directly probe the space of principal stresses. The differences in capabilities of the three deformation schemes are compared in Table 1.

All simulations in this thesis were performed using the LAMMPS MD package [163, 111] developed at Sandia National Laboratories. At time step of 1 fs was used to integrate the

atomic equations of motion. Snapshots of the simulated microstructures were rendered using the OVITO package [205].

2.7.3 Extracting information from atomistic simulations: Computational tools

In recent years, advances in computing technology have significantly increased the length and time scales accessible to atomistic simulation. This has resulted in massively parallel simulations of material mechanics that have sampled volumes containing up to a billion atoms [28]. In these studies, large-scale dislocation interaction/multiplication can been observed explicitly, and a variety of defect structures (dislocation debris) are introduced into the microstructure. Identification and classification of defect structures and microstructural rearrangement mechanisms is essential in order to benefit from the vast amounts of information that is typically obtained from atomistic simulations.

In metals, defects such as dislocations and grain boundaries can be resolved using the centrosymmetry parameter [99] which measures deviations from inversion symmetry in an atom's neighborhood containing nearest neighbor (NN) atoms. The centrosymmetry parameter vanishes for atoms in a perfect lattice (provided the lattice has inversion symmetry), but produces a positive value for atoms that belong to defects. A more precise metric of local crystallinity is Common Neighbor Analysis (CNA) [232], where an atom is classified as belonging to one of several crystal structures (fcc, bcc, hcp etc.) by counting the number of NNs shared by an atom and its nearest neighbor. CNA distinctly resolves atoms of different local crystallinity and produces consistent results even in elastically-deformed atomic configurations. For a review of various other structure identification methods used in atomistic simulations, the reader is referred to Stukowski [206].

Metrics that classify atoms based on nearest neighbor coordination, such as centrosymmetry and CNA, can be used to distinguish atoms belonging to dislocations and GBs from perfectly stacked, lattice atoms. However, these metrics are based on the instantaneous configuration of atoms and do not necessarily capture the kinematics of the deformation. Therefore, in order to extract information pertaining to microstructural rearrangements due to deformation, metrics based on the *change* in atomic positions with respect to a reference

configuration are needed. For example, the slip vector [295] is one such metric that attempts to quantify the characteristic shear deformation occurring in the neighborhood of an atom, and converges to the Burgers vector in the case of atoms that lie in the wake of dislocations.

Recently, more generalized metrics of deformation at the scale of NNs have been developed. Zimmerman et al. [297] formulated an atomic deformation gradient tensor using interatomic distances, which captures the full tensorial nature of deformation occurring in the neighborhood of an atom with different degrees of non-locality (achieved by extending the computation to include neighbor shells beyond the first NN shell, also see [76]). Tucker et al. [234] extended this approach to compute an instantaneous velocity gradient tensor and used it to visualize footprints of GB migration, sliding and dissociation in bicrystals under shear loading. Based on different decompositions of the deformation gradient and the velocity gradient, an entire family of *continuum metrics*[4] are available. These continuum metrics can help estimate deformation fields in the neighborhood of atoms and when used in conjunction with coordination-based metrics, can decouple deformation fields in different phases and around defect structures.

The atomic deformation gradient $\mathbf{F}$ maps interatomic distances in the reference configuration to those in the current configuration *in a particular atom's neighborhood*:

$$x_i^{\alpha\beta} - F_{iI} X_I^{\alpha\beta} = 0 \tag{11}$$

Here, α and β refer to an atom and its neighbor, respectively, and x denotes the interatomic distance vector. In conformity with standard continuum mechanics conventions, uppercase (lowercase) symbols refer to quantities in the reference (current) configuration. Since $\mathbf{F}$ cannot be completely determined using only one $(\alpha - \beta)$ atom pair, several neighbors of an atom need to be considered in a region defined by the neighbor shell(s) of the atom. However, a single value of $\mathbf{F}$ may not satisfy Equation 11 exactly for all (α, β) pairs; it will lead to a small error on the right hand side. The deformation gradient $\mathbf{F}$ for atom α is the 'best-fit' tensor obtained by minimizing the sum of squares of the errors, B_i,with respect to $\mathbf{F}$, where B_i is defined as below:

[4]named so due to their continuum–like formulation.

$$B_i^{\alpha} = \sum_{\beta=1}^{n_\beta} (x_i^{\alpha\beta} - F_{iI} X_I^{\alpha\beta})^2 \tag{12}$$

A list of neighboring atoms in the reference configuration is constructed for every atom and maintained throughout the deformation. Note that $\mathbf{F}$ is a neighborhood dependent, *per-atom quantity* and not a generalized mapping of displacements in the bulk from the reference to the deformed configuration.

Other useful metrics can be derived from $\mathbf{F}$. The *microrotation* vector ($\boldsymbol{\phi}$) is obtained by taking a multiplicative decomposition of $\mathbf{F}$ into rotation $\mathbf{R}$ and stretch $\mathbf{U}$ tensors:

$$\mathbf{R} = \mathbf{F}\mathbf{U}^{-1}$$

$$\mathbf{R}_{skew} = \frac{1}{2}(\mathbf{R} - \mathbf{R}^T) \tag{13}$$

$$\phi_k = -\frac{1}{2}\epsilon_{ijk}(R_{skew})_{ij}$$

where ϵ_{ijk} is the permutation tensor. Also derived from $\mathbf{F}$ is the Green strain, $\mathbf{E}$, which is a strain measure in the deformed atomic neighborhood, defined by:

$$E_{IJ} = \frac{1}{2}(F_{iI}F_{iJ} - \delta_{IJ}) \tag{14}$$

and δ_{IJ} is the Kronecker delta symbol.

Metrics for deformation kinematics based on instantaneous configuration rely on the velocity gradient $\mathbf{L}$, and these can be used to extract *vorticity* or spin in the neighborhood of an atom, i.e.,

$$\mathbf{L} = \frac{\partial \mathbf{v}}{\partial \mathbf{x}}$$

$$\mathbf{L} = \mathbf{D} + \mathbf{W} \tag{15}$$

In Equation 15, $\mathbf{L}$ is the spatial gradient of the atomic velocity vector field ($\mathbf{v}$), and is decomposed into a deformation rate $\mathbf{D}$ (symmetric) and a spin $\mathbf{W}$ (skew-symmetric). The vorticity vector $\mathbf{w}$ is the dual vector of $\mathbf{W}$, i.e.,

$$w_k = -\frac{1}{2}\epsilon_{ijk}W_{ij} \tag{16}$$

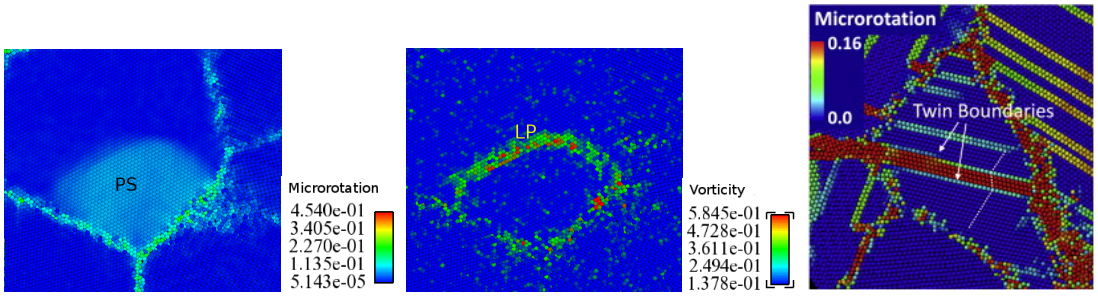

(a) (b) (c)

Figure 20: Resolving the footprint of defect structures using non-local deformation metrics. (a), (b): Snapshots of a Shockley partial dislocation loop in a NC Cu sample (15 nm grain size) at 4% uniaxial strain rendered using (a) microrotation and (b) vorticity metrics (absolute values only). Notice that the partially slipped region (PS) and the leading partial (LP), are separately resolved. (c) shows a different grain in the same sample, where atoms belonging to a twin are distinguished by their characteristic value of microrotation.

The metrics $\mathbf{F}$, $\boldsymbol{\phi}$, $\mathbf{E}$, and $\mathbf{w}$ can be employed to resolve deformation fields that develop as a result of competing deformation mechanisms in NC metals. An example of the utility of these deformation metrics is shown in Figure 20. Specifically:

- Tensorial measures of strain can reveal correlation between distortion and dilatation in and around defect structures.
- The vorticity vector $\mathbf{w}$ can assist in identifying activated sub-volumes and cooperative mechanisms of defect evolution.
- Microrotation $\boldsymbol{\phi}$ can resolve the rotational component of microstructure rearrangement (especially twinning or GB migration) in the atomic neighborhood. Over longer ranges, the gradient of microrotation relates to the lattice curvature.

The procedure used to obtain $\mathbf{F}$ can be extended to derive expressions for spatial gradients of the rotation $\mathbf{R}$ and stretch $\mathbf{U}$. Equation 11 is a linear approximation of the deformation, i.e., it expresses $x^{\alpha\beta}$ as a 1st order Taylor series expansion in $X^{\alpha\beta}$. The linear approximation accounts for 3-D rotations and stretches, but does not capture gradients in these quantities. Zimmerman et al.'s original work [297] introduced an analytical expression for the 2nd gradient of deformation, $H_{iKL} = \frac{\partial x_i^2}{\partial X_K \partial X_L}$, via a two-term Taylor series

expansion of $x^{\alpha\beta}$ in terms of $X^{\alpha\beta}$:

$$x_i^{\alpha\beta} = F_{iI} X_I^{\alpha\beta} + \frac{1}{2} H_{iKL} X_K^{\alpha\beta} X_L^{\alpha\beta} \tag{17}$$

The reader is referred to [297] for precise expressions for F_{iI} and H_{iKL}. Note that F_{iI} in Equation 11 and Equation 17 is not the same quantity. Assuming that $\mathbf{F}$ and $\mathbf{H}$ have been computed for a particular deformation, the gradients of $\mathbf{R}$ and $\mathbf{U}$ can be obtained from $\mathbf{F}$ and $\mathbf{H}$ via tensor manipulations only, without invoking neighbor distances (e.g., $x^{\alpha\beta}$) in the reference and/or current configurations. For that reason, the rest of the derivation uses lowercase indices only.

To compute gradients $\vec{\nabla}\mathbf{R}$ and $\vec{\nabla}\mathbf{U}$ in terms of $\mathbf{F}$ and $\mathbf{H}$ (both obtained from eq. 17), we begin with the right polar decomposition of the deformation gradient F:

$$F_{ij} = R_{ip} U_{pj} \tag{18}$$

Differentiating once:

$$F_{ij,k} = R_{ip} U_{pj,k} + R_{ip,k} U_{pj} \tag{19}$$

Rearranging terms:

$$R_{ip,k} = (F_{ij,k} - R_{ip} U_{pj,k}) U_{pj}^{-1} \tag{20}$$

Interchanging j and p:

$$R_{ij,k} = (H_{ipk} - R_{ij} U_{jp,k}) U_{jp}^{-1} \tag{21}$$

On the right hand side of Equation 21, the only unknown is the spatial gradient of $\mathbf{U}$, i.e., $U_{jp,k}$. To express $U_{jp,k}$ in terms of known quantities, we use the fact that U is the square root of the right Cauchy-Green deformation tensor $\mathbf{C}$, which is itself a function of the deformation gradient $\mathbf{F}$.

$$C_{ij} = U_{ip} U_{pj} = F_{pi} F_{pj} \tag{22}$$

Differentiating once:

$$C_{ij,k} = U_{ip,k} U_{pj} + U_{ip} U_{pj,k} = F_{pi,k} F_{pj} + F_{pi} F_{pj,k} \tag{23}$$

Since C is symmetric:

$$C_{ij,k} = U_{jp,k}U_{pi} + U_{ip}U_{pj,k} \tag{24}$$

And since U is also symmetric:

$$C_{ij,k} = 2U_{iq}U_{qj,k} = F_{pi,k}F_{pj} + F_{pi}F_{pj,k} \tag{25}$$

This implies that:

$$U_{qj,k} = \frac{1}{2}U_{iq}^{-1}(F_{pi,k}F_{pj} + F_{pi}F_{pj,k}) \tag{26}$$

Or in terms of the 2nd gradient of deformation:

$$U_{ij,k} = \frac{1}{2}U_{qi}^{-1}(H_{pqk}F_{pj} + F_{pq}H_{pjk}) \tag{27}$$

Substituting Equation 27 into Equation 21, the rotation gradient tensor is obtained:

$$R_{ij,k} = H_{ipk}U_{jp}^{-1} - \frac{1}{2}R_{ij}U_{qi}^{-1}(H_{rqk}F_{rp} + F_{rq}H_{rpk})U_{jp}^{-1} \tag{28}$$

Besides $R_{ij,k}$ and $U_{ij,k}$, the strain gradient, $E_{ij,k}$, can be obtained directly from Equation 24.

The tensors $R_{ij,k}$ and $U_{ij,k}$ extend the deformation gradient formulation to compute atomic-scale measures of curvature and strain gradients in atomistic simulations. Although expressions have been derived for these gradient quantities, their utility and limitations are yet to be systematically explored for simple atomistic geometries, e.g., defect-free single crystals. Therefore, neither $R_{ij,k}$ nor $U_{ij,k}$ has been used for the purpose of analysis in this thesis.

CHAPTER III

RESOLVING DEFORMATION-INDUCED DEFECT AVALANCHES IN ATOMISTIC SIMULATIONS

Note: The results presented in this chapter have also appeared in Tiwari et al. [217].

3.1 Introduction

Many of the unique mechanical properties of nanocrystalline (NC) metals in the grain size range 5-20 nm arise from the interplay between various interface-mediated deformation mechanisms, namely, grain boundary (GB) sliding/migration processes and dislocation nucleation at the scale of nanograins. Several kinetic aspects of these mechanisms, e.g., tension-compression strength asymmetry [187, 56, 230], role of non-Schmid stresses in dislocation nucleation [201], and glass-like shear transformations in GBs [73, 128], suggest that the 3-D inelastic yield and flow behavior of fcc NC metals might exhibit anisotropy. However, quantification of this anisotropy is problematic in NC metals due to two reasons: first, due to the partial reversibility of deformation in the non-linear regime of the stress-strain curve [25, 26, 168]. This implies that the use of standard strain offsets on the stress-strain curve(s) may not necessarily capture the onset of inelasticity. Second, inelastic yield in NC Cu occurs via a combination of inter-granular and intra-granular mechanisms; therefore, empirical measures of the yield anisotropy cannot be easily related to the sensitivity of individual deformation mechanisms to the stress state.

The present chapter introduces methods via which Molecular Dynamics (MD) simulations could be used to unambiguously demarcate the elastic-plastic transition during the deformation of NC Cu. In this context, it is helpful to view plasticity as the primarily stress–driven motion of material defects that dissipates stored elastic energy in the process. The material defect motion may refer to any of the following processes: dislocation glide between pinning obstacles, GB sliding 'events', or twinning, among others. Rather than going into the details of the precise atomic rearrangement underlying these different classes

of defect motion, it is worthwhile from a statistical standpoint to quantify the contribution of individual inelastic rearrangements in the form of generalized microstructural rearrangement events (MREs) of a dissipative nature, with the only distinction among inelastic events being the magnitude of dissipation. With this perspective, the elasto-plastic deformation can be interpreted in terms of a gradual proliferation of MREs, from sporadic, uncorrelated events (pre-yield), to a cooperative *avalanche* of events (yield). Such an avalanche is a definitive indicator of elastic-plastic transition, regardless of the complexity of the underlying deformation mechanisms, or the nature of the stress-strain response. In the present work, stress-controlled, isothermal deformation of NC Cu is simulated using MD, and the yield transition is demarcated using a thermostat coupled to the atomic dynamics, which compensates for the localized heating due to dissipative MREs. As the deformation proceeds, the proliferation of dissipative MREs is manifested as an increase in rate at which the thermostat withdraws heat energy from the atomistic ensemble. To the author's knowledge, such a study of the stress–space dissipation profile in context of the elastic–plastic transition in a heterogeneous atomistic system has not been reported to date.

This chapter is organized as follows: in Section 3.2, the formulation of the isothermal MD framework has been reviewed, and the rationale behind selecting the thermostat as the indicator of an avalanche in inelastic dissipation has been discussed. In Section 3.3, we describe the methodology of isothermal stress–controlled loading, which is subsequently applied to two NC Cu microstructures having different geometric constraints. Section 3.4 presents several results that demonstrate the efficacy of the thermostat in resolving dissipative defect avalanches, and inspect correlations between the thermostat compensation rate and the evolving microstructure. The potential merits and limitations of a thermostat–based quantification of the elastic–plastic transition are discussed in Section 3.4. We conclude that a dissipation avalanche approach to yielding can serve as the preliminary theoretical basis for a physically-faithful, atomistically-informed, multiaxial theory of yield and plastic flow for fcc NC metals.

3.2 Theory

MD simulations are used to evaluate the response of a material by numerically solving for trajectories of atoms or molecules in an interatomic potential field subject to appropriate laws of motion. The numerical methods in MD usually employ the Hamiltonian formulation of classical dynamics. In a Hamiltonian system, the total energy of a N-particle system is conserved and is the sum of the microkinetic energy and potential energy of the particles, i.e.,

$$H = \sum_{i=1}^{N} \frac{\mathbf{p}_i^2}{2m_i} + U(\mathbf{r}_1, \mathbf{r}_2, \mathbf{r}_3 \ldots, \mathbf{r}_N) \tag{29}$$

where H is the system's Hamiltonian (or total energy functional), $\mathbf{p}_i(t)$ and $\mathbf{r}_i(t)$ are respectively the momentum and position of the ith particle, m_i is the particle mass, and $U(\mathbf{r}_1, \mathbf{r}_2, \mathbf{r}_3 \ldots, \mathbf{r}_N)$ is the potential energy of the system.

From a statistical mechanics standpoint, dynamics of a Hamiltonian system samples the microcanonical ensemble (NVE) where the number of particles (N), system volume (V) and internal energy (E) are constant over time. While such a system is necessarily isolated, real material systems *can* exchange heat, work and/or mass with their surroundings. Therefore, to simulate real materials, techniques have been developed to regulate the independent variables of temperature (T) and pressure (P) during a simulation. As a common feature, all such techniques of thermodynamic control employ a feedback mechanism to drive the system to the desired thermodynamic state. In the canonical (NVT) ensemble, the feedback is through deviations in the instantaneous micro-kinetic energy of the system and can be visualized as a virtual *heat–bath* coupled to the system. In the isothermal–isobaric (NPT) ensemble, an additional feedback from the instantaneous system volume is also included; here, one can visualize virtual *pistons* that adjust the bounds of the simulation domain to approach the target pressure.

The conservation of thermodynamic variables and associated feedback mechanisms constrain the dynamics of particles in the system, and the atomic equations of motion need to be modified accordingly. Several temperature control methods (henceforth called *thermostats*) exist, such as trivial periodic rescaling of atomic velocities, stochastic thermostats

developed by Anderson [6] and Berendson et al. [18], deterministic "extended system" approaches based on Nosé–Hoover (NH) dynamics [155, 88], and more recent formulations that have improved upon the NH framework [141, 133].

Although stochastic thermostats can sample thermodynamic ensembles correctly, the atomic trajectories they produce are unsuitable for modeling solid systems where continuous atomic trajectories are desired, e.g., in predicting the evolution of non-equilibrium defect structures. The extended system approaches do not have this issue, since they augment the system with extra degrees of freedom and result in deterministic, time reversible equations of motion. For a system with N particles in the NPT ensemble, the extended Hamiltonian $H^{'}$ is (from [133]):

$$H^{'} = \sum_{i=1}^{N} \frac{\mathbf{p}_i^2}{2m_i} + \frac{p_\omega^2}{2W} + \frac{p_\eta^2}{2Q} + U(\mathbf{r}_1, \mathbf{r}_2, \mathbf{r}_3 \ldots, \mathbf{r}_N, V) + (N_\mathrm{f} + 1)k_\mathrm{B}T\eta + P_\mathrm{ext}V \qquad (30)$$

In Equation 30, the stabilizer variables are integrated into the system as virtual 'particles', each possessing a displacement, mass, and momentum. For the thermostat, these quantities are respectively η, Q and p_η, and for the barostat, ω, W, and p_ω. Note that P is stabilized to the value of P_ext through fluctuations in V, hence, the barostat displacement ω does not appear explicitly in Equation 30 but is in fact proportional to $\log V$. Overall, $(N_\mathrm{f} + 1)k_\mathrm{B}T\eta$ and $P_\mathrm{ext}V$ are the potential energies associated with the thermostat and barostat 'particles' respectively. N_f refers to the number of degrees of freedom ($= dN$ for a d dimensional system). Note that the system in Equation 30 produces NPT dynamics in the space of physical variables but is still energy–conserving in the extended space of physical and virtual variables. The associated equations of motion for target temperature

T and pressure P_{ext} are from Martyna, Tobias and Klein (MTK) [133]:

$$
\begin{aligned}
\dot{\mathbf{r}}_i &= \frac{\mathbf{p}_i}{m_i} + \frac{p_\omega}{W}\mathbf{r}_i, \\
\dot{\mathbf{p}}_i &= \mathbf{F}_i - \left(1 + \frac{d}{N_{\text{f}}}\right)\frac{p_\omega}{W}\mathbf{p}_i - \frac{p_\eta}{Q}\mathbf{p}_i, \\
\dot{V} &= \frac{dVp_\omega}{W}, \\
\dot{\eta} &= \frac{p_\eta}{Q}, \\
\dot{p}_\omega &= dV(P_{\text{int}} - P_{\text{ext}}) + \frac{d}{N_{\text{f}}}\sum_{i=1}^{N}\frac{\mathbf{p}_i^2}{m_i} - \frac{p_\eta}{Q}p_\omega, \\
\dot{p}_\eta &= \sum_{i=1}^{N}\frac{\mathbf{p}_i^2}{m_i} + \frac{p_\omega^2}{W} - (N_{\text{f}} + 1)k_{\text{B}}T
\end{aligned}
\tag{31}
$$

for a system that allows only isotropic volume fluctuations. The evolution equation for $\dot{V}$ acts as the barostat, since $\dot{\omega} = p_\omega/W = \dot{V}/(dV)$. The fluctuations in the virtual 'stabilizer' variables η and ω provide a dynamic force to the particle momenta ($\mathbf{p}_i$) driving the average particle kinetic energy and internal pressure P_{int} respectively towards equilibrium. The equation set 31 can be extended to anisotropic systems by ascribing several barostat variables corresponding to different components of the stress tensor $\boldsymbol{\sigma}$, a scenario that is relevant to solids.

Nosé–Hoover chains (NHC) [132] were initially developed to induce ergodicity in stiff systems, something the original Nosé–Hoover (NH) equations lacked. In this method, besides the atomic velocities, the thermostat η itself is thermostatted using a series of n secondary thermostats forming a chain (η_1, η_2, $\ldots\eta_n$). Of these n thermostats, only η_1 is directly coupled to the the atomic velocities. Just as η_1 drives the fluctuations in the atomic momenta to a time averaged kinetic energy of $N_{\text{f}}k_{\text{B}}T/2$, η_k drives the fluctuations in the "kinetic energy" of η_{k-1}, i.e., $p_{\eta_{k-1}}^2/2Q_{k-1}$ such that η_{k-1} fluctuates with a time averaged kinetic energy of $k_{\text{B}}T/2$ at thermal equilibrium. To obtain the NHC equations of motion, in equation set 31, the equation for p_η is modified as shown below, η is replaced by η_1 and

the evolution equations for the various η_k variables are appended (from [132]):

$$\begin{aligned}
\dot{p}_{\eta_1} &= \sum_{i=1}^{N} \frac{\mathbf{p}_i^2}{m_i} + \frac{p_\omega^2}{W} - (N_\mathrm{f}+1)k_\mathrm{B}T - \frac{p_{\eta_2}}{Q_2}p_{\eta_1} \\
\dot{p}_{\eta_k} &= \frac{p_{\eta_{k-1}}^2}{Q_{k-1}} - k_\mathrm{B}T - \frac{p_{\eta_{k+1}}}{Q_{k+1}}p_{\eta_k} \\
\dot{p}_{\eta_n} &= \frac{p_{\eta_{n-1}}^2}{Q_{n-1}} - k_\mathrm{B}T \\
\dot{\eta_k} &= \frac{p_{\eta_k}}{Q_k}
\end{aligned} \tag{32}$$

$$k = 2, 3, 4 \ldots n$$

where every η_k is stabilized by η_{k+1}, except η_n, which evolves freely. In a similar manner, the NHC equations can be used to stabilize a barostat variable ω in the form of chain variables $\omega_1, \omega_2 \ldots \omega_n$, effectively creating a 'thermostat' chain for the barostat. In this chain, the barostat ω_1 is driven by the deviation of the system's pressure from the target pressure, the next chain variable ω_2 drives ω_1 to a "kinetic energy" ($p_{\omega_1}^2/2W_1$) of $k_\mathrm{B}T/2$, and so on for subsequent ω_k variables. Thermostat chains drive a system towards thermodynamic equilibrium quicker than single thermostat and barostat variables, since these chains explicitly stabilize the thermodynamic stabilizer variables (η_1 and ω_1) themselves.

Although the set of ordinary differential equations 31 and 32 were proposed to regulate temperature and pressure in systems at equilibrium, they hold special significance with respect to the evolution of dissipative systems. In general, any dissipative structural change in a system will disturb the (stable) internal temperature and pressure and will force the stabilizer variables η, ω to evolve so as to cancel out the effects of the disturbance. A material undergoing deformation from the elastic to the plastic regime is one such system where stored strain energy is released through various mechanisms of irreversible atomic rearrangement— dislocation glide, twinning, grain boundary processes (GBPs) or stress assisted phase transformations. Each mechanism, upon activation, locally releases some stored potential energy (elastic strain energy) that is immediately manifested as a localized temperature rise, or a *burst* in the kinetic energy of some subset of atoms. The thermostat and barostat together counteract this simultaneous temperature rise and stress–relaxation by exchanging heat/work with the system. The activity of the thermostat and

barostat system over the course of elastic–plastic deformation can potentially contain novel information about not only possible correlations in the activation of different deformation mechanisms, but also the magnitude and frequency of inelastic events from isolated *bursts* to a cooperative avalanche.

3.3 Methodology

3.3.1 Microstructure and morphology

Stress–controlled deformation was carried out on two Cu 'samples', a nanocrystalline thin film (TF) and a fully 3D NC microstructure (PC): as shown in Figure 21. The TF sample consists of 15 grains created through a two–dimensional Voronoi [253, 176] construction extruded to a thickness of 2 nm. The PC sample was similarly constructed by tessellating a cubical domain into 100 polyhedral grains through a three–dimensional Voronoi construction. The mean grain size was obtained as the side length of a square (cube) whose area (volume) is equal to the mean grain area (volume) in the TF (PC) sample and sample sizes were chosen to create a mean grain size of 5nm. The lattice orientations of constituent grains were chosen randomly from the set of 3D rotations with respect to the global Cartesian coordinate system aligned parallel to the simulation domain edges. In both samples a more stable starting structure was achieved by selectively removing atoms that are closer than one half of the lattice parameter to any of their neighboring atoms. Both initial structures were further stabilized by a conjugate gradient energy minimization algorithm at 0 K to a binding energy convergence criterion of 10^{-25} per minimization step. Finally, the samples were equilibrated under NPT control, to zero external pressure for a period of 1 ns at the intended temperature of deformation (10 K or 300 K).

3.3.2 Deformation procedure

For the TF sample, deformation was performed at a temperature 10 K. At this temperature, there is very little thermal activation, and plastic events are primarily stress driven. The PC sample was tested both at 10 K and at 300 K in order to observe changes in kinetics of inelasticity due to thermally-assisted microstructural rearrangement. A proportional loading scheme was implemented within the MTK framework as follows: the simulations

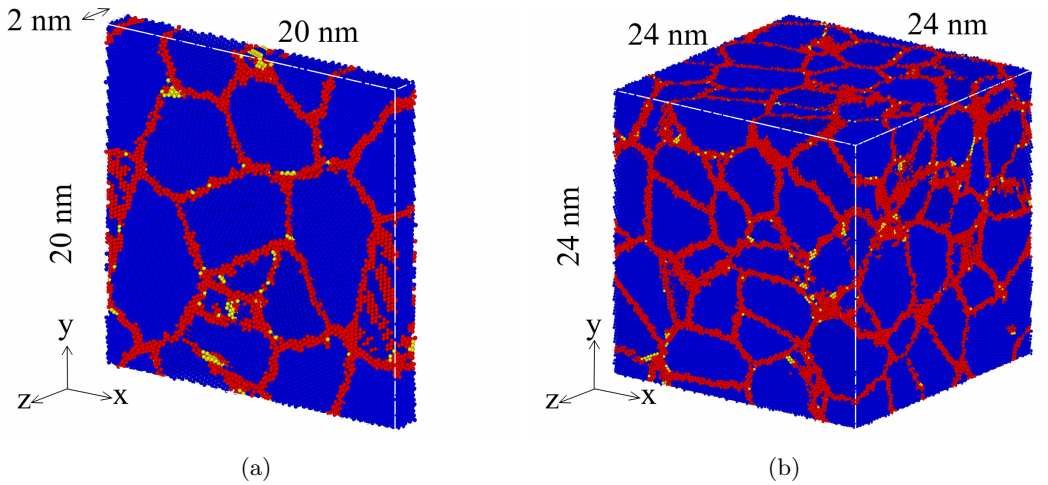

Figure 21: Initial geometries of the material samples under consideration. (a) NC thin film and (b) 3D NC microstructure. The atoms are colored according to local crystalline class as computed through common neighbor analysis [232]. Blue denotes atoms that are locally face centered cubic (class fcc), yellow denotes hexagonal close packed (class hcp) atoms, and red represents non-12 coordinated atoms (class $other$), constituting the GB network.

were performed in an orthogonal 3D spatial domain, with edges oriented along the Cartesian x, y and z axes and periodic boundary conditions along each pair of opposite box faces. The average pressures on the box faces perpendicular to the x, y and z direction were controlled independently.

To induce deformation, the pressures on each pair of opposite faces were ramped proportionally according to the desired stress ratio, up to the point of ductile failure (this is the ramped principal stress deformation scheme as described previously in Section 2.7.2). For a coordinate system oriented along the box edges, the imposed pressures correspond to normal stresses σ_{xx}, σ_{yy} and σ_{zz} acting on the faces of the box. Since there are no net shear tractions, these normal stresses are also principal stresses and are related according to:

$$\sigma_{xx}(t) = \lambda_1 \sigma_{yy}(t) = \lambda_2 \sigma_{zz}(t) = \lambda t \tag{33}$$

where λ, λ_1 and λ_2 are proportionality constants. Equation 33 constrains the imposed principal stresses to rise with time, while remaining in the desired ratio to each other. Different choices of λ_1 and λ_2 can lead to a variety of multiaxial stress states. In this chapter, we restrict our focus to uniaxial loading ($\sigma_{yy} = \sigma_{zz} = 0$); multiaxial loading paths

have been explored in chapters 4-6.

Using the ramped–stress deformation scheme, the transition from elastic to plastic behavior can be approached in a proportional manner at a finite temperature. This stress–controlled loading scheme contrasts with a strain–controlled scheme, implemented quite commonly in past atomistic studies [21, 55, 197, 227, 234, 237] or a quasistatic loading scheme of 0 K deformation–relaxation cycles [128, 23].

In Equation 33, the stress ramping rate λ is an important parameter. Under dynamic loading, care must be taken to avoid straining a system too fast. In strain–controlled loading, strain rates of 10^8 s^{-1} to 10^9 s^{-1} are common in MD and are a consequence of the short time scales accessible, on the order of nanoseconds. Very high strain rates are known to cause spurious stress increases near the elastic–plastic transition in NC MD simulations due to the inability of inelastic deformation mechanisms to compete with the imposed strain rate [21]. Therefore, for stress–controlled loading, several stress ramping rates were compared spanning three orders of magnitude from 0.005 GPa ps^{-1} to 0.5 GPa ps^{-1}.

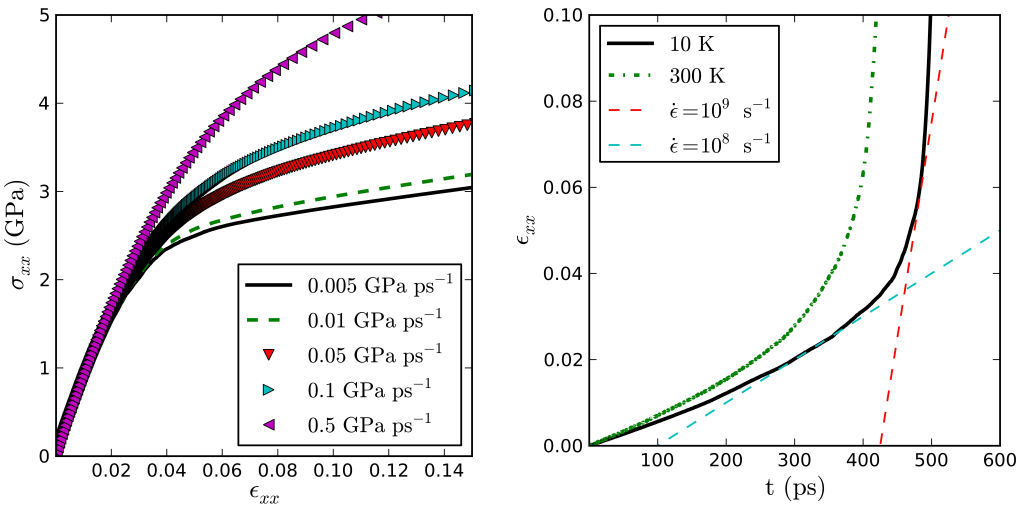

Figure 22: (a) The stress–strain response of the PC sample at 10 K loaded in uniaxial tension along the x direction, comparing five stress ramping rates ($\dot{\sigma}_{xx}$). (b) Plot of tensile strain vs. time for $\dot{\sigma}_{xx} = 0.005$ GPa ps^{-1}, at 10 K and 300 K. The straight lines denoting constant strain rates of 10^8 s^{-1} and 10^9 s^{-1} are shown for reference.

The response of the PC sample loaded along the x direction for five different tensile

stress rates is shown in Figure 22(a). The stress rates selected were as follows: $\lambda = \dot{\sigma} =$ 0.005 GPa ps^{-1}, 0.01 GPa ps^{-1}, 0.05 GPa ps^{-1}, 0.1 GPa ps^{-1} and 0.5 GPa ps^{-1}. Since the tensile stress escalates faster for the higher $\dot{\sigma}$, the strain rate induced also varies directly with $\dot{\sigma}$. Although it is theoretically desired that the induced strain rate be as small as possible to facilitate comparisons with quasi-static loading, the timescale limitation of MD requires—for the same reason as in the case of strain–controlled deformation—that several percent deformation be achieved within simulation times on the order of nanoseconds. In Figure 22(a), the markers are drawn at equally spaced time intervals and it can be seen that under 0.5 GPa ps^{-1}, the same amount of strain is achieved very quickly as compared to the smaller stress–rates. As expected, the upper three curves register higher tensile stresses before flow begins while the lower curves (0.005 GPa ps^{-1} and 0.01 GPa ps^{-1}) appear to converge. Naturally, any further reduction of flow stress due to operation of thermally activated deformation processes cannot be achieved at these rates. The stress–strain behavior can be attributed to the fact that activation of dislocations and/or GBPs cannot keep pace with the rate of stress increase if the imposed stress escalates too quickly. To avoid bypass of deformation mechanisms to the greatest extent possible, the lowest rate of 0.005 GPa ps^{-1} was selected for further simulations.

The uniaxial tensile strain evolution at the selected $\dot{\sigma}$ of 0.005 GPa ps^{-1} was computed at 10 K and 300 K for the PC sample and is shown in Figure 22(b). Since there is no upper bound on the applied stress, the deformation becomes unstable at some point of time no matter how small $\dot{\sigma}$ is chosen. The strain rates from the curves shown in Figure 22(b) were measured to be less than $10^9 s^{-1}$ for deformation up to 6% tensile strain at 10 K and up to $\approx$ 5.5% at 300 K. These strain rates, though very high, are well within the range of strain rates previously used [21, 197, 227, 234, 237] in MD simulations of dynamic strain–controlled deformation to predict properties of Cu bicrystals and nanocrystals.

3.3.3 Thermodynamic control

Due to the multiaxial nature of the loading scheme, it is desired that the material have enough degrees of freedom to deform in the directions of the principal stresses. Therefore,

the approach of thermodynamic control outlined in Section 3.2 needs to be extended to allow for anisotropic box deformations. This was achieved through one NHC thermostat chain and three NHC barostat chains. The barostat chains were separately coupled to the internal pressures obtained from the Cartesian components of atomic velocities. Three primary barostat variables ω^x, ω^y and ω^z were thus coupled to components of the system's internal pressure arising from the respective atomic velocity components v_x, v_y and v_z. A NHC of length three was chosen for all primary stabilizer variables. Therefore, the temperature was controlled through a single set of thermostats of chain length three: (η_1, η_2, η_3) and the principal stresses (pressures) through three sets of barostats, each of chain length three, i.e., $(\omega_1^x, \omega_2^x, \omega_3^x)$, $(\omega_1^y, \omega_2^y, \omega_3^y)$ and $(\omega_1^z, \omega_2^z, \omega_3^z)$.

The onset of bond breaking (fracture) or bond switching (plasticity) produces substantial kinetic energy fluctuations, significantly larger than those in the elastic regime where the atomic displacement field is expected to conform (approximately) to the global deformation field. Admittedly, the Equation sets 31 and 32 are very complex. The NH equations are inherently chaotic and the NHC equations even more so. While it unrealistic to try and precisely predict the dynamics of the stabilizer variables themselves in a deforming NC system under $\boldsymbol{\sigma}, T$ control, it is reasonable, as a first approximation, to assume that the thermostat activity can provide a thermometric measure.

In Equations 32, the evolution of the primary thermostat momentum ($\dot{p}_{\eta_1}$) indicates that the thermostat and barostat evolution is coupled. However, even with this coupling, for large systems the kinetic energy content of the system ($=N_{\mathrm{f}} k_{\mathrm{B}} T$) is generally several orders of magnitude larger than that of a single barostat 'particle' (recall that the thermostat and barostat variables are treated like oscillators with total energy $k_{\mathrm{B}} T$). While looking at the thermal differential due to dissipation in a sufficiently large system, it is therefore safe to ignore the contribution of the barostat kinetic energy to the total kinetic energy fluctuation. With regards to dissipation, it is also expected that a disturbance in the system's kinetic energy will propagate across the entire chain of thermostats η_1, η_2 and η_3 since they are dynamically linked.

3.4 Results

3.4.1 TF sample

The response of the 15–grain TF sample is shown in Figure 23 in the form of evolution curves for strain (ϵ_{xx}), $\dot{\eta_1}$, $\dot{\eta_2}$, $\dot{\eta_3}$, $\sqrt{\dot{\eta_1}^2 + \dot{\eta_2}^2 + \dot{\eta_3}^2}$ and the sample temperature (T) with respect to tensile stress along the x direction (σ_{xx}). The strain increases unbounded starting around 3.0 GPa, indicating the point at which the microstructure loses its resistance to the applied stress. Notably, the stress–strain response of the TF sample is quite smooth, whereas the thermostat response ($\dot{\eta_1}$) is not. All thermostats in the chain show a characteristic oscillatory behavior at low stresses, which is indicative of proximity to thermal equilibrium (see also the evolution of temperature T). However, well within the linear regime of the stress–strain curve, there are isolated disruptions in the oscillatory behavior of $\dot{\eta_1}$ at around 0.5 GPa, 1.0 GPa, 1.7 GPa until the last (also the largest) spike is seen at 2.0 GPa.

These disturbances are consistently reproduced in the velocities of the subsequent chain thermostats $\dot{\eta_2}, \dot{\eta_3}$ with a progressively increasing magnitude. $\dot{\eta_3}$, being the last thermostat and also the only one without a thermostat of its own, is by far the most sensitive to these fluctuations. It is also the least noisy. The occurrence of well-resolved isolated dissipation spikes in the TF sample is consistent with the fact that the TF sample is thin and consists of only 15 grains; it is therefore not representative of the bulk material behavior and was used only as a preliminary test of our methodology. The contribution of each GBP or dislocation propagation event makes a sizable contribution to the dissipation, even though no strain bursts can be seen in the stress–strain response. Additionally, at stresses nearing the flow stress, the nucleation of dislocations can be delayed due to limited slip systems available in the restricted 2nm (periodic) sample thickness, leading to higher stresses before failure.

3.4.2 PC sample

The response of the PC sample to uniaxial tensile stress along the x direction is shown in Figure 24 on the same template as Figure 23. The results have some common features: a smooth stress–strain response and a progressive increase in magnitude of dissipation features (peaks) in going from $\dot{\eta_1}$ to $\dot{\eta_3}$. However, in the PC sample, the dissipation spikes are poorly

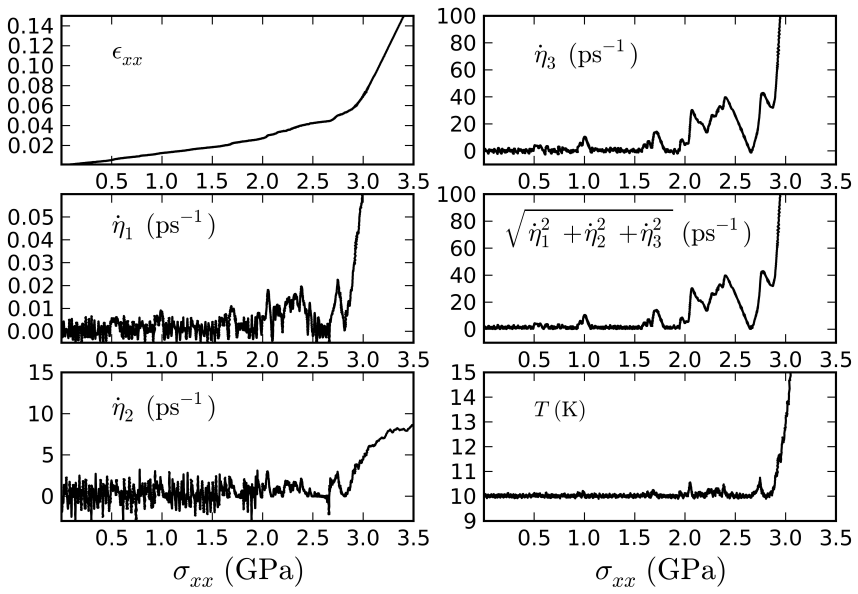

Figure 23: Response of the TF sample loaded in tension along the x direction at 10 K. The evolution of the thermostat velocities $\dot{\eta}_i$ and $\sqrt{\dot{\eta}_1{}^2 + \dot{\eta}_2{}^2 + \dot{\eta}_3{}^2}$ is compared to the evolution of strain (ϵ_{xx}) and temperature (T) w.r.t. tensile stress (σ_{xx}).

resolved in the range 0.7 GPa to 2.0 GPa, comprising a nearly continuous dissipation region, with intermittent depressions. Here too, the uniaxial stress of $\sigma_{xx} \approx 0.8$ GPa at which $\dot{\eta}_1$ shifts from a near-equilibrium (oscillatory) to a dissipative (positive $\dot{\eta}_1$) regime is well within the linear part of the stress–strain curve. The multi-stage dissipation region can be explained on the premise that events comprising GB deformation processes are both more numerous as well as individually small compared to the system size. In the PC sample, unlike the TF sample, there is no geometric restriction on slip and the presence of 100 grains makes the PC sample considerably less anisotropic as well as immune to the dominance of a few discrete inelastic events. The PC sample that exhibits a dissipation profile that is quite diffuse in stress space.

The PC sample's stress-strain responses under uniaxial tension (T) and compression (C) are compared in Figure 25(a), and the evolution of $\dot{\eta}_1$ for these two cases is compared in Figure 25(b). Qualitatively, the evolution of $\dot{\eta}_1$ is quite similar in both cases, where *attempts* towards yielding manifest as peaks separated by depressions. Since deviation from $\dot{\eta}_1 = 0$ represents the severity of a yielding *attempt*, we employ the standard deviation of $\dot{\eta}_1$ to

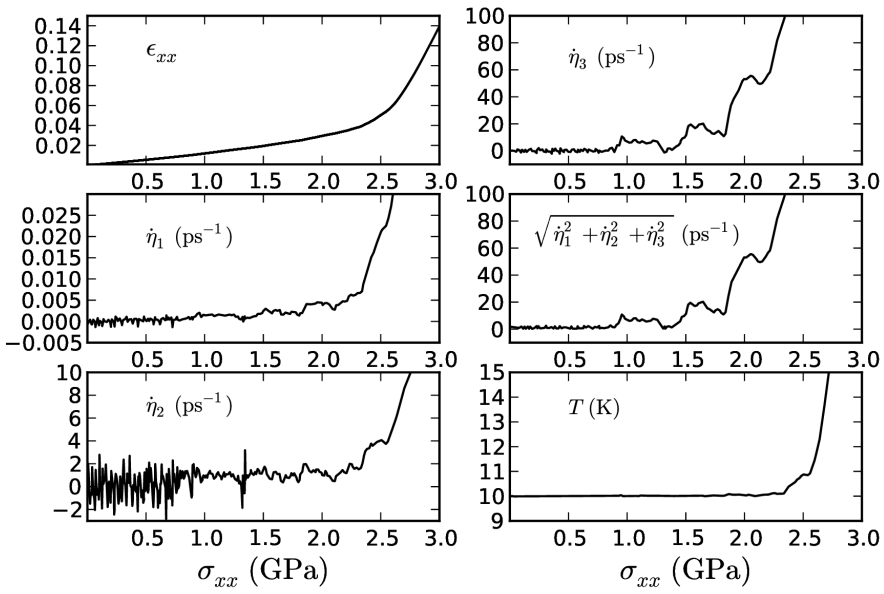

Figure 24: Response of the PC sample loaded in tension along the x direction at 10 K. The evolution of the thermostat velocities $\dot{\eta}_i$ and $\sqrt{\dot{\eta_1}^2 + \dot{\eta_2}^2 + \dot{\eta_3}^2}$ is compared to the evolution of strain (ϵ_{xx}) and temperature (T) w.r.t. tensile stress (σ_{xx}).

gauge the cumulative 'history' of these attempts. The standard deviation Σ[1] is defined as:

$$\Sigma = \sqrt{\frac{1}{n}\sum_{\sigma=0}^{\sigma=\sigma_t}(\dot{\eta}_1(\sigma) - \mu)^2}, \quad \mu = \frac{1}{n}\sum_{\sigma=0}^{\sigma=\sigma_t}\dot{\eta}_1(\sigma) \tag{34}$$

where n values of $\dot{\eta}_1$ are considered between stresses 0 and σ_t. On curves shown in Figure 25(b), given a stress magnitude σ_t, it is possible to compute the standard deviations Σ_{T} and Σ_{C}, using values of $\dot{\eta}_1$ corresponding to stresses lower than σ_t. For stress magnitudes between 0.26 GPa and 2.6 GPa, the relation between Σ_{T} and Σ_{C} is shown in Figure 25(c). In the early stages of deformation characterized by sparse, weakly-correlated rearrangement events, the ratio $\Sigma_{\mathrm{C}}/\Sigma_{\mathrm{T}}$ fluctuates (predominantly below value 1.0), before approaching a value of 0.8 in a fully developed avalanche. Figure 25(c) suggests that attempts towards yielding are statistically less severe in compression than in tension for the same magnitude of applied stress. This manifests in Figure 25(a) as a slight T-C asymmetry of the stress-strain response.

The deformation of the PC sample was also carried out at 300 K, to compare and

[1]Note: Σ here is a symbol for the standard deviation, and should not be confused with Σ, the GB CSL index described in Section 2.4.

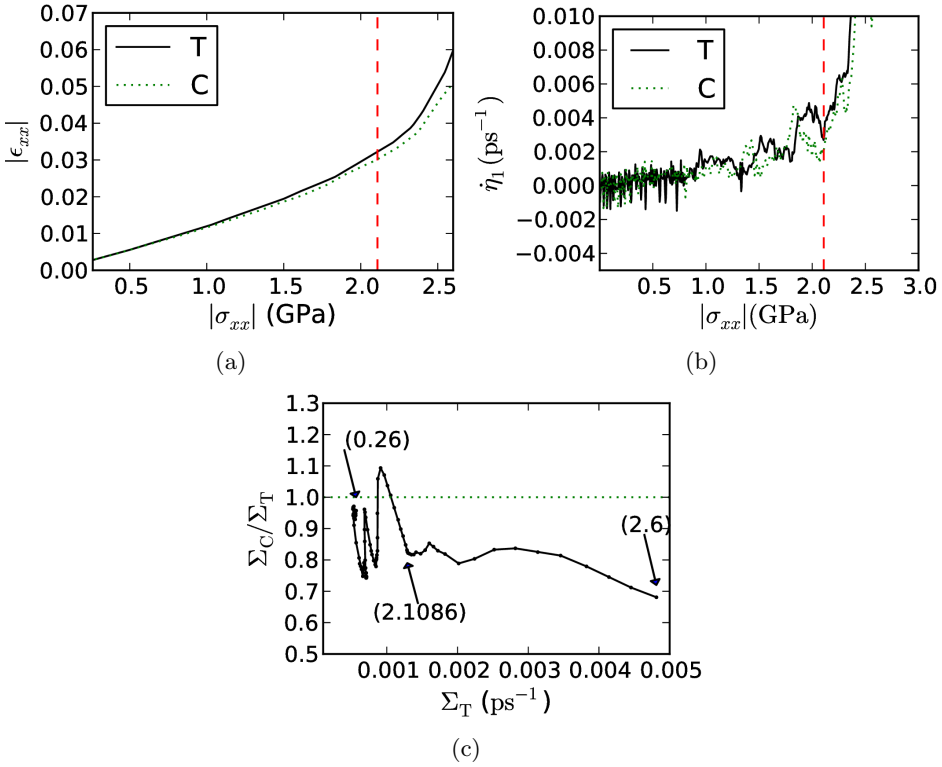

Figure 25: (a) Stress-strain curves of the PC structure under uniaxial tension (T) and compression (C) at 10 K. (b), evolution of $\dot{\eta}_1$ under tension and compression superimposed. (c), ratio of Σ_C and Σ_T as it evolves between stresses of 0.26 GPa and 2.6 GPa. Numbers in parentheses indicate stress in GPa. The dashed lines on plots (a) and (b) denote the stress magnitude of 2.1086 GPa, at which the asymmetry in S stabilizes.

contrast the manner in which the potential energy landscape was traversed in the presence of significant thermal activation. Figure 26 shows the thermostat activity for the PC sample loaded in tension at 300 K. Here, it is no longer possible to resolve multiple stages of dissipation, instead from 0 GPa to 2.1 GPa, there is a continuous *background* of thermostat activity followed by a surge of the thermostat signal at the avalanche. Recall here that the time averaged kinetic energy of the thermostat η_1 is externally driven (i.e., by η_2) to a value $k_{\mathrm{B}}T/2$. At 300 K, the value of $k_{\mathrm{B}}T$ is thirty times its value at 10 K, i.e., η_1 has 30 times the kinetic energy. With this increased thermostat energy content, it is expected that dissipation spurts that required significant compensation by η_1 at 10 K in the form of a sustained positive $\dot{\eta_1}$, can be accommodated within the equilibrium fluctuation of $\dot{\eta_1}$ at 300 K.

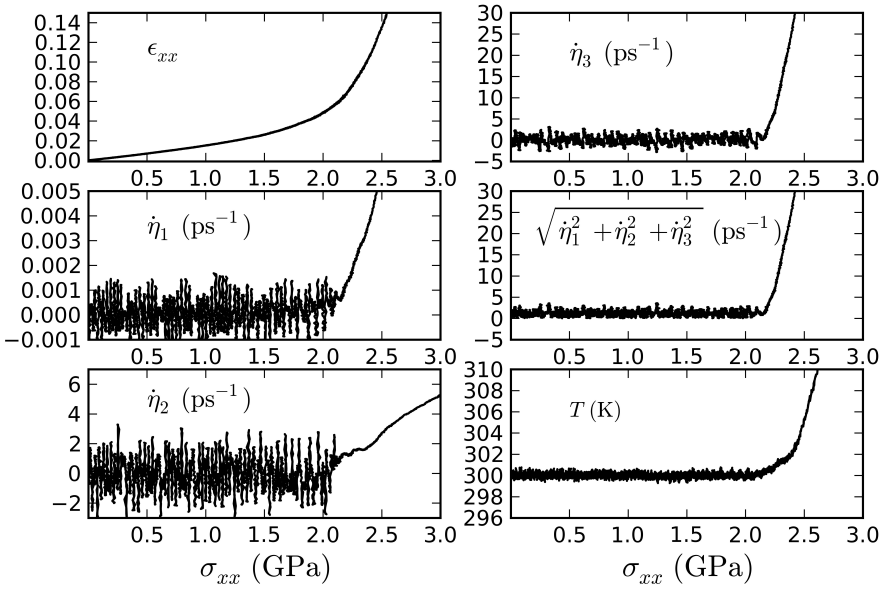

Figure 26: Response of the PC sample loaded in tension along the x direction at 300 K. The evolution of the thermostat velocities $\dot{\eta}_i$ and $\sqrt{\dot{\eta_1}^2 + \dot{\eta_2}^2 + \dot{\eta_3}^2}$ are compared to the evolution of strain (ϵ_{xx}) and temperature (T) w.r.t. tensile stress (σ_{xx}).

3.4.3 Distribution of MREs

The thermostat compensation patterns visible in Figure 23 and Figure 24 contain no information regarding the intergranular or intragranular nature of the causative MREs. While

it is well known that GBs, rather than dislocations, are the dominant carriers of deformation at very small grain sizes such as those considered in this work, the correlation of thermostat compensation to stress-driven microstructure evolution nevertheless needs to be substantiated.

Since the thermostat activity peaks are well-resolved in the TF sample, it is possible to visually ascertain whether those peaks represent interatomic rearrangement in localized regions or sample–wide rearrangements. However, when rendered through CNA (similar to Figure 21(a)), the TF sample did not provide any visible footprint of MREs in the GB network over the course of deformation, except after the emission of dislocations near a stress of 2.0 GPa. Therefore, in order to better render the occurrence of interface–mediated deformation mechanisms, a *slip vector*-based criterion was used. The slip vector $\mathbf{s}_\alpha$ (see Zimmerman et al. [295]), defined for every atom α in the system, provides a measure of local inelastic displacement of nearest neighbor atoms with respect to their positions in a reference configuration. By definition, $|\mathbf{s}_\alpha|$ is non-zero only for atoms that have at least one nearest neighbor displaced by more than half of the Burgers vector of a Shockley partial dislocation ($b_{partial}/2$) . In the case of atoms displaced through dislocation glide, $\mathbf{s}_\alpha$ approaches the Burgers vector. Although no characteristic value of the slip vector can be expected for interatomic rearrangements in the interface regions, we select $|\mathbf{s}_\alpha| > 0$ as a criterion to identify MREs in the present work. This criterion merely determines the existence of interatomic nearest neighbor rearrangement events beyond a threshold displacement (i.e., $> b_{partial}/2$); investigating the detailed mechanism or quantifying the kinematics of such events is not the aim within this chapter.

Figure 27 shows snapshots of the TF sample at various stages of deformation. Only atoms having a non-zero slip vector with respect to the *previous snapshot* have been shown, i.e, the undeformed configuration is the reference for snapshot (a), (a) is the reference for (b) and so on. The snapshots have been taken at stresses immediately beyond the dissipation peaks visible in Figure 23 (best resolved in $\dot{\eta}_3$). It is apparent that the first couple of peaks in the region $\sigma_{xx} < 1.1$ GPa in Figure 23 correspond to localized inelasticity at one triple junction each, indicated by arrows in Figure 27(a) and (b). The larger peaks beyond

1.1 GPa, however, cannot be correlated to any specific event, and instead correspond to *sample-wide* deformation of the GB network. Dislocations were observed after the largest (split) peak beyond 2.0 GPa, very close to the vertical tail in Figure 23, at the onset of runaway failure of the microstructure.

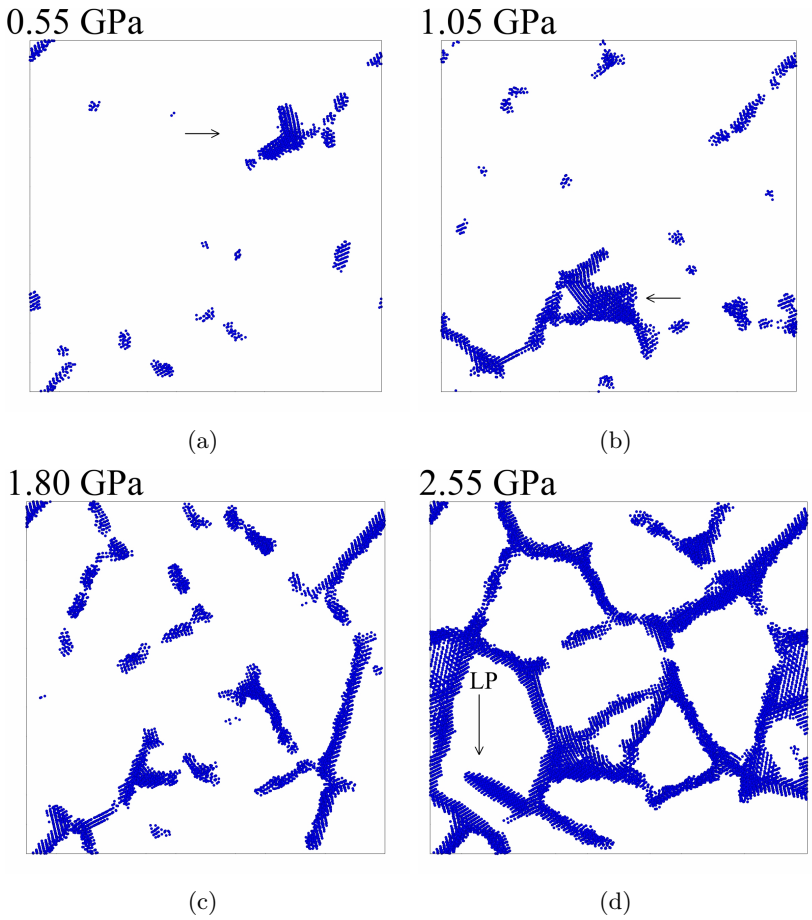

Figure 27: Snapshots of the TF sample projected on the x–y plane at tensile stresses indicated. The axis of deformation is the horizontal direction. Only those atoms are shown that have $|\mathbf{s}_\alpha| > 0$ w.r.t. the atomic configuration in the previous snapshot (the reference for snapshot (a) was the undeformed microstructure, not shown here). Snapshots (a) and (b) indicate localized inelastic events at triple junctions, shown by arrows. However, the MREs corresponding to snapshot (c) are delocalized and network-wide. The emergence of a leading Shockley partial dislocation (LP) is indicated by the arrow in (d).

In the PC sample, since there are no isolated peaks of dissipation, a one to one correspondence of MREs and features on the thermostat evolution curve (in Figure 24) cannot be expected. Due to the considerably large number of grains in the PC sample, we use

a statistical measure of cumulative rearrangement separately in the intergrain and intragrain phases, again based on the slip vector criterion. In each of the phases fcc, hcp and $other$, we define N_s: the number of atoms that satisfy the criterion $|\mathbf{s}_\alpha| > 0$. In contrast to the TF sample, here, a single reference configuration (the undeformed one) is used to compute $\mathbf{s}_\alpha$. Figure 28(a) shows the evolution of N_s with strain. At both 10 K and 300 K, N_s^{other} rises more steeply than N_s^{hcp}. However, the evolution of N_s^{other} at 10 K and 300 K is very different at very low strains. At 300 K, N_s^{other} rises almost *immediately* starting from $\epsilon_{xx} = 0$, indicating that rearrangement in the GB network evolves with no significant stress–threshold.

The relation of the 'slipped' atom population (N_s) to $\dot{\eta}_1$ is shown in Figure 28(b). At 10 K, the rise in N_s^{other} is accompanied by a concurrent rise in $\dot{\eta}_1$, indicating that the dissipative signal arises due to MREs in the GB network. No such concurrency can be observed between N_s^{other} and $\dot{\eta}_1$ at 300 K. Instead, the growth of the hcp phase (N_s^{hcp}) correlates with the increase in $\dot{\eta}_1$ at 300 K. Since the hcp phase grows in the nanograins through intragranular mechanisms of dislocation glide and deformation twinning, it can be inferred that the thermostat avalanches in Figure 24 and Figure 26 have different mechanisms. While the 10 K avalanche arises primarily from MREs in the GB network (before runaway breakdown of the material), the avalanche at 300 K is entirely dominated by intragrain processes such as dislocation glide and/or twinning. Although MREs in the GB network contribute significantly to the deformation at 300 K, they do not produce the prominent bursts of dissipation observed at 10 K. The implications of this behavior are further discussed in Section 3.5.

3.5 Discussion

In this chapter, we have described a method to resolve avalanches in the dissipation of stored elastic energy in isothermal MD simulations of deformation. As plastic yielding occurs through a critical avalanche of MREs, our method captures the separate stages of both intergranular and intragranular inelasticity. By itself, an idea describing yielding in the perspective of an avalanche is not new; simulations through discrete dislocation dynamics

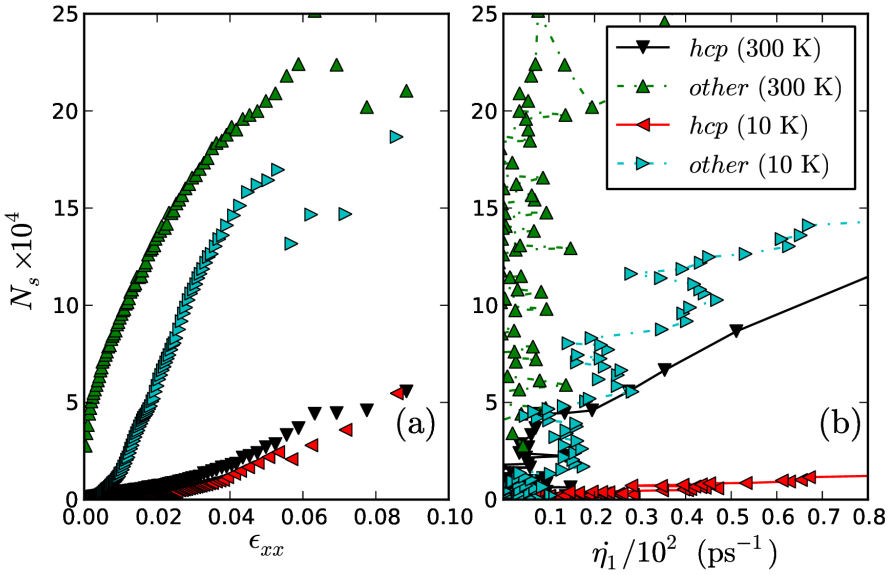

Figure 28: (a) Plot of N_s vs. strain shown separately for the non-12 coordinated GB phase (*other*) and the hcp phase (*hcp*) at 10 K and 300 K for the PC sample. Interatomic rearrangements at the scale of nearest neighbors are predominantly concentrated in the *other* phase at both temperatures. However, the initial growth of N_s in the *other* phase is much more rapid at 300 K than at 10 K, before both approach a similar trend. (b) shows the evolution of N_s w.r.t. $\dot{\eta_1}$. At 10 K, the rise in N_s^{other} is accompanied by a similar rise in $\dot{\eta_1}$, but at 300 K, this trend breaks down.

[93] and experimental acoustic emission studies [215] have attempted to characterize the elastic–plastic transition in the past, albeit in significantly different materials. The novelty of this work lies in its potential to quantify yielding in terms of a homogenized, scalar signal obtained from a computed material response, while simultaneously incorporating vital information of inelastic avalanches that originate from the microstructure.

In our results, we observe a jerky, multi–stage evolution of the thermostat rate at 10 K, even when the stress–strain response is smooth, as observed in Figures 23 and 24. The jerky response was found to correlate well with intergranular stress–driven inelastic events in the material. At 10 K, the thermostat rate conspicuously rises above the thermal background due to considerable elastic strain energy storage that subsequently gets dissipated. In contrast, at 300 K, the equilibrium thermal energy of the system ($N_{\mathrm{f}} k_{\mathrm{B}} T$) can easily cross the configurational energy barrier (defined for the entire GB network) for structural relaxation without large-amplitude deviations of the thermostat. That is not to say that there is no dissipation in the system deforming at 300 K, only that the dissipation is not significant enough to rise above the thermal noise, and is gradual. It appears, therefore, that the deformation mechanism in the intergranular phase as a whole at 10 K is of a *pinning–depinning* nature, which however, becomes effectively *threshold–less* at 300 K. Still, the overall avalanche behavior at the critical point of cooperative yield is clearly registered at 300 K. This raises the possibility of applying temperature accelerated dynamics [196] to explore the effects of thermally activated mechanisms on the initial yield point.

The yielding transition is difficult to unambiguously define for most materials, and the discovery of novel inelastic deformation mechanisms makes this quantification even more difficult. Qualitatively, deformation mechanism maps can help predict these mechanisms as a function of length scale, stress and temperature. Yamakov et al. [275] have suggested that bulk NC fcc metals can plastically deform through full dislocation slip, partial slip or GB mediated deformation. In restricted geometries such as thin films, nanostructuring leads to a transition from threading dislocations to surface-assisted grain boundary diffusion. Buehler et al. [29] have explored the role of substrate constraints where additionally, crack–like GB diffusion wedges [69] cause dislocation glide parallel to the substrate. In comparison, the

thin film sample considered in this work is very small compared to experimental thin films. The 2 nm thickness restricts available slip systems and thereby forces the activation of grain boundary processes to satisfy compatibility. If substrates are present, the grain boundary processes are effectively 'locked' too, and the activation of parallel glide [29] can possibly occur. In these (and other) scenarios of mixed kinetics, the thermostat compensation can be used to unambiguously define criticality, especially since explicitly treating individual mechanisms in a plasticity theory is fraught with complexity.

In this chapter, we show that the nature of the dissipation avalanche in stress–space depends strongly on the frequency of dissipative events, the size of such events relative to the system size, and the thermodynamic temperature. These factors together determine whether yield is gradual or catastrophic. No explicit modeling of internal material length scales or the activation/suppression of specific deformation mechanisms is needed in estimating the dissipation. Additionally, there is no need to assume a solely deviatoric-driven sub-scale material deformation model. These characteristics motivate the application of our approach to generalized multiaxial inelasticity.

Comparing the thermostat response under compressive vs. tensile loading allows us to compute the ratio $\Sigma_{\mathrm{C}}/\Sigma_{\mathrm{T}}$, which is a statistical measure of the asymmetry in inelastic event magnitude. The ratio reveals the differences in the fine-structure of the elasto–plastic avalanche under two opposite loading directions, allowing a novel, more direct quantification of tension-compression asymmetry than yield stress. In continuum models of plasticity, model selection and parameter optimization can be additionally constrained to match the energetics of inelastic avalanches as computed through MD. Such a fit will effectively encapsulate the effect of interatomic sliding, shuffling, crystallographic slip, as well as the respective obstacles to these mechanisms and therefore can be very useful from a coarse–graining standpoint.

In perspective, a theory of plasticity benefiting from estimates of dissipation in full atomistic models will have some key advantages: a), its simplicity—since there is no need to explicitly model nanoscale microstructural components b), the cumulative effect of even complex and atypical defect avalanches will, nevertheless, be preserved, and (c), it can

potentially facilitate extensions of uniaxial deformation theories towards a full multiaxial form.

As a statement of caution, it is important to realize that non-equilibrium fluctuations in the thermostat may not be the only contributors to dissipation, even though they correlate rather well with MREs. Since the simulations in this work involve transient force-type boundary conditions and anisotropic volume fluctuations, an estimate of the absolute dissipation (i.e., in energy units) is thermodynamically complex and therefore difficult to compute. However, even a *relative* estimate of dissipation compared across inelastic events is sufficient to resolve the avalanche that constitutes yielding.

We have provided a preliminary demonstrative test of our approach for two microstructures having different morphologies and a similar average grain size. However, more simulations are needed to characterize the transitions in deformation mechanisms due to material scaling in NC microstructures, particularly in grain size regimes where dislocation–GB coupling is more significant. Figure 29 shows one example of the effect of material scaling. Here, we compare the inelastic avalanche (resolved using $\dot{\eta}_1$) observed in the PC structure under uniaxial tensile deformation at 10 K, to avalanches observed in scaled-up[2] microstructures of higher grain sizes (10nm, 15nm), for the same deformation path. Two key features of the avalanches in Figure 29 are noted: first, the fluctuations that are observed at applied stresses below 2.0 GPa in PC sample (5 nm grain size, solid line) are not present in structures of higher grain size. In the structure scaled up to 10 nm grain size (dashed curve), some fluctuations can be observed leading up to ductile failure, i.e., the 'knee' of the curve; however, even these fluctuations disappear as the grain size is scaled up further (dotted curve). This reveals that dislocation nucleation from interfaces results in a sharper yield transition than the progressive activation of GB sliding processes. Second, as the grain size increases, the knee of the curve shift to higher applied stresses, in accordance with inverse Hall-Petch scaling [45] of yield strength.

Plots such as Figure 29 can significantly simplify the demarcation of material failure

[2]These microstructures have the same grain morphology and grain orientations as the PC structures, but a different grain size. They were created by filling atoms into an isotropically-scaled Voronoi tesellation of the PC structure.

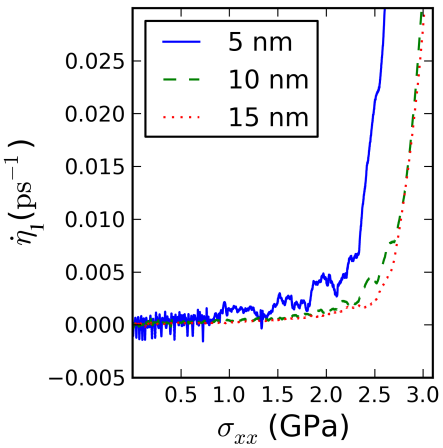

Figure 29: Evolution of $\dot{\eta}_1$ for uniaxial tensile deformation of three NC Cu microstructures. Labels in the legend correspond to mean grain size. '5 nm' refers to the PC structure (see Figure 21(b)); '10 nm' and '15 nm' pertain to microstructures obtained by isotropic scaling of the PC microstructure.

surfaces in isothermal MD simulations of plasticity and/or fracture under general multiaxial loading paths. Yield/failure surfaces computed in this manner are expected to naturally capture the stress state-dependence of various underlying deformation mechanisms.

3.6 Summary

The findings in this chapter are summarized as follows:

1. Over the course of deformation, we demonstrate that the activity of an atomic thermostat under imposed isothermal conditions can contain vital information regarding the frequency and magnitude of dissipative microstructure rearrangement 'events'. In particular, the transition from isolated to cooperative events is captured by the thermostat but not by the stress–strain curve.

2. The dissipation footprint due to an event directly varies as the *size* of the event relative to the simulated sample size.

3. When individual events are comparable to the system size (TF sample), under increasing stress, dissipation occurs as isolated spurts whose magnitude increases with applied stress.

4. In a larger, more homogeneous system (PC sample), the combined effect of several rearrangement events can be detected as a diffuse, almost continuous *dissipation rate* at 10 K. At 300 K, however, this dissipative signal is absorbed within the thermostat noise, and the events leading to the dissipation avalanche (the grain-boundary sliding/migration processes) become effectively threshold-less.

5. The stress–threshold for intergranular rearrangement (grain boundary sliding/migration) is well within the linear region of the stress–strain response, even with very little thermal activation.

6. Compressive loading suppresses the avalanche response relative to tension, with a statistical asymmetry of ≈ 0.8 in the avalanche.

The approach described in this work is quite general, i.e., it can be applied to atomistic modeling of any heterogeneous structure where inelastic dissipation occurs. NC metals are particularly suited to this kind of analysis since simulated ensembles offer a variety of dissipation mechanisms at the same length scale. This scale also happens to be convenient for fully atomistic simulation with current computational capabilities. The present chapter provides a basis for a generalized, scalar criterion approach toward criticality that can be applied to non-equilibrium transitions occurring in discrete particle aggregates simulated at a finite temperature.

CHAPTER IV

INITIAL YIELD AND PLASTIC FLOW BEHAVIOR OF CU NANOCRYSTALS UNDER MULTIAXIAL STRESS STATES

4.1 Introduction

Interest in nanocrystalline (NC) metals and alloys is motivated by the potential improvements these materials offer in terms of strength, hardness and wear resistance over conventional coarse-grained (CG) materials. NC metals, by virtue of their small mean grain size (<100 nm), contain a significant volume fraction of interfaces in the form of grain boundaries (GBs), and, in some cases, twin boundaries. Such extreme refinement in grain size greatly reduces the mean free path of dislocation glide, suppressing both dislocation multiplication via Frank-Read sources and strengthening due to dislocation pile-ups. Instead, inelastic deformation in NC metals is largely *interface-mediated*, exhibiting mechanisms such a shear transformation zones (STZs) in the GBs, twinning, and dislocation nucleation from GB sources. Interface-mediated deformation mechanisms are believed to be the cause of anomalous behavior that occurs in an NC metal but not in the CG metal of similar composition, e.g., yield strength asymmetry under tension vs. compression (T–C asymmetry) [187], non-Schmid effects in dislocation nucleation [287, 226, 231], and a non-linear stress-strain response with recoverable 'plasticity' [26, 168], otherwise known as anelasticity.

The departure from lattice dislocation-mediated plasticity in NC metals and associated macroscale effects presents a challenge towards developing predictive models of plasticity for these materials, especially under multiaxial deformation paths where fully 3-D constitutive models are necessary. Deformation mechanisms that are significantly influenced by normal stress and/or pressure could result in macroscale behavior that does not conform to isotropic initial yield governed by the von Mises yield criterion, and subsequent flow aligned with the instantaneous deviatoric stress (Prandtl-Reuss flow rule). In particular, hydrostatic pressure could influence the activation of shear transformation zones in the interface regions

(a 'frictional' effect), as well as the critical resolved shear stress for dislocation nucleation from the interface network. While purely phenomenological models of plasticity based on extensive mechanical testing data could be developed, there are substantial challenges in doing so, since mechanical testing of NC material samples under complex loading conditions is difficult, and fabricating nano-grained samples of pure metals is non-trivial. Experimental techniques to study the multiaxial stress-strain response of nanocrystalline samples, for example, have been reported only recently [4].

The length scale at which deformation processes operate in NC metals is particularly well suited for analysis via molecular dynamics (MD) simulations. Indeed, MD offers the unique advantage of providing extremely detailed information regarding atomic rearrangements and defect dynamics that manifest as irrecoverable deformation. While atomistic simulations of inelastic deformation in nanocrystals have been reported previously in the literature (for representative work see [183, 245]), typically, those data have not been analyzed in a way that can readily inform continuum models.

Several top-down constitutive models of the mechanics of NC metals [35, 268, 289, 267] have been proposed and offer several interesting perspectives regarding the interplay of the role of the interface network vs. that of the crystalline grains. However, these models rely on assumed kinematics and kinetics (e.g., regarding microstructure evolution and nucleation and annihilation rates of defect population(s)) and therefore, are not necessarily realistic. On the other hand, concurrent multiscale methods that approximate atomistic forces and trajectories with continuum fields [287, 108, 273], despite being immensely useful in modeling lattice strain fields and dislocation glide, still lack a reduced order description of interfaces and non-crystalline phases. To better model interface-mediated inelasticity, hierarchical multiscale strategies that pass information from atomistics to reduced order models (e.g., [199]) seem well suited. In that direction, there is plenty of room for improvement in terms of statistical and computational methods that analyze microstructural aspects and collective atom trajectories to yield information in terms of the evolution of relevant state variables.

In this chapter, we have performed a detailed study of the effects of a multiaxial stress

state on the elastoplastic deformation behavior of NC Cu using molecular dynamics (MD) simulations. We have studied deformation under plane stress as well as triaxial stress states, while focusing on the role of hydrostatic stress in affecting the shear strength of nanostructures in a grain size regime where deformation is dominated by shear transformations (sliding/migration) in the interfaces. The primary question addressed in this chapter is: How is the kinetics and kinematics of stress-driven irreversible microstructure rearrangement in NC metals influenced by the stress state? The term *irreversible microstructural rearrangement* is a deliberate generalization that includes all possible mechanisms of inelastic deformation, of both intergranular and intragranular character. With this perspective, inelastic yielding is simply the combined (and possibly, cooperative) effect of the propagation of a statistically significant population of mobile defects via an avalanche.

Our present work differs from previous efforts aimed at probing the inelastic yield behavior of NC metals cf. [128, 55] in two respects. First, we estimate the inelastic strain through explicit unloading, thereby accounting for any nonlinear elasticity, or inelasticity, in the stress-strain response. Second, we resolve the yield transition of a nanocrystalline ensemble according to a fundamental, dissipation-based metric (introduced in Chapter 3), by tracking the response of a Nosé-Hoover thermostat [88, 133] coupled to a deforming microstructure. Further, we analyze the inelastic deformation fields in the vicinity of interface regions using per-atom metrics of stress [77], strain [297, 234, 237], and free volume [233], observing correlations that help clarify the mechanism(s) of pressure-dependent inelastic flow in nanocrystalline microstructures.

4.2 Methodology

4.2.1 Microstructure

The simulated Cu nanocrystal consists of 100 grains inside a periodic cubic simulation domain. Grains were constructed by a Voronoi tessellation of 100, randomly placed seed-points. Grain orientations were selected randomly from the group of 3-D rotations, creating an equiaxed, untextured microstructure with a mean grain size of 5nm, referred to as S_5 in Figure 30. For a cubical box of edge-length l, tessellated with n grains, the mean grain size

is defined as $d = \sqrt[3]{l^3/n}$, i.e., the 'volume averaged grain size'[1].

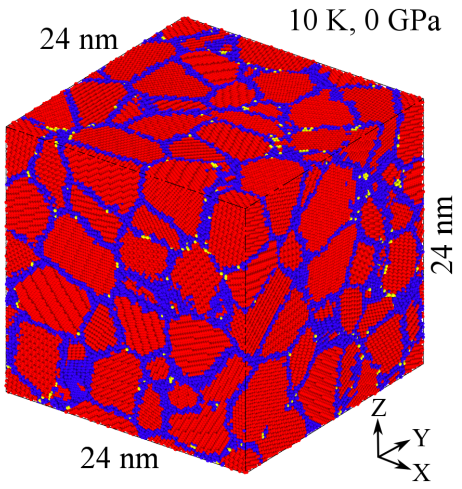

Figure 30: Configuration of the NC Cu microstructure of mean grain size 5 nm (S_5, where the subscript denotes mean grain size in nanometers) shown prior to any deformation. The structure consists of $\approx 1.2 \times 10^6$ atoms. The atoms have been colored according to common neighbor analysis [232], with locally face centered cubic atoms shown in red, locally hexagonal close packed atoms in yellow and other, non-12 coordinated atoms in blue.

This initial structure was relaxed and equilibrated at a temperature of 10 K and zero external pressure through a series of steps involving proximity-based atom-deletion, energy minimization, and isothermal-isobaric dynamics as described in previous work [217, 237]. At the end of this equilibration step, the configuration simulates a volume element of nanocrystalline Cu in physical and thermal equilibrium with the bulk.

4.2.2 Simulation setup

The relaxed microstructure S_5 was deformed via independent control of three normal stress components while subjecting the atoms to $N\boldsymbol{\sigma}T$ dynamics (i.e., control over the number of atoms, the stress tensor, and the temperature) and periodic boundary conditions in all three dimensions. All MD simulations were performed with the temperature held constant at 10 K, in order to suppress thermally activated mechanisms and ensure that atomic rearrangements in the NC ensemble were primarily stress-driven.

[1]This measure of mean grain size and other measures used experimentally (e.g., derived from planar slices of microstructure) need not agree for the same microstructure.

4.2.3 Initial yield behavior: Proportional loading

To study the initial yield behavior in the space of principal stresses, the equilibrated ensemble S_5 was deformed via a deformation scheme that uses ramped principal stresses (see Section 2.7.2) while holding the temperature constant at 10 K. A normal pressure (σ) was applied to each pair of opposite faces of the simulation box. No shear tractions were applied and, as a result, the applied normal stresses (σ_{xx}, σ_{yy} and σ_{zz}) are also the principal stresses σ_1, σ_2 and σ_3 (in some order). Proportional loading was imposed by maintaining a fixed ratio between principal stress increments, i.e.,

$$\lambda_1 \dot{\sigma_1} = \lambda_2 \dot{\sigma_2} = \lambda_3 \dot{\sigma_3} \tag{35}$$

where $\dot{\sigma}_i$ denotes the time derivative of σ, and λ_1, λ_2 and λ_3 are constants. Assuming that loading begins at time $t = 0$, the Cauchy stress tensor for a time $t > 0$ is given by:

$$\boldsymbol{\sigma} = \begin{pmatrix} \sigma_1^o + t\dot{\sigma_1} & 0 & 0 \\ 0 & \sigma_2^o + t\dot{\sigma_2} & 0 \\ 0 & 0 & \sigma_3^o + t\dot{\sigma_3} \end{pmatrix} \tag{36}$$

In Equation 36, each stress component consists of a part that is applied instantaneously (superscript o) upon loading, and a part associated with the subsequent ramping of pressures on the box faces via $\dot{\sigma}_i$. This scheme simulates general triaxial loading, and reduces to proportional loading if the initial normal stress components (σ_i^o) are zero.

For uniaxial loading, a stress ramping rate of 0.005 GPa/ps was found to result in strain rates of $10^9 \mathrm{s}^{-1}$ up to a uniaxial true strain of ≈ 0.06 [217]. Under biaxial, plane-stress proportional loading, we selected the ramping rates of the principal stress components $\dot{\sigma_1}$ and $\dot{\sigma_2}$ such that the rate of von Mises stress, i.e, $\sqrt{\dot{\sigma_1} + \dot{\sigma_2} - \dot{\sigma_1}\dot{\sigma_2}}$ was a constant for all loading directions.

The strategy of stress-controlled multiaxial loading presented here is simple to implement at a finite temperature and does not require prescription of strain increments, unlike previous work [128, 55]. However, since the present method is stress-controlled, it is unsuitable for probing post-yield defect avalanche behavior. For that we employ a strain-controlled method, described in Section 4.2.4.

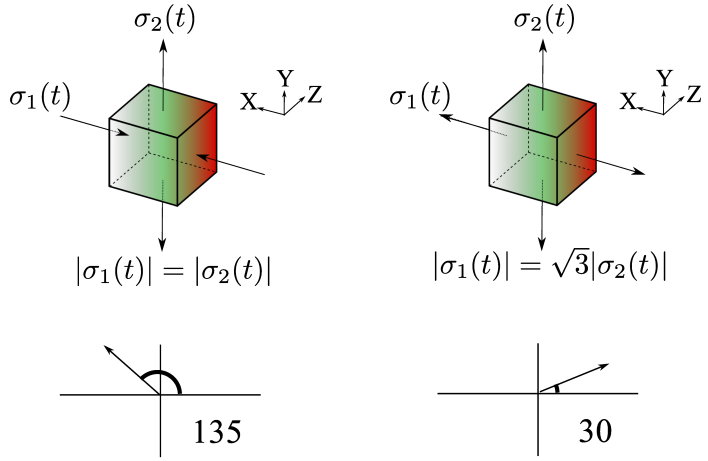

(a)

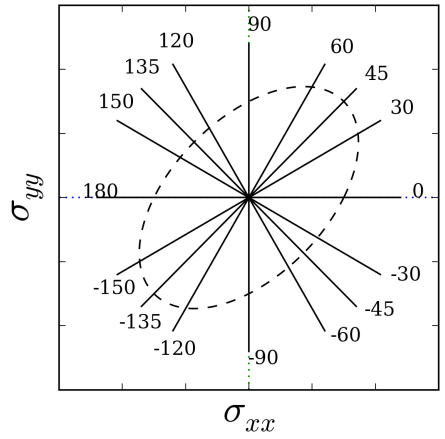

(b)

Figure 31: (a) Schematic showing the convention used to specify proportional loading paths in $(\sigma_{xx}, \sigma_{yy})$ principal stress sub-space with σ_{zz} fixed at 0. (b) Sixteen loading paths considered in the present work, including uniaxial tension (0,90), uniaxial compression (180,-90), pure shear (135, -45), and balanced biaxial loading (45, -135). The dashed line indicates the yield locus.

Loading directions were specified in terms of the angle (in degrees) made by the principal stress vector $(\sigma_{xx}, \sigma_{yy})$ with the positive direction of σ_{xx}-axis, as shown in Figure 31(a). To compare deformation as a function of the loading direction, we employ the following scalar measures:

$$\begin{aligned}
\bar{\sigma} &= \sqrt{\frac{1}{2}((\sigma_1 - \sigma_2)^2 + (\sigma_2 - \sigma_3)^2 + (\sigma_3 - \sigma_1)^2)} \\
\bar{\epsilon} &= \sqrt{\frac{2}{9}((\epsilon_1 - \epsilon_2)^2 + (\epsilon_2 - \epsilon_3)^2 + (\epsilon_3 - \epsilon_1)^2)} \\
\bar{\epsilon}^{\text{in}} &= \sqrt{\frac{2}{9}((\epsilon_1^{\text{in}} - \epsilon_2^{\text{in}})^2 + (\epsilon_2^{\text{in}} - \epsilon_3^{\text{in}})^2 + (\epsilon_3^{\text{in}} - \epsilon_1^{\text{in}})^2)} \\
\hat{\sigma} &= \frac{\sigma_1 + \sigma_2 + \sigma_3}{3} \\
\hat{\epsilon} &= \frac{\epsilon_1 + \epsilon_2 + \epsilon_3}{3} \\
\hat{\epsilon}^{\text{in}} &= \frac{\epsilon_1^{\text{in}} + \epsilon_2^{\text{in}} + \epsilon_3^{\text{in}}}{3}
\end{aligned} \tag{37}$$

In the set of equations 37, quantities with a bar (e.g., $\bar{\sigma}$) pertain to distortion in the structure, while quantities with a hat (e.g., $\hat{\sigma}$) signify dilatation. $\bar{\sigma}$, $\bar{\epsilon}$, and $\bar{\epsilon}^{\text{in}}$ are von Mises equivalents of true stress ($\boldsymbol{\sigma}$), true strain ($\boldsymbol{\epsilon}$), and inelastic true strain ($\boldsymbol{\epsilon}^{\text{in}}$) respectively. Similarly, $\hat{\sigma}$, $\hat{\epsilon}$ and $\hat{\epsilon}^{\text{in}}$ are the hydrostatic/dilatational invariants. Note, however, that the definition of $\bar{\epsilon}$ used in equation set 37 traditionally applies in the case of *volume-conserving inelastic strains* [100], rather than the total strain measure employed here. Since we are applying the definition to total strains instead of purely inelastic ones, an equivalence between $\bar{\epsilon}$ and the axial strain under uniaxial deformation does not hold.

The nanocrystalline structure S_5 was deformed along the 16 loading directions as shown in Figure 31(b), until at least one principal strain exceeded 10%. These directions represent a thorough parametric sampling of the biaxial plane-stress space, including states of uniaxial loading, shearing, and both balanced and unbalanced biaxial loading. During the loading stage, the thermostat compensation rate, $\dot{\eta}$, was measured every 100 timesteps (1 timestep = 1 fs). $\dot{\eta}$ indirectly captures the release of stored elastic energy (i.e., dissipation) associated with stress-driven microstructure rearrangement events [217]. Note that thermostatting in these simulations is performed via three thermostat variables η_1, η_2, η_3 present in a chain [132] (see Equations 32). Of these, $\dot{\eta}$ refers to the rate of the first thermostat η_1, which is

the only thermostat that directly couples to thermal fluctuations in the system.

4.2.4 Strain-controlled deformation: Post-yield behavior

The stress-controlled deformation scheme used in the previous section is inherently unstable after initial yield, and does not allow us to simulate stable inelastic flow. In order to investigate deformation behavior in the post-yield regime, we used the method of ramped principal strains (see Section 2.7.2). In this method, the length of the simulation box along a given axis is modified after every timestep so as to produce a specified (constant) true strain rate along that axis. Effectively, this method simultaneously imposes proportional strain rates along one or more Cartesian axes. Surfaces normal to other axes are prescribed as traction-free.

Biaxial deformation simulations were performed along sixteen loading directions in the $\epsilon_{xx}, \epsilon_{yy}$ space, with σ_{zz} held at 0. The directions were the same as those specified in Figure 31(b), albeit in the space of (normal) strain components. Similar to the stress-controlled case, for each simulation, the absolute value(s) of $\dot{\epsilon}_{xx}, \dot{\epsilon}_{yy}$, and $\dot{\epsilon}_{zz}$ were chosen so as to reach the same value of $\bar{\epsilon}$ (see Equation 37) within the same duration. All simulations corresponded to an 'effective' strain rate of $\dot{\bar{\epsilon}} = 10^9$ s^{-1}. While this biaxial deformation simulations employ plane-stress conditions, they do not ensure proportionality of stresses beyond the linear elastic deformation regime.

4.2.5 Strain relaxation via unloading

NC metals are known to exhibit an extended, non-linear elastic-plastic regime with partially recoverable microstructure evolution [26, 25, 168]. The unloading response in CG metals, in contrast, is linear elastic, since it predominantly consists of lattice relaxation. In other materials that show complicated relaxation behavior, such as glassy polymers, it has been argued that the yield point should be determined using non-recoverable strain instead of strain-offset based methods [166].

During the course of the deformation, snapshots of the atomic positions and velocities were captured at intervals of 20 ps, corresponding to stress increments of 0.1 GPa. Each

snapshot (loaded state) was unloaded by equilibrating to zero external stress and the temperature of deformation (10 K) via isothermal-isobaric dynamics ($N\boldsymbol{\sigma}T$) for a duration of 30 ps, leading to rapid strain recovery and relaxation of interatomic forces. In this manner, a sequence of unloaded configurations were obtained, each identified by the von Mises stress ($\bar{\sigma}$) from which the unloading was initiated. The inelastic strain tensor $\boldsymbol{\epsilon}^{\text{in}}$ was measured in the fully-relaxed configuration, using box dimensions prior to deformation (Figure 30) as the reference.

4.3 Results

4.3.1 Stress-controlled deformation response

In the first part of this work, the NC structure S_5 was deformed at 10 K under plane-stress proportional loading along the sixteen loading directions shown in Figure 31(b). The thermostat compensation rate $\dot{\eta}$ was computed throughout the deformation process, and the inelastic strain evolution was obtained by periodically capturing snapshots of the atom positions in the loaded state and subsequent unloading under $N\boldsymbol{\sigma}T$ conditions to $T = 10$ K and $\boldsymbol{\sigma} = 0$ GPa.

4.3.1.1 Strain recovery upon unloading and relaxation

Some key aspects of the strain recovery process during unloading are shown in Figure 32, for the case of pure shear deformation. Figure 32(a) shows the recovery of von Mises strain ($\bar{\epsilon}$) as unloading is performed from various snapshots corresponding to total (loaded) von Mises strains between 0 and 0.04. Most of the strain is recovered within the first 5 ps, before stabilizing at what is considered a residual inelastic von Mises strain $\bar{\epsilon}^{\text{in}}$. Here, we regard $\bar{\epsilon}^{\text{in}}$ as the measure pertinent to the classical yield criteria. However, there is no requirement for $\bar{\epsilon}^{\text{in}}$, computed in the fully-relaxed state, to be purely deviatoric (i.e., volume-conserving), since it is a natural outcome of the relaxation dynamics. In Figure 32(b), the unloading paths are shown with respect to the loading stress-strain curve. In the case of loading beyond the initial linear regime ($\bar{\sigma} \approx 0.7$ GPa), unloading leads to rapid stress and strain relaxation; however, strain relaxation continues even after the stress has reduced to zero. By constructing a hypothetical reloading line, of slope equal to the slope of the initial linear

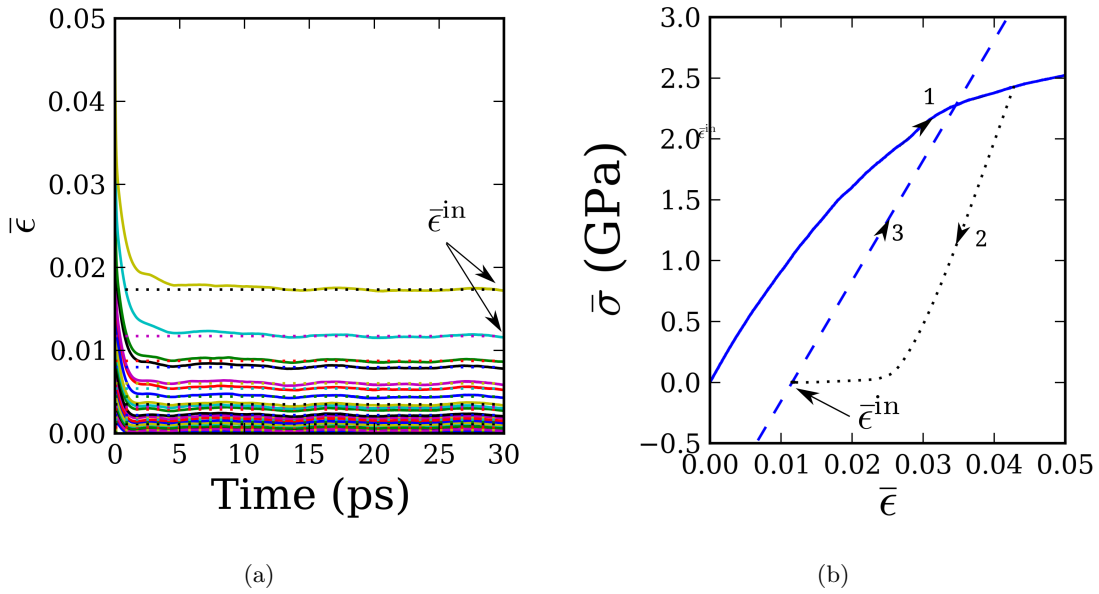

(a) (b)

Figure 32: Unloading of the structure S_5 from different stress levels, following loading under pure shear. (a) Recovery of von Mises strain over the period of 30 ps during unloading. The asymptotic inelastic strain ($\bar{\epsilon}^{\text{in}}$) is shown as the dotted horizontal lines. (b) Strain recovery during unloading shown on a $\bar{\sigma}$ vs. $\bar{\epsilon}$ loading curve. The sequence of arrows 1 and 2 respectively denote loading and unloading. Arrow 3 shows a hypothetical re-loading line (of slope equal to the initial linear elastic slope) drawn from the unloaded state.

regime, from the unloaded state, we observe that the strain recovery exceeds that expected from pure linear elastic unloading, since the reloading line falls short of the point on the loading curve from which the unloading was initiated.

Such behavior is not expected if the recoverable strain was composed only of lattice strains, as is the case in CG metallic polycrystals. These observations support the view that recoverable deformation in the GB network is a substantial component of the total strain in NC metals, and grain-size dependent anelasticity should be accounted for while assessing the yield strength based on strain offsets on the stress-strain curve. Previous work, at higher temperature, has documented both time dependent strain recovery [168, 120], as well as anelasticity [211] in nanocrystalline fcc metals. The present result suggest that substantial anelasticity is present even with very little thermal activation.

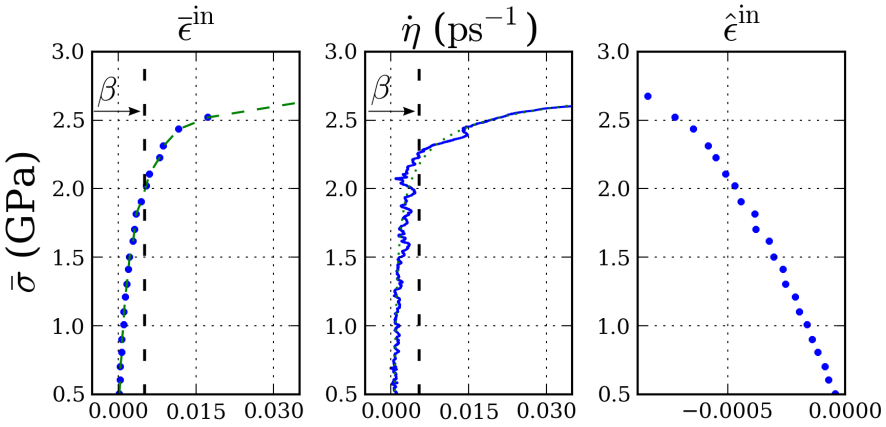

Figure 33: Evolution of the inelastic von Mises strain ($\bar{\epsilon}^{\text{in}}$) and the thermostat compensation rate ($\dot{\eta}$) with the von Mises stress ($\bar{\sigma}$) for the case of plane-stress biaxial deformation of structure S_5 under *pure shear*. The "yield point" is defined as the value of $\bar{\sigma}$ that corresponds to a small vertical offset β taken from the origin along the horizontal axis.

4.3.1.2 Initial yield

The relaxed asymptotic inelastic von Mises strain $\bar{\epsilon}^{\text{in}}$ and the dissipation metric $\dot{\eta}$ were used as two independent criteria to demarcate the elastic-plastic transition in the deforming NC ensemble. Figure 33 shows the evolution of $\bar{\epsilon}^{\text{in}}$ and $\dot{\eta}$ with $\bar{\sigma}$ for the case of pure shear (path '-45' in Figure 31(b)). Trajectories of both $\bar{\epsilon}^{\text{in}}$ and $\dot{\eta}$ exhibit similar shapes, indicating little atomic rearrangement at low stresses, followed by an avalanche growth as the stress increases. In particular, $\dot{\eta}$ exhibits a 'jerky' behavior capturing dissipation events involving stress-driven atomic rearrangements [217]. The yield stress $\bar{\sigma}^{\text{Y}}$ was obtained by taking a small horizontal offset β on the evolution curve(s), as marked in Figure 33. The evolution of $\bar{\epsilon}^{\text{in}}$ was interpolated between snapshots using a cubic spline, while $\dot{\eta}$ was smoothed via a least-square fit to the function $\bar{\sigma} = A + B/(C - \dot{\eta})^D$, a hyperbola with parameters A, B, C and D. For all loading-unloading cases, the inelastic dilatation ($\hat{\epsilon}^{\text{in}}$) was found to be quite small: less than 0.05%, as shown in Figure 33 (for more detailed results, see Section 4.2.4).

Two sets of yield loci, corresponding to the yield conditions defined by $\bar{\epsilon}^{\text{in}}$ and $\dot{\eta}$, are shown in Figures 34 (a) and (b), respectively. The locus of constant $\bar{\epsilon}^{\text{in}}$, shown in Figure 34(a) and fit to a von Mises ellipse, shows slight asymmetry in the first and third quadrants, although the deviation is quite weak. Similar behavior was observed in the locus of constant

$\dot{\eta}$. Overall, our simulations suggest that initial yield in NC Cu under biaxial loading is isotropic for the grain size studied, with very weak T-C asymmetry of uniaxial yield strength. The yield loci shown in Figure 34 seem to agree with the findings of Dongare et al. [55], which were conducted under strain control, although at a higher temperature of 300 K. As such, the grain size regime of 4-5 nm is predicted to lie near a minimum of the T-C asymmetry, as claimed in previous MD-based work [56].

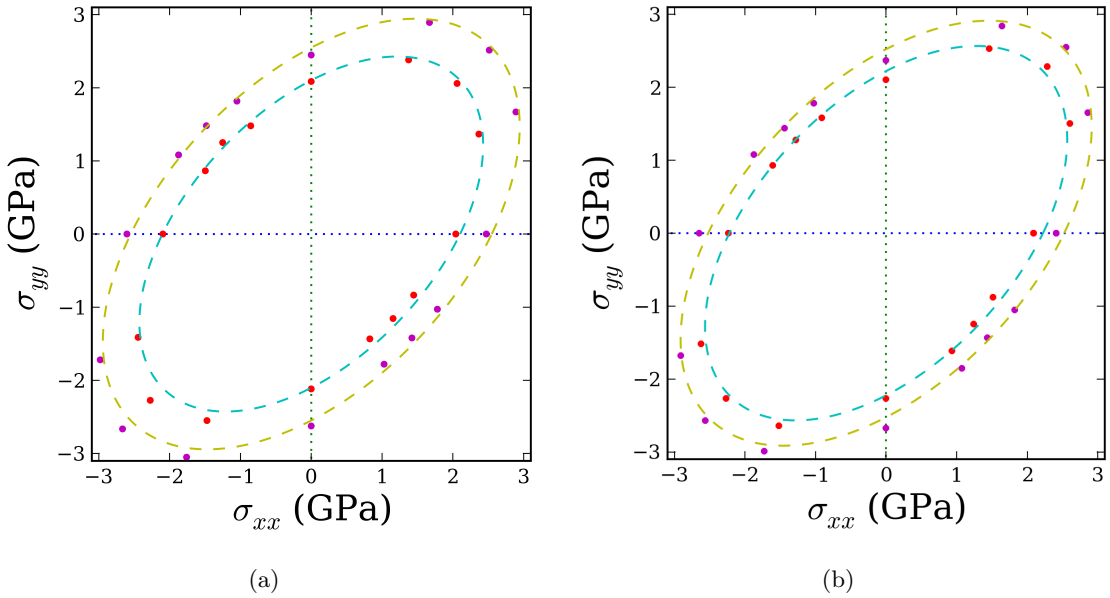

Figure 34: Biaxial yield loci of the structure S_5 computed according to two distinct yield criteria. (a) the inelastic von Mises strain $\bar{\epsilon}^{\text{in}}$, and (b) the thermostat compensation rate $\dot{\eta}$. In both (a) and (b), the inner locus corresponds to a threshold of $\beta = 0.005$ and the outer locus corresponds to a threshold of $\beta = 0.01$. Dashed curves are von Mises ellipses fit to the data.

4.3.2 Strain-controlled deformation: Exploring the stable flow regime

Post-yield behavior under biaxial loading was analyzed for the structure S_5 (shown in Figure 30) via the strain-controlled biaxial deformation method described in Section 4.2.4. The stress-strain curves for five loading directions are shown in Figure 35(a). While the deformation path -135 (biaxial compression) appears to exhibit the highest peak stress, differences among the flow curves are comparable to fluctuations within each curve. Figure 35(b) compares the evolution of the inelastic dilatation ($\hat{\epsilon}^{\text{in}}$) to the von Mises inelastic strain ($\bar{\epsilon}^{\text{in}}$). While $\hat{\epsilon}^{\text{in}}$ increases in magnitude with deformation, it is quite small, remaining below

0.12% at all strains.

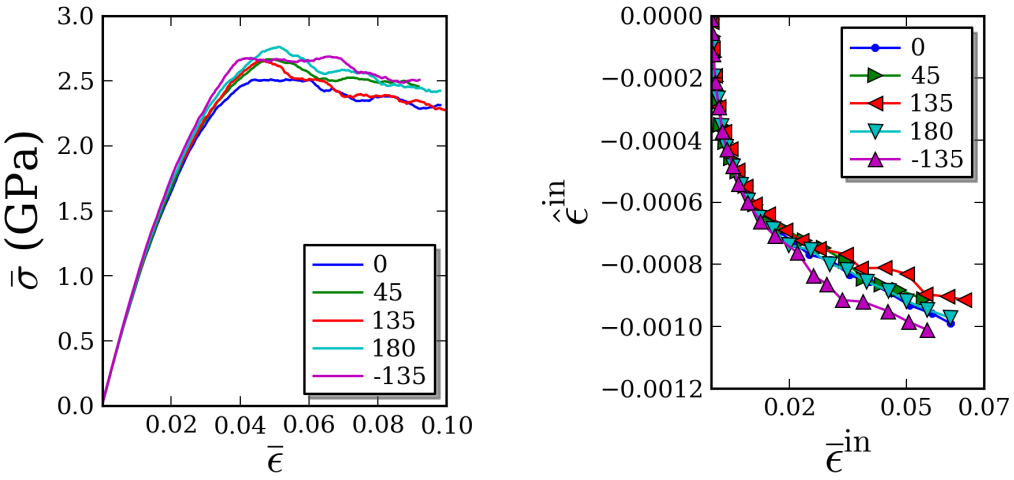

(a) (b)

Figure 35: (a) von Mises stress-strain curves for strain-controlled plane-stress biaxial loading of structure S_5. (b) Comparing the inelastic von Mises strain $\bar{\epsilon}^{\text{in}}$ and the inelastic dilatation $\bar{\epsilon}^{\text{in}}$ for the same loading paths.

Defining θ as the angle between the inelastic strain increment ($\mathrm{d}\boldsymbol{\epsilon}^{\text{in}}$, computed in the unloaded configuration) and the deviatoric stress ($\mathbf{S} = \boldsymbol{\sigma} - \hat{\sigma}\mathbf{I}$, computed in the corresponding loaded configuration), Figure 36 shows the evolution of $\cos\theta$ with $\bar{\sigma}$ for a variety of loading paths. In all cases, following a small initial deviation from collinearity ($\cos\theta = 1$), it is observed that $\cos\theta$ tends to approach a value of 1 for all loading paths. These results suggest that inelastic flow in NC Cu occurs in a direction normal to the von Mises yield surface, and that the inelastic strain tensor is almost purely deviatoric, even under the high applied strain rate and conditions of low thermal activation, as well as the limited statistical volume (100 grains) considered.

4.3.3 Effect of hydrostatic pressure on the yield transition

In addition to the biaxial deformation response, we also explored the effect of superimposed hydrostatic pressure on the shear stress–strain response of a Cu nanocrystal. Multiaxial generalizations of T-C asymmetry can be parameterized either in terms of hydrostatic pressure (i.e, the Drucker-Prager yield criterion), or normal stress (e.g., modifications to Schmid's law or the Mohr-Coulomb yield criterion). It is common to ignore pressure-dependence

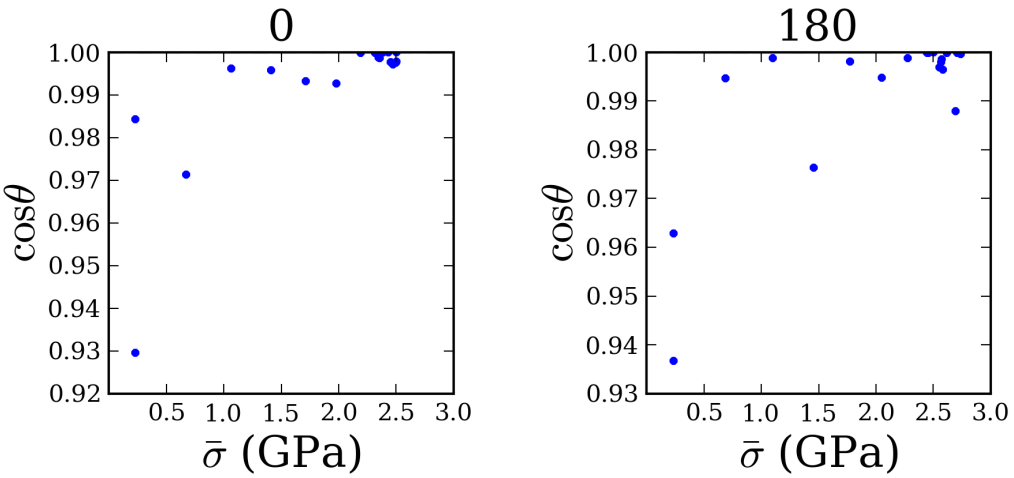

(a)

(b)

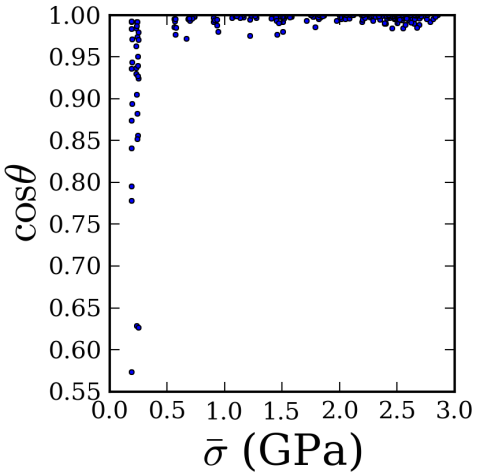

(c)

Figure 36: Evolution of $\cos\theta$ with the von Mises stress $\bar{\sigma}$, where θ is the angle between the inelastic strain incement tensor ($\Delta\boldsymbol{\epsilon}^{\text{in}}$) and the instantaneous deviatoric stress tensor ($\boldsymbol{\sigma} - \hat{\sigma}\mathbf{I}$). (a) and (b) show results of specific loading directions corresponding to uniaxial tension ('0') and uniaxial compression ('180'), while (c) shows all 16 loading directions superimposed.

in initial yield and flow rules for CG metals and alloys, although a pressure effect on the large-deformation stress-strain behavior of CG metals has been observed [202] and has been attributed to the change in dislocation line energy with imposed pressure [96]. In NC metals, hydrostatic pressure can be expected to additionally influence interface-mediated deformation via interface sliding/migration, and such pressure-dependence is being considered in the present work.

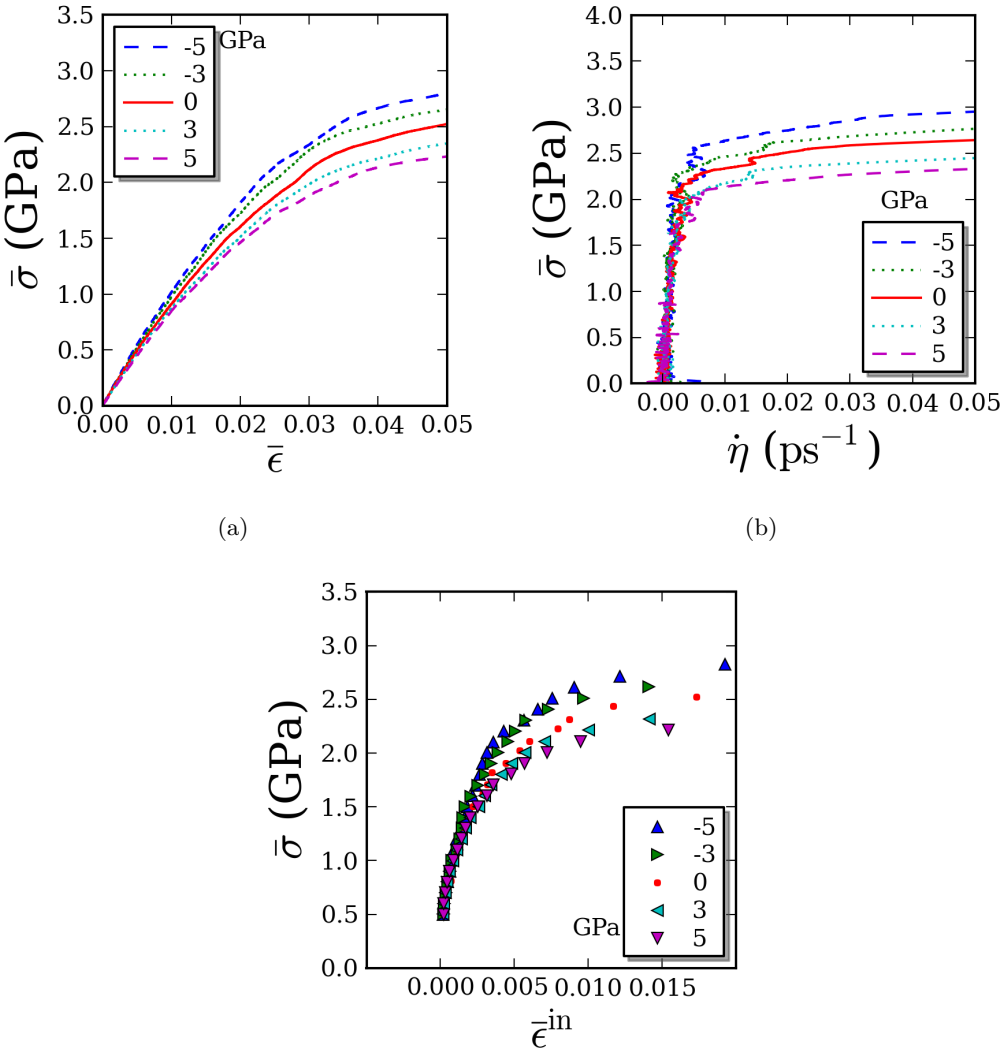

Figure 37: Deformation paths consisting of increasing applied shear stress with a time-variant superimposed hydrostatic stress between -5 GPa and 5 GPa visualized using (a) von Mises stress-strain curves, (b) thermostat compensation rates, and (c) inelastic von Mises strain.

Loading was performed via the ramped-stress scheme as given by Equation 36, after initially equilibrating the structure under a desired superimposed hydrostatic pressure $\hat{\sigma}$ for 5 ps. The principal stress components were selected such that the hydrostatic stress $\hat{\sigma}$ at any stage of the loading was constant. Figure 37(a) compares the von Mises stress–strain responses for structure S_5 under $\hat{\sigma}$ in the range -5 GPa to 5 GPa. We observe that under these elevated pressures, there are significant differences in the stress–strain response. There is also a decrease in the initial elastic slope (related to the shear modulus) with increasing $\hat{\sigma}$. Avalanche curves based on $\dot{\eta}$ and $\bar{\epsilon}^{\text{in}}$ (Figure 37(b) and (c) respectively) reveal a distinct elevation of the yield stress with applied compressive hydrostatic stress.

The variation of yield stress $\bar{\sigma}^{\text{Y}}$ with $\hat{\sigma}$ is shown in Figure 38(a) and (b), where (a) refers to a strain offset-based yield criterion and (b) refers to the thermostat-based ($\dot{\eta}$) criterion. The results obtained using the inelastic strain-based criterion ($\bar{\epsilon}^{\text{in}}$) have not been shown but were very similar to 38(b). Regardless of the choice of criterion, $\bar{\sigma}^{\text{Y}}$ appears to vary linearly with $\hat{\sigma}$. However, a linear relationship is not readily apparent when using the 0.2% offset strain definition of yielding. This is consistent with previous work [25] and suggests that a 0.2% offset strain-based yield definition is below the threshold for statistically-significant defect cascades, for the grain size studied. On the other hand, upon using the 0.7% offset criterion, an unambiguous linear trend relating $\bar{\sigma}^{\text{Y}}$ and $\hat{\sigma}$ is obtained. Assuming a simple relation between $\bar{\sigma}^{\text{Y}}$ and $\hat{\sigma}$: $\bar{\sigma}^{\text{Y}} = \bar{\sigma}_0^{\text{Y}} - k\hat{\sigma}$, where $\bar{\sigma}_0^{\text{Y}}$ is the yield strength under pure shear and k is the *pressure coefficient of the shear strength*, we obtain $k = 0.048$ for the strain offset-based yield criterion and $k = 0.05$ for the thermostat-based yield criterion.

Figures 38(c), (d) compare the ratio of the yield strength $\bar{\sigma}^{\text{Y}}$ and the initial elastic slope $\bar{\sigma}^{\text{Y}}$ of the corresponding stress-strain curve for all values of $\hat{\sigma}$ considered. We observe that $\bar{\sigma}^{\text{Y}}$ exhibits a nearly constant ratio to the initial elastic slope $d\bar{\sigma}/d\bar{\epsilon}$. This observation supports a simple picture of the effect of hydrostatic pressure on STZ-mediated plasticity, where the barrier to STZ-activation is simply raised or lowered in proportion to the change in material stiffness. Note that while an increase in yield strength with material stiffness (in this case, measured by the initial slope) is expected, this increase may not be proportional to the stiffness increment if any pressure-dependent deformation mechanisms *different* from

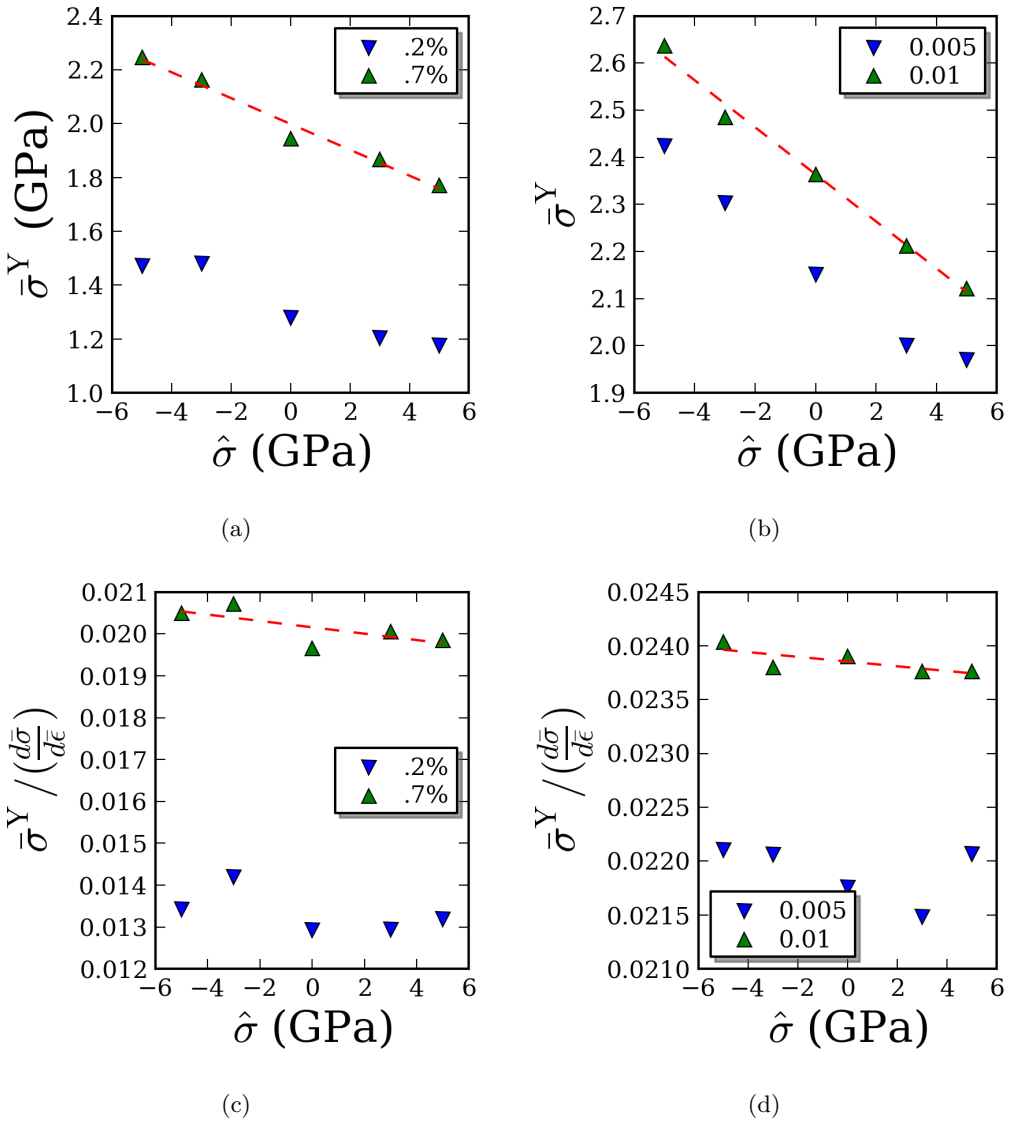

Figure 38: (a), (b) Comparing the effect of imposed hydrostatic stress $\hat{\sigma}$ on the yield strength ($\bar{\sigma}^{\mathrm{Y}}$) under shear deformation. $\bar{\sigma}^{\mathrm{Y}}$ is computed using (a) an offset strain from the initial elastic slope in Figure 37(a), and (b) a horizontal offset taken on the $\bar{\sigma}$ vs. $\dot{\eta}$ curve in Figure 37(b). (c), (d) Comparing the evolution of the yield strength scaled by the initial elastic slope $\bar{\sigma}^{\mathrm{Y}}/(d\bar{\sigma}/d\bar{\epsilon})$ with $\hat{\sigma}$, for (c) the strain offset-based yield criterion, and (d) the thermostat-based criterion.

those available at $\hat{\sigma} = 0$ GPa are activated (e.g., the formation of nano-sized voids or the nucleation of dislocations) under different superimposed pressures.

4.3.4 Defect evolution under hydrostatic pressure

Shear deformation under superimposed imposed hydrostatic pressure offers a way to artificially bias the mean interatomic separation, and therefore, the respective energy barriers for atomic rearrangement events. Several mechanisms can contribute to the pressure-dependence of shear strength in nanocrystals, e.g., non-Schmid effects in dislocation nucleation and pressure-dependence of the dislocation line energy, unstable stacking fault energy, and migration/sliding thresholds for interfaces. Since the nanocrystal with grain size considered in the present work exhibits mainly interface STZ-mediated plasticity, it is potentially helpful to analyze two important aspects of interfaces in NC microstructures that can influence the coupling of STZ activity with pressure: initially high internal von Mises stresses, and the interfacial free volume (FV).

4.3.4.1 Internal stress

Very high internal von Mises stresses (even in the absence of an externally-applied deformation field/tractions) have been reported in simulated Cu nanocrystals of various grain sizes by [77], using a virial definition of stress. It has been further asserted, intuitively, that high internal stresses in the vicinity of the interfaces could have a role in facilitating local 'yield' at low applied stresses, in a manner similar to the role of residual stress fields in polycrystals. This mechanism might also be invoked to explain the smooth, extended elastic-plastic transition in nanocrystals, where the driving force for plasticity is partially provided by stress relaxation in the interface network. However, this intuitive effect of the internal stress has not been studied systematically in the literature, and the coupling of such stresses to pressure is unclear.

Figures 39(a-c) show planar cross-sections through the structure S_5 colored by $\bar{\sigma}/atom$ for three cases of constant superimposed hydrostatic stress ($\hat{\sigma}$): (a) 5 GPa (tension), (b) 0 GPa (no superimposed hydrostatic stress) and (c) -5 GPa (compression), in a state prior to any shear deformation. From visual inspection of Figures 39 (a-c), we observe a slight

thickening of the red (i.e., high-stress) regions near the interfaces in going from a tensile to a compressive $\hat{\sigma}$. Upon plotting the distribution of $\bar{\sigma}/atom$ for the three cases in Figure 40(a), we confirm that a compressive superimposed $\hat{\sigma}$ indeed leads to a *thicker* tail of the distribution (shown by the arrow), while a tensile $\hat{\sigma}$ has the opposite effect. Further, as shown in Figure 40(b), atoms that correspond to the tail of the distribution (beyond 7.5 GPa, the cross-over point of the curves in Figure 40(a)) all belong to the interface network, implying that $\hat{\sigma}$ affects the interatomic forces in the interfaces most strongly. It also implies that internal stresses that might affect yielding must be the ones that contribute to the tail of the distribution in Figure 40(a), since stress-driven atomic rearrangement primarily occurs in the interfaces.

The behavior in Figure 40(a), however, does not support the hypothesis that high internal von Mises stresses in the interfaces facilitate premature yielding. Rather, they seem to have the opposite effect, since the structure with elevated internal von Mises stresses under imposed hydrostatic compression was also found to register a higher yield stress. In Section 4.3.5, we analyze more detailed correlations to better ascertain the precise role of internal stresses towards driving interface-mediated plasticity.

4.3.4.2 Interfacial excess volume

Stress-driven free volume migration is a common deformation mechanism in disordered media. In nanocrystals containing predominantly high-angle interfaces with a high degree of positional disorder, free volume is likely to play a role in determining the STZ-mediated deformation behavior. MD simulations of uniaxial deformation as well as shear in symmetric bicrystal interfaces have suggested that the activation of inelastic events can significantly evolve the amount as well as the connectivity of free volume clusters in the interface [233].

Figure 41(a) shows the internal hydrostatic stresses ($\hat{\sigma}/atom$) present in the structure S_5. Both tensile and compressive stresses appear to be present at and near the interface regions. However, it does not appear that the interface network, overall, is under a tensile or compressive stress due to a volume mismatch with the crystalline grains.

The distribution of $\hat{\sigma}/atom$ closely resembles the distribution of $Volume/atom$ for the

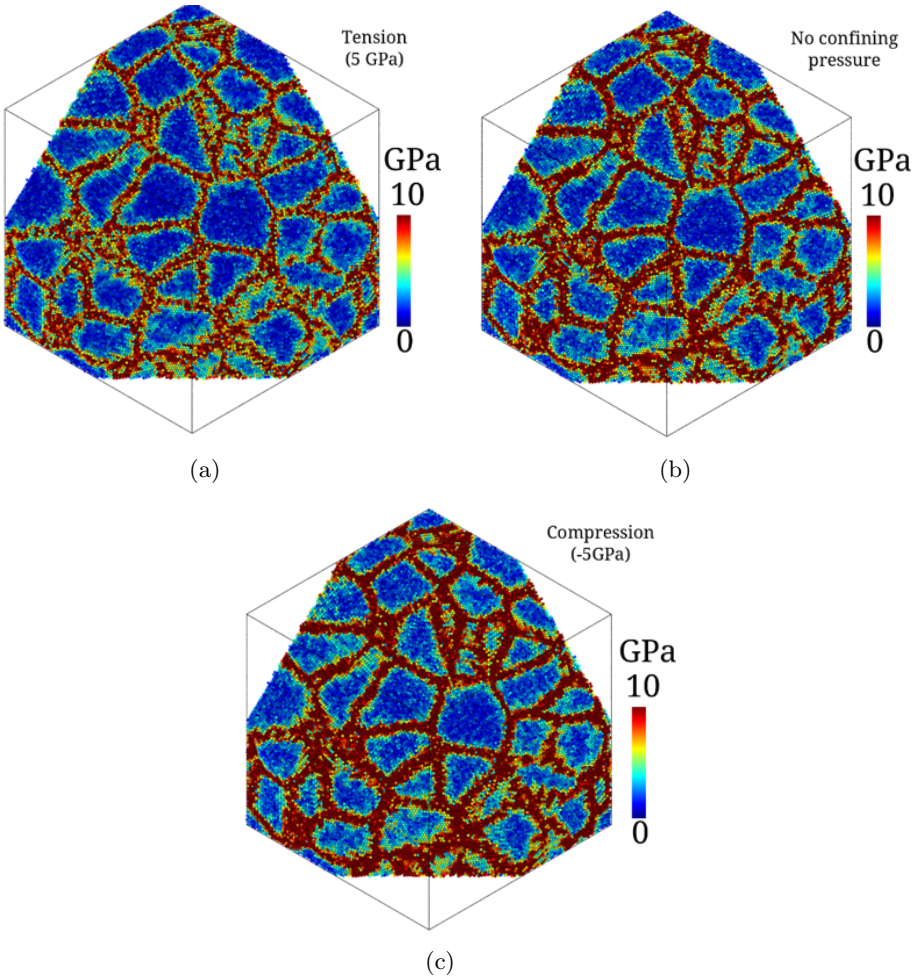

(a) (b) (c)

Figure 39: (a),(b) and (c): Planar cross-sections through the structure S_5 shown under three different states of superimposed hydrostatic stress, with atoms colored according to the per-atom von Mises stress ($\bar{\sigma}/atom$). (b) denotes the relaxed and equilbrated configuration at zero external pressure ($\hat{\sigma} = 0$ GPa), while (a) and (c) correspond to states of tensile and compressive stresses, respectively ($\hat{\sigma} = \pm 5$ GPa).

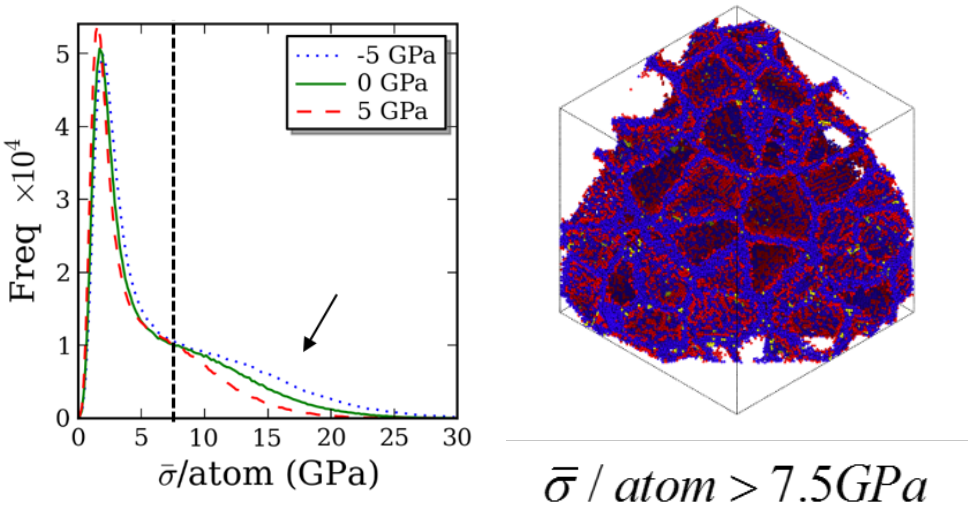

(a) (b)

Figure 40: (a) Distribution of $\bar{\sigma}/atom$ over all atoms for the three cases of hydrostatic confinement shown in Figure 39, exhibiting a cross-over point at around 7.5 GPa. (b) shows only the atoms with $\bar{\sigma}/atom > 7.5$ GPa in S_5, using the same color scheme as Figure 30.

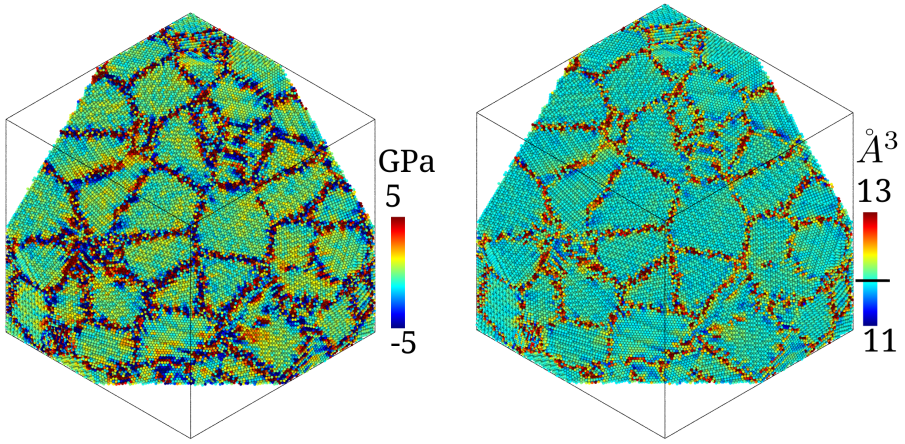

(a) (b)

Figure 41: (a) Section through the structure S_5 with atoms colored according to $\hat{\sigma}/atom$, shown in the absence of superimposed $\hat{\sigma}$ and prior to any deformation. (b) The same section, colored according to $Volume/atom$. The black marker on the color map denotes the atomic volume in a defect-free, undeformed crystal.

same structure, which is shown in Figure 41(b). The atomic volumes were computed for the structure S_5 using a Voronoi tesellation, where the atoms' instantaneous positions serve as seed points for the tessellation. As expected, both extremes of the volume are present in the interface regions. Pockets of dilatation or compression (shown as yellow and blue, respectively) can be observed near interfaces and triple junctions, measured relative to the ideal atomic volume in Cu, $V_0 = 11.8\text{Å}^3$ (computed as $V_0 = a_0^3/4$, where $a_0 = 3.615\text{Å}$ is the lattice parameter). The distribution of atomic volumes was not symmetric around this ideal value, showing a thicker tail towards higher (excess) volumes.

Note that our measure of $Volume/atom$ as computed via Voronoi tesellation is as described in work by [77] and bears no similarity to the grid-based algorithm employed to compute free volume in previous work [233] concerning Cu bicrystals. The current measure was selected due to its lower computational cost. Although the excess volume computed by the present algorithm is not directly comparable to the 'free' volume as defined in [233], both measures are qualitatively similar and can be used to estimate the unfilled space in a configuration of atoms.

4.3.5 Correlations between per-atom quantities

The per atom von Mises stress ($\bar{\sigma}/atom$) and the atomic volume carry information regarding the local atomic neighborhood, in terms of interatomic forces as well as the pre-existing excess volume around atoms. Combined with kinematic information of atomic trajectories developed in response to applied deformation, it is possible to analyze correlations between these per-atom quantities that might help reveal the nanoscale physics of localized, pressure-sensitive shear transformation in the NC interfaces. The objective here is to identify substructural 'state variables' that seem to best explain the influence of $\hat{\sigma}$ on $\bar{\sigma}^{\mathrm{Y}}$. Specifically, we test two hypotheses here: high values of (a) $\bar{\sigma}/atom$ as well as (b) $Volume/atom$ facilitate local stress-driven atomic rearrangements.

To capture the kinematics of localized atomic rearrangement, the per-atom strain tensor was computed as the Lagrangian (Green) strain tensor derived from the atomic-scale deformation gradient formulation of Zimmerman et al. [297]. This strain metric has been

used previously by Tucker and coworkers [237] to resolve rotation and dilatation fields in simulated NC Cu. For strain computations, the reference configuration was chosen as the undeformed configuration prior to loading ($\bar{\sigma} = 0$ GPa), and the current configuration as the one deformed to $\bar{\sigma} = 2$ GPa. The strain tensor was computed using all nearest neighbors lying within the cutoff radius of the interatomic potential. A weighting function [76] was used to balance the contribution of second and farther nearest neighbor shells on the computed strain tensor. For shear deformation with superimposed hydrostatic pressure, the pre-compressed/dilated configuration (prior to any shear deformation) was used as reference. This was done to ensure that any measurement of per-atom dilatation did not include the initial dilatation $\hat{\epsilon}$ suffered due to the imposition of $\hat{\sigma}$.

Heatmaps were computed for atomic configurations corresponding to various stress levels in the stress-strain curves shown in Figure 37(a). In this context, the reference configuration refers to the state of the system equilibrated under the superimposed pressure $\hat{\sigma}$, but prior to any shear deformation ($\bar{\sigma} = \bar{\epsilon} = 0$). The current configuration pertains to a deformed state ($\bar{\sigma}, \bar{\epsilon} > 0$).

In Figure 42, correlations between per-atom quantities in the interface regions (comprising only the atoms shown in Figure 40(b)) have been plotted as heatmaps. The color of the map at each point corresponds to the frequency of atoms having the particular combination of per-atom quantities. In each plot, x-axis labels refer to reference-configuration quantities, while y-axis labels correspond to current-configuration quantities. In Figure 42(a), we notice that extreme values of $\bar{\sigma}/atom$ prior to deformation do not correspond to large von Mises strains in the deformed state. The observed strains peak at $\bar{\sigma} \approx 10$ GPa, before falling off. More significantly, a similar behavior is observed in (b) in the case of atomic volumes. The strains tend to peak close to the ideal atomic volume (11.8 $\mathring{A}^3$). However, atoms with higher atomic volumes prior to deformation, which ostensibly have more 'space' to rearrange, actually register lower strains, close to those observed for atoms that were more constricted than the ideal fcc lattice prior to deformation. Finally, in (c), $\hat{\sigma}/atom$ in the reference configuration produces no bias in the per-atom von Mises strains, i.e., the largest strains are clustered around $\hat{\sigma}/atom = 0$ GPa.

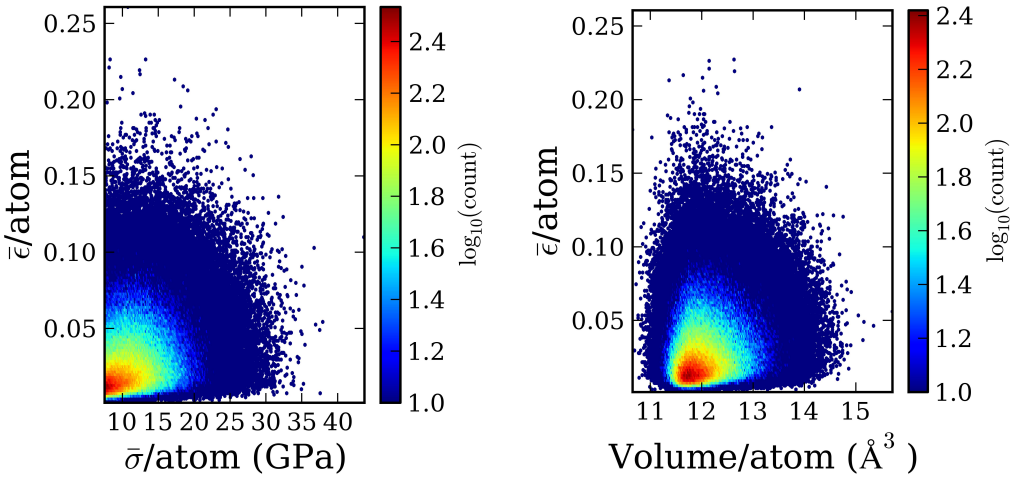

(a)

(b)

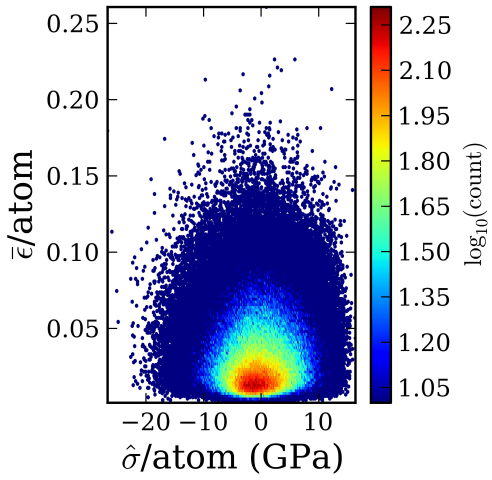

(c)

Figure 42: Heatmaps comparing various per-atom quantities both prior to and during pure shear deformation in the structure S_5. In all plots, the y-axis shows the strain $\bar{\epsilon}/atom$ in the *deformed* configuration ($\bar{\sigma} = 2.0$ GPa) while the x-axis shows quantities in the *reference* configuration ($\bar{\sigma} = 0.0$ GPa): (a) the von Mises stress/atom, (b) the volume/atom, and (c) the hydrostatic stress/atom. Colors indicate atom populations (*count*) and are shown on a logarithmic color scale.

The heatmap of $\bar{\sigma}/atom$ and $Volume/atom$ in the reference configuration is shown in Figure 43(a) for the case $\hat{\sigma} = 0$. Here, we observe that maximum atomic volume corresponds to $\bar{\sigma}/atom$ in the range of 5–10 GPa, and atoms with higher $\bar{\sigma}/atom$ have less $Volume/atom$. Although each value of $\bar{\sigma}/atom$ admits a wide range of atomic volumes (owing to the inherent structural disorder in the interfaces), these volumes, on average, tend towards the ideal atomic volume of 11.8 $\mathring{A}^3$ as $\bar{\sigma}/atom$ increases.

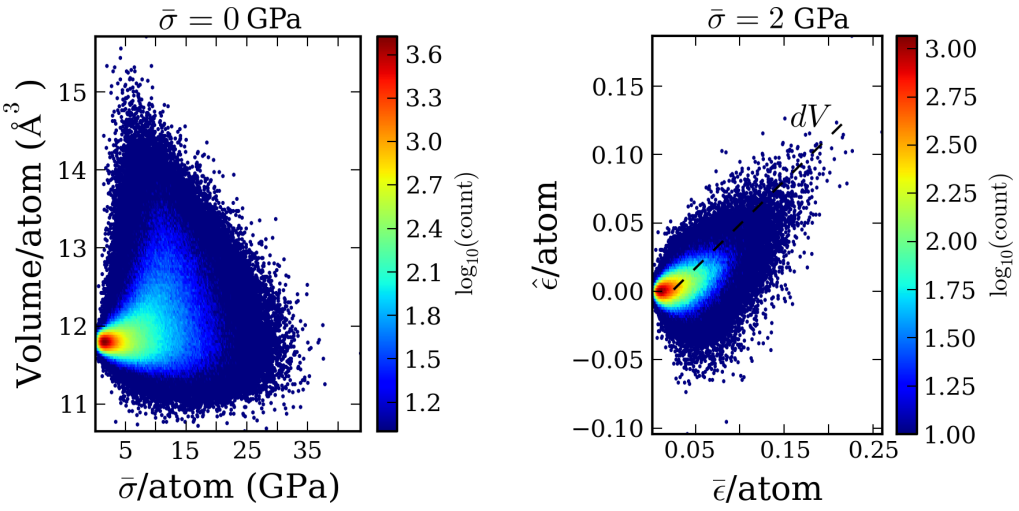

(a) (b)

Figure 43: (a) Heatmap comparing atomic volume and per-atom von Mises stress in the reference configuration for the structure S_5. (b) Heatmap comparing dilatational and distortional atomic strain ($\hat{\epsilon}/atom$ and $\bar{\sigma}/atom$, respectively) in the deformed configuration.

Figure 43(b) compares per-atom strains in the deformed configuration for the case $\hat{\sigma} = 0$, with the intent to resolve volume changes accompanying pure shear deformation. We observe that the dilatational strain $\hat{\epsilon}/atom$ positively correlates with the von Mises strain $\bar{\epsilon}/atom$ even though no external $\hat{\sigma}$ was applied. This positive correlation was found to significantly diminish upon unloading, implying that a part of the volume change (dV) associated with shear transformation in the interface is *transient*. Additionally, almost the same correlation between $\hat{\epsilon}/atom$ and $\bar{\epsilon}/atom$ was observed for all loading cases, even the ones with superimposed compressive hydrostatic stress, indicating that the observed dilatation is inherent to the deformation mechanism(s), and not a result of the imposed boundary conditions.

Further, we analyzed the effect of imposed $\hat{\sigma}$ during shear deformation on the preceding correlations. No qualitative differences could be observed in the shapes of the heatmaps. Regardless, in order to facilitate direct comparison of the respective correlations, heatmaps were plotted as contours for the case of $\hat{\sigma} = 5$ GPa and $\hat{\sigma} = -5$ GPa and are shown superimposed in Figure 44. Note that here, all quantities are *current* configuration quantities, unlike Figures 42 and 43(a). In Figure 44(a) it can be observed that the distributions are similar in shape but offset by the change in mean atomic volume due to tension/compression. There indeed seems to be a connection between excess volume and ease of interatomic rearrangement, but it is apparently a mean-field effect, independent of the statistical variation in the atomic volumes themselves. In (b), while shear+hydrostatic compression elevates the internal von Mises stresses, these (instantaneous) elevated stresses do not correspond to higher strains. Rather, we suspect that the upper extreme values of $\bar{\sigma}/atom$ corresponds to an increased likelihood of interatomic *jamming*, and the relative immobility of atoms in the jammed state is the reason these atoms can develop such high internal stresses. Similarly in Figure 44(c), extreme values of $\bar{\sigma}/atom$ don't appear to have any correlation with the instantaneous atomic volume, and tend towards the mean volume.

4.3.6 Summary of correlations

The correlation analysis suggests that there may not be a direct, *atomic-scale* correspondence between spatially-localized measures of atomic volume, internal stresses, and deformation. Rather, such a correlation is only valid in a mean field sense over relatively large material volumes. On one hand, while an overall increase in mean atomic volume appears to positively correlate with lower yield strength, there is no evidence to support the intuitive assessment that initial high internal stresses in the interface facilitate STZ activity, leading to a lowering of the yield strength. An overall increase in internal von Mises stresses prior to deformation was actually found to inhibit yielding, most likely due to interatomic jamming in highly stressed atomic neighborhoods.

Analysis of the evolution of atomic strains under multiaxial loading conditions suggest that the activation of STZs in the interfaces is associated with a *transient dilatancy*, which is

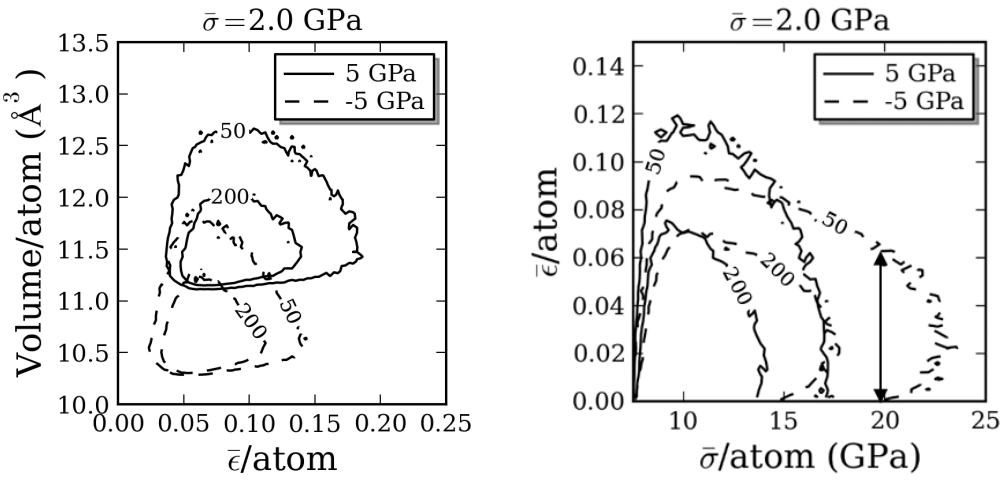

(a) (b)

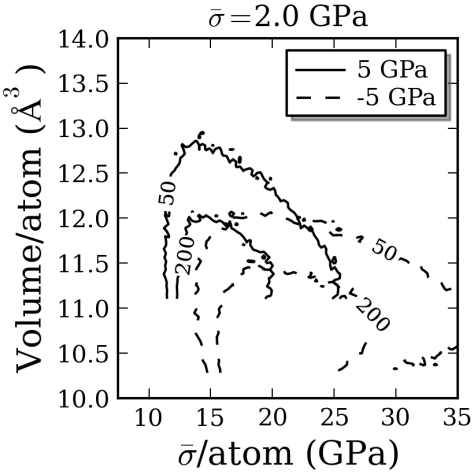

(c)

Figure 44: Contour maps comparing correlation of per-atom quantities in the deformed configuration of structure S_5. Contour lines connect similar atom populations (which were represented by color in Figures 42 and 43) and have been used instead of heat maps to better distinguish between population distributions under imposed hydrostatic pressures ($\hat{\sigma}$) of ± 5 GPa. All plots compare per-atom quantities in the deformed configuration.

independent of the applied deformation path. Such dilatancy has been discussed in previous work by Bulatov et al. [31] in the case of dislocation glide in Al, and it is expected that the transient volume change (dV) will couple with the applied pressure ($\hat{\sigma}$) to introduce a penalty of $\hat{\sigma}dV$ in the activation energy of shear transformation, thereby affecting the yield strength. Overall, our results seem to suggest that STZ-mediated deformation in NC materials could be described reasonably well in terms of the evolution of free/excess volume, with transient dilatancy inherent to the deformation mechanism(s).

4.4 Discussion

The metrics $\bar{\epsilon}^{\text{in}}$ and $\dot{\eta}$ represent different perspectives of yielding, and both can supplement traditional engineering measures, such as offset strain, in MD simulations of nanomechanics. While $\bar{\epsilon}^{\text{in}}$ is free from effects of anelasticity, $\dot{\eta}$ captures the dissipation avalanche associated with the nucleation, propagation, and annihilation of material defects. The proposed criteria are effectively independent, and application to MD simulations of dynamic mechanical processes (e.g., plasticity, fracture) in other material systems and microstructures could potentially be quite useful. For example, Lissenden and Arnold [123] have shown (analytically) that dissipation-based failure surfaces and inelastic strain-based failure surfaces are expected to differ in shape for any material that includes terms other than the second invariant of the stress deviator, J_2, in the failure criterion.

Although the biaxial yield surfaces for structure S_5 were found to be nearly isotropic, we observed a clear pressure-dependence of initial yield. The negative pressure coefficient for the yield strength under shear indicates that hydrostatic confinement (or expansion) does affect local interatomic rearrangement in the interface network. However, the pressure dependence isn't strong enough to be apparent under uniaxial or biaxial deformation.

To the the present author's knowledge, the normality of flow behavior as investigated in Section 4.3.2 has not been addressed previously in the context of NC materials. While the present approach is fairly general and extensible to other material systems and microstructures (particularly, higher grain sizes in NC materials, where dislocation plasticity

becomes important), it could be quite computationally intensive to compute relaxed, unloaded inelastic strains in cases where relaxation times of the elastic strain are several orders of magnitude longer than what is feasible via MD. Notably, molecular statics methods as employed by Vitek et al. [250] cannot be directly used due to the presence of multiple, inter-dependent deformation mechanisms prevalent in nanocrystals.

Based on our results, it also appears that the role of internal von Mises stresses in NC metals towards affecting deformation behavior is quite different from that of residual stresses in CG metals. While the latter is known to facilitate local yielding via dislocation glide by superimposing on the applied stress, the former, at least at the atomic scale, appears to correlate better with increased likelihood of interatomic jamming and low free volume. This inference is supported by the observation that applied hydrostatic compression intensifies the upper extremes of the internal von Mises stress distribution, yet concurrently increases the ensemble-scale yield strength.

Rather, free volume in the interface appears to be a better candidate as a constitutive state variable to be incorporated in a continuum level theory of STZ-mediated inelastic deformation. However, it is important to note that local atomic rearrangement events appear to be accompanied by a transient dilatancy, or *change in free volume*; this change is likely to couple with the applied pressure [31], thereby determining the pressure-coefficient of the shear strength in nanostructures. MD based exploration of geometrically well-ordered interfaces from the standpoint of this transient dilatancy can be particularly fruitful towards improving theories of pressure-dependent interfacial sliding/migration. Lastly, the NC grain size regime dominated by dislocation nucleation from interfaces (>10–20 nm) remains open for analysis; pressure-effects on inelastic deformation in this grain size regime have been studied in Chapter 6.

4.5 Summary

In this chapter, we have explored the effect of a variety of multiaxial deformation paths on the inelastic deformation behavior of NC Cu. To resolve the inelastic yield transition, two different yield criteria have been proposed. One is derived from statistical mechanics

and was introduced by the present author in the previous chapter. The other employs explicit relaxation of (an)elastic strains. These criteria provide measures of defect avalanches associated with inelasticity, independent of the active deformation mechanisms. Further, using measures of atomic-scale stress, volume and strain, the effect of internal stresses and free volume have been extensively compared for the cases of both pure shear deformation as well as shear deformation under superimposed hydrostatic pressure.

The results presented in this chapter suggest that inelastic deformation of nanocrystalline Cu (in a 5 nm mean grain size regime dominated by the activation of shear transformation zones in the interfaces) is pressure-dependent. However, the pressure dependence is weak enough to not manifest a significant tension-compression strength asymmetry for the 5nm grain size studied. Additionally, inelastic strains in the nanocrystalline Cu sample were observed to be almost purely deviatoric, suggesting that flow occurs normal to the von Mises yield surface.

An analysis of correlations between various per-atom metrics (stress, volume, strain) reveals novel information regarding the physical origins of the pressure-dependence of shear strength. Chiefly, it appears that internal stresses in the interface network increase under compressive hydrostatic stress and inhibit yielding via a jamming effect at the atomic scale. On the other hand, excess volume in the interfaces eases interatomic rearrangement in shear transformation zones. It is likely that transient dilatancy associated with interatomic rearrangement couples with imposed pressure to change the activation barrier for inelastic deformation. These effects are relevant to an improved understanding of interface-mediated plasticity in fcc metals.

CHAPTER V

SHEAR DEFORMATION BEHAVIOR OF SYMMETRIC TILT INTERFACES IN CU

5.1 Introduction

The role of interfaces in determining the mechanical properties of metals in the nanocrystalline (NC) and ultra fine-grained (UFG) state is well-documented in the literature [71, 110, 245]. It has been observed that interfaces act as dislocation sources in NC and UFG materials in the absence of traditional dislocation multiplication and storage mechanisms [122, 200, 228]. Besides dislocation nucleation, interfaces can also contribute to inelastic deformation via inter-granular sliding and stress-induced interface migration. These mechanisms have been observed in numerical simulations [183, 243, 62, 33, 178] as well as experiments [115, 190, 191, 175, 116, 270].

The dynamics of interface motion driven by an external stress (as opposed to capillarity) has been the subject of significant interest in recent years. Olmsted et al. [157] studied the mobility of 388 Ni grain boundaries under the driving force of a biased interatomic potential and found a wide range of boundary mobilities, revealing an unequivocal but complex dependence of interface mobility on the interface structure. In symmetric tilt interfaces belonging to the $\langle 100 \rangle$ family of tilt misorientations, molecular dynamics (MD) simulations predict a stick-slip behavior via highly correlated atomic motion [146], and a well-defined geometric coupling factor relating displacements parallel and normal to the interface plane [33]. Coupled interface motion was observed at a wide range of low to medium homologous temperatures. These findings form the basis of an emerging idea in the mechanics of nanomaterials: interfaces need to be treated as dynamic constituents of the microstructure, rather than just static barriers to dislocation glide.

Several models of shear-coupled migration have been proposed in recent years. For symmetric tilt interfaces belonging to the $\langle 100 \rangle$ family of tilt directions in fcc metals, dislocation-based model of migration interpret interface motion in terms of the cooperative glide of dislocations on unusual slip planes [32], or, in the case of general tilt boundaries (non-CSL), via a lattice distortion assisted by short-range atom shuffling at the interface [34]. Alternatively, a disclination-based approach interprets interface motion as the migration of disclination dipoles driven by couple stresses arising from an elastic shear strain [213, 67]. These models are promising candidates for inclusion into mesoscopic theories of interface-mediated elasto-plasticity, although they still lack an extension to general interfaces of a mixed tilt-twist character, or non-equilibrium grain boundaries. Further, recent work in the shear-driven interface motion has focused largely on the kinematics of interface motion, in terms of linearized mobilities and geometrical coupling factors [32, 33, 94, 146, 157]. In comparison, the kinetic aspect of interface motion, including energy barriers, threshold stresses, and the ease of activation of alternate modes of interface motion, have been the subject of relatively fewer studies, e.g., [90, 256].

MD simulations can complement mesoscopic modeling efforts by providing full-resolution studies of mechanism(s) of interface motion, as well as other important aspects such as critical stress for interface motion and stress-state dependence of the interface motion 'event'. There is significant evidence from atomistic simulations to suggest that the effects of non-deviatoric (in dislocation theory, non-glide) stresses on defect nucleation and propagation are not negligible. Spearot et al. [201] showed that interface-mediated dislocation nucleation tends to exhibit a normal stress dependence, likely contributing to the observed tension-compression strength asymmetry [187] in the nanocrystalline state. Molecular statics simulations performed by Tschopp and McDowell [226] reported an increase in the unstable stacking fault energy (USFE) of Cu under the effect of a compressive stress normal to the slip plane. In light of these observations, a natural question is whether non-deviatoric stress components influence stress-driven interface motion as well. The answer to this question is not only interesting from a fundamental physics standpoint, but also potentially helpful towards understanding microstructure evolution during highly constrained severe plastic

deformation. For example, a significant effect of hydrostatic stress on the shear flow stress of Cu has been observed by Zehetbauer et al. [283] during high pressure torsion.

In the present chapter, we have used MD simulations to study the effect of hydrostatic pressure on the shear deformation behavior of eleven symmetric tilt interfaces in Cu. Interfaces of different characteristics are studied, spanning a range of interface energies, low-order and high-order coincidence site lattice (CSL) misorientations, and including interfaces with structural units that have been found to facilitate atomic shuffling [178, 233]. The purpose of the current work is to explore the variety of interface responses and relate them to structural transitions in the interfaces. The chapter is organized as follows: Section 5.2 provides an overview of the simulation methodology and structural characteristics of the interfaces studied as a part of this work. Section 5.3 reports findings from simulation of shear deformation of these interfaces under multiaxial pressure+shear loading paths. Section 5.4 discusses the implications and limitations of the present work, and a summary of major findings have been provided in Section 5.5.

5.2 Methodology

5.2.1 Interface structure

Homophase interfaces are described using five degrees of freedom [171], leading to a very large number of possible interface structures. The present study was restricted to symmetric interfaces in Cu with a pure tilt, coincidence site lattice (CSL) [107] misorientation along the $\langle 100 \rangle$ or $\langle 110 \rangle$ crystallographic axis (see Table 2). In selecting specific interfaces, the focus was on interfaces with 'special' characteristics such as low energy and/or high free volume.

Interfaces were constructed as 3-D periodic bicrystals by bringing together two disoriented single crystals into a minimum-energy interface configuration via a process of relative lattice translation, atom deletion, energy minimization, and isobaric-isothermal equilibration (for details of this process, see [229]). The resultant structures exhibit long-range periodicity in the plane of the interface, and were in good agreement with experimental observations [144, 140]. Since all interfaces considered are symmetric tilt boundaries of a CSL

misorientation, each boundary can be identified uniquely by the order of its CSL and the crystallographic index of the interface plane. According to this nomenclature, for instance, the coherent twin is a $\Sigma3\{111\}$ interface, and the $\theta = 36.9°$ interface in the $\langle 100 \rangle$ family of misorientations is designated $\Sigma5\{210\}$.

To provide the necessary context, we summarize the salient features of the interfaces studied in this work and the rationale behind their selection. Interfaces in the $\langle 100 \rangle$ family of tilt misorietations were selected from those already studied extensively in the literature. Two of these interfaces, $\Sigma5\{210\}$ and $\Sigma5\{310\}$, correspond to preferred misorientations (i.e., their interfacial energies lie at local minima in the space of misorientations). All three $\langle 100 \rangle$ interfaces are composed of "kite-shaped" structural units as defined by the structural unit (SU) model [209].

Interfaces in the $\langle 110 \rangle$ family of misorientations were further subdivided into the following categories:

- *Low-energy:* These interfaces are characterized by their low interfacial energy and good atomic fit in the interface plane. These misorientations correspond to very prominent 'cusps' in the energy landscape of $\langle 110 \rangle$ interfaces in Cu.

- *E structural unit:* These interfaces have a misorientation angle θ in the range $109.5° < \theta < 180°$ and contain the 'E' structural unit according to the SU model. The E structural unit has been associated with excess free volume and a tendency to facilitate localized atomic shuffling, resulting in a lowered threshold stress for dislocation nucleation [229, 233].

- *ITB structure:* In Cu, these interfaces are made up of Shockley partial dislocations periodically occurring in the direction of the interface period. Two interfaces are considered; the $\Sigma3\{112\}$ incoherent twin boundary (ITB) and a near-ITB $\Sigma353\{8\ 8\ 15\}$ interface with misorientation within 5° of the ITB and a similar structure.

- *Other:* This category contains a high-order CSL boundary $\Sigma491\{5\ 5\ 21\}$ not categorized according to any of the previous three classifications.

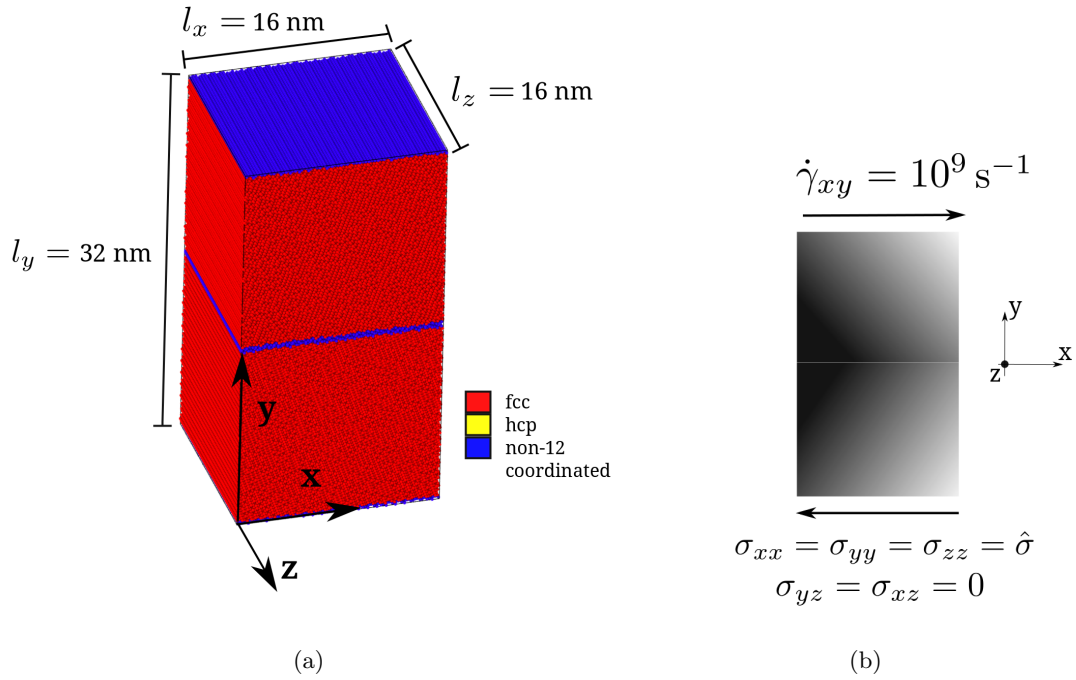

Figure 45: (a) A bicrystal sample, containing two disoriented crystals separated by Σ9{221} symmetric tilt grain boundaries, shown following energy minimization and relaxation. Atoms are colored according to common neighbor analysis [232], a measure of local crystallinity. The structure is periodic along all three Cartesian directions. (b) Schematic showing the deformation applied to the bicrystal sample(s). A constant strain rate is applied parallel to the grain boundary plane and all stress components except σ_{xy} are prescribed and held constant throughout the deformation.

Although these interface misorientations cannot be claimed to adequately sample the general, 5-dimensional misorientation subspace, they include several preferred interface structures that can occur in real microstructures. Further, many constituent elements of these interfaces (e.g., the E structural unit) have already been extensively studied in the literature.

5.2.2 Simulation setup

Figure 45(a) shows a bicrystal interface prior to deformation (the Σ9{221} interface has been shown for the purpose of illustration). The number of atoms in each bicrystal varied between 7.0×10^5 and 1.2×10^6. Periodic boundary conditions were imposed along all three Cartesian directions. Direct control of the six-component global stress tensor ($\boldsymbol{\sigma}$) and

Table 2: List of Cu symmetric tilt interfaces studied in the present work, distinguished based in the Coincidence Site Lattice (CSL) Σ number, and the crystallographic index of the interface plane. θ indicates the misorientation based on rotation around the tilt axis ($\langle 110 \rangle$ or $\langle 100 \rangle$), and *Mechanism* indicates the deformation mechanism observed under simple shear deformation. (M) denotes pure shear-coupled migration, (S) indicates sliding, (PBM) indicates phase boundary migration, and (D) indicates dislocation nucleation from the interface. Simultaneous activation of two or more mechanisms is shown by the '+' sign. See Figure 47 for details of deformation mechanisms. The interface classification scheme has been discussed in Section 5.2.1.

Interface	θ (°)	*Mechanism*
Tilt axis $\langle 110 \rangle$		
Low-energy		
$\Sigma 3\{111\}$	109.5	M
$\Sigma 11\{113\}$	50.5	M
E structural unit		
$\Sigma 9\{221\}$	141.1	S
$\Sigma 11\{332\}$	129.5	M+S
$\Sigma 19\{331\}$	153.5	M+S
$\Sigma 129\{881\}$	169.9	M
ITB structure		
$\Sigma 3\{112\}$	70.5	PBM
$\Sigma 353\{8\ 8\ 15\}$	74.1	PBM
Other		
$\Sigma 491\{5\ 5\ 21\}$	37.2	D+S
Tilt axis $\langle 001 \rangle$		
$\Sigma 5\{210\}$	53.1	M
$\Sigma 5\{310\}$	36.9	M
$\Sigma 13\{510\}$	22.6	M

temperature (T) was ensured via a Nosé-Hoover chain thermostat [132] and an anisotropic Parinello-Rahman (PR) [161] barostat, which allowed for volume change and shape change of the simulation cell in response to prescribed stress-type boundary conditions. Prior to any deformation, the bicrystal was equilibrated under isothermal-isostress ($N\boldsymbol{\sigma}T$) conditions to a temperature of 10 K, until all six components of the global stress tensor were relaxed to zero. Then, prior to shear deformation, the simulation cell was placed under an isotropic hydrostatic stress $\hat{\sigma}$ and allowed to equilibrate for an additional 5 ps.

The shear deformation scheme and relevant boundary conditions are shown in Figure 45(b). The interfaces were oriented to deform under in-plane shear along the interface period. In the context of Figure 45(a), this deformation corresponds to the xy-component of the stress/strain tensor (i.e., the plane normal to the positive y-axis is displaced in the direction of the positive x-axis). A linear displacement gradient ranging from 0 at $y = 0$ to δ_{xy} at $y = l_y$ was applied to all atoms, producing a shear strain of $\gamma_{xy} = \delta_{xy}/l_y$, at the rate of 10^9 s^{-1}. Assuming shear deformation begins at time $t = 0$, the global stress and strain tensors at any time $t > 0$ are expressed as follows:

$$\boldsymbol{\sigma} = \begin{pmatrix} \hat{\sigma} & \sigma_{xy}(t) & 0 \\ \sigma_{xy}(t) & \hat{\sigma} & 0 \\ 0 & 0 & \hat{\sigma} \end{pmatrix} \tag{38}$$

$$\boldsymbol{\epsilon} = \begin{pmatrix} 0 & \gamma_{xy}(t)/2 & 0 \\ \gamma_{xy}(t)/2 & 0 & 0 \\ 0 & 0 & 0 \end{pmatrix} \tag{39}$$

In Equations 38 and 39, $\hat{\sigma}$ is a time-invariant pressure, imposed prior to deformation and maintained throughout the deformation stage. The shear strain, $\gamma_{xy}(t)$, is prescribed as a (linear) function of time, and $\sigma_{xy}(t)$ is the shear stress produced as a result. Note that the application of $\hat{\sigma}$ causes net compression/expansion of the simulation cell prior to any shear deformation. However, we select this cell deformed under the influence of $\hat{\sigma}$ as the reference configuration to compute the strain tensor $\boldsymbol{\epsilon}$. This ensures that the strain tensor at any stage of the shear deformation does not include the strain suffered due to the

imposition of $\hat{\sigma}$, but does include dilatation or distortion of the simulation cell occurring during the shear deformation.

The present deformation method differs significantly from previous work (e.g., [33, 234, 256]), where shear was imposed by prescribing a velocity gradient in the canonical (constant volume) ensemble. Unfortunately, that method inherently limits the types of stress states accessible during deformation, and also suppresses any changes in volume of the simulation domain. The current method, in contrast, imposes a displacement gradient, and P-R boundary conditions permit free anisotropic expansion as well as warping of the simulation domain. Further, due to periodic boundary conditions along all Cartesian directions, any kind of free surface effects (cf. [178, 90]) are precluded and the simulation is expected to better pertain to the evolution of defect structures in the bulk. Simulations of shear deformation with P-R boundary conditions can be found, for example, in [31, 39] and [193]. Finally, although 3D periodic boundary conditions effectively introduce a "pair" of identical grain boundaries in each simulation cell, these grain boundaries are separated by a sufficient distance ($\approx$ 15 nm) so that their distortion fields don't overlap. Spearot [198] concluded that a 15 nm separation is sufficient to avoid influencing dislocation nucleation from the interface.

5.2.3 Dilatation and free volume

To compute the dilatation associated with shear stress-driven interface motion, the atomic-scale deformation gradient formulation of Zimmerman et al. [297] was used. The process takes two atomic configurations as input (a reference configuration and a current configuration) and yields a per-atom tensor $\mathbf{F}$ that estimates the 3-D deformation in the sphere containing an atom and its nearest neighbors. The per-atom dilatation ($\hat{\epsilon}/atom$) can be obtained from $\mathbf{F}$ following [237]:

$$\mathbf{E} = \frac{1}{2}(\mathbf{F}^{\mathrm{T}}\mathbf{F} - \mathbf{I}) \tag{40}$$

$$\hat{\epsilon}/atom = \mathrm{tr}(\mathbf{E})/3 \tag{41}$$

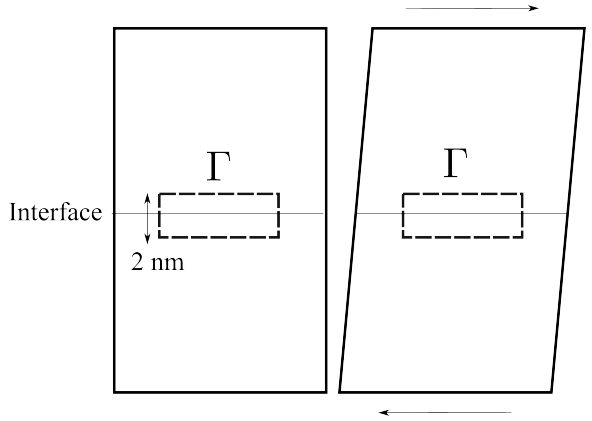

Figure 46: A schematic showing the box-shaped sub-volume Γ, containing the interface, within which the free volume (FV) is computed. As the bicrystal deforms under shear, the region Γ translates, such that its center coincides with the centroid of the simulation domain in each deformed configuration.

where $\mathbf{E}$ is the Lagrangian strain tensor, $^{\mathrm{T}}$ denotes the matrix transpose operation, tr is the trace operation, and $\mathbf{I}$ is the 3×3 identity tensor. $\hat{}$ is used to denote the hydrostatic/dilatational invariant of a tensor. A $/atom$ suffix is attached to $\hat{\epsilon}$ to distinguish it from another symbol, $\hat{\sigma}$, frequently used in this thesis, which pertains to the hydrostatic stress tensor of the *entire* atomistic ensemble.

Free volume (FV) was computed within a box-shaped sub-volume of the simulation domain, Γ, containing the interface (see Figure 46), using the grid-occupancy algorithm of Tucker et al. [233]. In this algorithm, the interior of Γ is overlayed with a 3-D grid of points spaced at 1/20th of the lattice parameter ($a = 3.615$ Å). Then, points that have no atom centers within a cut-off radius of $a/2$ are designated 'free volume' (FV) of magnitude $(a/20)^3$ Å^3. This condition ensures that a perfect fcc lattice without interfaces has zero free volume. Using Tucker et al.'s algorithm, we computed the free volume content of each of the interfaces studied. The total free volume content (unit Å^3) was divided by the x-z cross-section of the region Γ, yielding FV per unit area (unit Å^3/Å^2).

5.2.4 A phenomenological model of pressure-sensitive shear flow

To analyze the pressure-dependence of shear deformation, a simple phenomenological framework is proposed. The hydrostatic stress imposed on the simulation domain is designated $\hat{\sigma}$, where negative $\hat{\sigma}$ corresponds to a compressive hydrostatic stress by convention. We

express the bicrystal's initial yield strength under shear with zero superimposed pressure ($\hat{\sigma} = 0$) as a fraction of the bicrystal shear modulus, i.e.,

$$\sigma_0^{\mathrm{Y}} = \alpha_0 G_0 \tag{42}$$

where subscripts 0 indicate a state of zero superimposed pressure, and σ_0^{Y} denotes the yield strength (superscript Y) of the bicrystal under shear deformation in the plane of the interface (i.e., normal to the y-direction in Figure 45(a)) and in the direction of the positive x-axis, the interface period). To avoid clutter in notation, the xy subscript has been dropped. G_0 is the bicrystal shear modulus along the deformation direction (xy), and α_0 is a constant of proportionality. Under a state of non-zero superimposed pressure ($\hat{\sigma} \neq 0$), the total change in σ^{Y} can be decomposed into two parts: (a) a part that varies in proportion to the pressure-dependent change in elastic modulus, and (b) the remainder, i.e.,

$$\sigma^{\mathrm{Y}}(\hat{\sigma}) = \alpha G(\hat{\sigma}) = \alpha_0 G(\hat{\sigma}) + \sigma^*(\hat{\sigma}) \tag{43}$$

In Equation 43, σ^* represents the *additional yield strength elevation* and captures the deviation of the computed yield strength from the 'expected' yield strength $\alpha_0 G(\hat{\sigma})$. To the first order, G, σ^{Y} and σ^* can be expressed as linear functions of pressure, i.e.,

$$G = G_0 - k_G \hat{\sigma} \tag{44}$$

$$\sigma^{\mathrm{Y}} = \sigma_0^{\mathrm{Y}} - k_Y \hat{\sigma} \tag{45}$$

$$\sigma^* = -k_* \hat{\sigma} \tag{46}$$

where k_G, k_Y and k_* are pressure-coefficients of the bicrystal's shear modulus, shear yield strength, and additional yield strength elevation respectively. Also, using Equations 42, 44, 45 and 46, we obtain:

$$k_Y = \alpha_0 k_G + k_* \tag{47}$$

Since compressive hydrostatic stresses are considered negative according to the convention adopted in this work, a positive value of k_G, k_Y or k_* corresponds to a stiffening/strengthening of the material with increasing compressive stress.

5.3 Results

5.3.1 Shear deformation kinematics

The twelve interfaces studied in this work exhibited a variety of deformation mechanisms under simple shear with zero superimposed pressure. The kinematics of interface motion has been classified into shear-coupled migration, sliding and/or dislocation-based mechanisms in the third column of Table 2. Figure 47 shows three major deformation mechanisms, resolved with the aid of a marker comprised of a vertical slice of atoms hidden from view over the course of the deformation. In the undeformed configuration, this slice is straight. Pure shear-coupled interfacial migration tends to shear the crystal in the wake of the migration event while maintaining continuity of the marker (Figure 47(a)). Note that the interface maintains its geometrical structure in cases of pure shear-coupled migration. On the other hand, pure sliding tends to break the continuity of the marker without any interface motion normal to the interface plane (Figure 47(b)). A third deformation mechanism is simultaneous sliding and migration, shown in Figure 47(c), where interface motion normal to the interface plane is accompanied by translation of atoms parallel to the interface plane, thereby breaking the continuity of the marker. A fourth deformation mechanism was noted in the case of interfaces with incoherent twin boundary (ITB) structure. As shown in Figure 48, these interfaces tended to bifurcate into two phase boundaries separated by phase containing periodic stacking faults.

Based on Table 2, some trends in the deformation behavior can be noted: all three interfaces in the $\langle 100 \rangle$ family of misorientations undergo shear-coupled migration, in agreement with previous work [33]. So do the low-energy interfaces from the $\langle 110 \rangle$ family (for the coherent twin, see [90]). Pure sliding was observed in the $\Sigma 9\{221\}$ interface, consistent with Tucker et al. [234]. Other interfaces with the E structural unit, however, sheared via a combination of migration and sliding, while the $\Sigma 129\{881\}$ interface underwent pure migration. Interfaces with the ITB structure were found to dissociate into two phase-boundaries, enclosing a phase with periodic stacking faults (in the case of the ITB, this is the *9R* phase). This shear-driven phase boundary migration has been previously reported by Wang et al. [256]. Based on visual inspection, we conclude that shear deformation kinematics of the

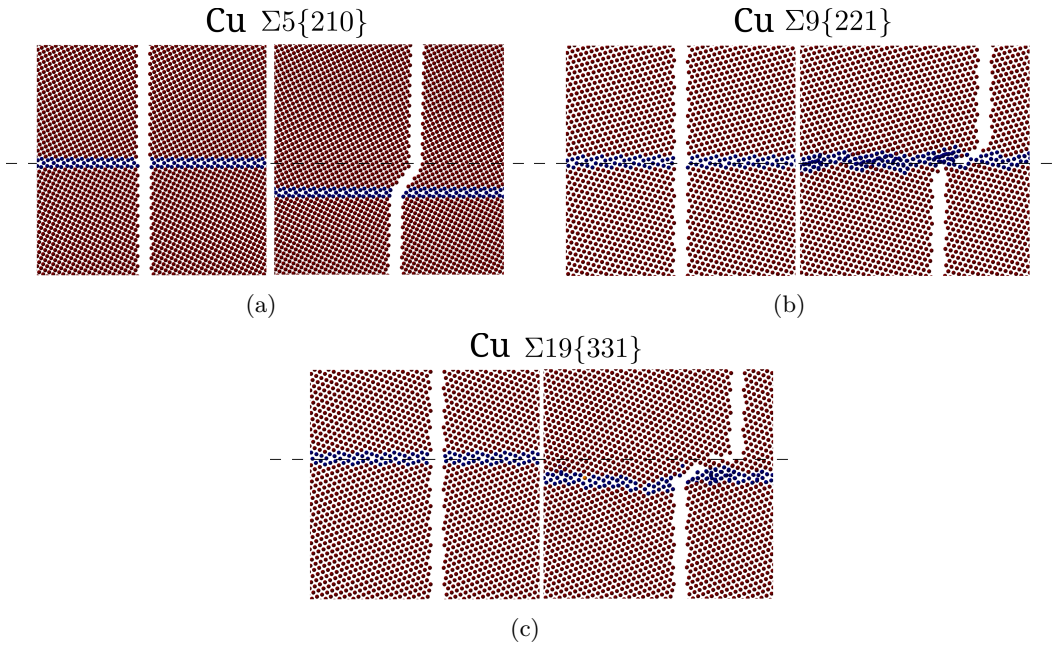

Figure 47: Three types of shear deformation mechanisms: (a) pure shear-coupled migration, (b) pure sliding, and (c) sliding+migration.

interfaces studied in this work agree with previous atomistic studies, despite significant differences in boundary conditions and the deformation algorithm.

5.3.2 Elastic properties of interfaces

The pressure derivatives of the elastic constants of single-crystal Cu were experimentally determined by Daniels and Smith [48]. Later, Adams et al. [1] showed that these derivatives can be reproduced with reasonable accuracy using an EAM potential developed by Foiles et al. [66]. Adams et al. further observed that the presence of an interface with miscoordinated atoms (in their case, a Σ5 twist boundary in Cu) reduces the shear modulus in the plane of the interface.

The elastic moduli of the twelve interface structures studied in this work were computed in the x-y shear direction based on the linear elastic part of the shear stress (σ_{xy}) vs. shear strain (γ_{xy}) curve, both under simple shear as well as under shear with an imposed pressure $\hat{\sigma}$. The stress-strain curves used to perform this computation can be found in Figures 50–59. The results of the computation are shown for four interface structures in Figure 49. To resolve the effect of the interface on the elastic properties of the bicrystal, the bicrystal

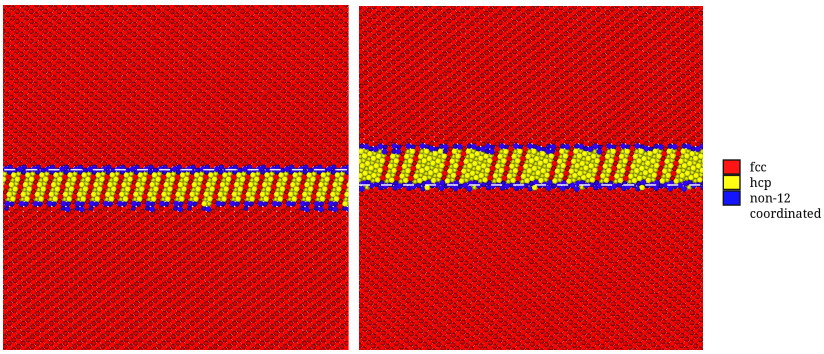

(a) (b)

Figure 48: Shear deformation via phase boundary migration in two interfaces classified under the ITB structure: (a) the incoherent twin boundary $\Sigma3\{112\}$, and (b) $\Sigma353\{8\ 8\ 15\}$ grain boundary, showing snapshots at 0.5% global shear strain. The dashed line shows the boundary position prior to any shear deformation.

shear modulus was compared to the shear modulus of a similarly-oriented defect-free Cu single crystal. Note that this comparison is valid for symmetric tilt interfaces, such as those considered in this work, since the crystallographic directions along the shearing direction on either sides of the interface are equivalent. For details of this analytical procedure used to compute the single crystal elastic modulus, the reader is referred to Appendix A.

The change in elastic modulus G_{xy} of the $\Sigma3\{111\}$ interface (the coherent twin) due to applied pressure is shown in Figure 49(a). The zero-pressure shear modulus of the bicrystal containing the twin interface was observed to be very close to the single-crystal value, likely due to the good atomic fit in the interfacial regions. For other interfaces, the bicrystal shear modulus was observed to be lower than the single-crystal value, the difference being moderate (≈ 5 GPa) in Figure 49 (b),(c) to large (≈ 12 GPa) in Figure 49(d), for the ITB structure.

Although only four interfaces have been shown, in general, G_{xy} for all interfaces was found to be lower than the single crystal values at zero pressure and was observed to increase directly with the imposed (compressive) pressure. While a linear variation in G_{xy} was observed for all interfaces, the quality of the linear fit varied. The relatively low quality of fit for the $\Sigma5\{210\}$ interface (Figure 49(c)), for example, occurred due to small deviations

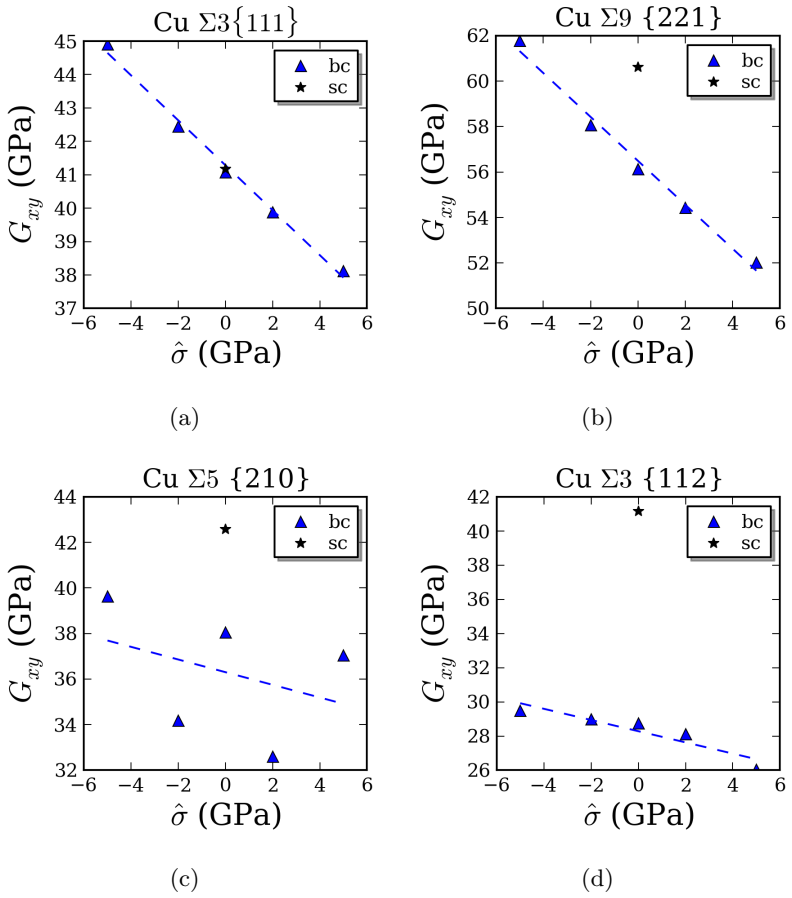

Figure 49: Variation in the shear modulus (G_{xy}) of four bicrystalline interfaces with pressure ($\hat{\sigma}$). 'bc' denotes the bicrystalline shear modulus and 'sc' is the analytically-computed shear modulus of a similarly-oriented single crystal.

from a linear stress-strain response at low shear strains. For all bicrystals, k_G, the pressure-coefficient of shear modulus (see Section 5.2.4), was obtained via a linear fit to G_{xy}. Values of k_G are compiled in Table 3.

5.3.3 Deformation behavior: Initial yield

The twelve interface structures described in Table 2, after relaxation and equilibration to 10 K, were deformed under strain control with a constant superimposed hydrostatic stress $\hat{\sigma}$ in the range -5 GPa (compressive) to 5 GPa (tensile). The strain was applied till slightly beyond initial yield, allowing for relaxation of the peak stress reached during the deformation. To analyze the stress-strain evolution, the same interface classification scheme as Section 5.2.1 was used. The following sections describe the shear deformation kinetics and the effect of pressure. For a short summary of results (based on terms defined in Section 5.2.4), the reader is referred to Table 3.

5.3.3.1 $\langle 100 \rangle$ *tilt axis*

The elasto-plastic deformation behavior of interfaces in the $\langle 100 \rangle$ family of tilt misorientations is shown in Figure 50. Under zero superimposed pressure, the energetically favorable interfaces, $\Sigma 5\{210\}$ and $\Sigma 5\{310\}$ were much weaker under shear as compared to the $\Sigma 13\{510\}$ interface and reached their peak stress at lower strains. The deformation mechanism was shear-coupled migration in all three cases.

These results can be interpreted in terms of the dislocation-based shear-coupled grain boundary migration model of Cahn et al. [33]. The direction of migration in all three cases was the -y direction, which corresponds to a negative coupling coefficient β and the activation of the $\langle 110 \rangle$ coupled migration mode. This behavior is consistent with Cahn et al.'s prediction that at low temperatures, all interfaces in the $\langle 100 \rangle$ tilt axis family tend to switch into the $\langle 110 \rangle$ mode, regardless of misorientation. Cahn et al. also estimated the critical shear strength (τ_{ci}) of such a migration event as $\tau_{ci}(\theta) = \sigma_{ci}(\theta)/S_i(\theta)$, where σ_{ci} is the critical resolved shear stress required to move a $\langle 110 \rangle$ dislocation, and S_i is the Schmid factor for resolving τ_{ci} onto the dislocation glide plane. According to this model, τ_{ci} is directly proportional to $1/S_i(\theta)$, where $S_i(\theta) = \cos(\pi/2 - \theta)$ for the $\langle 110 \rangle$ migration mode.

Based on the boundary misorientation, it is expected that τ_{ci} for the $\Sigma5\{210\}$,$\Sigma5\{310\}$, and $\Sigma13\{510\}$ interfaces would be in ratio 1:1.33:2.08. However, the observed ratio is very different: 1:0.64:3.95, which indicates that a shear deformation model based on the motion of an array of non-interacting $\langle 110 \rangle$ dislocations fails to capture the low-temperature shearing kinetics of these interfaces.

The effect of imposed hydrostatic stress on the shearing kinetics is particularly interesting. In Figure 50, the shear stress-strain curves under the influence of different imposed pressures are significantly different, and the differences were quantified according to the phenomenological model presented in Section 5.2.4, based on stresses σ^{Y}, σ^*, and pressure coefficients k_y and k_*. An interesting observation is that the yield strength (as defined by the peak stress) for the $\Sigma5\{210\}$ interface *decreases* with increasing compressive stress, while the other two interfaces in this family of misorientations strengthen under shear with imposed compressive stress. The latter behavior is relatively common—occurring in glasses, soils, and NC and UFG metals–but the former behavior is unprecedented to our knowledge.

The effect of imposed pressure $\hat{\sigma}$ on the shear strength σ_{xy}^{Y} is quantified in Figure 51. In all plots, a linear trend can be identified. However, in Figure 51(a) and (b), the variation of σ^{Y} with $\hat{\sigma}$ can better be described as bilinear, since there is a different 'slope' in the interval [-2,2] GPa. This bilinearity could imply that the barrier for shear migration is affected differently by the imposed hydrostatic pressure at low pressures, vs. high pressures for these interfaces. In contrast, a simple linear trend was quite clear for the $\Sigma13\{510\}$ interface (Figure 51(c)).

A potentially more informative metric of the effect of hydrostatic stress on the shear yield strength is σ^*. Recall from Section 5.2.4 that σ^* is the difference between the observed shear yield strength σ^{Y} and the expected yield strength if only pressure-induced elastic stiffening/softening was taken into account. Figure 52 shows the evolution of σ^* with pressure $\hat{\sigma}$ for the three interfaces in the $\langle 100 \rangle$ misorientation family. Immediately, it is noted that the range of σ^* is quite significant for the $\Sigma5\{210\}$ and $\Sigma13\{510\}$ interfaces: around 0.6-0.8 GPa for a 10 GPa change in $\hat{\sigma}$. σ^* varies much more weakly for $\Sigma5\{310\}$ interface; it is smaller by an order of magnitude compared to the other two interfaces. Finally, a locally

increasing portion can be observed in Figure 52(b). This indicates a 'reversal' of slope in the range [-2,2] GPa similar to Figure 51(b), implying that σ^* increases with pressure for imposed pressure magnitudes below 2 GPa. The magnitude of this increase, however, is quite small (0.01 GPa/GPa).

At this point, it is worthwhile to discuss the interpretation of σ^*. Generally, the application of an external compressive (tensile) pressure will cause an an increase (decrease) in the elastic constants of a material, and thereby of its shear moduli along different directions. The transition from the elastic to the plastic regime of deformation typically involves transit of some kind of configurational barrier. While the change in elastic modulus will correctly predict the increase in loading stress required to reach the configuration just prior to inelastic yield, the complex atomic rearrangements involved in surmounting this barrier could get affected by the pressure in complex ways. So while an increase in the shear yield strength σ^{Y} with compressive pressure $\hat{\sigma}$ is trivial and expected to occur in proportion to the change in the shear modulus, in reality, the extent to which σ^{Y} deviates from this trivial prediction is captured by σ^*. Similarly, k_Y and k_* are metrics of how strongly σ^{Y} and σ^* vary with pressure.

Across the interfaces analyzed so far, values of k_* were quite varied, ranging from quite small (0.011) for the $\Sigma5\{310\}$ interface, to relatively large (-0.047 and 0.069) for the $\Sigma5\{210\}$ and $\Sigma13\{510\}$ interfaces, respectively. Most importantly, the negative value of k_* for the $\Sigma5\{210\}$ interface indicates that the atomic rearrangement processes involved in migration of the interface are *facilitated* by the application of an external compressive pressure (to some extent, the same could be argued for the $\Sigma5\{310\}$ interface in the range $-2 < \hat{\sigma} < 2$ GPa). Note that the net effect of pressure on σ^{Y} involves an interplay of two phenomena: (a) pressure-induced elastic stiffening/softening, and (b) the effect of pressure on the kinetics of atomic rearrangements during initial yield (see Equation 47). For some interfaces, an increase in shear modulus can be offset by a simultaneous decrease in the stress required to cross the migration barrier. If the magnitude of the latter decrease is large enough, it could reverse the sign of k_Y, resulting in decrease (increase) of the yield stress under shear with an imposed compressive (tensile) hydrostatic stress.

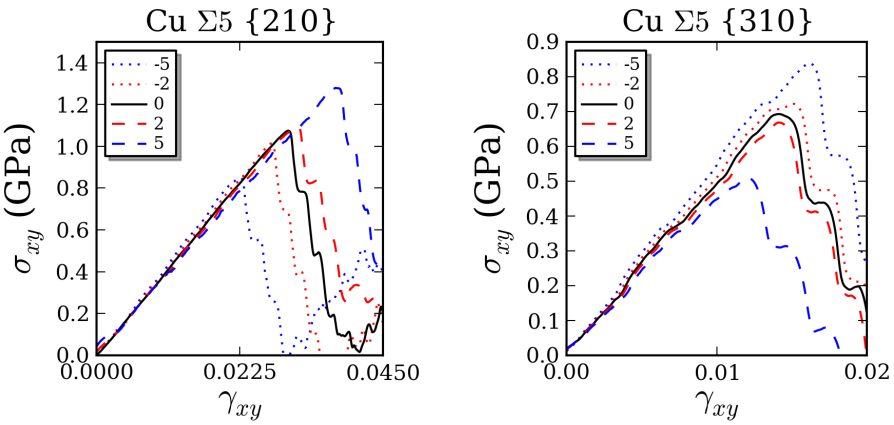

(a) (b)

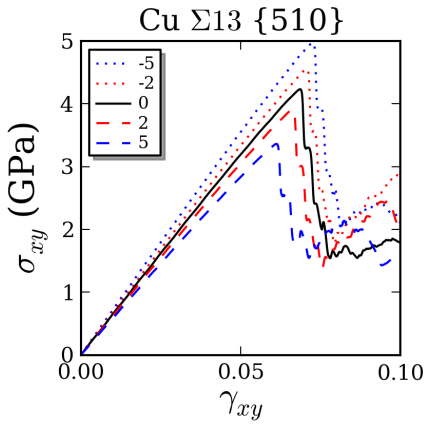

(c)

Figure 50: Effect of pressure on the shear stress-shear strain response of ⟨100⟩ interfaces. The legend denotes imposed pressure in GPa.

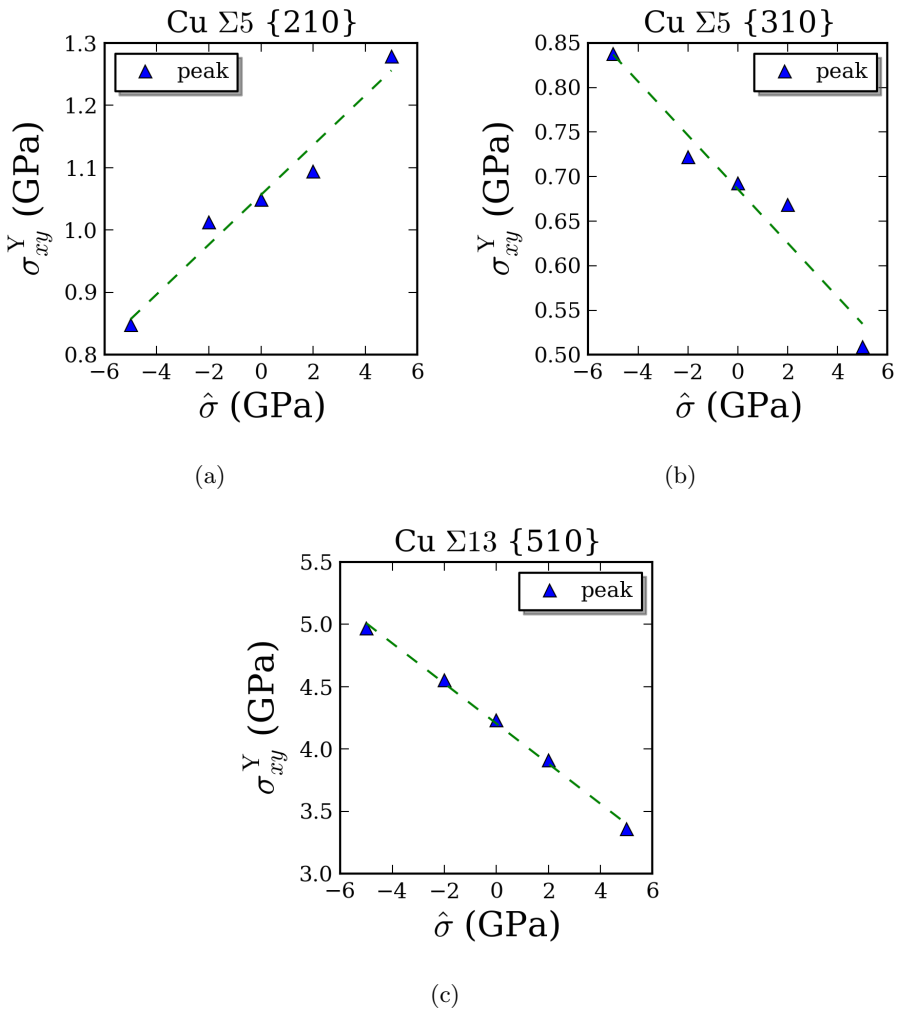

(a) (b)

(c)

Figure 51: Effect of pressure on σ^{Y} for $\langle 100 \rangle$ interfaces.

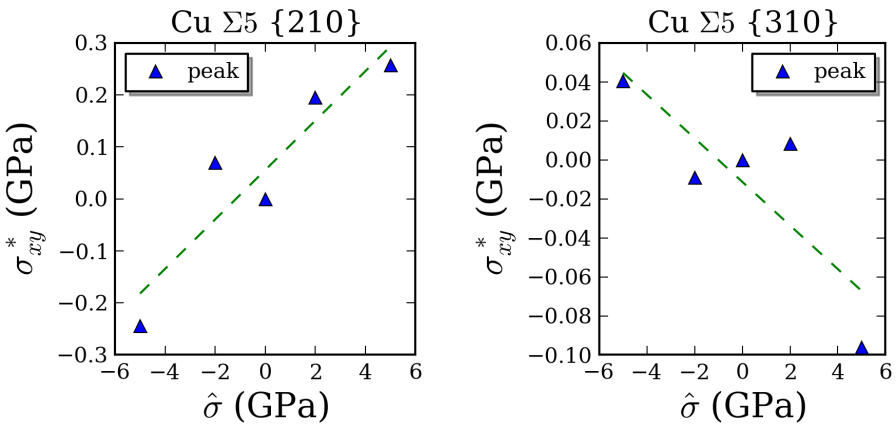

(a)

(b)

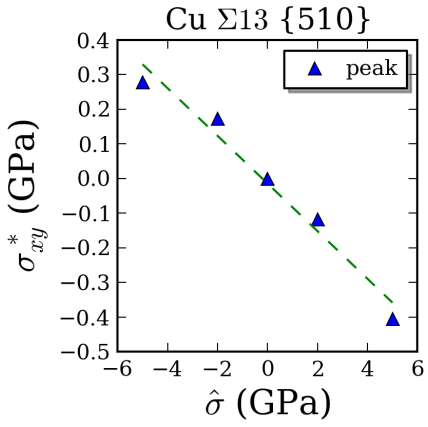

(c)

Figure 52: Effect of pressure on σ^* for $\langle 100 \rangle$ interfaces.

5.3.3.2 ⟨110⟩ tilt axis: Low-energy interfaces

The shear stress-strain responses of the two low-energy interfaces in the ⟨110⟩ misorientation family are shown in Figure 53. Here too, the deformation mechanism was shear-coupled migration in both cases, but the directions of normal boundary motion were opposite: along the -y direction for the Σ3{111} coherent twin, and along +y for the Σ11{113} interface. For the coherent twin, the nucleation of a twinning partial dislocation on a {111} plane adjacent to the twin boundary was observed, consistent with previous reports in the literature [90]. In both 53(a) and (b), the yield strength (peak shear stress) increased with increasing compressive pressure. In (a), the interface was observed to yield at progressively higher strains as the compressive stress was increased. In (b), this trend was reversed.

The evolution of σ^{Y} and σ^{*} for the low-energy interfaces in the ⟨110⟩ misorientation family is shown in Figures 54 and 55 respectively. In both interfaces, the shear strength increased with compressive pressure (i.e, k_Y was positive). However, as seen in Figure 55, k_* was negative in the case of the Σ11{113} interface. This suggests that although the barrier to migration for the Σ11{113} is lowered under an imposed compressive stress (i.e., negative k_*), unlike the Σ5{210} interface from the previous section, k_* is not large enough in magnitude to reverse the sign of k_Y for the Σ11{113} interface. This conclusion is further supported by the increase in yield strain as the imposed pressure goes from compressive to tensile (Figure 53(b)).

5.3.3.3 ⟨110⟩ tilt axis: Interfaces with the E structural unit

Of the symmetric tilt interfaces in the ⟨110⟩ family of misorientation, interfaces with the E structural unit (SU) are particularly interesting on account of the high free volume content and ease of atomic rearrangement at the E SUs [229, 233, 178]. The effect of these characteristics on interfacial mechanical properties is significant, leading to a lowering of dislocation nucleation stress under loading normal to the interface plane, and the activation of interface sliding under shear, following localized atomic shuffling at the E SUs. While all interfaces studied so far underwent shear-coupled migration, interfaces with the E structural unit present examples of simultaneous migration and sliding.

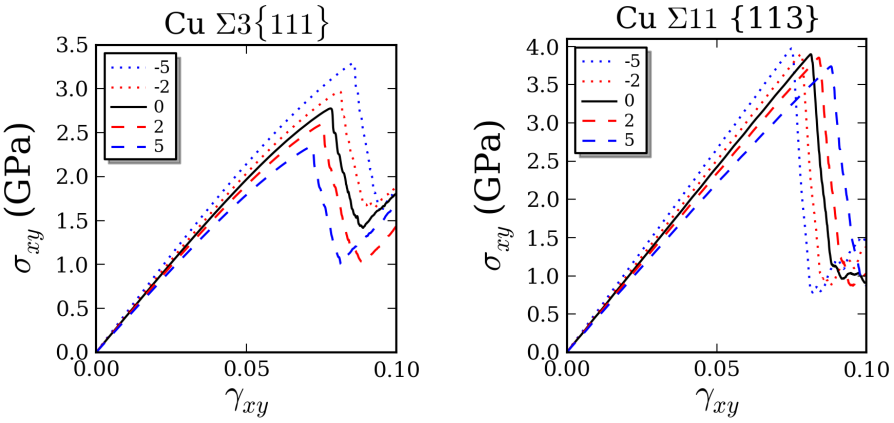

(a) (b)

Figure 53: Effect of pressure on the shear stress-shear strain response of low-energy ⟨110⟩ interfaces. The legend denotes imposed pressure in GPa.

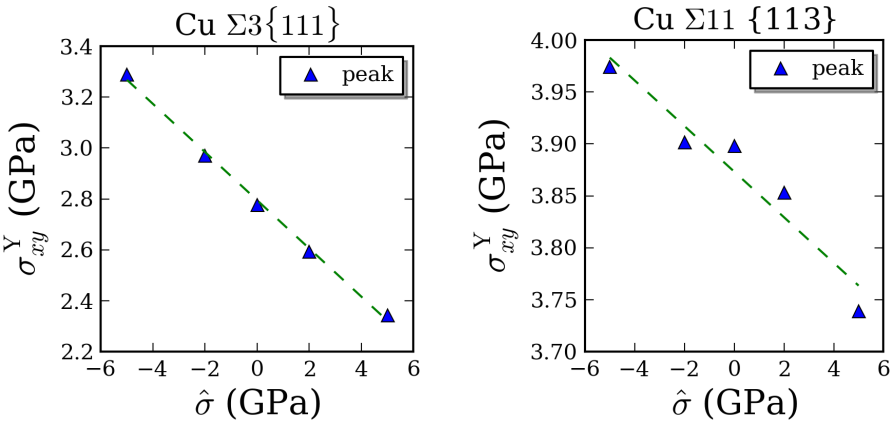

(a) (b)

Figure 54: Effect of pressure on σ^{Y} for the low-energy ⟨110⟩ interfaces.

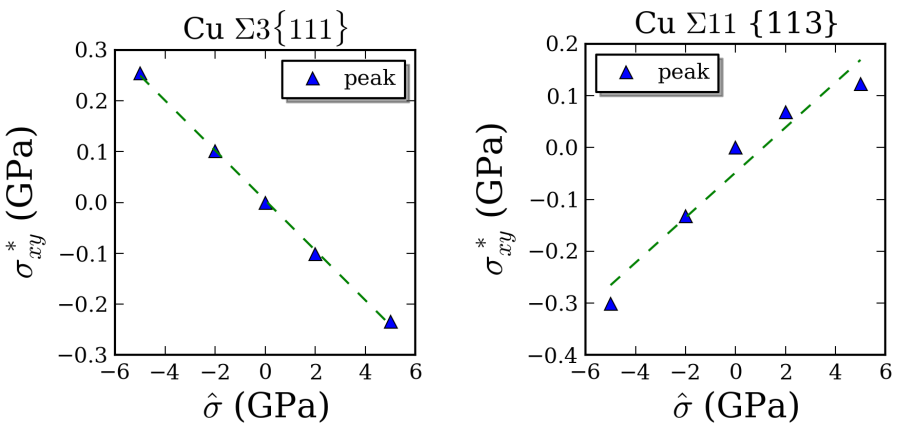

(a) (b)

Figure 55: Effect of pressure on σ^* for the low-energy $\langle 110 \rangle$ interfaces.

Figure 56 shows the shear stress-strain responses of four interfaces with the E SU, for imposed pressures in the range [-5,5] GPa. The deformation mechanism varied from pure sliding in (a), to sliding+migration in (b) and (c), to pure (shear-coupled) migration in (d). The Σ19{331} interface was the strongest while Σ129{881} was the weakest of the four interfaces containing the E SU. Stress-strain curves at different pressures showed a variety of behaviors: compressive hydrostatic pressures led to an increase in strength for the Σ19{331} and the Σ11{332} interfaces, lowered the strength of the Σ9{221} interfaces, but had very little effect on the Σ129{881} interface. The effect of pressure on σ_Y and σ^* is shown in Figures 57 and 58. In Figure 57, it is clear that Σ9{221} weakens with increasing compressive hydrostatic pressure. Among all interfaces studied in this work, it is the only interface besides Σ5{210} (see Section 5.3.3.1) to exhibit this behavior. In other interfaces with the E structural unit, the effect of pressure on σ_Y was weaker compared to the Σ9{221} interface.

The evolution of σ^* with pressure is shown in Figure 58. Here, an important feature can be observed: σ^* decreases with increasing compressive pressure for *all* E SU interfaces studied in this work, implying, in other words, a negative k_*. The absolute value of k_* was highest in the case of the Σ9{221} interface ($k_* = -0.102$), and lowest for the Σ19{331} ($k_* = -0.009$). The atomistic mechanisms suspected of contributing to this behavior are

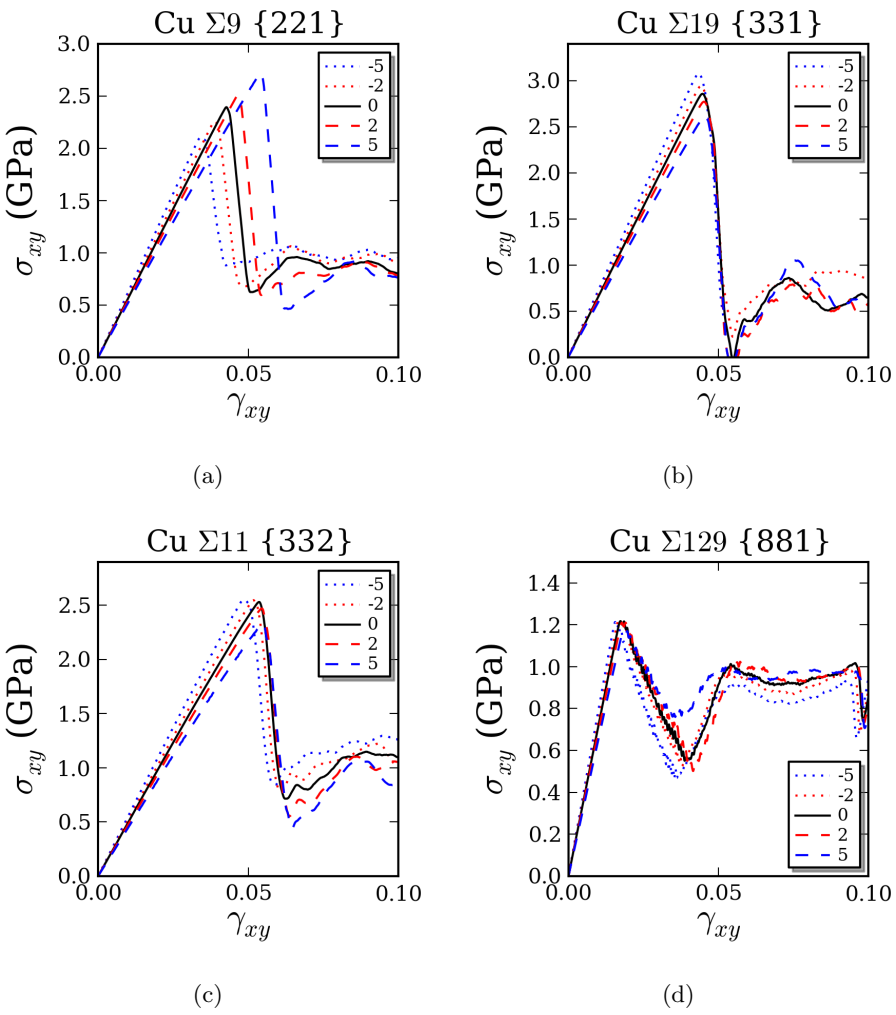

Figure 56: Effect of pressure on the shear stress- shear strain response of interfaces containing the E structural unit. The legend denotes imposed pressure in GPa.

discussed in detail in Section 5.3.5.

5.3.3.4 ⟨110⟩ tilt axis: Interfaces with the ITB structure

Figure 59 shows the shear stress-strain response of the Σ3{112} and the Σ353{8 8 15} interfaces. In both cases, the interface was quite weak under shear. Due to the oscillatory nature of the stress-strain curves (noticeable over strains beyond those shown in Figure 59) it was difficult to identify the yield transition in these interfaces using the peak stress. Therefore, the stresses corresponding to strain offsets of 0.2% and 0.7% from the elastic slope were used as the yield stress(es). Figure 60 shows the effect of pressure on σ^{Y}. In (a),

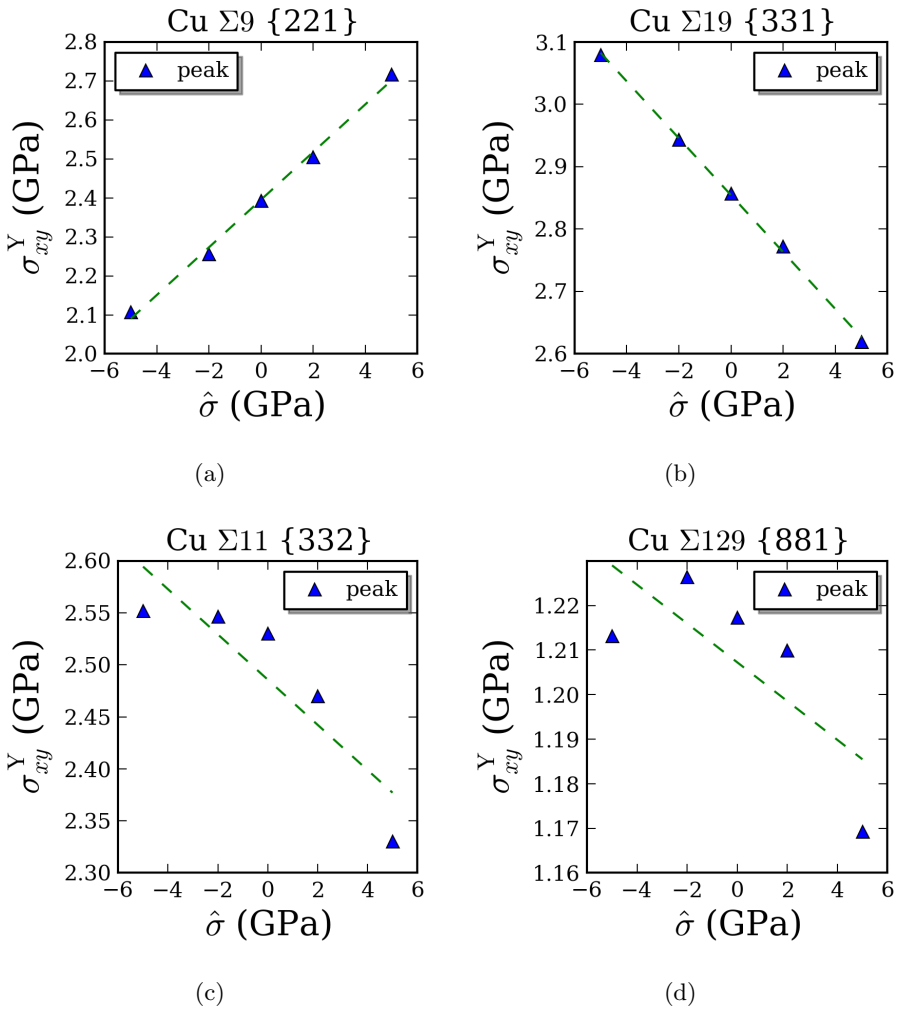

Figure 57: Effect of pressure on σ^{Y} for interfaces containing the E structural unit.

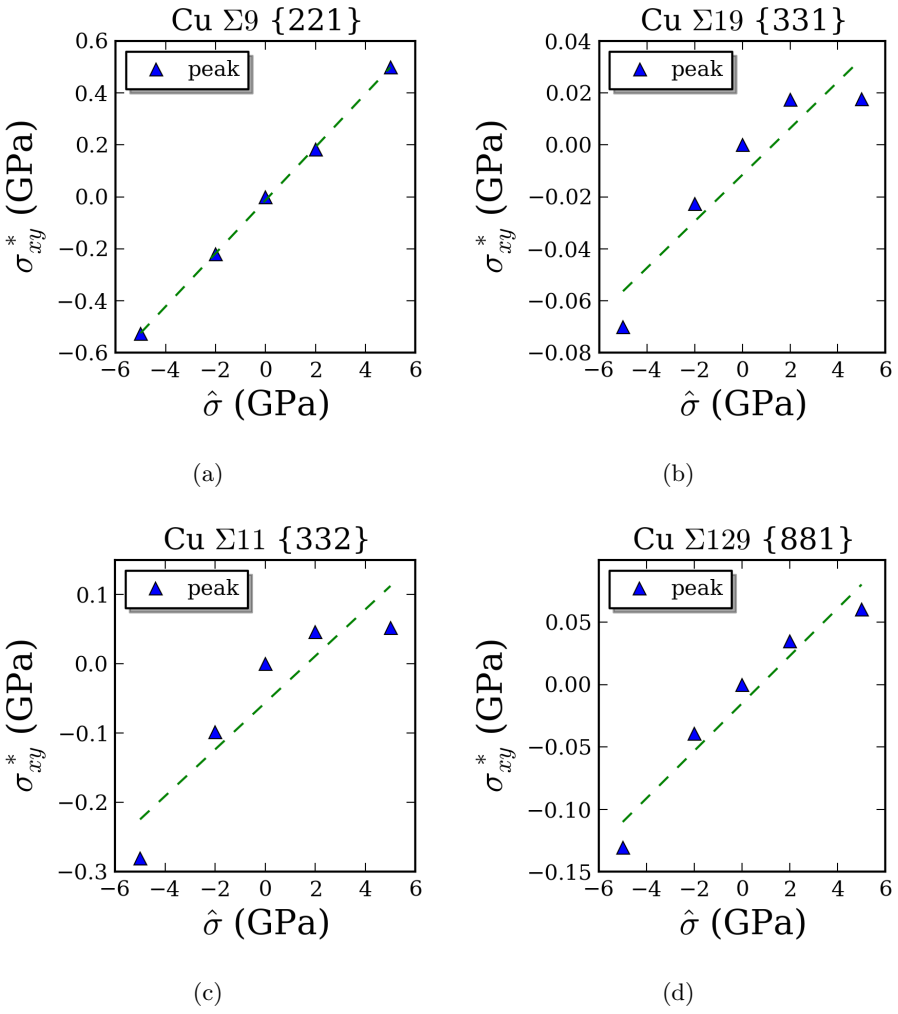

Figure 58: Effect of pressure on σ^* for interfaces containing the E structural unit.

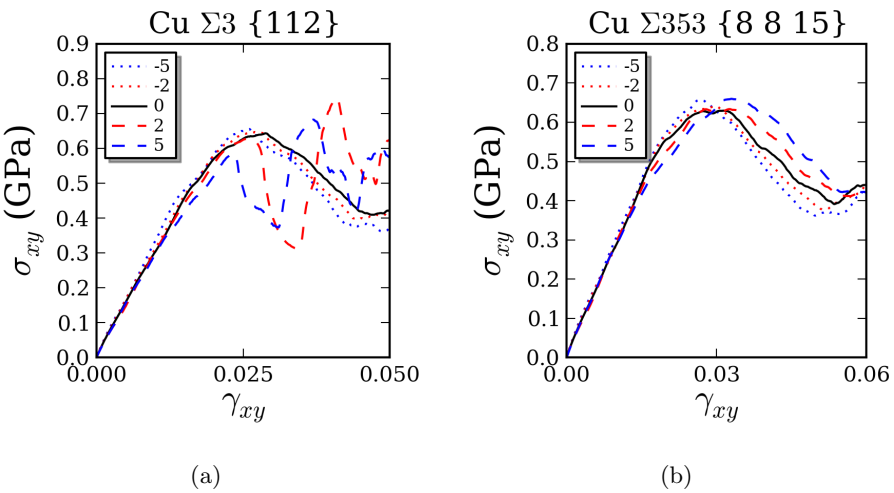

(a) (b)

Figure 59: Effect of pressure on the shear stress- shear strain response of interfaces with the ITB structure. The legend denotes imposed pressure in GPa.

a somewhat decreasing trend can be seen, although the scatter of individual data points is too large to arrive at a conclusion regarding the effect of pressure. In (b), the 0.7% offset yield stress exhibits monotonicity, but here too, the range of yield stresses (0.60-0.65 GPa) is quite small. In the evolution of σ^* (see Figure 61), the scatter is even higher, and a linear fit captures no trend whatsoever. Most importantly, the fact that the stress-strain curves in Figure 59(a)-(b) cross one another suggests that (a), the effect of pressure on σ_Y is weak, and (b) the variation in yield stresses obtained from the current yield criteria makes it difficult to accurately estimate k_Y.

It is worth mentioning, however, that interface with the ITB structure deform via a distinct deformation mechanism (see Figure 48) that involves, effectively, the propagation of *pre-nucleated* partial dislocation cores that require atomic rearrangements on the order of the length of the Burgers vector. This mechanism is very different from other interfaces studied in this work, where a cooperative motion of a larger number of atoms is required, and more 'efficient' shear deformation mechanisms, such as dislocation glide, are not available. It is not too surprising, therefore, that the effect of hydrostatic pressure on the shear strength of interfaces with the ITB structure is weak.

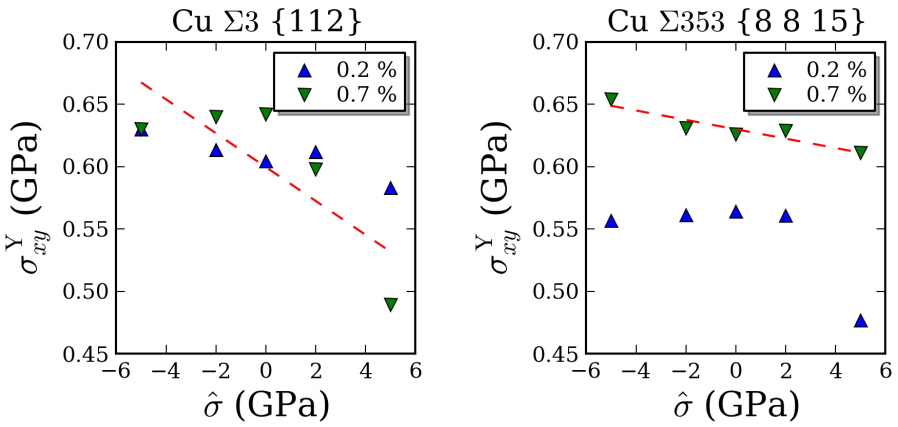

(a) (b)

Figure 60: Effect of pressure on σ^{Y} for interfaces with the ITB structure.

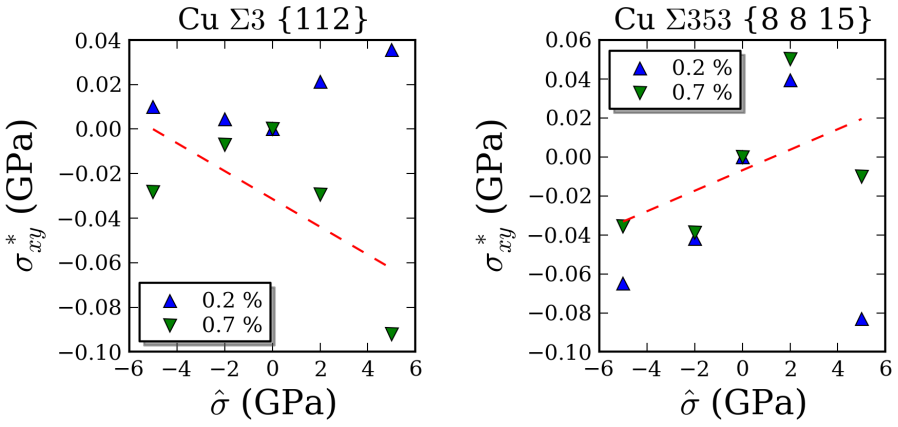

(a) (b)

Figure 61: Effect of pressure on σ^{*} for interfaces with the ITB structure.

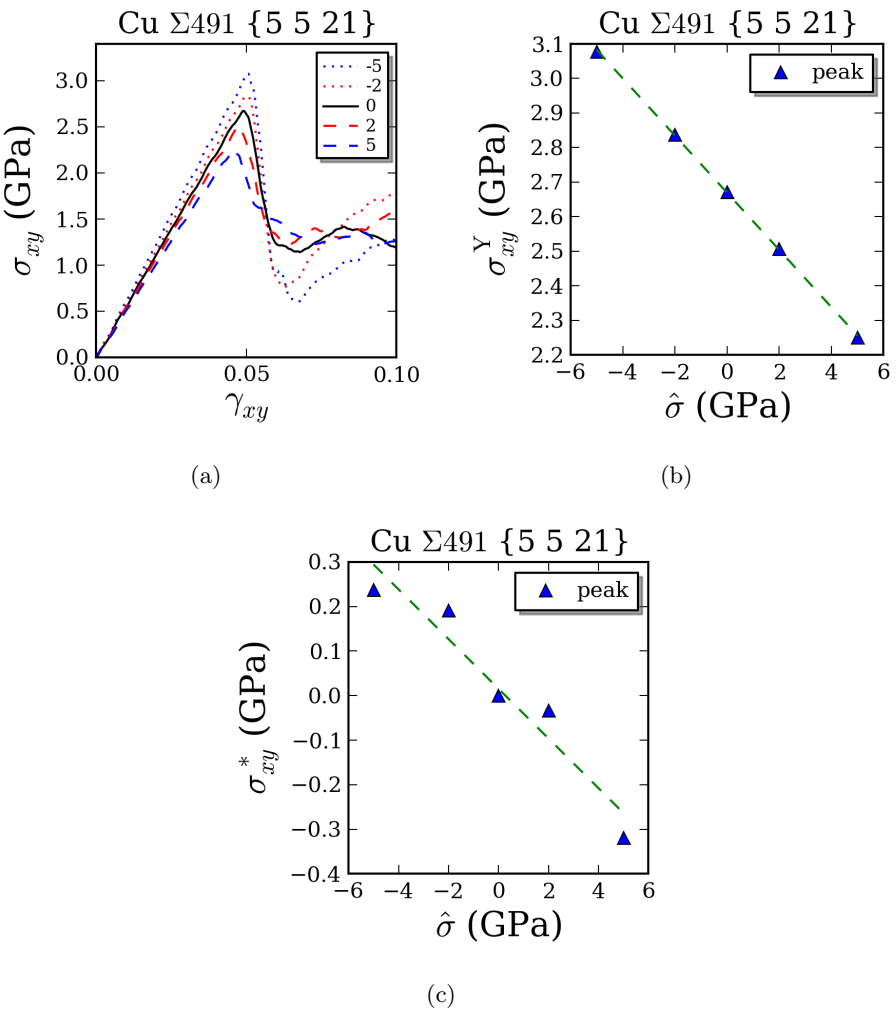

Figure 62: (a) Shear stress-strain curves, (b) the effect of pressure on σ^{Y}, and (c) the effect of pressure on σ^{*} shown for the Cu Σ491{5 5 21} interface.

5.3.3.5 ⟨110⟩ tilt axis: Other interfaces

As introduced in Section 5.2.1, only one interface, Σ491{5 5 21}, was classified as 'Other'. Unlike any other interfaces studied in this work, this interface deformed via a combination of dislocation nucleation from the interface, and sliding. The stress-strain curves, the evolution of σ^{Y} and σ^{*} for this interface are shown together in Figure 62 (a), (b) and (c) respectively. In this case, σ^{Y} and σ^{*} evolve in a linear fashion, similar to the results obtained for several other interfaces. Both k_Y and k_* were found to be positive, and quite large (0.083 and 0.056, respectively).

Table 3: A summary of pressure-sensitive elasto-plastic shear deformation behavior for twelve Cu interfaces studied in this chapter. An explanation of the quantities in columns 2–7 can be found in Section 5.2.4. k_Y, k_G, and k_* were obtained via linear fits to σ^{Y}, G, and σ^* as a function of hydrostatic pressure $\hat{\sigma}$. A † indicates that a poor-quality linear fit had to be used to obtain the value.

Interface	σ_0^{Y} (GPa)	G_0 (GPa)	α_0	k_Y	k_G	k_*
Tilt axis ⟨110⟩						
Low-energy						
Σ3{111}	2.78	41.07	0.07	0.095	0.672	0.049
Σ11{113}	3.9	47.41	0.08	0.022	0.795	-0.043
E structural unit						
Σ9{221}	2.39	56.14	0.04	-0.061	0.966	-0.102
Σ19{331}	2.86	65.45	0.04	0.046	1.25	-0.009
Σ11{332}	2.53	49.31	0.05	0.022	1.08	-0.034
Σ129{881}	1.22	71.97	0.02	0.004	1.382	-0.019
ITB structure						
Σ3{112}	0.64	28.76	0.02	$0.014^{\dagger}$	0.328	$0.006^{\dagger}$
Σ128{8 8 15}	0.63	29.41	0.02	$0.004^{\dagger}$	0.424	$-0.005^{\dagger}$
Other						
Σ491{5 5 21}	2.67	58.31	0.05	0.083	0.586	0.056
Tilt axis ⟨001⟩						
Σ5{210}	1.07	37.8	0.03	-0.04	0.266	-0.047
Σ5{310}	0.69	49.91	0.01	0.03	1.371	0.011
Σ13{510}	4.23	65.33	0.06	0.161	1.42	0.069

5.3.4 Summary of deformation behavior

The shear strengths, shear moduli, and various pressure coefficients for the twelve interfaces studied in this work are summarized in Table 3, where some features are noteworthy:

- The reduced shear strength α_0 (shear strength/ shear modulus) for all interfaces was within 0–0.1. The low-energy interfaces were the strongest according to this metric, while the interfaces with the ITB structure were among the weakest.

- In the context of Equation 47, the magnitude of the contributions of $\alpha_0 k_G$ and k_* to k_Y are, in general, comparable. This implies that neither k_G nor k_* can be assumed to dominate the pressure-dependent shear deformation behavior.

At this stage it is necessary to point out that the linear model introduced in Section 5.2.4 isn't universally applicable to all interface structures. Some interface structures that

were simulated, but not discussed in this work (e.g., $\Sigma 9\{114\}$ and $\Sigma 499\{15\ 15\ 7\}$), did not exhibit a monotonic change in σ^{Y} with $\hat{\sigma}$. Further, the stress-strain curves for these interfaces were qualitatively different under pressures of different signs. Therefore, it is not appropriate to assume the approximately linear evolution of shear strength with pressure for all interface structures. The twelve interface structures, in that sense, represent special cases where a simple linear model can be taken as a reasonable approximation.

5.3.5 Volume change associated with interface motion

In this section we analyze the evolution of atomic-scale dilatation ($\hat{\epsilon}/atom$) and free volume (FV) during shear deformation. The methods used to compute these quantities have been described earlier in Section 5.2.3. The objective of the present analysis is to attempt to explain the pressure-dependence of interfacial shear strength based on the evolution of dilatation and free volume under shear deformation *with zero imposed pressure*, based on the hypothesis that dilatation/free volume creation (resulting in volume change δV) can couple with the applied hydrostatic stress $\hat{\sigma}$ to introduce a penalty of $\hat{\sigma}\delta V$ [31] in the activation energy of stress-driven interfacial motion, thereby raising or lowering the interface yield stress under shear.

To compute the dilatation occurring at different stages of the shear deformation, two sets of reference and current configurations were used. First, dilatation was computed for a *pre-yield* configuration, using the configuration prior to any applied shear deformation as reference. Here, the pre-yield configuration is taken to be the atomic configuration just prior to the peak stress in the stress-strain curve. Second, dilatation was computed for the *post-yield* configuration (identified as the one where the shear stress has relaxed to a minimum following initial yield, although the bicrystal has not been unloaded), using the pre-yield configuration as reference. For all configurations of the system over the course of the deformation (configurations were saved at intervals of 0.5% strain), the free volume (FV) per unit area of the interface was also computed.

Figures 63-72 show the results of the dilatation/free volume calculations. The subfigures, labeled (a), (b), and (c) in Figures 63-72 should be interpreted as follows. In Figures 63-72:

- (a) shows the evolution of free volume with shear strain. Vertical red markers indicate the pre-yield and post-yield strains respectively.
- (b) shows the dilatation of atoms in the *pre-yield* configuration, using the configuration prior to any shear deformation as reference. The interface tilt axis is normal to the plane of the paper, and the shearing direction is to the right.
- (c) shows the dilatation of atoms in the *post-yield* configuration, using the pre-yield configuration as reference. The orientation of the interface is same as in (b).

Figure 63 shows the evolution of free volume and both pre-yield and post-yield dilatation for the $\Sigma 3\{111\}$ interface. This interface contains no free volume prior to deformation, and no changes in free volume were observed over the course of the deformation. No significant pre-yield dilatation was observed, while in the post-yield configuration, a dilatation >4% was noted in the wake of the migrated boundary. For the $\Sigma 11\{113\}$ interface, shown in Figure 64, the initial free volume was quite low (0.0025 $\text{Å}^3/\text{Å}^2$), but showed an increase while in the elastic deformation regime, prior to initial yield. The yielding transition caused a sharp decrease in the free volume, although precise estimates of this decrease were not possible since successive atomic configuration were sampled at a limited frequency (once per 0.5% strain). The initial increase in free volume agrees with observed dilatation in the pre-yield configuration. However, the most striking feature of the yielding transition is thin layer of atoms undergoing negative dilatation (i.e., contraction). These atoms were a part of the interface in the pre-yield configuration.

Figures 65-68 correspond to interfaces with the E structural unit, which are known to possess a high initial free volume. In all of these interfaces, free volume decreased sharply during the yield transition, corresponding to the collapse of the E structural unit. In the pre-yield configuration, the dilatation metric revealed the slight constriction of the structural units at the interface. In the post yield configuration, dilation was observed, although for the case of interface sliding, it was very difficult to interpret the dilation data, due to the uncorrelated shuffling of atoms and topological changes in the atomic neighborhood. For the case of interface migration in Figure 68, however, clear footprints of the collapse of the

E structural unit (blue patches) could be seen.

Figures 69-71 show the evolution of free volume and dilatation in interfaces in the $\langle 100 \rangle$ family of misorientations. In all three interfaces, free volume decreased initially, but its evolution during the yield transition did not reveal any features common to the three interfaces. Significant negative dilatation (contraction) was observed in the pre-yield configuration of the $\Sigma 5\{210\}$ interface, but not in the other two interface structures. In the post yield configuration, the atomic strain was predominantly dilatational, although some isolated atoms that constituted the interface prior to yield, registered negative dilatation.

Finally, the evolution of free volume and dilatation for the $\Sigma 3\{112\}$ ITB is shown in Figure 72. In this interface, except for a small decrease in free volume at the beginning of the deformation, the free volume changed very little over the course of the yield transition. Both dilatation and contraction were present in the pre-yield and post-yield configuration; however, the magnitude of the dilatation was smaller, less than 2%, as compared to values above 4% routinely attained by other interfaces in this study.

Some of these results provide encouragement to the transient dilatancy (δV) hypothesis proposed earlier in this section. For example, both pre-yield contraction as well as a decrease in free volume was observed for interfaces containing the E structural unit. In these interfaces, although geometric factors might determine the propensity towards a particular interface motion mode involving a combination of sliding and migration, it appears that the collapse/constriction of the E structural unit is a critical step in the shearing kinetics, and could be a major factor contributing to the yield strength elevation (σ^*), and its negative pressure coefficient k_*. For other interfaces, however, neither dilatation, nor free volume, as computed at present, seems to reliably predict the sign of k_Y or k_* for all interface geometries. For instance, both the $\Sigma 5\{210\}$ and $\Sigma 11\{113\}$ interfaces exhibit a negative k_*. However, the negative dilatation in the former occurs pre-yield, while in the latter, it appears post-yield. Similarly, neither free volume evolution nor dilatation appear to correlate with the observed pressure coefficients for the $\langle 100 \rangle$ interfaces.

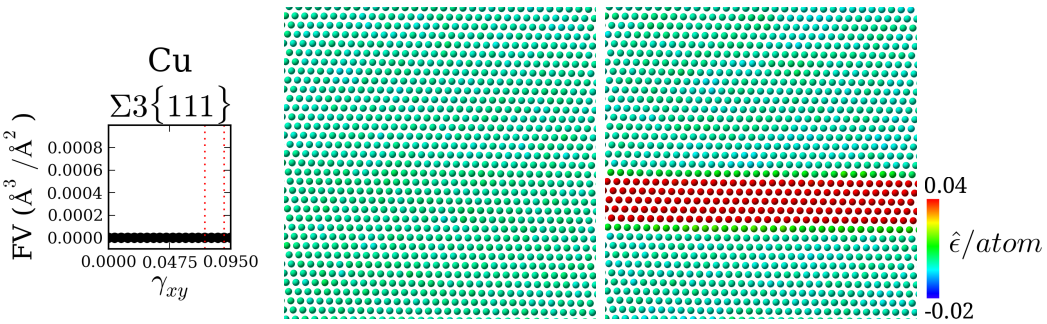

(a) (b) (c)

Figure 63: (a) Evolution of free volume per unit area, (b) pre-yield and (c) post-yield configurations, colored according to dilatation, for the Σ3{111} interface.

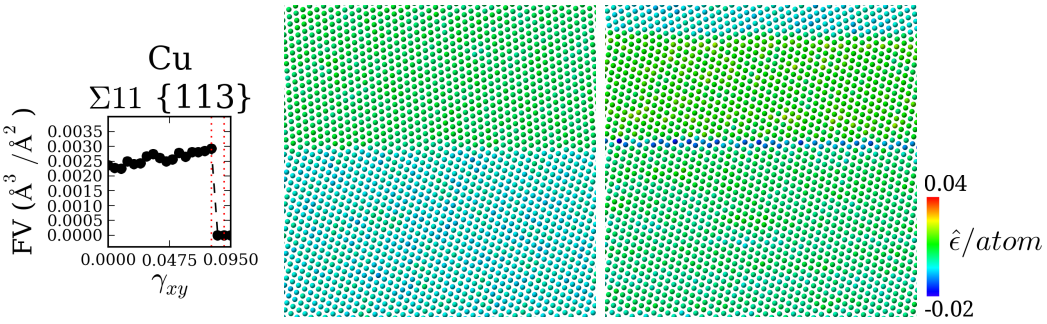

(a) (b) (c)

Figure 64: (a) Evolution of free volume per unit area, (b) pre-yield and (c) post-yield configurations, colored according to dilatation, for the Σ11{113} interface.

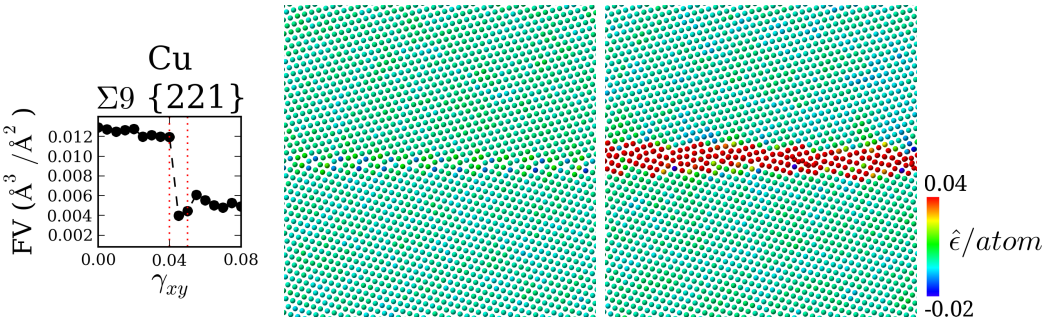

(a) (b) (c)

Figure 65: (a) Evolution of free volume per unit area, (b) pre-yield and (c) post-yield configurations, colored according to dilatation, for the Σ9{221} interface.

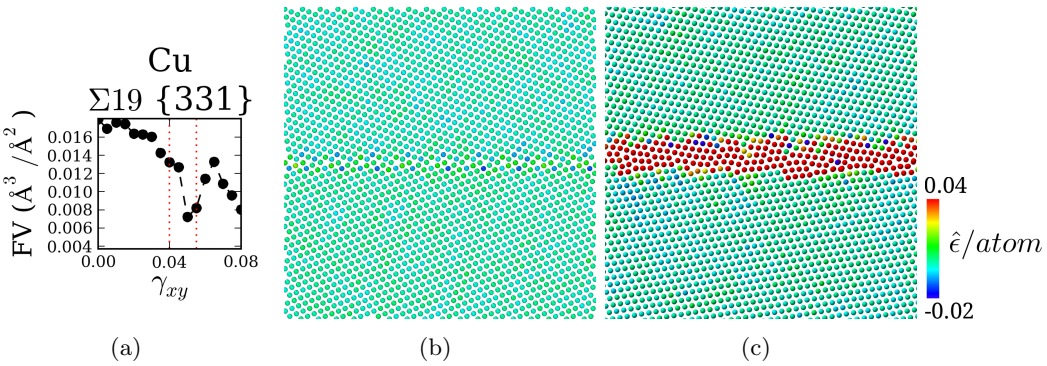

Figure 66: (a) Evolution of free volume per unit area, (b) pre-yield and (c) post-yield configurations, colored according to dilatation, for the Σ19{331} interface.

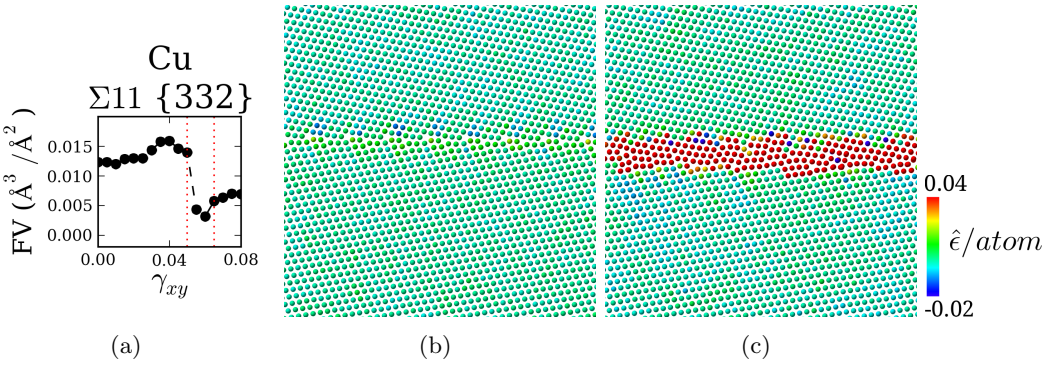

Figure 67: (a) Evolution of free volume per unit area, (b) pre-yield and (c) post-yield configurations, colored according to dilatation, for the Σ11{332} interface.

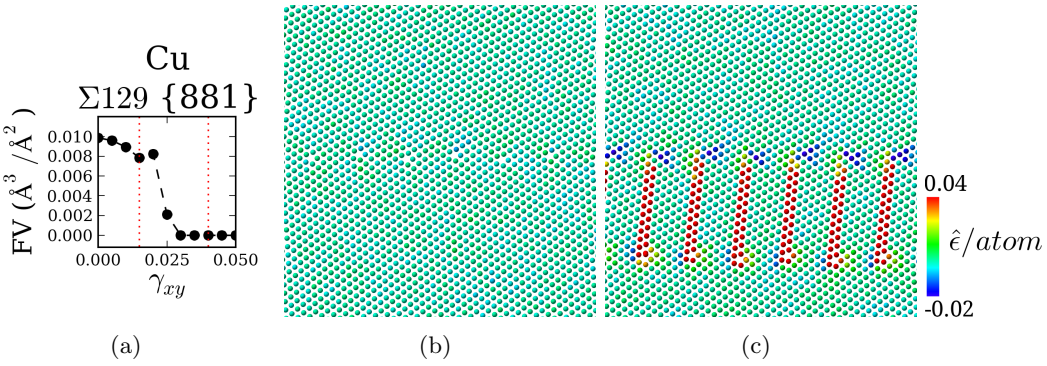

Figure 68: (a) Evolution of free volume per unit area, (b) pre-yield and (c) post-yield configurations, colored according to dilatation, for the Σ129{881} interface.

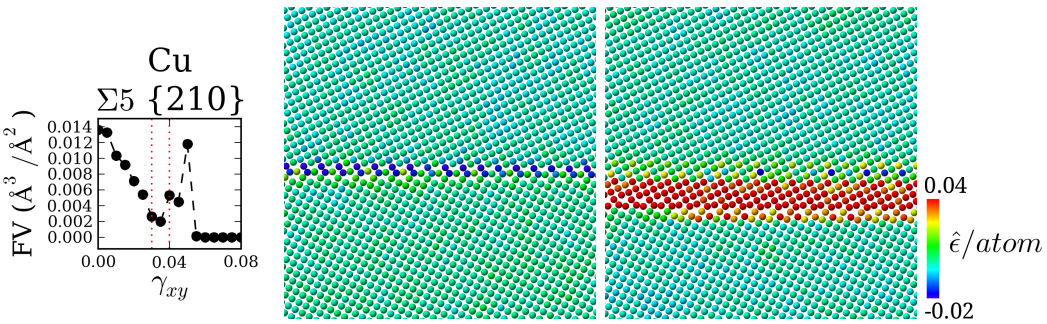

(a) (b) (c)

Figure 69: (a) Evolution of free volume per unit area, (b) pre-yield and (c) post-yield configurations, colored according to dilatation, for the Σ5{210} interface.

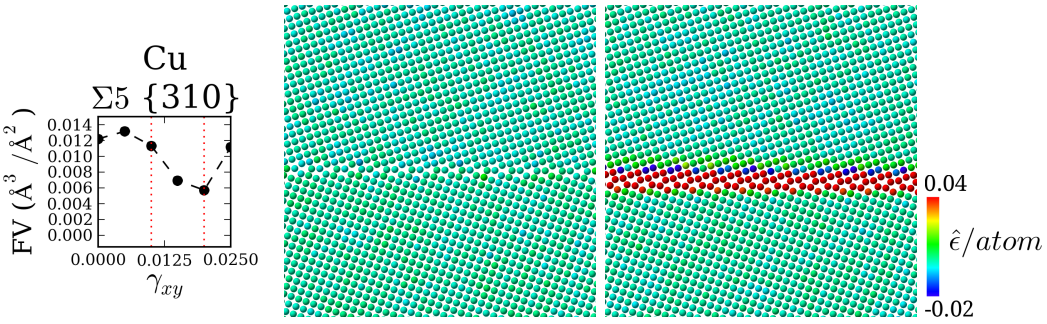

(a) (b) (c)

Figure 70: (a) Evolution of free volume per unit area, (b) pre-yield and (c) post-yield configurations, colored according to dilatation, for the Σ5{310} interface.

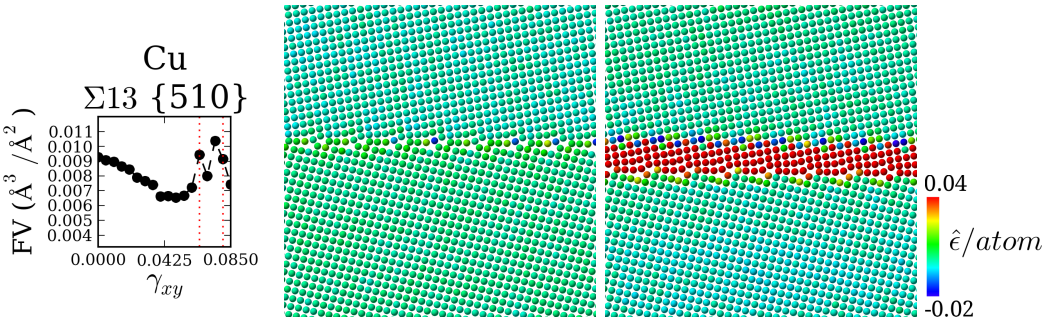

(a) (b) (c)

Figure 71: (a) Evolution of free volume per unit area, (b) pre-yield and (c) post-yield configurations, colored according to dilatation, for the Σ13{510} interface.

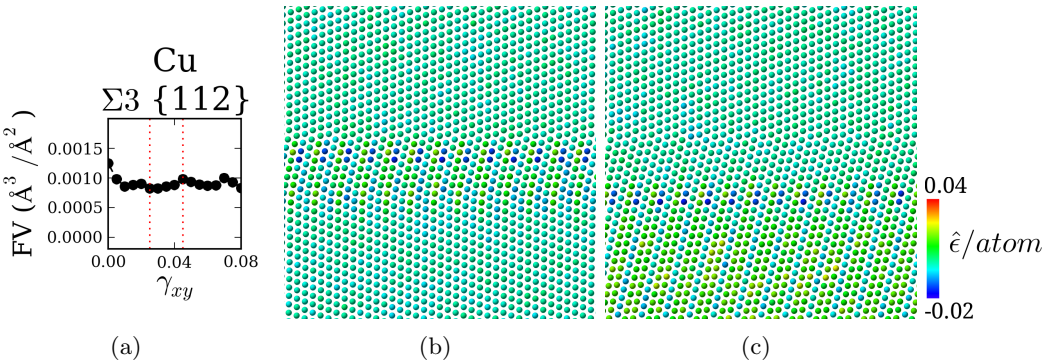

Figure 72: (a) Evolution of free volume per unit area, (b) pre-yield and (c) post-yield configurations, colored according to dilatation, for the Σ3{112} interface.

5.3.6 Quasi-static simulations

All simulations of shear deformation described so far were performed under a constant shear strain rate of $10^9 s^{-1}$, which is very high by experimental standards. Quasi-static[1] simulations, based on interleaved deform-relax cycles, preclude 'dynamic' effects such as undamped elastic waves, and the lack of atomic relaxation in between deformation steps. However, the timescale limitations of MD apply to quasi-static simulations too.

Three interfaces, Σ3{111}, Σ5{210}, and Σ9{221} were deformed under shear quasi-statically via 100 shear strain increments, each of magnitude 0.001. Each deformation step was followed by a relaxation step, in which the shape and size of the simulation domain was held fixed while the atomic positions and stresses at the simulation domain boundary were allowed to relax for a period of 2 ps at a temperature of 10 K (also see [226]).

Figure 73 shows the results of quasi-static deformation for two interfaces: Σ3{111} and Σ9{221}. The stress-strain curves, for pure shear, as well as for shear under imposed pressure, were similar to those obtained via MD. Table 4 compares the value of σ^Y and k_Y for the cases of dynamic (D) and quasi-static (Q) deformation methods. For the Σ3{111} interface, the dynamic and quasi-static values were nearly identical. For the Σ5{210} and the Σ9{221} interfaces, σ^Y was slightly lower for the quasi-static case. The pressure coefficients k_Y obtained from quasi-static deformation were close to those obtained via MD

[1]Not to be confused with quasi-static mechanical tests, which typically involve strain rates of $10^{-3} s^{-1}$

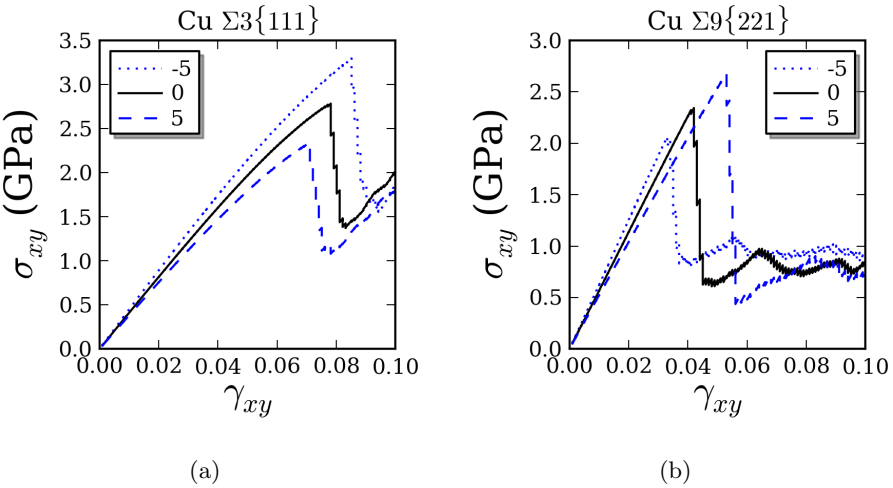

Figure 73: Results of quasi-static deformation simulations shown for (a) Σ3 coherent twin, and (b) Σ9 grain boundary containing the E structural unit. See Table 4 for a comparison with MD results.

Table 4: A comparison of values obtainted from dynamic (D) and quasistatic (Q) deformation simulations for three selected interfaces.

Interface	σ_0^Y (GPa) (D)	σ_0^Y (GPa) (Q)	k_Y (D)	k_Y (Q)
Σ3{111}	2.78	2.78	0.095	0.095
Σ9{221}	2.39	2.34	-0.061	-0.06
Σ5{210}	1.07	1.01	-0.04	-0.03

for the Σ9{221} interface. The Σ5{210} yielded a slightly lower k_Y (absolute value) under quasi-static deformation.

5.4 Discussion

We observe that the effect of pressure on the initial yield strength of the bicrystals under shear is significant and non-trivial. However, the computed pressure coefficients do not show any clear correlation with deformation mechanisms, or structural units in the interface. The only exception to this is interfaces with the E structural unit; however, even for those interfaces, the apparent connection of the collapse of the E structural unit and the pressure coefficient k_* is qualitative at best. It appears that the pressure-dependence of interfacial shear strength cannot be easily described in terms of finer-scale structural or kinematic characteristics, and a more highly-resolved analysis, including more interfaces sampled from

the misorientation subspace(s) would be needed to provide a clearer picture. Saddle point-finding methods such as the activation-relaxation technique [2] and nudged elastic band [290] could potentially be very useful, since they converge to transient configurations, and are therefore best-equipped to estimate the energy barrier to interface motion, as well as dilated/contracted transition states. In fact, one of the reasons behind the limited utility of the dilatation and free volume metrics in the context of Section 5.3.5 is that the actual transition state cannot be assessed using MD.

Direct numerical simulation techniques such as MD uniquely allow us to estimate the effect of hydrostatic stress of a tensile character, which is very difficult to attain in experiments. That said, the time-scale limitations of MD are well known and difficult to surmount. While simulations at higher temperatures and longer time scales (possibly with accelerated MD methods) could potentially reveal interesting transitions, e.g., mode-switching [32], the relatively high (nearly) athermal stresses required to drive most boundaries in this work suggests that crossing of the sliding/migration barrier requires a cooperative motion of several atoms in the interface plane, and this barrier may be expected to persist well into the thermally activated regime, albeit with lower values of σ^{Y}, k_Y and k_*. For example, Wang et al. [256] have reported qualitatively similar, geometrically-coupled stick-slip migration in a $\Sigma 3\{111\}$ twin boundary at temperatures well above room temperature. We performed a limited number of shear simulations at a temperature of 300 K for the $\Sigma 3\{111\}$ and $\Sigma 3\{221\}$ interfaces, and observed that the sign of k_Y in both cases was the same as that at 10 K. The absolute values of k_Y, in both cases, were lower.

Although bicrystalline samples have been simulated in the present chapter, atomistic simulations have reported interface migration in interfaces that are pinned by triple junctions [247] as well. The coupling factor has been reported to be slightly lower than that for un-pinnned boundaries, implying that the kinematics of interface motion is not significantly altered in a polycrystalline environment.

Finally, simulations in the present chapter have been restricted to a handful of tilt interfaces with periodic structure. However, these interfaces represent well-known structures that have been either verified via materials characterization, or are known to be structurally

stable through computational means. A better understanding of the mechanics of these interfaces could be very helpful in modeling the properties of microstructures fabricated via grain boundary engineering, or in predicting microstructure evolution during high-pressure fabrication processes, such as equi-channel angular processing, or high pressure torsion.

5.5 Summary

In this chapter, we have presented a molecular dynamics study of the low-temperature (10 K) shear deformation behavior of Cu bicrystals containing selected symmetric tilt interfaces under a superimposed hydrostatic pressure. A shear strain was applied with respect to the plane of the interface and in the direction of the interface period, using a flexible simulation domain with independent control of all six components of the stress/strain tensor. Twelve interfaces, from the $\langle 100 \rangle$ and $\langle 110 \rangle$ family of misorientations were studied. Results were interpreted based on the effect of hydrostatic pressure on the elastic modulus and the yield strength, as well as in terms of atomic-scale dilatation and free volume. The major findings of this chapter can be enumerated as follows:

1. Cu bicrystal interfaces deformed under shear with a superimposed hydrostatic pressure in the range of $\pm$ 5% of the bulk modulus showed a significant effect of pressure on the in-plane shear strength. The computed pressure sensitivity coefficients varied widely across different interfaces structures.

2. A combination of interface sliding, migration and dislocation mechanisms were observed in the $\langle 110 \rangle$ family of interfaces. However, all $\langle 100 \rangle$ interfaces deformed via shear-coupled migration.

3. The interfaces $\Sigma 9\{221\}$ and $\Sigma 5\{210\}$ exhibit an 'anomalous' behavior, where the shear strength increases with tensile hydrostatic stress. This anomaly was observed under both dynamic as well as quasi-static deformation.

4. The effect of pressure on the shear strength of an interface involves an interplay of k_G, which quantifies the effect of pressure on the bicrystal shear modulus, and k_*, the component of the pressure-induced shear strength elevation/depression that does

not include the change in elastic stiffness. While k_G was positive for all interfaces considered, k_* was found to be negative for several interfaces (positive values indicates increase with increasing imposed compressive stress). In the $\Sigma 9\{221\}$ and $\Sigma 5\{210\}$ interfaces, k_* was the most negative.

5. Mixed results were obtained from attempts to relate the pressure-dependence of shear strength to metrics of dilatation and free volume. In the case of $\langle 110 \rangle$ interfaces with the E structural unit, the pressure-dependence of the shear strength can be explained in terms of the collapse of the E structural unit, but for other interfaces, primarily those in the $\langle 100 \rangle$ family of misorientations, the relationship between free volume evolution/dilatation and the pressure coefficient of the shear strength is less clear.

CHAPTER VI

SHEAR DEFORMATION BEHAVIOR OF CU NANOCRYSTALS UNDER IMPOSED HYDROSTATIC STRESS: ROLE OF GRAIN SIZE AND DEFORMATION TEMPERATURE

6.1 Introduction

The proposed use of nanocrystalline (NC) materials for novel structural/tribological applications has traditionally been motivated by their unusual and improved mechanical properties [97, 280, 208, 75, 160, 142, 187] as compared to conventional microcrystalline materials. Material characterization and direct numerical simulation has shown that these properties arise from nano-scale and meso-scale phenomena [191, 190, 180, 24, 245] that are fundamentally different from classical crystal plasticity mechanisms that operate in microcrystalline materials. It has also been suggested [128] that the multiaxial yield/flow behavior of nanocrystals should include a dependence on pressure or the normal stress, since classical theories based on isotropic yield and the J_2 flow rule cannot account for certain aspects of plasticity in nanocrystals, e.g., non-Schmid effects [231, 201] in dislocation nucleation and tension-compression (T-C) strength asymmetry [78, 187, 56]. For example, Bitzek et al. [19] subsequently performed a detailed statistical analysis of dislocation nucleation in a simulated Al nanocrystal and found that the grain-level critical resolved shear stress (CRSS) for dislocation nucleation follows a distribution. Further, slip systems that nucleated dislocations were not necessarily the ones with the highest resolved shear stress, since the nucleation and subsequent pinning of dislocations at grain boundary (GB) facets is affected by the local stress state at the nucleation-pinning site(s). A grain size-effect on T-C asymmetry has been shown by Dongare et al. [56] who reported that T-C asymmetry in NC Cu is a non-monotonic function of grain size in the range 2-10 nm, reaching a minimum at around 4 nm.

The effect of imposed hydrostatic stress on shear strength of nanostructures has been explored in previous chapters of this thesis, for the case of a Cu nanocrystal having mean grain size 5 nm (Chapter 4), and for selected Cu symmetric tilt interfaces (Chapter 5). In both these cases, the effect of hydrostatic stress on shear strength was manifested via pressure-induced changes in the kinetics of sliding/migration/atomic shuffling in the interfaces. The present chapter continues the study of the effect of multiaxial stress state, extending it to NC microstructures having mean grain size >10 nm, where dislocation activity is expected to become the dominant deformation mechanism. While the focus of this chapter is the effect of hydrostatic stress on initial yielding under shear, the effect of stresses normal to the plane of shear deformation is also discussed briefly.

We present MD simulation results from the shear deformation of three NC Cu microstructures of different grain sizes in the range 5-20 nm, deformed under an imposed hydrostatic stress state. The chapter is organized as follows: Section 6.2 introduces the methodology for creating microstructures, applying deformation, and the algorithms/computational tools used to process data and interpret the results. Section 6.3 presents results pertaining to four aspect of pressure-sensitive shear deformation in NC Cu: (a) effect of pressure on the stress-strain response at the scale of individual grains, grain boundaries, and the entire microstructure, (b) effect of grain size and temperature on the stress-strain response, (c) effect of imposed pressure on the inelastic strain, and (d) activation parameters for inelastic deformation in microstructures of different grain sizes. Section 6.4 discusses the implications of the present work, and also presents a few results regarding the effect of an imposed stress normal to the shear direction on the shear deformation response. Section 6.5 contains a summary of important results.

6.2 Methodology

6.2.1 Building NC microstructures

NC microstructures were constructed via Voronoi tessellation of a 3-D periodic cubical simulation domain into 8 grains. Unlike NC structures used in previous chapters, the seed points for the tessellation were not selected randomly; they were generated so as to lie

on a hexagonal close packed lattice with its c-axis oriented along the z-direction of the simulation domain. This ensured that all grains occupied roughly the same volume, and individual polyhedral grains were stacked in a $ABABAB$ stacking sequence characteristic of the hexagonal close packed arrangement. In order to ensure that GB planes (shared faces of the polyhedral grains) were not identically-oriented with respect to any reference direction, the position of initial seed points were perturbed by 10% of the inter-seed spacing in a random direction. In the resultant microstructure, grains were of similar, but not identical, shape and size. Once the tessellation was computed, it was scaled to the desired grain size (the grain size is half the y-length of the simulation domain). Next, the lattice orientation for each grain was chosen randomly from the group of 3-D rotations; however, several sets of orientations were tried until a set was found that did not introduce any low-angle boundaries between grains. Once the grain morphology and grain orientations were fixed, three microstructures, of mean grain size 5 nm, 10 nm, and 20 nm, respectively, were constructed by generating atom positions according to each grain's lattice orientation. Finally, the usual steps of proximity-based atom-deletion, energy minimization, and equilibration to desired temperature and zero external pressure ([237, 217]) were applied to the microstructures. Figure 74(a-c) shows the relaxed microstructures $g = 5$ nm, $g = 10$ nm, and $g = 20$ nm, prior to any applied shear deformation, where g is the nominal grain size.

6.2.2 Deformation method

Shear deformation was simulated via a Parinello-Rahman (PR) barostat [161] that permits both expansion and distortion of the simulation domain, as well as independent control of all six global (i.e., domain-level) stress components. A constant shear strain rate of 10^9 s^{-1} was applied along the positive y-direction, in a plane normal to the z-direction. A constant external hydrostatic pressure $\hat{\sigma}$, in the range [-5,5] GPa (a negative pressure denotes compression) was applied prior to and during deformation of the microstructure. All normal stress components were prescribed equal to $\hat{\sigma}$, and all shear stress components other than σ_{yz} were prescribed as zero.

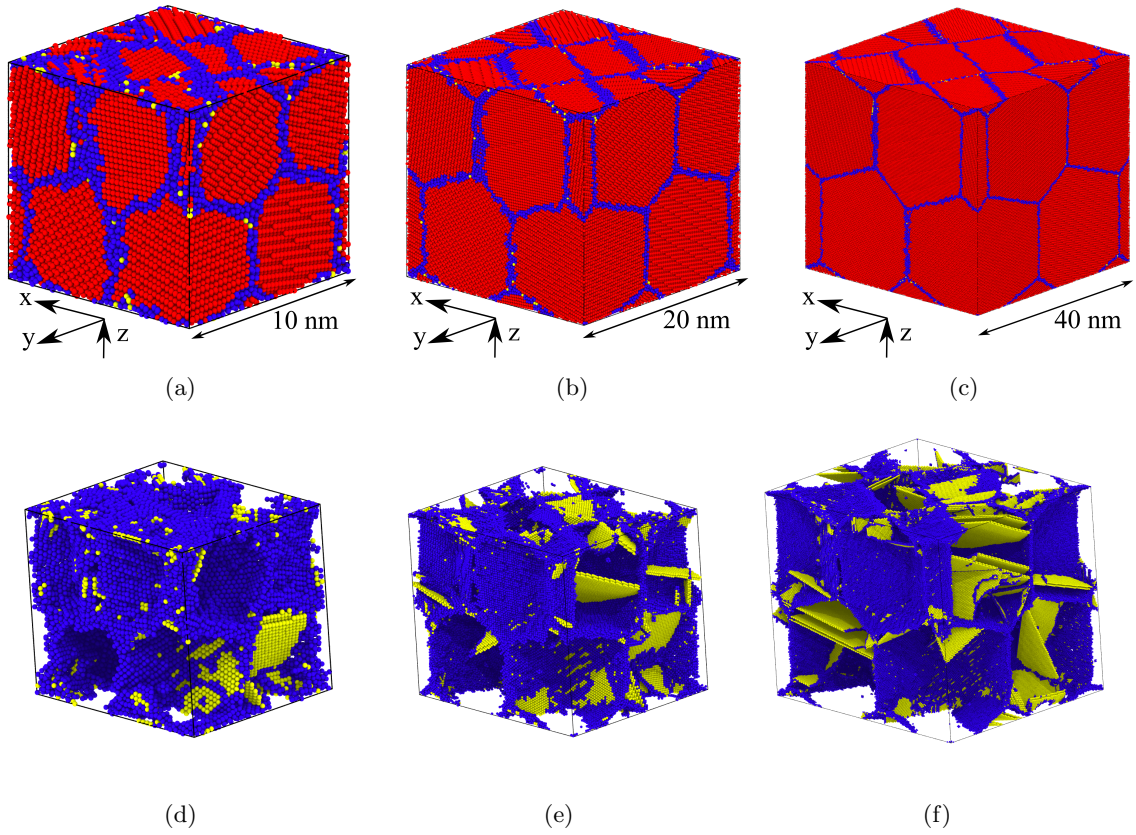

Figure 74: Snapshots of the nanocrystalline configurations (a) $g = 5$ nm, (b) $g = 10$ nm, and (c) $g = 20$ nm, relaxed to zero external stress. Color is according to common neighbor analysis [232]. Locally face centered cubic atoms are shown as red, hexagonal close packed atoms as yellow, and non-12 coordinated atoms as blue. (d), (e), and (f) show snapshots of each configuration deformed to a strain of $\gamma_{yz} = 0.1$, with fcc atoms hidden.

Simulations performed in this work were classified based on the grain size of the microstructure (g), the temperature during deformation T, and the imposed hydrostatic pressure $\hat{\sigma}$. Three grain sizes: $g = 5$ nm, $g = 10$ nm, and $g = 20$ nm, and three temperatures: $T = 10$ K, $T = 300$ K, and $T = 500$ K were explored, resulting in nine combinations of temperature and grain size. For each combination, simulations were performed under five imposed hydrostatic pressures: $\hat{\sigma}$ = -5 GPa, -3 GPa, 0 GPa, 3 GPa, and 5 GPa, resulting in a total of 45 simulations.

6.2.3 Analysis

In this section, we introduce a method to demarcate specific microstructural features in simulated NC microstructures, and compute the volume-averaged stress for those features in the deformed configuration(s). Inelastic deformation of a NC material occurs via a combination of deformation mechanisms, with different mechanisms operating in different sub-volumes (e.g., grain interiors vs. grain boundaries) of the microstructure. Whereas the precise kinetics of inter-granular dislocation activity may be quite different from inter-granular sliding/migration, any volume-averaged metric of domain-level deformation behavior only captures a mean response. To separately monitor the evolution of stress within grain interiors and grain boundaries, the stress is computed over specifically-defined contiguous sub-volumes in the microstructure. These sub-volumes are Lagrangian sets of atoms that are demarcated in the relaxed configuration prior to any deformation. The assignment of an atom to a sub-volume is done only once; no reassignments occur over the course of deformation.

6.2.3.1 A stress measure defined over a sub-volumes of the microstructure

Over a material volume V, the atomic stress tensor is computed using the virial relation ([47, 222]):

$$\boldsymbol{\sigma}_{ij} = \frac{1}{V}\sum_{\alpha}^{N}\left\{-m^{\alpha}v_i^{\alpha}v_j^{\alpha} + \frac{1}{2}\sum_{\beta\neq\alpha}^{N} r_i^{\alpha\beta}F_j^{\alpha\beta}\right\} \tag{48}$$

Here, $\boldsymbol{\sigma}_{ij}$ denotes the stress tensor computed over volume V in Cartesian coordinates (i, j). N is the number of atoms contained in the volume V, and atoms are referenced using

Greek letters α and β. The atomic stress consists of a kinetic term $m^{\alpha} v_i^{\alpha} v_j^{\alpha}$ and a virial term $\frac{1}{2} \sum_{\beta \neq \alpha}^{N} r_i^{\alpha\beta} F_j^{\alpha\beta}$. In the current work, we shall evaluate the stress tensor excluding the kinetic term, in a manner similar to some previous work [226, 237]. The effects of neglecting the kinetic term have been debated at length in the literature [288, 207, 296]. However, we find that these effects are negligible in the context of the present work. For a more detailed discussion regarding the stress computation, the reader is referred to Appendix B.

6.2.3.2 A layer growth algorithm

In atomistic simulations, defect structures such as interfaces or dislocations are usually identified via atomic coordination or graph algorithm-based analysis methods (e.g., centrosymmetry [99], and common neighbor analysis [232]). These methods, however, only resolve atoms that lie at the 'core' of defected regions. The stress and strain fields associated with defect structures are typically not restricted to the defect core; they extend into nearby regions. For example, the presence of a GB influences the potential energy of nearby atoms in the lattice [198]. Therefore, while computing a volume-averaged measure (e.g., stress) for a particular defect structure such as a GB, atoms in the vicinity of the defect structure should be included in the averaging process to capture certain spatial correlations of the extent of its action and associated sets of participating atoms/structures. These atoms belong to the "region of influence" of the defect. Similarly, while considering grain interiors, it is essential that the stress/strain fields of the grain's bounding interfaces be excluded.

To identify atoms in the region of influence of a defect structure, a layer growth algorithm is used. The steps of the algorithm are as follows:

1. Atoms forming the defect 'core' are identified, based on centrosymmetry, common neighbor analysis (CNA), or other methods.

2. An empty set $\mathbb{S}$ is created and the atoms belonging to the defect core are added to $\mathbb{S}$.

3. All first nearest neighbors of atoms in $\mathbb{S}$ are added to $\mathbb{S}$.

In the above algorithm, Step 3 grows the region of influence of the defect structure by

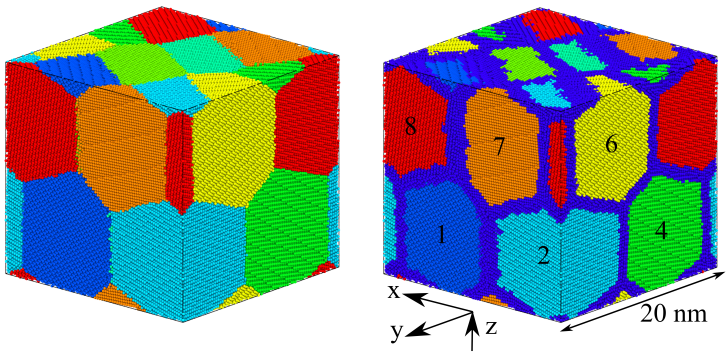

(a) (b)

Figure 75: The $g = 10$ nm NC microstructure colored according to grain identifier (a) at the time of structure creation, and (b) after the grain boundary affected zone (GBAZ) has been demarcated (dark blue). In (b), all grain identifiers are integers between 1 and 8, except the GBAZ, which is assigned grain identifier 0.

one layer of neighboring atoms. Repeatedly applying step 3 to the atom set $\mathbb{S}$ can be used to incrementally expand the set to include a larger volume, e.g., 2nd, 3rd neighbors and so on, around the defect core.

6.2.3.3 Microstructural regions

This section describes the procedures used to identify three types of microstructural regions over which the stress is computed:

1. *Grain interior*: The NC microstructure are built such that each atom is assigned a unique grain identifier in the range 1 to 8 (this numbering is arbitrary; it is the same as serial numbers assigned to the grains' Voronoi seeds). By this classification, even atoms at or near the interface network are assigned a grain identifier. This implies that the "grain-averaged" stress field includes undesirable interface stresses (it has been shown, by Guo et al. [77], as well as in a previous chapter, that these stresses are considerably higher than stresses in the grain interiors). To select atoms that belong to grain interior(s), first, a common neighbor neighbor analysis (CNA) is performed on all atoms in the microstructure. Then, a set of atoms called grain boundary affected zone (GBAZ) is created, which is initially empty. Based on the CNA computation, all 'non-12 coordinated' atoms (shown in blue in Figure 74(a-c))

are added to the GBAZ set. In subsequent steps, the set GBAZ is 'expanded' by the layer growth algorithm introduced in Section 6.2.3.2, up to 2nd nearest neighbors, and these atoms are assigned a special GBAZ identifier, instead of the usual grain identifier. Figure 75 illustrates the assignment of atoms to the GBAZ for the $g = 10$ nm microstructure. In (a), only grain identifiers 1-8 are present, which also include atoms at and near GBs. In (b), the GBAZ has been resolved (dark blue), and atoms with grain ids 1-8 now pertain only to the grain interior(s).

2. *Grain boundary*: This criterion selects atoms in the vicinity of the grain boundary between grain n_1 and n_2 (n_1 and n_2 are grain identifiers known at the time of structure creation). Atoms that belong to grain n_1, and which also have at least one neighbor from grain n_2, are added to a (initially empty) set GB$\{n_1/n_2\}$. At this point, the set GB$\{n_1/n_2\}$ contains only atoms in the GB plane. Following this step, the layer growth algorithm is repeated three times, to also include atoms in the fcc/hcp phase on either side of the GB plane. Figure 76 shows the results of this selection algorithm, for the GB separating grain 1 and grain 5. The selection includes the entire GB facet, as well as surrounding triple junctions.

3. *Domain*: This is stress computed over all atoms of the simulation domain, and therefore includes both the crystalline grain interiors as well as the GBs.

6.3 Results

6.3.1 Effect of imposed pressure on stacking fault energy

In the literature, both EAM and DFT have been used to compute the Generalized Stacking Fault Energy (GSFE) curves of several fcc metals to determine the energy barrier to slip along the $\{111\}\langle 112\rangle$ slip system. The maximum energy on this curve, called the *unstable* stacking fault energy (USFE), has been identified as one of the critical parameters affecting dislocation nucleation [174, 244]. However, the USFE is not strictly a material parameter and can be affected by deformation [298, 226]. Therefore, while assessing the influence of non-glide stresses on dislocation nucleation behavior, it is important to investigate changes

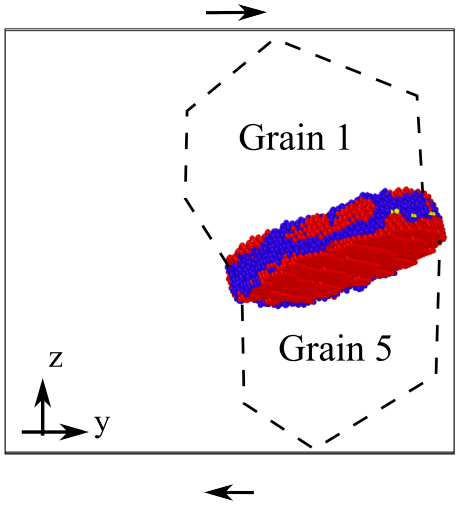

Figure 76: The region GB{1/5} in the $g = 10$ nm microstructure, in a state prior to any applied shear deformation. Red atoms are locally fcc and blue atoms are locally non-12-coordinated. Dashed outlines show the extent of grains 1 and 5 in the nanocrystal.

in the USFE.

GSFE curves were computed at 0 K for a cubical Cu single crystal with edges oriented along the $\langle 112 \rangle$, $\langle 111 \rangle$, and $\langle 110 \rangle$ crystallographic directions. First, the crystal was placed under a hydrostatic stress and the total potential energy was minimized via a modified Conjugate Gradient algorithm that includes the crystal's strain energy (as defined by Parinello and Rahman [161]) in the objective function[1] and adaptively deforms the crystal to achieve equilibrium with the prescribed pressure. To compute the GSFE curves, this deformed crystal was partitioned into two blocks of atoms of equal size, separated at a $\{111\}$ plane. One of the blocks was then displaced along the $\langle 112 \rangle$ direction in small increments, and the change in potential energy was computed for each displacement, relative to the crystal configuration prior to the displacement. This energy change was normalized by the area of the slip plane.

Figure 77(a) shows the effect of hydostatic pressure on the GSFE curve for Cu. The curves indicate that the USFE (i.e., the maximum of the curves in (a)) decreases (increases) in the dilated (compressed) lattice. In the range [-4,4] GPa, the USFE decreased from 200 mJ/m^2 to 161 mJ/m^2. For comparison, the result of an earlier work by Tschopp and

[1]This algorithm is implemented in the *fix box/relax* command of LAMMPS as of September 2014.

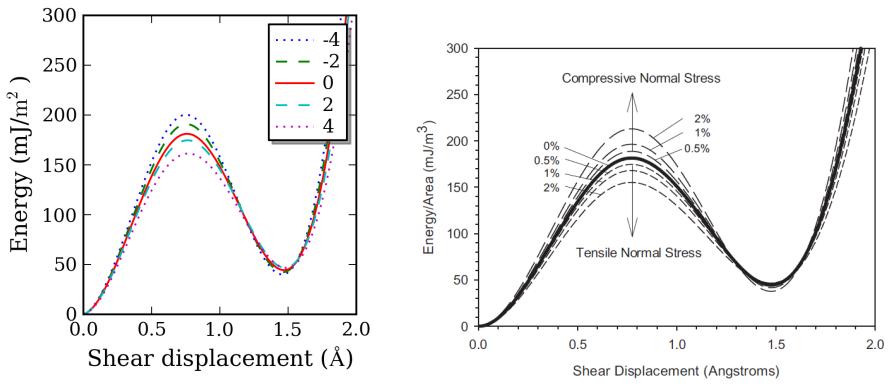

(a) (b)

Figure 77: Comparing Generalized Stacking Fault Energy (GSFE) curves for slip along the $\{111\}\langle 112\rangle$ direction in Cu, under the influence of two types of imposed deformation: (a) a hydrostatic stress (legend in GPa), (b) affine deformation (and associated normal stress) normal o the slip plane (from Tschopp and McDowell [226]).

McDowell [226] is shown in Figure 77(b). Tschopp and McDowell had studied the effect of tensile and compressive stresses normal to the slip plane, and observed an increase in USFE with compressive normal stress and vice versa. In both cases, however, no significant change was observed in the stable stacking fault energy (the first minimum on the GSFE curve after the USFE peak). These results suggest that an imposed hydrostatic stress state modifies the energy landscape and activation barrier(s) for the formation of a stacking fault.

6.3.2 Evolution of stress in microstructural elements

As described in Section 6.2.3, the volume-averaged atomic stress tensor $\boldsymbol{\sigma}$ was computed over three microstructural regions: the grain interiors, the grain boundaries, and the entire domain of the simulation. Stress-strain curves are plotted using the von Mises invariant of $\boldsymbol{\sigma}$, i.e., $\bar{\sigma} = \sqrt{\frac{1}{2}((\sigma_{xx}-\sigma_{yy})^2 + (\sigma_{yy}-\sigma_{zz})^2 + (\sigma_{zz}-\sigma_{xx})^2 + 6(\sigma_{xy}^2+\sigma_{yz}^2+\sigma_{xz}^2))}$, and the global, (i.e., domain-level) shear strain $\gamma_{yz} = d/l_z$, where d is the shear displacement between opposite faces of the overall simulation domain boundaries normal to the z-direction, and l_z is the length of the overall simulation domain along the z-direction.

Since individual grains are anisotropic, our use of $\bar{\sigma}$ to detect inelastic events in grain

interiors needs to be substantiated. Of course, a more 'natural' stress measure would be the resolved shear stress (RSS), evaluated along one or more slip systems. In the global coordinate system xyz, the deviatoric part of the domain-level stress tensor consists of only one non-zero component: σ_{yz}. When the grain level stress is resolved along a slip system $x'y'z'$ (where y' is along the slip direction, and z' normal to it) in a grain, the components $\sigma_{y'z'}$, $\sigma_{x'y'}$, and $\sigma_{x'z'}$ are, in general, not zero. One might posit that a grain-level yield function $f(\sigma_{y'z'}, \sigma_{x'y'}, \sigma_{x'z'}) = 0$ [2] be used to precisely predict the onset of slip. However, Bitzek et al. [19] have shown that dislocation slip in a nanocrystalline grain need not occur on the plane with the maximum RSS[3], and that the grain-level critical RSS for dislocation nucleation follows a distribution [19, 119]. Due to these peculiarities, it difficult to predict slip in nanograins deterministically, using only the grain level stress. It can, however, be assumed that any slip events in a grain will relax the elastic energy of distortion of the grain and will lead to a decrease in $\bar{\sigma}$. Therefore, while comparing inelastic yield in grains of different size (in different microstructures), but having the same lattice orientation with respect to the global coordinate system, $\bar{\sigma}$ effectively serves our purposes as a reduced order measure of yield.

6.3.2.1 Grain-level response

Figures 74 (d-f) show microstructures of different grain sizes, deformed to $\gamma_{yz} = 0.1$ at 10 K with no imposed hydrostatic pressure. The primary mechanism of deformation was a combination of GB sliding and dislocation activity under all imposed hydrostatic stresses $\hat{\sigma}$, except under $\hat{\sigma} = 5$ GPa in the $g = 20$ nm microstructure. In this structure, deformation beyond $\gamma_{yz} = 0.09$ resulted in a void being nucleated at a triple junction. However, the structure reached its maximum shear strength at approximately $\gamma_{yz} = 0.06$, well before the void appeared.

In Figures 74 (d-f), as expected, stacking faults (left in the wake of leading partial dislocations) are much more numerous in the deformed configurations as the grain size

[2] If Schmid's law is followed, the yield function is simply $\sigma_{y'z'} - \sigma_{cr} = 0$, where σ_{cr} is the critical resolved shear stress for the slip system.

[3] This is because dislocation nucleation and propagation in NC metals is also affected by the local state of stress at the nucleation/pinning site(s) in the interface network.

increases from 5 nm to 20 nm. However, despite every grain having the same orientation in all microstructures, several grains differ in terms of the precise slip systems activated, when comparing the $g = 10$ nm and the $g = 20$ nm microstructures. To permit a valid comparison of stress evolution in the grain interiors using $\bar{\sigma}$, therefore, it is preferable to analyze a grain in which the same slip system is activated for different grain sizes, deformation temperatures and applied hydrostatic stress. Upon visual inspection of the deformed configurations, Grain 3 was found to satisfy these requirements. Figure 78 shows partial dislocation loops nucleating from the GB network into Grain 3 in the $g = 20$ nm microstructure. All loops correspond to a single activated slip system lying approximately in the global x-y plane. Additionally, the same slip system was activated in both the $g = 10$ nm and $g = 20$ nm microstructure, for all temperatures and applied hydrostatic stress (although comparing Figures 78 (a-c), it can be observed that the precise location of dislocation loops changes under an applied hydrostatic pressure).

The evolution of the volume-averaged von Mises stress $\bar{\sigma}$ in the interior of Grain 3 is compared across different grain sizes, applied hydrostatic stresses, and temperatures of deformation, in Figure 79. In the grid of plots (a-i), the grain size increases down a column and the deformation temperature increases across a row. The grain size and temperature are shown in the title of each plot. Each plot shows three stress-strain curves, corresponding to different applied hydrostatic stresses ($\bar{\sigma}$). In Figure 79, note that $\bar{\sigma}$ is plotted against the *global* shear strain.

We focus on three aspect of grain-level deformation: (a) the role of grain size, (b) the role of deformation temperature, and (c) the role of applied hydrostatic stress. For (a) and (b), only curves corresponding to $\hat{\sigma} = 0$ (filled circles) have been considered. A general observation for all stress strain curves in Figure 79 (a-i): for the same γ_{yz} (global), the application of a compressive (tensile) hydrostatic stress increases (decreases) $\bar{\sigma}$. Responses corresponding to microstructures of different grain size are discussed below.

$g = 5$ nm; Figure 79 (a-c): Prior to shear deformation, we observed non-zero that the grain-level $\bar{\sigma}$ (plots (a,b)). This was due to the proximity of GBs, which prevent

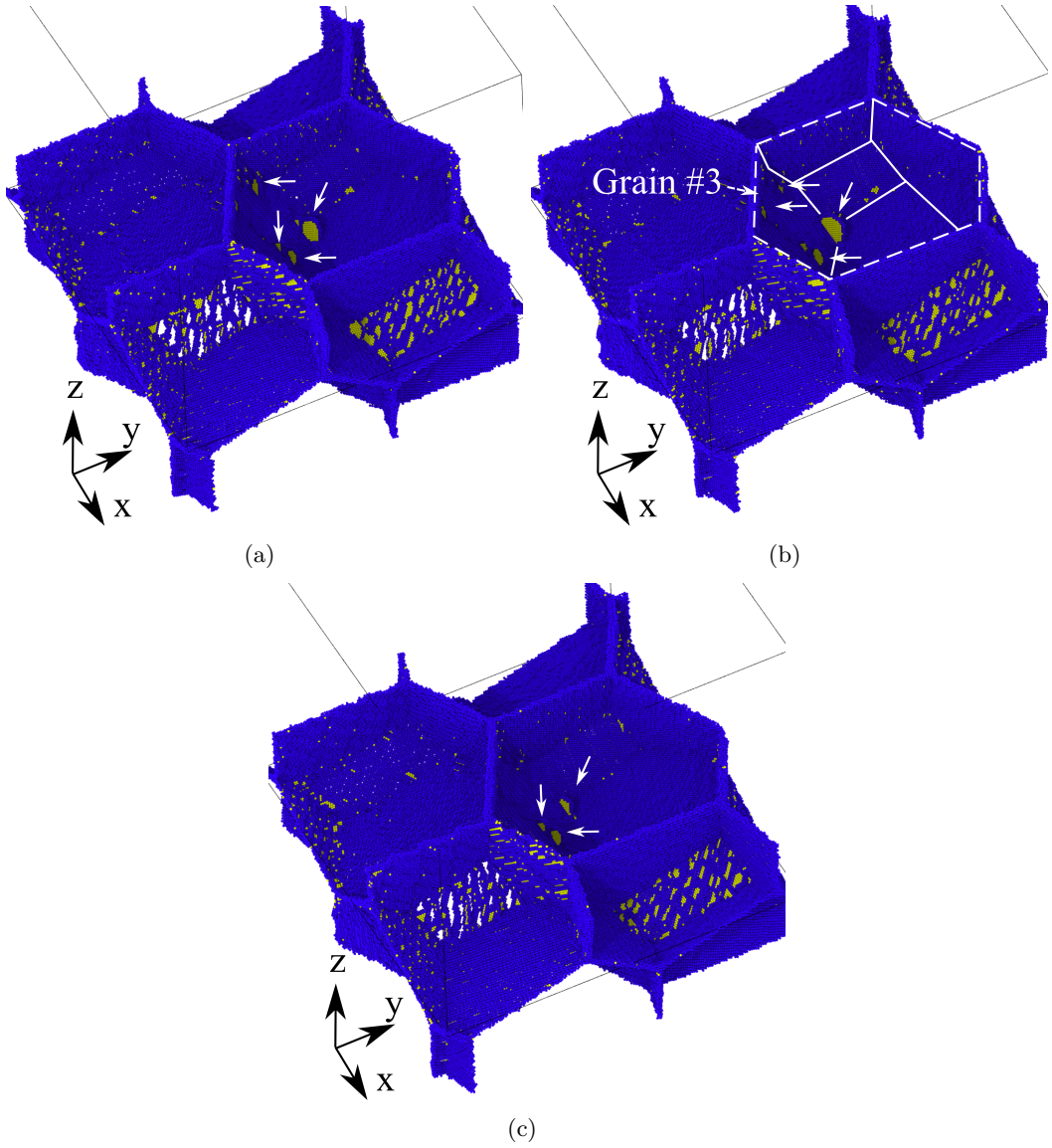

Figure 78: Deformed configurations ($\gamma_{yz} = 0.04$) of the $g = 20$ nm structure, showing GB-mediated dislocation nucleation. To reveal individual dislocation loops, a cross-section has been taken normal to the z direction, and all locally-fcc atoms have been hidden from view. Images show dislocation activity in structures that were pre-stressed under an imposed hydrostatic stress of (a) -5 GPa, (b) 0 GPa, and (c) 5 GPa prior to shear deformation. 3-4 leading partial dislocation loops (white arrows) are seen to nucleate from GB sources in Grain #3 (dashed line).

complete relaxation of stress in the crystalline region(s). At 10 K, the grain-level stress-strain response was linear up to a global shear strain >0.06. In these cases, although GB processes were active, the grain interior deformed in an approximately linear elastic manner. In contrast, no linear and non-linear regions could be demarcated at $T \geq 300$ K. This is because GB shear transformations occur more frequently as the temperature increases, and relax the grain-level stresses. As a result, the stress in the grain interior cannot reach the levels necessary to nucleate dislocations. This was confirmed via visual inspection of the deformed configurations at 10 K and 300 K: a nucleation event that occurred at a global strain of 0.06 in the $T = 10$ K simulation did not occur until 0.09 at the $T = 300$ K.

$g = 10$ *nm; Figure 79 (d-f):* Unlike the $g = 5$ nm microstructure, here, the stress response of Grain 3 shows an initial linear regime for all temperatures studied. Although GB processes continue to occur, their effect on grain-level stresses becomes much less significant due to the increase in grain volume with grain size. Beyond initial yield, fluctuations in $\bar{\sigma}$ are observed, however, these fluctuations do not appear to occur at similar values of the global strain, when comparing stress-strain curves corresponding to different applied hydrostatic stresses.

$g = 20$ *nm; Figure 79 (g-i):* To analyze the response of the $g = 20$ nm microstructure, we first recall that the same slip system (shown in Figure 78) was initially activated in the $g = 10$ nm and the $g = 20$ nm microstructures. Yet, the critical $\bar{\sigma}$ for dislocation nucleation was lowered to ≈ 2 GPa in the $g = 20$ nm microstructure from ≈ 2.5 GPa in the $g = 10$ nm microstructure (both estimated at 10 K). In the former, the stress-strain response is characterized by an initial linear increase, followed by a 'plateau'. Such a plateau was not seen in $g = 10$ nm. The reason for this behavior appears to be (a) the lower density of dislocations per grain in the $g = 10$ nm microstructure (multiple dislocations were observed to nucleate form GB sources, for the same global strain, in $g = 20$ nm vs. only one in $g = 10$ nm), and b) the higher grain-level stress at dislocation nucleation in the smaller grain, whereby an expanding dislocation loop is more likely to 'thread' across the grain rather than get pinned at the grain boundary. These pinning 'events' compete with the nucleation event as the rate-determining process for dislocation glide in NC materials [245].

These results permit a qualitative assessment of the effects of temperature (T) and imposed hydrostatic stress ($\hat{\sigma}$) on elasto-plastic deformation in grains of different size. A compressive hydrostatic stress increases the shear stress required for the activation of inelastic events such as dislocation nucleation or GB sliding/migration. In all stress-strain cures, the magnitudes of individual stress fluctuations (arising from localized atomic rearrangement), and the strain(s) at which they occur, seem to vary somewhat unpredictably across stress-strain curves corresponding to different applied $\hat{\sigma}$. For deformation at high temperatures ($T \geq 300$ K) these variations are enhanced further due to the probabilistic nature of thermally-assisted atomic rearrangement. In the transition grain size regime (e.g., $g = 10$ nm), the contribution of GB processes is reduced (cf. smaller grains), but the density of dislocation sources is still low (cf. larger grain sizes). A statistically-insignificant per-grain dislocation source density implies that grain-level stress-strain curves show great variability, making even qualitative comparison across different temperatures and imposed hydrostatic stress difficult.

6.3.2.2 Interface-level response

In the previous section, the kinetics of dislocation nucleation was resolved via a stress measure defined over the grain exhibiting the nucleation event(s). Ostensibly, this measure can be applied to the entire GBAZ, effectively treating the GBAZ as another 'grain' of the microstructure. However, the results of the latter computation can be difficult to interpret, since the GBAZ is not a convex region within the microstructure, and different GB facets can be subjected to different stress states depending on the deformation of the crystalline regions on either side of each individual GB facet. As an alternative, we focus our analysis on the deformation of a *single* GB in the microstructure. The criterion for selecting such as GB is as follows: (a) the GB should undergo significant atomic rearrangement (sliding/migration) over the course of the deformation, and (b) the sliding/migration 'event' in the GB should preferably occur in all microstructures simulated, across all temperatures of deformation.

Upon visual inspection of the deformed configurations, such a GB was found between grains 1 and 5. Only the structures $g = 10$ nm and $g = 20$ nm were inspected since below

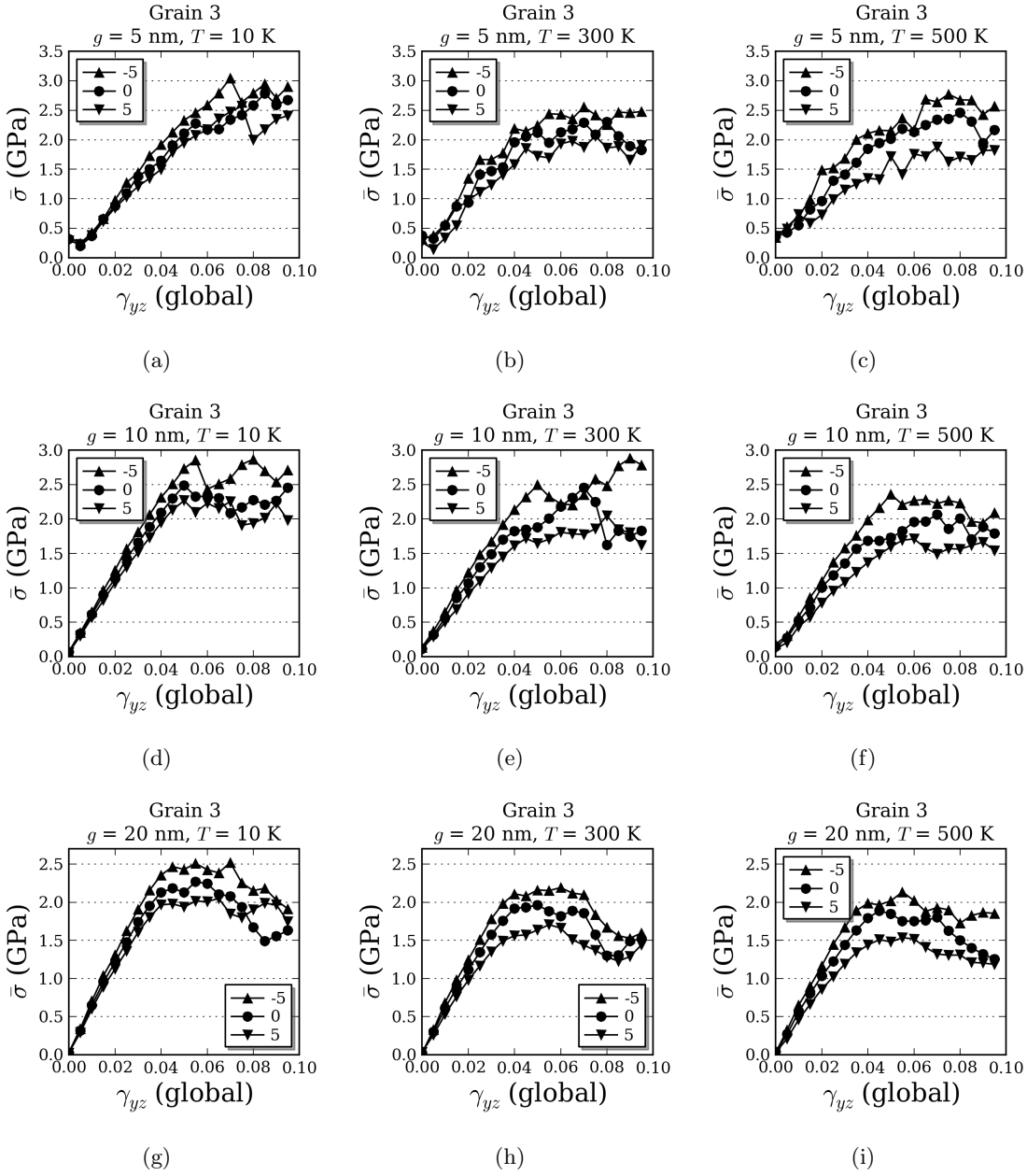

Figure 79: Evolution of $\bar{\sigma}$ in the interior of Grain 3, plotted with respect to the global shear strain γ_{yz}. Each plot corresponds to a different grain size (g), and deformation temperature (T). The legend in each plot denotes imposed hydrostatic pressure in GPa.

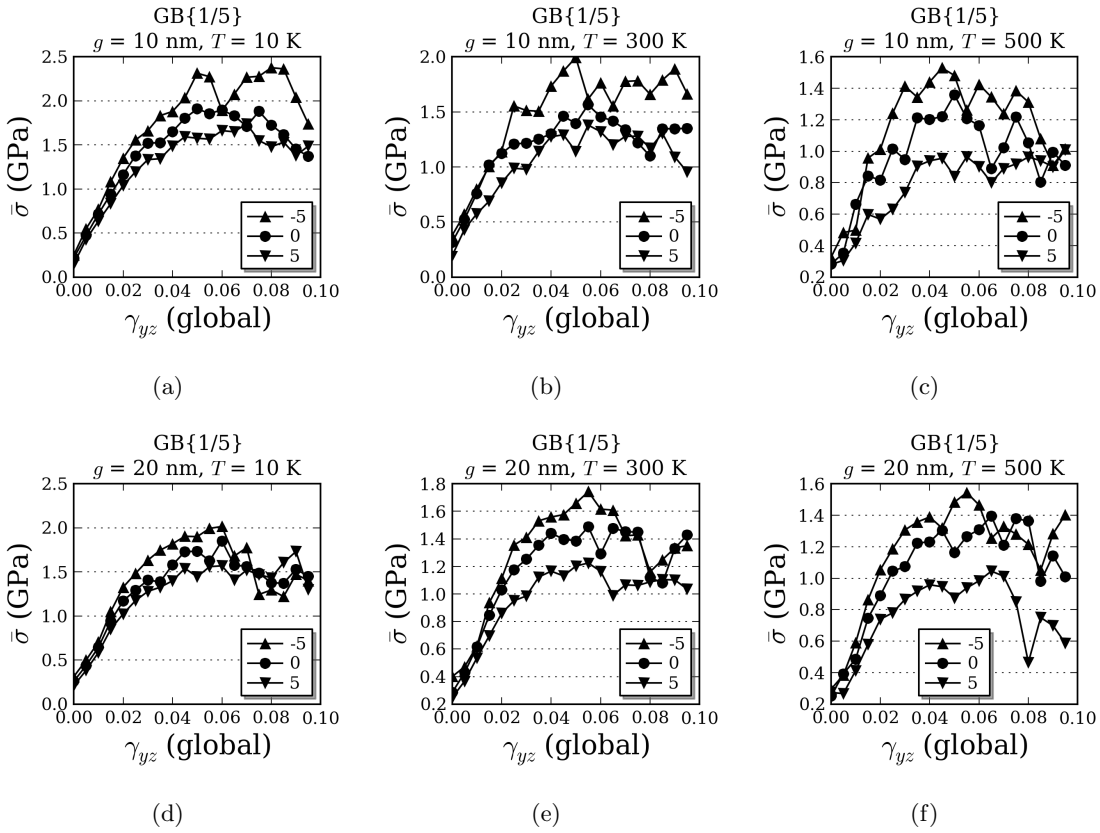

Figure 80: Evolution of $\bar{\sigma}$, computed over the region GB{1/5} (see Figure 76), with global shear strain. Each plot corresponds to a different grain size (g), and deformation temperature (T). The legend in each plot denotes imposed hydrostatic pressure in GPa.

these grain sizes, it becomes difficult to distinguish GB sliding from atom shuffling in the triple junctions. The set of atoms contained within this region, GB$\{1/5\}$, is shown in Figure 76, for the $g = 10$ nm microstructure. GB$\{1/5\}$ contained approximately 12000 atoms in the $g = 10$ nm microstructure, and around 49000 atoms in the $g = 20$ nm microstructure. Unlike the set GBAZ, GB$\{1/5\}$ occupies a continuous, convex region and therefore, the atomistic-based stress measure (Equation 48) can be evaluated over GB$\{1/5\}$. The von Mises invariant, $\bar{\sigma}$, of the GB-level stress was used to compare the evolution of stress in the GB across different grain sizes, temperatures, and applied hydrostatic stresses.

Figure 80 shows the evolution of $\bar{\sigma}$ over the GB$\{1/5\}$ region with respect to the global shear strain γ_{yz}, for two grain sizes (10 nm, 20 nm), and three temperatures (10 K, 300 K, 500 K). Here too, for the same γ_{yz}, an applied compressive hydrostatic stress increases $\bar{\sigma}$, and vice versa. Several features of the grain-interior response can be observed in the GB as well: e.g., stress-fluctuations corresponding to individual sliding 'events' do not occur at similar strains (plots (a),(b), and (d)) in plots corresponding to different applied hydrostatic stresses. However, some key differences from the grain-level response can be noted. First, there isn't a significant difference in the 'sliding resistance' (taken to be the peak $\bar{\sigma}$) of GB$\{1/5\}$ in $g = 10$ nm microstructure vs. the $g = 20$ nm microstructure, at all temperatures considered. This suggests that there is little to no grain size effect associated with the GB sliding process. Second, the regime of linear evolution of $\bar{\sigma}$ is restricted to a global strain below 0.03 at 10 K, as compared to around 0.04 for the grain interior. The breakdown of linearity at low shear strains, which was observed in the grain-interior response only for $T \geq 300$ K and $g = 5$ nm, seems to extend to higher grain sizes in the case of the GB's stress-strain response.

The results presented so far have explored the effects of grain size, temperature and applied pressure on the shear deformation occurring in intra-granular and inter-granular regions in NC Cu microstructures. However, since our averaging volumes (grain interior/grain boundary) admit only a few atomic rearrangement events over the course of the deformation, the inferences one can draw are mostly qualitative. Yet, these results capture important characteristics of microstructure evolution in a NC material, which could be used to guide

the development of microstructure-sensitive constitutive models of NC plasticity.

6.3.2.3 Domain-level response

Following the methodology introduced in Section 6.2.3, the stress tensor for the entire domain was computed by considering all atoms constituting the microstructure, and averaging over the volume of the entire periodic nanocrystalline domain. Unlike previous sections, the interpretation of $\bar{\sigma}$ in the context of the entire domain is much simpler. Since there is only a single non-zero component of the stress deviator acting at the domain-level (σ_{yz}), $\bar{\sigma} = \sqrt{3}\sigma_{yz}$. The evolution of domain-level stresses can be analyzed in terms of either $\bar{\sigma}$ or σ_{yz}; however, $\bar{\sigma}$ has been used in order to maintain consistency with previous results.

Figure 81 (a-c) shows the evolution of domain-level $\bar{\sigma}$ in the $g = 5$ nm microstructure. Here, unlike the grain-level response (Figure 79 (b),(c)), distinct linear and non-linear regimes can be identified, since the effects of small-scale stress fluctuations due to individual atomic rearrangement events are averaged out. This permits a quantitative analysis of inelastic yield stress(es). In plots (a-c), for shear deformation under each combination of grain size, temperature, and applied hydrostatic stress, the yield stress ($\bar{\sigma}^{\mathrm{Y}}$) was obtained as the maximum $\bar{\sigma}$ encountered over the course of the deformation. Figure 81 (d) shows the yield stresses obtained from the 15 simulations pertaining to the $g = 5$ nm microstructure, plotted against the applied hydrostatic stress $\hat{\sigma}$, for different temperatures during deformation. For each temperature, a linear fit is adequate to capture the relationship between $\bar{\sigma}^{\mathrm{Y}}$ and $\hat{\sigma}$. The quality of the fit, however, is best at lower temperatures, where stochastic effects are largely absent. The slope of the linear fit for each temperature quantifies the effect of the applied hydrostatic stress at reducing/elevating the shear yield strength at a particular temperature. These slopes, evaluated at 10 K, 300 K, and 500 K were, respectively, -0.052, -0.059, and -0.078 GPa/GPa.

A similar analysis, for the $g = 20$ nm microstructure, is presented in Figure 82. Plots (a-c) show that the evolution of $\bar{\sigma}$ is much smoother for this grain size compared to the $g = 5$ nm microstructure. Furthermore, the lack of statistical homogeneity in dislocation nucleation at the grain-level (see Figure 79 (g-i)) is also averaged out over several grains.

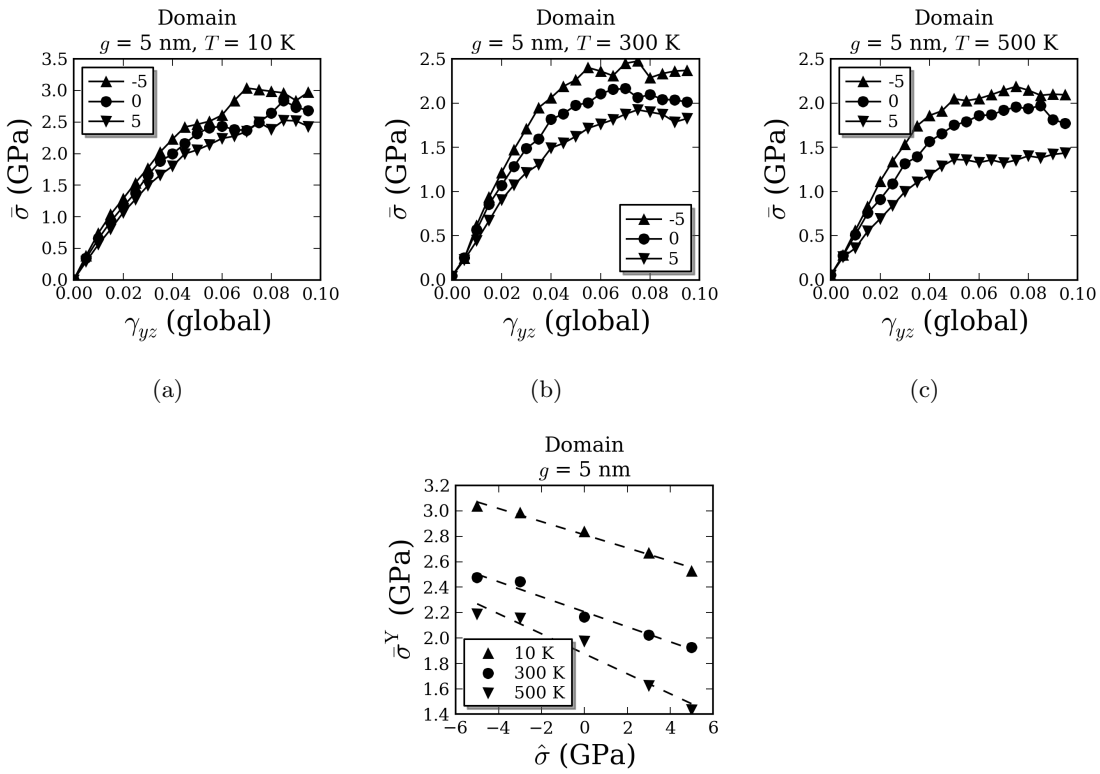

Figure 81: Evolution of $\bar{\sigma}$, computed over the entire $g = 5$ nm structure, with global shear strain (γ_{yz}). Each plot in (a-c) corresponds to a different deformation temperature (T). The legend in plots (a-c) denotes imposed hydrostatic pressure ($\hat{\sigma}$) in GPa. In (d), the yield stresses $\bar{\sigma}^{\mathrm{Y}}$ (the peak stresses in plots (a-c)) are plotted for different temperatures with respect to $\hat{\sigma}$.

Figure 82 (d) shows the variation of the yield stress $\bar{\sigma}^{\mathrm{Y}}$ in plots (a-c)) with respect to the applied hydrostatic stress $\hat{\sigma}$. Like the $g = 5$ nm microstructure, a linear fit adequately describes the relationship between $\bar{\sigma}^{\mathrm{Y}}$ and $\hat{\sigma}$ for all temperatures considered. The computed slopes of these fits for temperatures of 10 K, 300 K, and 500 K were, respectively, -0.071, -0.082, and -0.089 GPa/GPa.

The slopes of the lines in Figures 81 (d) and 82 (d) indicate that (1) the applied hydrostatic stress $\hat{\sigma}$ has a slightly stronger effect on $\bar{\sigma}^{\mathrm{Y}}$ as the temperature of deformation increases, and (2), $\bar{\sigma}^{\mathrm{Y}}$ for the $g = 20$ nm microstructure is more sensitive to the applied hydrostatic pressure than the smaller grain size $g = 5$ nm. These differences are interpreted in terms of defect activation parameters in the following section.

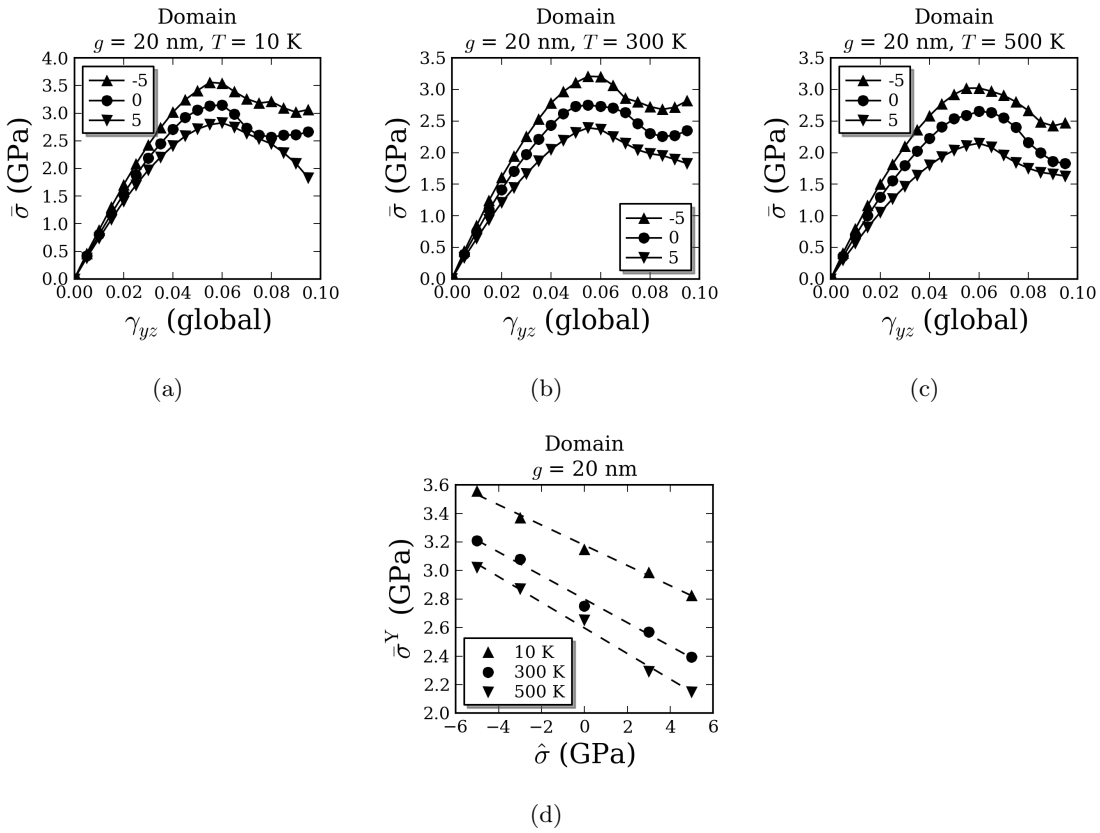

Figure 82: Evolution of $\bar{\sigma}$, computed over the entire $g = 20$ nm structure, with global shear strain (γ_{yz}). Each plot in (a-c) corresponds to a different deformation temperature (T). The legend in plots (a-c) denotes imposed hydrostatic pressure ($\hat{\sigma}$) in GPa. In (d), the yield stresses $\bar{\sigma}^{\mathrm{Y}}$ (the peak stresses in plots (a-c)) are plotted for different temperatures with respect to $\hat{\sigma}$.

6.3.3 Activation parameters for NC plasticity: The effect of hydrostatic stress

The most general description of inelastic deformation in solids is provided by the (primarily) stress-driven rearrangement of an initial configuration of atoms into an irreversibly deformed configuration, where both the initial and final configurations correspond to local minima in the potential energy landscape separated by a saddle-point configuration. The kinetics of such a rearrangement is affected by both the applied stress as well as the temperature, and these effects are captured by the activation volume (Ω) and the activation energy (Q), respectively. At zero applied stress, the potential energy difference between the initial configuration and the saddle point configuration is the activation energy barrier Q^*. An external applied stress σ lowers this barrier by an amount equal to $\sigma\Omega$, thereby yielding a new barrier $Q(\sigma) = Q^* - \sigma\Omega$. At moderate temperatures, this lowered barrier can be crossed with a higher probability via the random fluctuation of atoms.

We computed the activation parameters of NC plasticity based on methods described in earlier work by Zhu et al. [290] and Tschopp and McDowell [226]. For isothermal deformation of an atomistic ensemble at a finite temperature T and a constant applied strain rate $\dot{\epsilon}$, an expression can be derived relating the stress required to activate a particular deformation mechanism (σ), in terms of the activation volume (Ω), and the athermal activation stress ($\sigma_{ath} = Q^*/\Omega$) [290]:

$$\sigma = \frac{Q^*}{\Omega} - \frac{k_{\mathrm{B}}T}{\Omega} \ln \frac{k_{\mathrm{B}}TN\nu_0}{E\dot{\epsilon}\Omega} \tag{49}$$

Here, $\frac{Q^*}{\Omega}$ represents the stress required to surmount the activation barrier Q^* (Q^* is the activation energy barrier on the zero-stress potential energy surface). At a finite temperature T, this stress is lowered by an amount equal to the second term on the right hand side of Equation 49. This term includes a stress $\frac{k_{\mathrm{B}}T}{\Omega}$ and a logarithmic multiplier that compares the heat exchanged between the system and an external bath ($k_{\mathrm{B}}TN\nu_0$) with the rate of work done by the applied stress ($E\dot{\epsilon}\Omega$). N, ν_0, and E represent, respectively, the number of nucleation sites, the atomic jump frequency ($3 \times 10^{11}\mathrm{s}^{-1}$ for Cu [105]), and the elastic modulus.

While using Equation 49 to compute activation parameters, Q^* and Ω are unknowns. Input values are provided in the form of the yield stress under athermal conditions $\sigma_{ath} = Q^*/\Omega$, the yield stress ($\sigma$) at a finite temperature T, and the elastic modulus E. N and ν_0 are constants. Since the ratio of Q^* and Ω is known ($= \sigma_{ath}$), this leaves Ω as the only unknown in Equation 49, and can be solved for iteratively.

Equation 49 has traditionally been used to determine activation parameters for a single deformation mechanism. In the current work, admittedly, there is an added complication since in addition to dislocation nucleation from interfaces, interfacial sliding/migration can contribute to—or even dominate—the domain-scale deformation response. Fortunately, the dominant deformation mechanisms in the two of the three microstructures studied in this work were quite unambiguous: GB shear transformation in the $g = 5$ nm microstructure and GB mediated dislocation activity in the $g = 20$ nm microstructure. A number of assumptions were made in order to compute activation parameters from the available simulation data:

- Yield occurs *predominantly* via GB processes in the $g = 5$ nm structure, and via dislocation processes in the $g = 20$ nm structure. This assumption is valid to a first approximation, since the dominant deformation mechanism is unambiguous in all microstructures except $g = 10$ nm. However, it must be emphasized that activation parameters computed from domain-level yield stress(es) still pertain to mixed-mechanism deformation.

- The yield stress at 10 K is used as the athermal yield stress. Activation parameters are computed for deformation at 300 K.

- The population of available nucleation sites, N, is taken to be the number of atoms in the GBAZ.

Figure 83 shows the computed values of Ω, Q^*, and Q (a function of applied stress σ), plotted with respect to the imposed hydrostatic stress $\hat{\sigma}$, for the microstructures $g = 5$ nm (plot (a)) and $g = 20$ nm (plot (b)). At $\hat{\sigma} = 0$, computed values of Ω were 3.90 b^3 (b is the magnitude of the burgers vector for a full dislocation in Cu, 2.556 $\mathring{A}$) for $g = 5$ nm, and 7.5

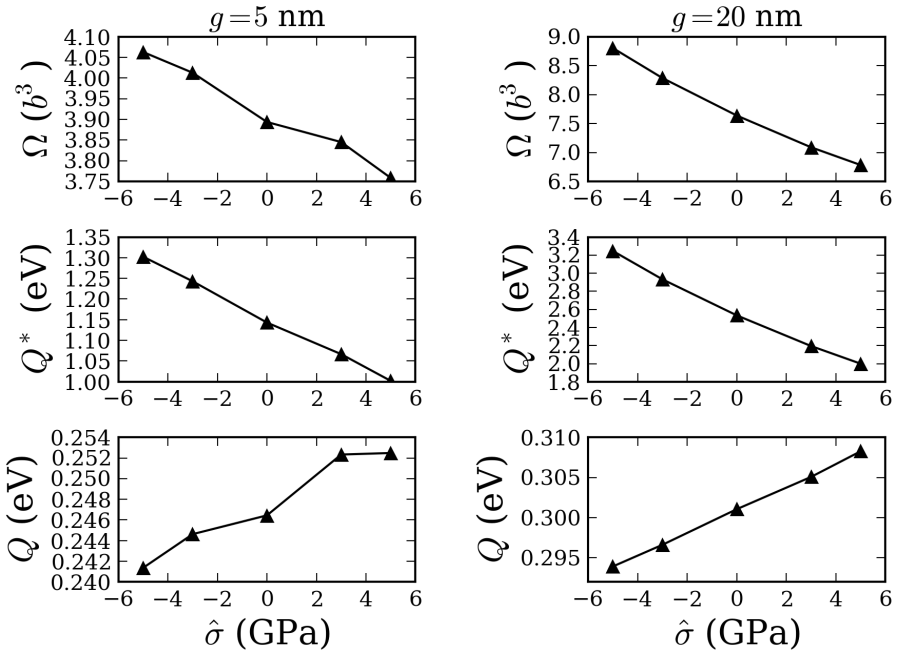

Figure 83: Evolution of activation volume (Ω), athermal activation energy barrier (Q^*), and activation energy (Q) of shear deformation with applied hydrostatic stress $\hat{\sigma}$. Results have been shown for two grain sizes: (a) $g = 5nm$, and (b) $g = 20$ nm.

b^3 for $g = 20$ nm. The corresponding values for Q^* were, respectively, 1.15 eV and 2.6 eV. Like Q^*, the activation energy Q was lower for the $g = 5$ nm microstructure (0.24 eV) as compared to $g = 20$ nm (0.3 eV).

Under the effect of a non-zero compressive (tensile) imposed hydrostatic stress, both Ω and Q^* appeared to increase (decrease). This change was largest in the $g = 20$ nm microstructure: 0.2 b^3/GPa for Ω, and 0.12 eV/GPa for Q^*. Further, although a clear monotonic variation in activation parameters can be noted in Figures 83 (a) and (b), these values were obtained from Equation 49 using linear fits to the yield stress, and therefore represent 'averaged' estimates obtained from the elasto-plastic response of only 8 grains. More accurate values for activation parameters can be obtained, for example, by repeating these simulations with statistically representative microstructures that sample more grains, although doing so would incur a large computational cost.

The computed activation parameters help quantify the kinetics of the deformation behavior. Both the activation volume (Ω), as well as the athermal barrier (Q^*), are smaller for GB shear transformation processes, as compared to GB-mediated dislocation nucleation. This result indicates that GB shear transformation events are not only energetically favorable as compared to dislocation nucleation from GBs in the $g = 5$ nm structure, but they also require cooperative atomic motion in (statistically) smaller sub-volumes of the microstructure.

The computed values of the activation parameters (at $\hat{\sigma} = 0$) agree with existing experimental and theoretical data. Computed activation volumes in the range 3-9 b^3 are within the range of predictions of theoretical models of Asaro, Suresh, and coworkers [11, 74], who predicted activation volume in the range 3-10 b^3 for NC metals. A similar range, 5-10 b^3, was obtained in experiments by Wang et al. [260] for NC Ni of grain size 30 nm. Grewer and Birringer [73] recently reported an activation volume of $6b^3$, and an activation free energy (Q, in the present notation) of 0.2 eV for a NC PdAu alloy of grain size ≤ 10 nm.

6.3.4 Quantifying strain accommodation in nanocrystals

This section provides a summary of earlier work performed by the author in collaboration with Dr. Garritt Tucker, to demonstrate the utility of continuum-based metrics of deformation in atomistic simulations [297, 234]. Details can be found in [237].

The development of continuum-based metrics (Section 2.7.3) has significantly aided in furthering our understanding of interface-mediated deformation kinematics. Primarily, continuum-based metrics can be used to interpret deformation-induced atomic displacement fields from the perspective of familiar continuum quantities such as deformation gradient, strain, and rotation. Therefore, structural transitions occurring over the course of deformation can be identified and categorized based on characteristic values of one or more continuum metrics. For example, atoms in the wake of dislocations can be identified on the basis of their characteristic shear strain, while atoms in a twinned lattice, or those lying in a region swept by a migrating interface, would show characteristic values of rotation. These metrics can be combined with widely-used atomic classifiers such as common neighbor analysis, or slip vector [295] to assess the nature and extent of deformation at interfaces and other defect structures.

A useful application of continuum-based metrics is to quantitatively assess the grain size-dependent contribution of different deformation mechanisms to the global (domain-level) strain. To demonstrate this, three NC Cu microstructures were deformed at 10 K (NPT) under a uniaxial strain rate of 10^9 s^{-1}. Figure 84(a) shows one NC Cu microstructure, named S_1, containing 25 grains and having a mean grain size of 5 nm (note that these microstructures are *not* the same as the ones shown in Figure 74 (a-c), which were used to obtain all other results in this chapter). NC microstructures of higher grain sizes were obtained by uniformly scaling S_1 by the appropriate scaling factor, while maintaining the same grain morphology and grain orientations. In this manner, two additional microstructures, of mean grain size 10 nm and 15 nm (shown in Figure 84(b)), were obtained. They were named S_2 and S_3, respectively.

Figure 85(a) shows stress-strain plots for the uniaxial tensile deformation of structures

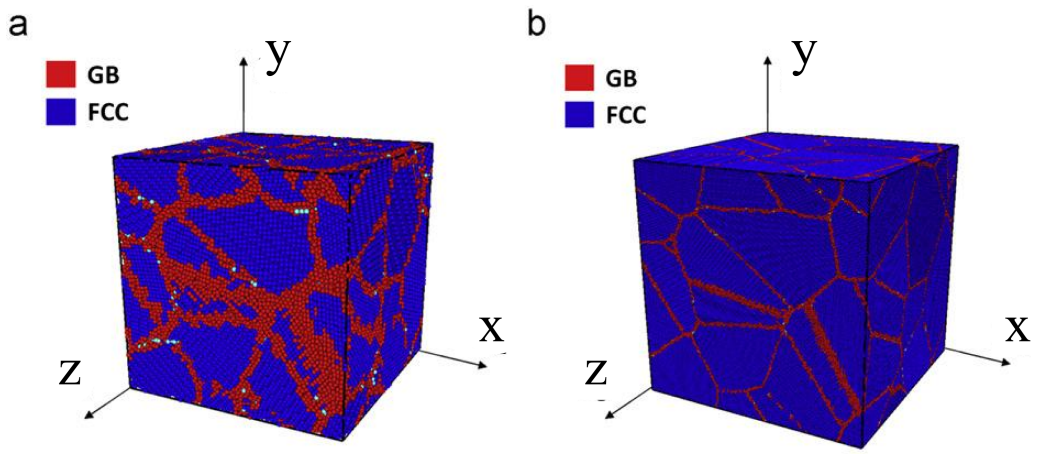

Figure 84: Cu microstructures of mean grain size (a) 5 nm, and (b) 15 nm, having identical grain morphologies. Atoms have been colored based on common neighbor analysis [232].

S_1, S_{10}, and S_{15}. The stress-strain response is elastic perfectly-plastic for all microstructures, with saturation occurring at ≈ 0.04 strain. For the same deformation, Figure 85(b) shows the contribution of various deformation mechanisms to the total uniaxial strain (plotted on the x-axis) for microstructures of different grain sizes. Atoms were ascribed categories based on CNA and magnitude of the slip vector in the following manner: atoms with a slip vector magnitude near the Burgers vector for partial slip (1.48 Å) or full slip (2.56 Å), were categorized as 'Dislocation'. Atoms that were non-12 coordinated (based on CNA) were classified as 'Other'. These atoms predominantly belonged to the GB network. Finally, atoms that were both fcc and did not undergo either full slip or partial slip were classed as 'FCC'.

Until up to 0.02 strain, the strain contribution from both 'FCC' and 'Other' categories rises, since the deformation is predominantly elastic, and no dislocation activity has yet occurred. At higher strains, dislocations begin to get emitted from GB sources, thereby reducing the contribution of the (purely elastic) strain in the unslipped grain interiors. Eventually, the strain contribution of all three categories stabilizes. At these large deformations, it is evident that the contribution of the GB network (Other) to the deformation is larger in the case of the structure S_1, as compared to the structure S_3, of a larger mean grain size. Conversely, the contribution of dislocations to the global strain is larger for the

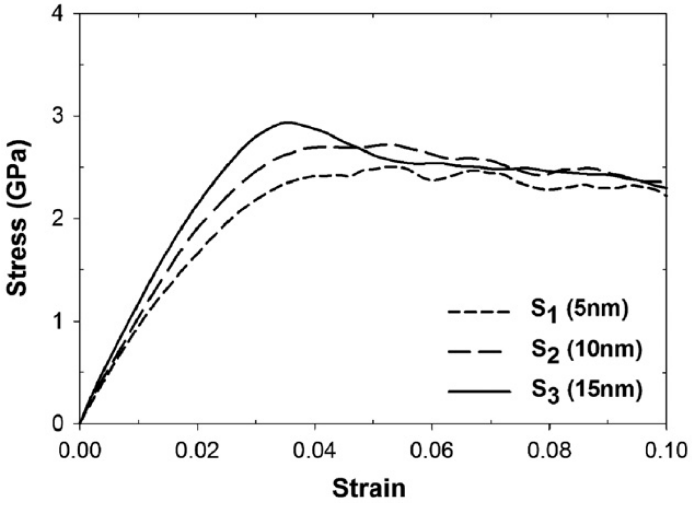

(a)

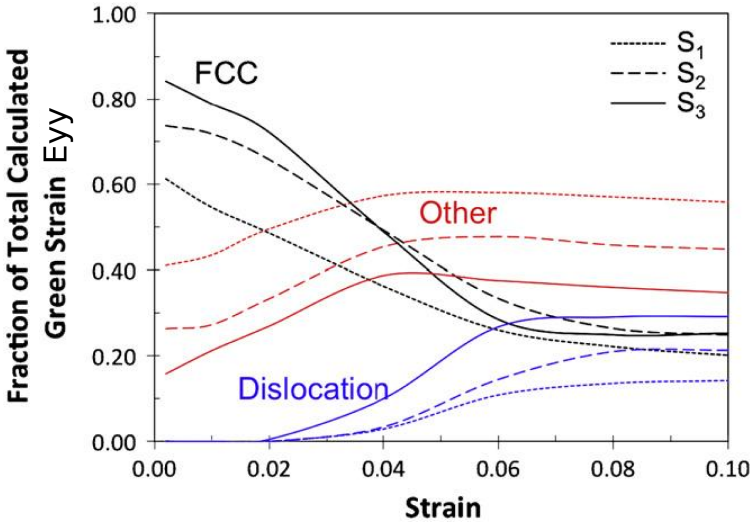

(b)

Figure 85: (a) Stress-strain curves for uniaxial tensile deformation of Cu microstructures of three mean grain sizes: 5 nm (S_1), 10 nm (S_2), and 15nm (S_3).(b) The contribution of various deformation mechanisms to the global uniaxial strain. For each microstructure, per-atom Green strain was accumulated over lattice atoms deforming purely elastically (FCC), atoms lying the in the wake of gliding dislocations (Dislocation), and atoms in non-crystalline regions (Other).

structure S_3, as compared to S_1. Further, the strain at which the contribution of GB deformation saturates (0.04), also corresponds to the saturation of the stress-strain curves in Figure 85(a). This is due to the onset of dislocation activity, which relaxes the stress in (a), and also checks the growth of strain accommodation in the GBs by opening intra-granular pathways to accommodate strain. These results demonstrate the utility of atomic-scale continuum-based metrics towards resolving the kinematics of elastic-plastic deformation. Further, these results are based on a direct quantification of correlated interatomic displacements, and are therefore more rigorous than an earlier attempt [251] that relied on the relative displacement of atoms to distinguish between dislocations and GB processes.

6.3.5 Effect of hydrostatic stress on the inelastic strain

In a deformed configuration which is under an applied load, continuum metrics of deformation compute the total per-atom strain tensor $\boldsymbol{\epsilon}/atom$, not the inelastic strain tensor ($\boldsymbol{\epsilon}^{\text{in}}/atom$). To compute $\boldsymbol{\epsilon}^{\text{in}}/atom$, the unloaded configuration must be known. Recently, methods have been proposed to partition the atomic-scale deformation gradient into elastic and inelastic parts, without prior knowledge of the unloaded configuration [204]. However, these methods are unsuitable for non-periodic atomic structures, such as the high-angle GBs present in NC microstructures. Therefore, to obtain $\boldsymbol{\epsilon}^{\text{in}}/atom$, we explicitly 'unload' a deformed configutation by equilibrating it under $N\boldsymbol{\sigma}T$ control to the temperature of deformation, and $\boldsymbol{\sigma} = 0$ (both constant). The unloading step permits relaxation of the yz components of the domain-level stress and strain.

Deviatoric invariants of the total strain $\boldsymbol{\epsilon}$ and the inelastic strain $\boldsymbol{\epsilon}^{\text{in}}$ were used as scalar measures of the per-atom shear strains, i.e.,

$$\bar{\epsilon} = \sqrt{\frac{2}{9}((\epsilon_{xx}-\epsilon_{yy})^2+(\epsilon_{yy}-\epsilon_{zz})^2+(\epsilon_{zz}-\epsilon_{xx})^2+6(\epsilon_{xy}^2+\epsilon_{yz}^2+\epsilon_{xz}^2))}$$

$$\bar{\epsilon}^{\text{in}} = \sqrt{\frac{2}{9}((\epsilon_{xx}^{\text{in}}-\epsilon_{yy}^{\text{in}})^2+(\epsilon_{yy}^{\text{in}}-\epsilon_{zz}^{\text{in}})^2+(\epsilon_{zz}^{\text{in}}-\epsilon_{xx}^{\text{in}})^2+6((\epsilon_{xy}^{\text{in}})^2+(\epsilon_{yz}^{\text{in}})^2+(\epsilon_{xz}^{\text{in}})^2))}$$

For the three microstructures $g = 5$ nm, $g = 10$ nm, and $g = 20$ nm, Figure 86 shows distributions of $\ln \bar{\epsilon}/atom$ and $\ln \bar{\epsilon}^{\text{in}}/atom$ (atoms up to the first nearest neighbors were

considered while computing per-atom strains). Unloading was performed at a temperature of 10 K from a total strain of $\gamma_{yz} = 0.1$. Plots (a-c) pertain to the total strain $\bar{\epsilon}/atom$, while plots (d-f) show the inelastic strain $\bar{\epsilon}^{\text{in}}/atom$. In these distributions, GB processes manifest as a broad 'background', while dislocation glide leads to sharp peaks whose location along the horizontal axis depends on the characteristic per-atom strain associated with the particular dislocation process (e.g., full dislocation slip vs. partial slip).

In the case of the $g = 5$ nm microstructure, neither the total strain distribution (plot (a)), nor the inelastic strain distribution (plot (d)), is significantly affected by the imposed hydrostatic stress. For the $g = 10$ nm microstructure (plots (b) and (e)), imposed hydrostatic stress appears to affect the strain due to dislocation glide (peaks), while the effect on GB processes (background) is not significant. However, this result is likely an anomaly, arising from the the low density of dislocations in deformed states of the $g = 10$ nm microstructure. This conclusion is supported by plots (c) and (f), which show the distribution of per-atom strains in the $g = 20$ nm microstructure. Here, no difference can be observed in the total strain distribution, either in dislocation slip (peaks) or GB processes (background), under the influence of an imposed hydrostatic stress. Upon unloading, however, the relative height of the two major peaks changes. This is because the smaller peak at $\ln \bar{\epsilon}^{\text{in}}/atom \approx -2.5$ corresponds to partial dislocation slip, while the higher peak at $\ln \bar{\epsilon}^{\text{in}}/atom \approx -1.9$ corresponds to full dislocation slip. Since full dislocation slip leaves a defect-free lattice in its wake, atoms that have slipped by an amount greater than the full dislocation Burgers vector tend to relax to a defect-free lattice via partial slip in the reverse direction.

Figure 87 shows the distributions of $\ln \bar{\epsilon}/atom$ and $\ln \bar{\epsilon}^{\text{in}}/atom$ for deformation/relaxation performed at 500 K. In the $g = 5$ nm microstructure, although a slight difference can be observed in the distributions of $\ln \bar{\epsilon}/atom$, the distribution of $\ln \bar{\epsilon}^{\text{in}}/atom$ are very similar. At larger grain sizes, unlike Figure 86 (relaxation at 10 K), the prominent dislocation peaks are no longer present. This is due to (a), an increase in the contribution of GB sliding to the total strain at higher deformation temperatures, and (b) the increased propensity for the thermally-activated depinning of partial dislocations that have been absorbed into GBs.

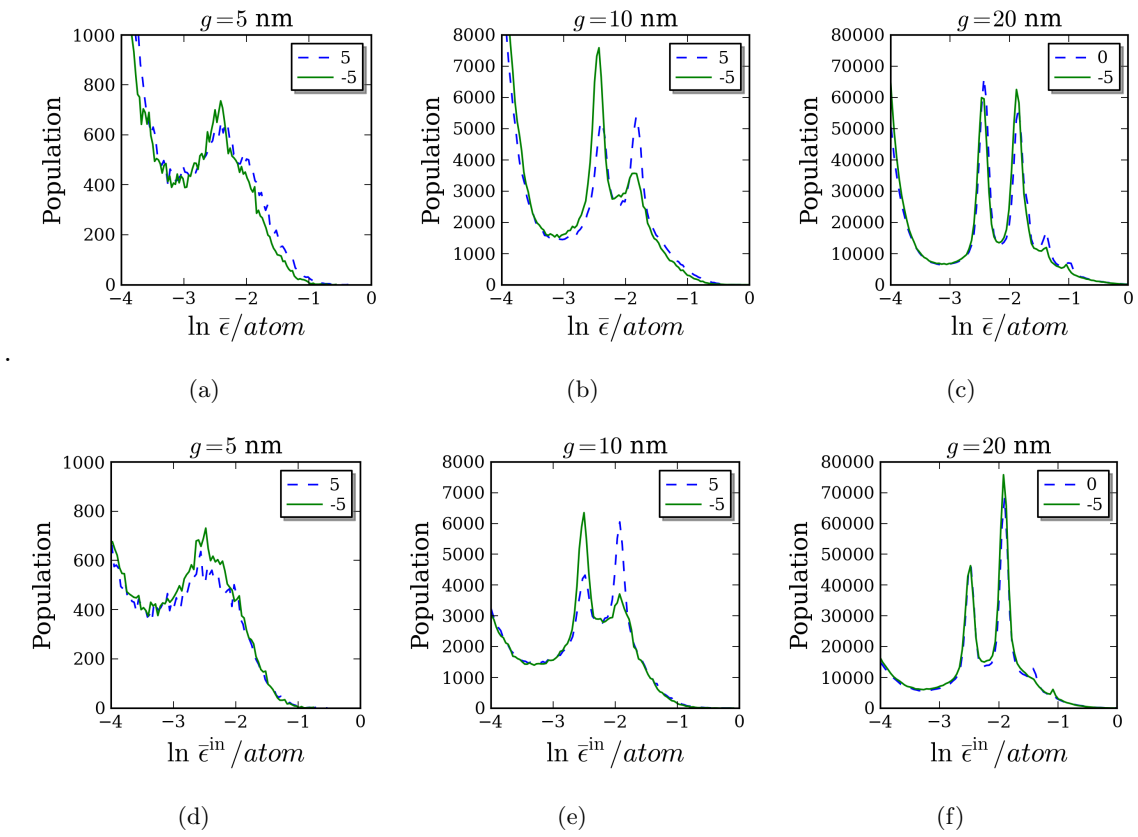

Figure 86: The distribution of per-atom inelastic von Mises strains ($\bar{\epsilon}^{in}/atom$) in microstructures that were deformed at a temperature of 10 K under different imposed hydrostatic pressures, to a total shear strain of $\gamma_{yz} = 0.1$. The imposed hydrostatic pressure (in GPa) is shown in the legend of each plot.

In both the $g = 10$ nm and $g = 20$ nm microstructures, differences in strain distributions (whether total or inelastic) were small.

These results suggests that imposed hydrostatic stress does not have a significant effect on the distribution of inelastic strain in NC Cu. Additionally, although pockets of per-atom dilatation and contraction were present in all unloaded microstructures, the overall NC domain-level inelastic dilatational strain was negligibly small.

6.4 Discussion

The elastoplastic deformation of nanocrystalline materials involves contributions from both interfaces as well as grain interiors. In the present chapter, we have described algorithms to demarcate microstructural elements such as individual grain interiors and grain boundaries

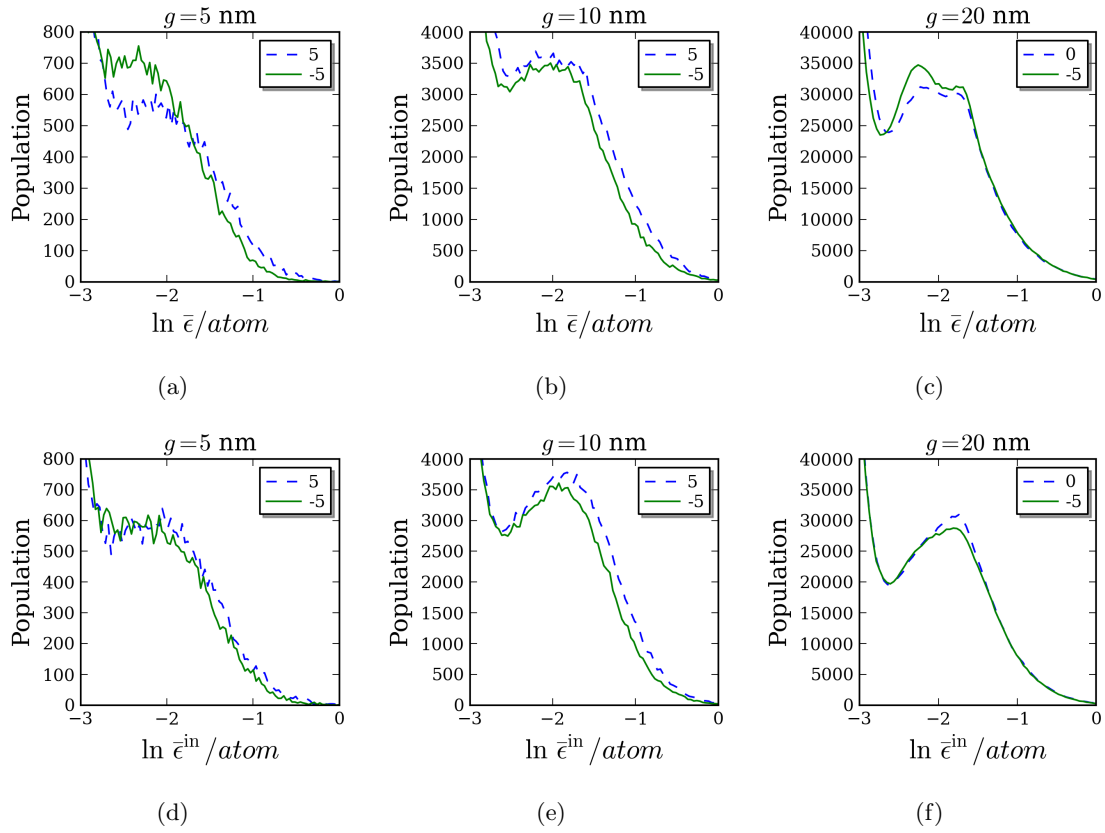

Figure 87: The distribution of per-atom inelastic von Mises strains ($\bar{\epsilon}^{\text{in}}/atom$) in microstructures that were deformed at a temperature of 500 K under different imposed hydrostatic pressures, to a total shear strain of $\gamma_{yz} = 0.1$. The imposed hydrostatic pressure (in GPa) is shown in the legend of each plot.

in a simulated nanocrystal, and have quantified the stress-response of these elements as the nanocrystal is deformed. These responses tend to often be assumed a priori in various constitutive theories of elasto-plasticity in NC materials. While some continuum models (e.g., [35]) treat the GB network as a viscous phase, others (e.g., [266]) prefer to treat interface regions as cohesive zones with prescribed elastic-plastic traction separation relation(s). Our results suggest that the appropriateness of either description depends on the grain size and deformation temperature. For example, the viscous description appears to better describe GB shear transformation processes at low grain sizes and high temperatures (notice the lack of distinct linear and non-linear regimes in Figure 79(b) and (c); similar stress-strain curves were obtain for the GBAZ). At larger grain sizes, however, even the interfaces exhibit distinct linear and saturation regimes (see Figures 80 (d-f)), suggesting that a cohesive zone treatment is relevant for these cases. Further, the sliding/migration resistance of individual GB structures, in a full NC environment, may be estimated using the layer-growth algorithm described in this chapter.

Our computed values of activation parameters for NC inelasticity show reasonable agreement with experiemental values reported in the literature. This is despite the high strain rates employed in our simulations, where diffusive processes are suppressed. GB diffusion (Coble creep) in NC can be an important deformation mechanism in NC materials at medium to high temperatures. However, recent experimental estimates of activation parameters in NC Ni [260] and PdAu [73] at room temperature and quasi-static deformation rates have ruled out creep mechanisms, in favor of intragranular dislocation activity and shear shuffling at GBs, consistent with the mechanism observed in MD studies. For dislocation nucleation from GB sources, Asaro and Suresh [11] had predicted a grain size-independent activation volume of πb^3, based on dislocation nucleation via a GB sliding event that acts as a crack-like stress concentrator. We found direct evidence of what appears to be Asaro and Suresh's mechanism operating in our NC microstructures. Figure 88 shows this nucleation mechanism operating in the $g = 10$ nm microstructure. The snapshot has been taken just prior to the nucleation of a dislocation in Grain 3. First, a sliding event at the GB separating Grains 5 and 7 produces a stress concentration in Grain 3, visible as the

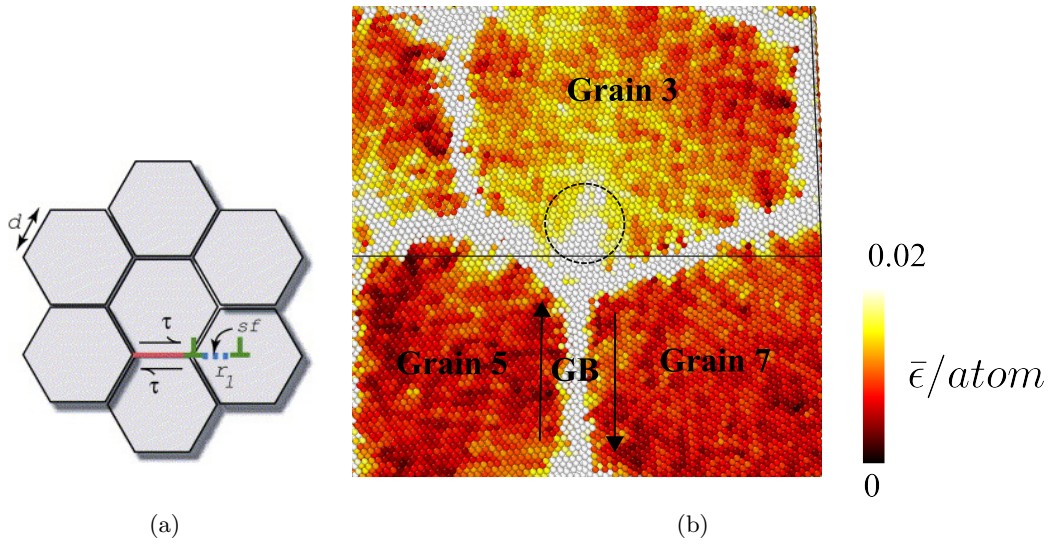

(a) (b)

Figure 88: (a) The dislocation nucleation mechanisms proposed by Asaro and Suresh [11], where a shear stress τ in the plane of a GB initiates sliding, leading to the formation of stacking fault in an adjacent grain. (b) A section of the $g = 10$ nm microstructure, at global strain $\gamma_{yz} = 0.045$, showing a concentration in the atomic strain field inside Grain 3 (dashed circle), arising from the GB sliding event between Grains 5 and 7.

light-colored region enclosed within the dashed circle. As the strain increased, dislocations were nucleated from within the dashed region. Although GB sliding was observed to occur at several locations within the GB network, not all sliding events led into grains that were favorably oriented for slip.

The activation parameters presented in Figure 83 (a) and (b) pertain to "GB-dominated" and "dislocation-dominated" regimes, respectively. However, contributions of the non-dominant mechanism (e.g., GB sliding in the $g = 20$ nm microstructure) were not negligible, and as a result, the computed activation parameters pertain to a combination of dislocation activity and GB sliding. Additionally, athermal barriers to atomic rearrangement have not been explicitly computed, based on energy differences on the zero temperatures potential energy surface (Q^*). While such explicit computations have been performed in cases where the kinematics of defect nucleation/reaction is known, using variants of the Nudged Elastic Band [84] method, it is not clear how such methods can be applied to NC metals, where many variants of inter-granular and intra-granular deformation unit processes tend to operate together.

We have also assessed the effect of an applied hydrostatic stress ($\hat{\sigma}$) on the shear yield strength of Cu nanocrystals of different grain sizes. At the scale of individual microstructural elements, $\hat{\sigma}$ leads to overall strengthening mixed with rather unpredictable stress fluctuations. At the overall NC domain-level, a clear elevation (depression) in shear yield strength $\bar{\sigma}^{\mathrm{Y}}$ with imposed compressive (tensile) $\hat{\sigma}$ is observed. The effect of $\hat{\sigma}$ on $\bar{\sigma}^{\mathrm{Y}}$ appears to become more significant as the grain size or the temperature of deformation increase. However, it is worth noting that a imposed $\hat{\sigma}$ also changes the effective stiffness of the nanocrystal. We computed the *reduced* domain-level shear strength of several NC microstructures, by normalizing $\bar{\sigma}^{\mathrm{Y}}$ by the initial slope of the $\bar{\sigma} - \gamma_{yz}$ curve, for each imposed $\hat{\sigma}$. The reduced shear strengths showed some scatter, but no monotonic trend could be observed. This suggests that the pressure-induced change in yield strength is primarily associated with the pressure-induced change in the elastics stiffness of the overall NC ensemble. Note, however, that predicting the effect of pressure on the elastic moduli of microstructures with a significant volume fraction of interfaces can be non-trival, and would need to be obtained from experimental/atomic-resolution computations.

6.4.1 Deformation under multiaxial stress states: Hydrostatic stress vs. Normal stress

In the space of six independent stress components, several 'families' of multiaxial stress states can be defined, depending on the constraint(s) placed on individual stress components in relation to each other, as well as on the temporal evolution of these components. Based on this classification, our current method of shear deformation under a superimposed hydrostatic stress explores only a single family of multiaxial stress states: one where the normal stresses are constrained to be equal, and all shear stress components, except one, are zero. Clearly, a very large number of families of multiaxial stress states can be conceived by varying combinations of different stress components; however, some are expected to be more relevant from the standpoint of defect nucleation/migration. The case of stress applied *normal* to the characteristic plane of atomic rearrangement (e.g., GB planes, or dislocation slip planes) is particularly interesting, since the dislocation nucleation stress in Cu appears to better correlate with the stress resolved normal to the slip plane for some

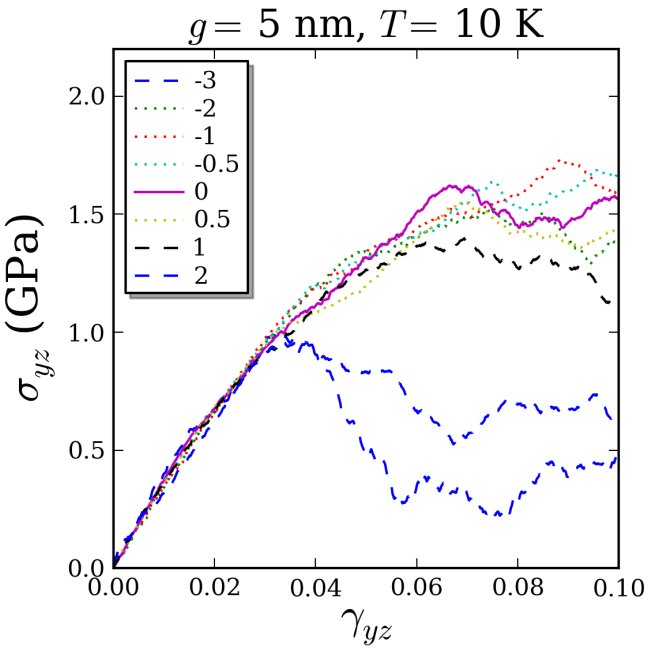

(a)

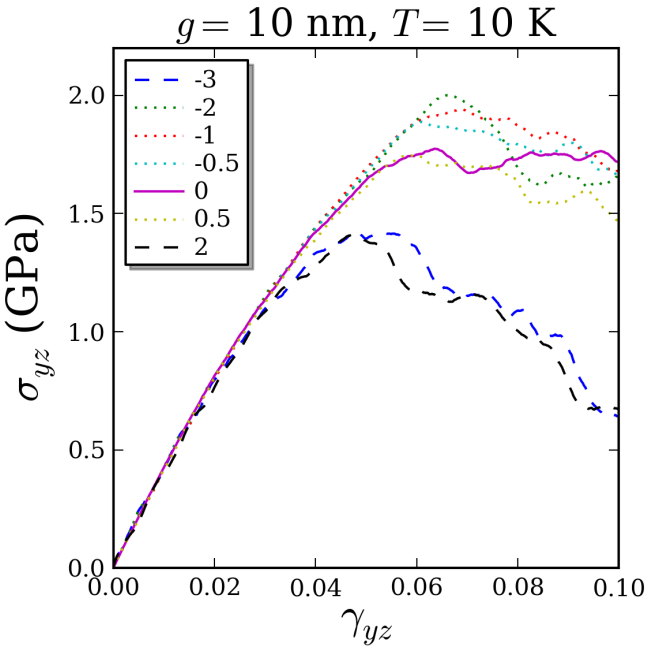

(b)

Figure 89: Shear stress-strain response of the (a) $g = 5$ and (b) $g = 10$ nm structures under an imposed normal stress applied along the z-axis (i.e., $\sigma_{xx} = \sigma_{yy} = \sigma_{xy} = \sigma_{xz} = 0$, σ_{zz} =constant). The applied normal stress σ_{zz} (in GPa) is shown in the legend. Tensile normal stresses are positive.

loading orientations [226].

To qualitatively assess the effect of imposed normal stress, two structures, $g = 5$ nm and $g = 10$ nm were deformed under yz-shear with a constant normal stress imposed in the direction of the z-axis (i.e., normal to the plane in which shear occurs) at a temperature of 10 K. Several normal stresses, in the range (-3,3) GPa, were applied prior to shear deformation and the stress-strain response ($\sigma_{yz} - \gamma_{yz}$) was computed.

The computed responses are shown in Figure 89. The most noteworthy feature of the plots in both (a) and (b) is the *non-monotonicity* of the strengthening as a consequence of the applied stress. In (a), for example, blue dashed lines show that applied stresses of -3 GPa and 2 GPa, despite their opposite signs, cause the structure to yield at a significantly lower stress as compared to deformation with no applied normal stress (0 GPa). A smaller tensile stress of 1 GPa (black dashed line) also lowers the yield strength, although much less severely. Compressive normal stresses in the range (-0.5,2) GPa lead to a slight elevation of the peak stress. The stress-strain response of the $g = 10$ nm structure, shown in Figure 89, was qualitatively similar to that of the $g = 5$ nm structure. Here too, extreme normal stresses of either sign ($|\sigma_{zz}| \geq 2$ GPa) were found to significantly depress the yield strength, while intermediate values of applied compressive stress ($-1 \leq \sigma_{zz} < 0$) led to moderate strengthening. This strengthening appears to be slightly larger than that produced by the same normal stress(es) in the $g = 5$ nm mirostructure. This difference is consistent with the MD results of Dongare et al. [56], who reported an increase in tension-compression asymmetry as the grain size increases from 4 to 10 nm.

Note that although an imposed hydrostatic stress naturally produces a stress component normal to the dislocation slip plane, the isotropic constraint on the diagonal stress components leads to non-zero transverse (i.e., in-plane) stresses. In contrast, under unconstrained normal loading (e.g., Figure 89), these transverse stress components are zero. In the literature, some authors [44] have attempted to explain the tension-compression strength asymmetry of NC materials by incorporating the effect of hydrostatic stress on dislocations/GB processes. However, the present study indicates that the role of hydrostatic stress and that of stresses normal to characteristic planes associated with atomic rearrangement

mechanisms are very different. More work is necessary before a theory for dislocation nucleation could be developed that includes the effect of multiaxial stress states, as well as a variety of heterogeneous nucleation sources.

6.5 Summary

We have computationally explored the effects of superimposed hydrostatic stress on the shear deformation behaviour of nanocrystalline Cu, over a range of grain sizes (5-20 nm) and temperatures (10-500 K) over which deformation is applied. The results suggest that shear strength increases under imposed compression and decreases under imposed tension, by around 0.05-0.09 GPa for every GPa of imposed hydrostatic pressure. The pressure-induced change in shear strength increases as the grain size and/or the temperature of deformation increases. Activation volumes and activation energies for the deformation of microstructures of different grain sizes were computed at 300 K. The computed activation volumes (3.5-9 b^3) and activation energies (0.2-0.3 eV) appear to agree with values reported in existing experimental and theoretical work. Additionally, shear deformation under an imposed compressive hydrostatic stress tends to increase both the activation volume (Ω) as well as the athermal activation barrier (Q^*) slightly. Finally, although an imposed hydrostatic stress affects the yield strength under shear, no discernable pressure effect was observed on the distribution of inelastic shear strain, nor the inelastic dilatation.

CHAPTER VII

CONTROLLING DEFECT NUCLEATION IN MD SIMULATIONS: DISCRETE NOSÉ-HOOVER DYNAMICS

7.1 Introduction

7.1.1 An overview of deformation rate-effects in molecular dynamics simulation

In previous chapters, a number of MD-based studies have been presented, investigating the role of interfaces in mediating the elasto-plastic deformation response of nanostructured materials, especially under multiaxial loading conditions. The computed response has been identified as arising from a combination of deformation mechanisms, where the activation of individual deformation mechanisms is affected by the volume fraction of the interface regions and the precise geometry of atomic arrangements in the interfaces.

However, the results discussed so far in this thesis apply to material behavior under high applied stresses, where the role of random thermal motion of atoms towards assisting inelastic atomic rearrangements is greatly diminished. The timescales accessible to MD are on the order of nanoseconds, which is several times shorter than typical "wait times" for thermally activated deformation unit processes. Consequently, it is nearly impossible to capture thermally-activated defect nucleation/migration during the course of an isothermal MD simulation. In practice, MD simulations of deformation are often performed in the "overdriven" regime, characterized by higher deformation rates ($> 10^7 \mathrm{s}^-1$) and high stresses (on the order of several GPa) as compared to experiments. In this regime, defect nucleation/migration is primarily stress-driven. Results based on MD are directly useful only in predicting a material's response under shock loading conditions.

Another limitation of overdriven MD arises in the cases of stochastic dislocation nucleation from free surfaces [54] or GB dislocation sources. In the case of dislocation nucleation from GB sources, several sources, having similar activation parameters, may be present. In the thermally-activated regime, the activation of a particular dislocation source would

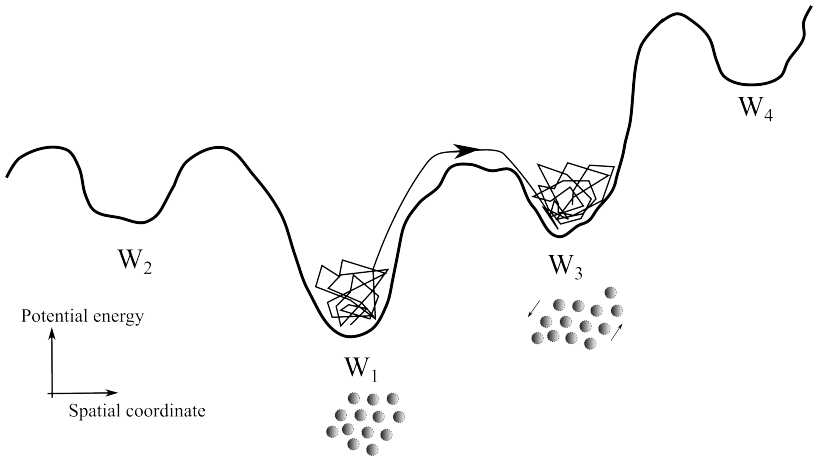

Figure 90: Schematic for a thermally-activated rearrangement of a system of particles, showing an infrequent transition event that transforms a locally-stable configuration (W_1) to another locally stable configuration (W_3). The system explores several configurations in the vicinity of W_1 before rearranging into a different configuration. Transition to other stable configurations, e.g., W_2 and W_4 , may be accessible, but may involve higher energy barriers and thereby lower transition probabilities. Note that the application of an external stress can lower the barrier for a particular transition and increase its probability of occurrence.

depend on specific uncorrelated thermal atomic motion(s). Since MD often does not provide the time duration necessary for such a thermally-assisted event to occur, overdriven simulations are much more likely to predict multiple nucleation, i.e., arrays of dislocation sources activated simultaneously. The transition state corresponding to this multiple nucleation event differs from what would be encountered in thermally-activated nucleation from a single dislocation source, or from a limited number of sources in close proximity to each other. A similar argument could be made for the case of a dislocation propagating through a nanograin while pinned at adjacent GB facets [245, 23]: MD at high deformation rates may not capture the effect of weaker, secondary obstacles to dislocation glide, such as pinning obstacles in the GB network. These obstacles are interface-mediated, but do not participate in the dislocation nucleation event.

Since most mechanical testing and in-situ material characterization involve thermally-activated deformation processes, a knowledge of defect nucleation and propagation at temperatures on the order of room temperature and higher is clearly necessary. Thermally-assisted atomic rearrangement is an infrequent, probabilistic, and collaborative transition of a cluster of atoms between one or more stable configurations or "energy wells". Figure

90 shows a schematic of an infrequent transition between stable configurations W_1 and W_3 of an atomic system. Under overdriven MD, any transitions away from configuration W_1 tend to occur by a stress-induced lowering of the energy barrier to rearrangement, and the rearrangement itself occurs inertially. During this process, the transition $W_1 \rightarrow W_3$ may be observed; however, generally, it is also possible for the driving stress to completely skip the configuration W_3 and push the system into a different configuration, such as W_4 in Figure 90. Whether overdriven MD accurately reproduces the deformation kinematics operating at low deformation rates/higher temperatures for a particular microstructure would depend on the energy landscape of that microstructure with respect to perturbations in the configuration space. In the literature, overdriven MD correctly predicts the kinematics of deformation in some cases (see MD results [245, 274] confirmed via experiments [191, 42]). In other cases, for example, involving the nucleation of trailing partials from the GB [244], or competing cross-slip and glide mechanisms for a dislocation pinned at GB facets [21], the deformation kinematics could depend on the rate at which the externally-applied deformation is driven.

In essence, overdriven MD is likely to miss subtle structural transitions that occur infrequently and under low applied stresses. This argument is the basis behind atomistic methods that aim to explore the configuration space of an atomic system, and search for possible structural transitions. These methods can broadly be classified into two categories: (a) saddle-point finding methods (e.g., Nudged Elastic Band [84] and the Activation-Relaxation technique [151]) and (b) accelerated dynamics methods, such as temperature accelerated dynamics [196], hyperdynamics [254], and parallel replica dynamics [255]. Saddle-point finding methods compute the energy barrier associated with the transformation of an aggregate of atoms from an initial state and an (irreversibly) rearranged state, along a minimum energy path (MEP).

In the context of computing MEPs for dislocation nucleation from interfaces, it is difficult to account for complex atomic shuffling in the interface [245], or the correlated, but diverse, atomic rearrangements within interfacial structural units prior to nucleation [201].

This implies that atomic trajectories that correspond to the nucleation event cannot be easily generated *a priori*, e.g., by imposing a simple shear displacement in the slip direction, and must be obtained from dynamics. Unfortunately, as mentioned earlier in this Section, the propensity for simultaneous activation of several dislocation sources in MD simulations means that atomic trajectories correspond to multiple nucleation. MD timescales are too short to observe thermally-activated single nucleation events, and the current chapter proposes a strategy to modify the dynamics so as to increase the chance of encountering single-source dislocation nucleation within MD timescales.

7.1.2 Discrete Nosé-Hoover dynamics

Atomistic models at finite temperature may be simulated via isothermal MD techniques, where Newtonian (more precisely, Hamiltonian) dynamics is modified in order to control the system's temperature. In popular methods of temperature control such as Nosé–Hoover (NH) dynamics [155, 88] (discussed earlier in Chapter 3), the temperature adjustment is spatially uniform, irrespective of the local heterogeneities in the temperature field that can develop when the system undergoes stress-driven atomic rearrangement. In contrast, continuum models do incorporate temperature fields, but there remains a classic difference between atomistics and continuum in the perception of temperature: temperature is a phase average in the context of dynamics, but a scalar field in the context of a continuum. Among methods of selectively coarse-graining from the atomistic to the continuum regime, the Quasicontinuum method [108] bridges this gap to some extent by proposing generalized continua based on a variational principle, where non-equilibrium temperature 'fields' can exist. However, the description of defect structures still evades these methods, as does the problem of propagating the entire spectrum of phonon modes into a region of reduced degrees of freedom.

A fully dynamic, atomistic model of a material can benefit from a field-like description of temperature, even if it involves some added computational cost. In the following sections, first, a far-field heating/cooling effect that occurs as a consequence of NH dynamics is discussed. Thereafter, two modification have been suggested to the NH dynamical equations of

motion, hereafter called Type I and Type II discrete Nosè-Hoover (DNH) dynamics. Both modifications spatially tessellate a dynamic system into a grid of 'cells' where individual thermostats act over each cell. Each thermostat may be coupled to a separate heat bath, or to its adjacent thermostats in the grid, in which case, the only heat bath available is at the edges of the system and temperature adjustments occur through nearest neighbor cells only. Despite being completely dynamical (i.e., no thermodynamic coarse graining or renormalization), the proposed techniques allows for fine grained control of a temperature field within the system. The two variants of the DNH algorithm perform complementary functions: one accelerates the diffusion of local thermal disturbances away from their sources, while the other maintains heterogeneous temperature fields with the system, compensating for phonon heat conduction. In both cases, no immediate far-field heating or cooling effects are produced.

7.2 Theory

The development of molecular dynamics in the past few decades has produced several useful algorithms to sample characteristic phase-space distributions from chaotic dynamics. Among these, the Nosé-Hoover technique has been widely used to sample the canonical ensemble, where the system's number of particles (N), volume (V) and temperature (T) are prescribed, and these quantities are conserved over the course of the dynamics. The dynamical equations of motion, introduced earlier in Chapter 3, are recalled for context:

$$\dot{\mathbf{r}}_i = \frac{\mathbf{p}_i}{m_i}, \tag{50a}$$

$$\dot{\mathbf{p}}_i = \mathbf{F}_i - \frac{p_\eta}{Q}\mathbf{p}_i, \tag{50b}$$

$$\dot{\eta} = \frac{p_\eta}{Q}, \tag{50c}$$

$$\dot{p}_\eta = \sum_{i=1}^{N} \frac{\mathbf{p}_i^2}{m_i} - dNk_\mathrm{B}T \tag{50d}$$

Here, the mass, position and momentum of particle i is denoted by m_i, $\mathbf{r}_i$ and $\mathbf{p}_i$ respectively, and $\mathbf{F}_i$ denotes the force acting on the particle. The quantity η is known as the *thermostat*, and represents coupling between the microkinetic energy of the system

and a heat bath at thermodynamic temperature $k_{\mathrm{B}}T$. The quantity η provides a dynamic force to the particles depending on the instantaneous difference of the system's microkinetic energy from the ideal value $dNk_{\mathrm{B}}T/2$ (d is the dimensionality of the system, usually 3). The strength of coupling between the system and the bath is determined by the thermostat mass Q.

Dynamic thermostats such as NH are global in their effect; they raise (lower) the speeds of *all* particles in the system whenever heat is taken away from (added to) even a part of the system. This is evident in Equation 50b, where the 'drag' force $(p_\eta/Q)\mathbf{p}_i$ on particle i depends on a 'global' variable p_η. This produces an unrealistic "remote cooling" effect in regions away from internal heat sources such as mobile defect structures. When the system's boundary conditions evolve so as to dissipate stored elastic energy within the system, the NH thermostat adjustment reflects only the magnitude of heating and not its location or concentration, since only the global average measure of temperature is utilized in adjusting the system's temperature.

The coupling of the *entire* system to a single thermostat has a subtle, but interesting effect on heat transfer within the system, as shown in Figure 91. Under phonon heat conduction, when a thermal inhomogeneity develops, it is spread spatially around the "hot spot" in a way that reduces the curvature of the instantaneous temperature field, distributing heat in the surroundings. However, when a NH thermostat is used, the velocity of *every* particle in the system is scaled in response to this hot spot. Effectively, the NH thermostat lowers the distribution of atomic speeds for the entire system, even affecting regions where conductive smearing (that draws energy from the hot spot at the elastic wave speed) has not yet had the chance to take effect.

7.2.1 Discrete Nosé-Hoover Dynamics: Type I

We propose a modification to traditional NH dynamics, called discrete Nose–Hoover (DNH) dynamics, to avoid the effect of the remote heating/cooling caused by NH dynamics, and to permit spatially fine-grained control of temperature in MD simulations. In this approach, the simulation domain containing the system of interest is subdivided into a grid of cells,

each cell referenced by its grid coordinates (I, J) for a 2-D discretization (3-D discretization will obviously require another coordinate). Each cell contains N_{IJ} particles and has its own thermostat η_{IJ}. Taking K_{IJ} as twice the microkinetic energy of atoms in cell (I, J), we define a quantity *target microkinetic energy* $\langle K_{IJ} \rangle$, which is the average of the K values over cell (I, J) and all its neighboring cells. If cell (I, J) lies on the system boundary, each K values from the missing neighbors is replaced by a $dN_{IJ}k_{\mathrm{B}}T$ term. The deviation of K_{IJ} from $\langle K_{IJ} \rangle$ drives $p_{\eta_{IJ}}$. The Type I DNH equations are as follows:

$$\dot{\mathbf{r}}_i = \frac{\mathbf{p}_i}{m_i}, \tag{51a}$$

$$\dot{\mathbf{p}}_i = \mathbf{F}_i - \frac{p_{\eta_{IJ}}}{Q}\mathbf{p}_i, \tag{51b}$$

$$\dot{\eta_{IJ}} = \frac{p_{\eta_{IJ}}}{Q}, \tag{51c}$$

$$K_{IJ} = \sum_{i=1}^{N_{IJ}} \frac{\mathbf{p}_i^2}{m_i}, \tag{51d}$$

$$\langle K_{IJ} \rangle = \left(K_{IJ} + \sum_{n_\alpha} \sum_{i=1}^{N_\alpha} \frac{\mathbf{p}_i^2}{m_i} + \sum_{n_\beta} (dN_{IJ}k_{\mathrm{B}}T) \right) / (n_\alpha + n_\beta + 1), \tag{51e}$$

$$\dot{p}_{\eta_{IJ}} = K_{IJ} - \langle K_{IJ} \rangle \tag{51f}$$

where subscript α refers to neighbor cells and β refers to the neighbor cells absent (if cell (I, J) lies on the system's boundary) with n denoting the number of each. For example, a cell on the corner of the structure in Figure 92(b) has $n_\alpha = 3$ and $n_\beta = 5$.

To implement the DNH scheme, an atomistic ensemble is overlayed with a grid of cells, where each cell has its own temperature function as well as its own thermostat. The thermostats along with their respective domains of effect are shown in Figure 92 for 1-D and 2-D structures. The radial extent of directly interacting neighbor cells influences the non-locality of temperature adjustment (if necessary, with an appropriate weighting function).

For a 1-D arrangement, Equations 51e and 51f reduce to:

$$\langle K_I \rangle = (K_I + K_{I-1} + K_{I+1}) / 3, \tag{52a}$$

$$\dot{p}_{\eta_I} = (2K_I - K_{I-1} - K_{I+1})/3, \tag{52b}$$

indicating that the target kinetic energy is simply the arithmetic mean of all kinetic energies over the cell and its neighbors, and the terms on the right hand side of Equation 52b appear similar to those in the 1-D discrete solution of the heat equation, on account of the evolution law defined for p_{η_I}.

7.2.2 Discrete Nosé Hoover Dynamics: Type II

The current section introduces another variant of NH dynamics, which resembles the Type I dynamics (Equation set 51) in its use of a spatially discretized grid of thermostats, but differs from Type I dynamics in the following aspects:

- Each grid cell (I, J) is coupled to its own heat bath, at thermodynamic temperature $k_B T_{IJ}$.
- There is no coupling between adjacent thermostats.

Based on these differences, the equations of motion for Type II DNH dynamics are as follows:

$$\dot{\mathbf{r}}_i = \frac{\mathbf{p}_i}{m_i}, \tag{53a}$$

$$\dot{\mathbf{p}}_i = \mathbf{F}_i - \frac{p_{\eta_{IJ}}}{Q}\mathbf{p}_i, \tag{53b}$$

$$\dot{\eta_{IJ}} = \frac{p_{\eta_{IJ}}}{Q}, \tag{53c}$$

$$K_{IJ} = \sum_{i=1}^{N_{IJ}} \frac{\mathbf{p}_i^2}{m_i}, \tag{53d}$$

$$\dot{p}_{\eta_{IJ}} = K_{IJ} - dN_{IJ}k_{\mathrm{B}}T_{IJ} \tag{53e}$$

Notice that Equation sets 51 and 53 differ only in the definition of $\dot{p}_{\eta_{IJ}}$. Yet, this produces a major difference in the behavior of a dynamical system under Type I and Type II DNH dynamics:

- Since thermal variations across nearest neighbor cells drive the thermostat in the case of Type I dynamics, it causes rapid thermal homogenization across the system, at a rate that is determined by the thermostat mass(es) Q_{IJ}. While different choices of Q_{IJ} for different locations within the system permit some degree of control over the rates

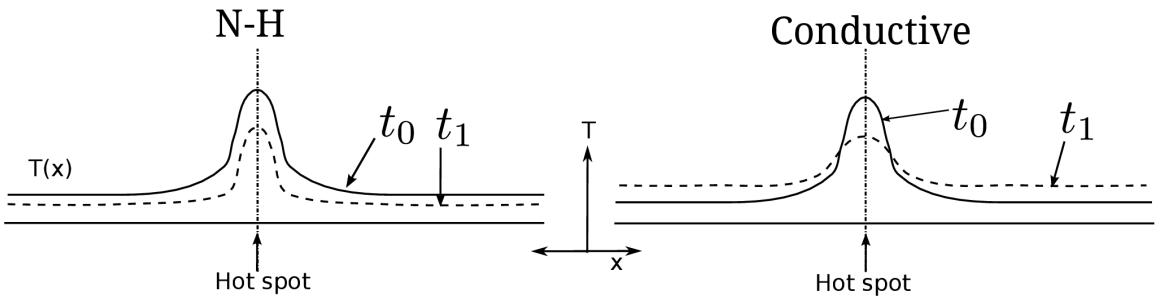

Figure 91: Evolution of the temperature field T(x) along spatial dimension (x) under Nosé-Hoover (NH) thermostatting vs conductive heat transfer. The hot spot represents the temperature inhomogeneity. Temperature profiles are shown at times t_0 and t_1 where $t_1 > t_0$.

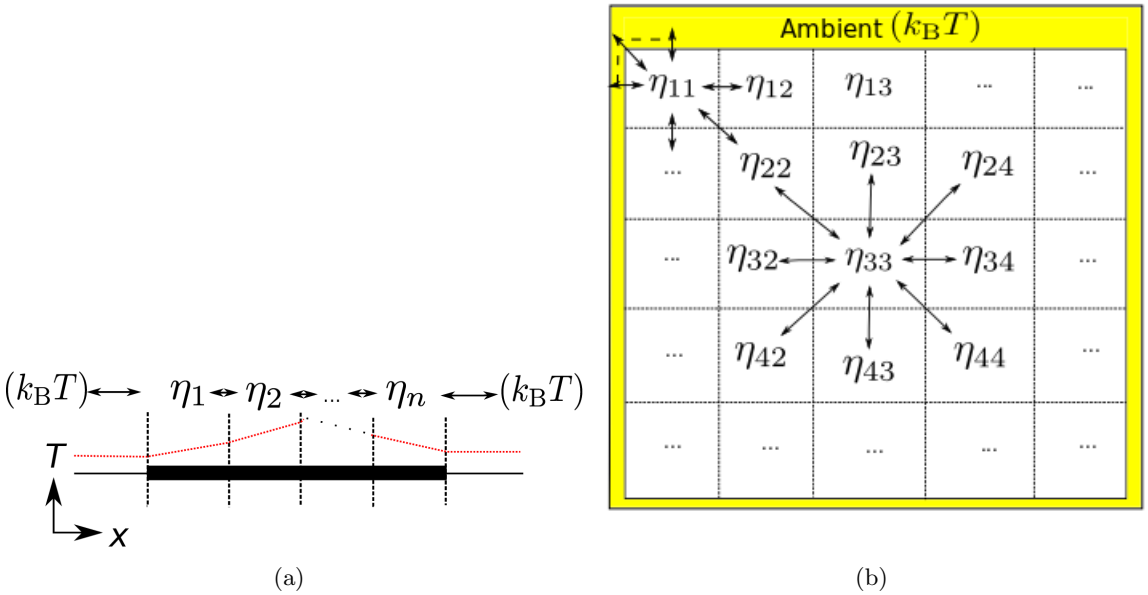

(a) (b)

Figure 92: (a) Arrangement and interdependence of thermostats (η_1 to η_n) in a 1-D ensemble (b) the same arrangement shown for grid thermostats η_{IJ} in a 2-D ensemble. Each cell interacts with 2 neighbors in (a) and with 8 neighbors in (b). Neighbors absent due to boundaries each contribute a multiple of $k_B T$ to Equation 51e.

of transfer of heat throughout the system, it is only a transient effect. Regardless of the choice of Q_{IJ}, Type I DNH dynamics provides a driving force for thermal homogenization, in addition to phonon-based heat transport.

- Type II dynamics decouples adjacent thermostats, and is equivalent to separate NH thermostats operating in different regions. Based on selection of cell temperatures T_{IJ}, different regions of the simulation domain can be driven to different temperatures using Type II DNH dynamics.

7.3 Results

7.3.1 Type I DNH dynamics

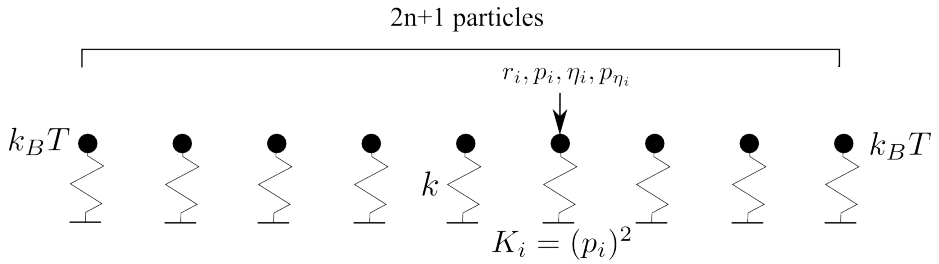

Figure 93: Array of 2n+1 harmonic oscillators used as a test case for Equation set 52. The intrinsic (spring) force F is given by $F_i = \dot{p}_i = -k\Delta r_i$ where p_i denotes particle momentum and Δr_i is the displacement from the mean position. Each particle is dynamically coupled only to its first nearest neighbors and at the system boundaries, also to the heat bath.

The Type I DNH equations of motion were tested for a very simple system, containing three harmonic oscillators. A general schematic for such a system (containing 2n+1 oscillators) is shown in Figure 93. Each oscillator was assigned its own thermostat and the system was exposed at its boundaries to an ambient temperature of $k_{\mathrm{B}}T$. After providing an initial velocity to the oscillators, the evolution of the velocity of oscillator 2 is shown in Figure 94 for several values of $k_{\mathrm{B}}T$. The integration was performed using the 4th order Runge-Kutta (RK) integrator as implemented in the *ode45* solver of MATLAB®(similar results were obtained by using a velocity-verlet intergrator [87] instead of the 4th-order RK). It is observed that an indirect interaction between oscillator 2 and the ambient heat bath adjusts the time averaged amplitude of oscillation (i.e., temperature) by either reinforcing the oscillations, or by damping them. In performing such an adjustment, all intermediate

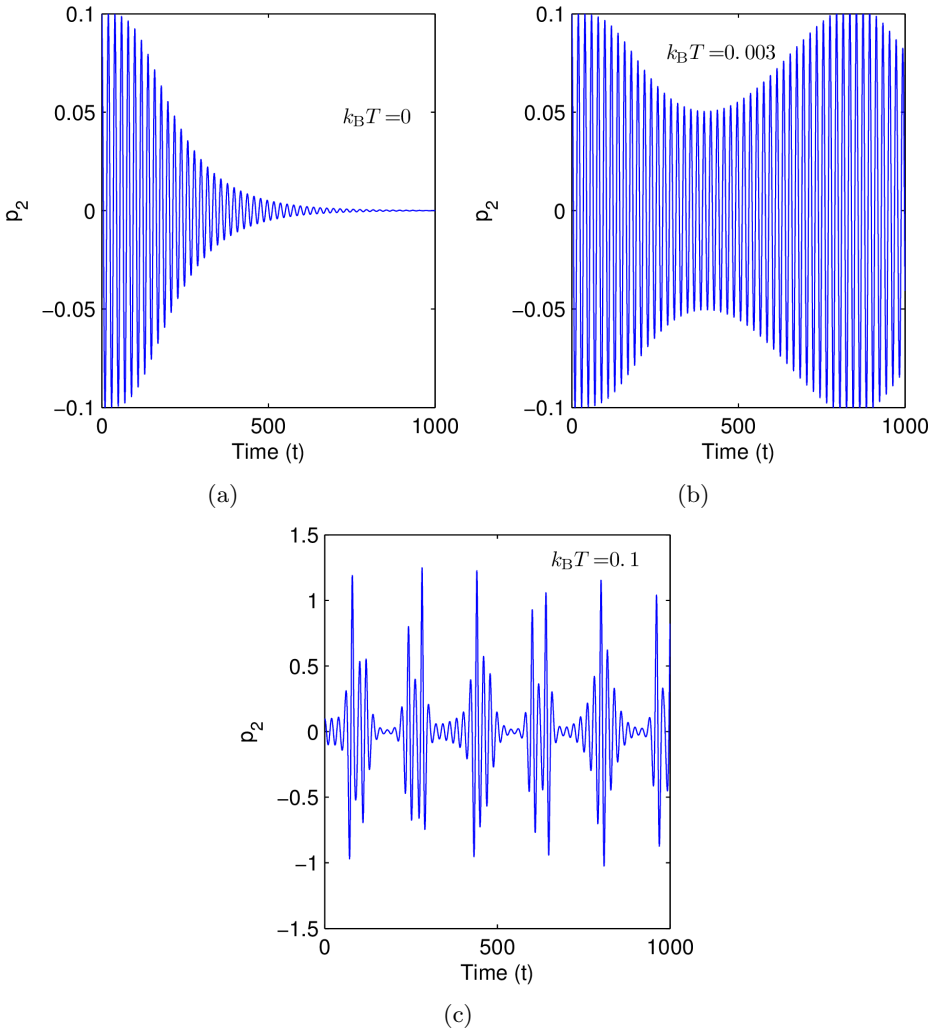

Figure 94: Evolution of particle momentum p_2 with time for different temperatures ($k_B T$) of the ambient heat bath. In (a), the initial sinusoidal oscillations of the particle gradually decay, since the ambient heat bath is at absolute zero. In (b), however, the heat bath (indirectly) influences the particle velocity maintaining a characteristic time averaged temperature while in (c), the heat bath causes vigorous heating. Note that since the particle is not at the system's boundary, it can interact with the heat bath only 'indirectly' through thermostats η_1 and η_3. To obtain this behavior, the following dimensionless parameters were used: particles per thermostat (N) = 1, particle mass (m) = 1, thermostat mass (Q) = 10.0, and particle force constant (k, assuming harmonic oscillator approximation) = 0.1. Each particle was imparted a momentum of 0.1 at $t = 0$.

cells leading to the system boundary are involved, and the process is completely dynamic with a characteristic time of propagation determined by the thermostat mass Q. Also, no aphysical heating or cooling away from regions of thermal concentration occurs.

In Figures 93 and 94, non-interacting harmonic oscillators have been chosen to clearly illustrate the effect of the thermostat on the particle velocities. For the case of coupled oscillators (i.e., the spring force acts between adjacent particles), similar results were observed, as is expected, although for such a small system, inter-particle energy exchange due to phonons is very rapid, and it is difficult to resolve the contribution of the thermostat to the thermal equilbration.

While further exploration of Type I DNH dynamics is desirable—especially regarding its ability to influence heat transfer over length scales over several hundered nanometers—an investigation in that direction does not fit within the objectives of the current work, and is being pursued as a separate project. However, in the context of current objectives, Type II DNH dynamics is much more promising from the standpoint of achieving fine-grained control over defect nucleation processes in MD simulations. Therefore, properties of Type II DNH dynamics are studied in greater detail in the following sections.

7.3.2 Type II DNH dynamics

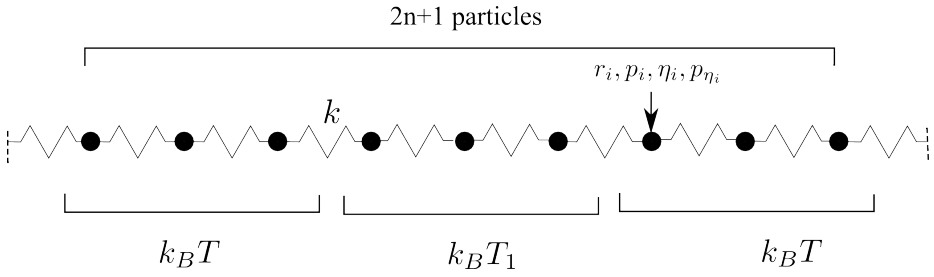

Figure 95: Array of 2n+1 coupled harmonic oscillators with periodic boundary conditions at the ends. In the temperature field prescribed, the particles are divided into three groups equilibrated to different temperatures.

For the system of non-coupled oscillators shown in Figure 93, Type II DNH dynamics is trivial and reduces to independent NH dynamics for each individual oscillator. A more interesting, as well as more realistic, scenario occurs when these linear oscillators are coupled, since vibrational energy exchange between adjacent oscillators is expected to compete with

the thermostats' attempts to drive each oscillator to a prescribed temperature. A general schematic for a coupled oscillator system is shown in Figure 95. Type II DNH dynamics was tested on a similar system with three oscillators (i.e., 2n+1=3), using separate thermostats η_1, η_2, η_3 and target temperatures $k_{\mathrm{B}}T$=1.0, 5.0 and 1.0 for oscillators 1, 2 and 3, respectively.

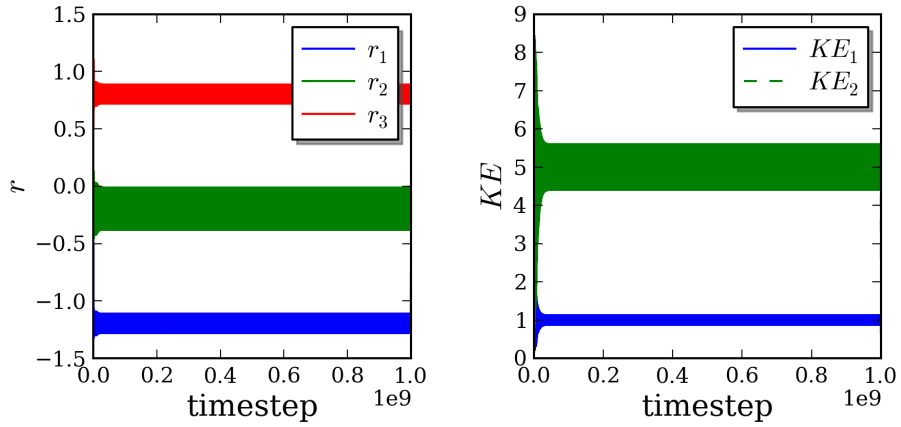

(a) (b)

Figure 96: Type II DNH dynamics used to equilibrate a system of three linear, one-dimensional coupled oscillators with periodic boundary conditions (similar to Figure 95, but with n=1). The oscillators r_1 and r_3 have been equilibrated to the same temperature, and r_2 has been equilibrated to a temperature five times that of r_1. (a) shows the oscillations of particle positions r_1,r_2, and r_3 over time. (b) shows the evolution of Kinetic energy of oscillators 1 and 2, clearly showing equilibrium values that differ by a factor of five.

Figure 96 shows the evolution of particle position (r) and kinetic energy KE under Type II DNH dynamics. In both (a) and (b), it can be observed that the long-timescale, stable dynamics of the system conforms to the prescribed temperature(s) for each particle. Simulations were repeated for different values of spring stiffness k and thermostat mass Q (same for all thermostats), spanning three orders of magnitude, and similar results were obtained (the timescales of equlibration were, of course, different).

MD under Type II DNH dynamics was also tested for a full-3D, single-crystal 'bar' of Cu metal, modeled using Mishin et al.'s embedded atom method potential [145]. The results are shown in Figure 97. The bar was divided into three regions, 1,2, and 3, with prescribed temperatures of 300 K, 500 K, and 300 K, respectively. After equilibration for 100 ps, a

snapshot of the bar with atoms colored according to instantaneous speed is shown in Figure 97(a), where a concentration of high-speed atoms in the center (region 2) of the simulation domain can be seen. Notably, since atoms near a boundary separating adjacent regions can vibrationally interact with other atoms across the boundary, the variation of atomic speeds across the region boundaries is quite diffuse. However, as can be seen in Figure 97(b), the total micro-kinetic energy of atoms contained within each thermostatted region is bounded for times beyond 10 ps, and equilibrates to the expected value.

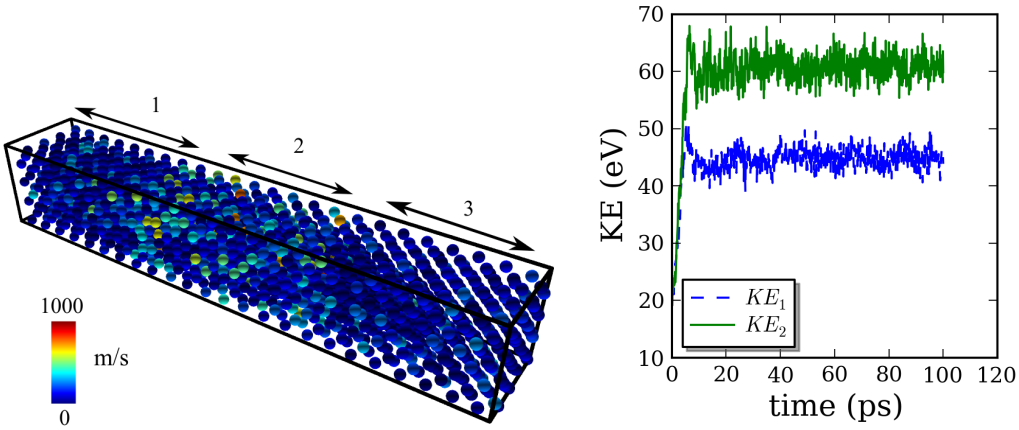

(a) (b)

Figure 97: (a) A snapshot of a bar of single crystal Cu, with three regions (named 1,2, and 3) heated to different temperatures (300 K, 500 K, and 300 K respectively) via Type II DNH dynamics. Atoms have been colored according to their instantaneous speeds. (b) Evolution of the total atomic microkinetic energy (K in Equation sets 51 and 53) in regions 1 and 2 over time. Notice that region 2 equilibrates to a higher temperature (i.e., K) despite unrestricted exchange of vibrational energy between regions 1 and 2.

7.3.3 Dislocation nucleation from interfaces under Type II DNH dynamics

The results so far demonstrate the efficacy of DNH dynamics at controlling the temperature as a spatially-discretized field in MD simulations. In Section 7.1.1, the high likelihood of simultaneous dislocation nucleation from multiple dislocation sources was cited as a limitation of MD simulations of material deformation. In that context, Type II DNH dynamics can presumably serve as a useful strategy to restrict the activation of dislocation sources to within a localized 'region' containing only a few sources. As a hypothesis, it can be expected

that dislocation nucleation from an array of sources can be better controlled via a careful choice of the spatially-discretized temperature field and the rate of the externally-applied deformation. To test this hypothesis, uniaxial deformation of a Cu $\Sigma 9\{221\}$ symmetric tilt interface was performed, in a direction normal to the interface plane, under Type II DNH dynamics. The dislocation nucleation behavior is shown in Figure 98, where it is compared to deformation under traditional isothermal MD at 10 K, using a single, global thermostat [230]. For the DNH dynamics, the bicrystal containing the interface was divided into three regions of equal width along the interface period direction, with peripheral regions maintained at 10 K and the center region heated to 800 K. In Figure 98(b), nucleation of leading partial dislocations from multiple sources along the interface period can be clearly seen. In contrast, under DNH dynamics (Figure 98(a)), nucleation preferentially occurs near the edge of the 'hot' center region, with secondary nucleation events occurring in close proximity, soon after the primary nucleation event. These results are encouraging, but come with their own complications. On the upside, DNH dynamics does indeed lead to a localization of the dislocation nucleation event. However, it does not ensure isolated nucleation at the deformation rate imposed ($10^9 s^{-1}$). There can be several reasons for this behavior. First, the rate of deformation is still too high for individual dislocations to nucleate, such that even at 800 K, thermal fluctuations that lead to an isolated event are never encountered. Second, it is not always necessary that isolated dislocation nucleation should be energetically favorable, as compared to simultaneous nucleation at a group of adjacent nucleation sites, especially in cases where individual nucleation sites are closely spaced. This could be a factor in Figure 98, given the small spacing of E structural units (the dislocation nucleation sites) in the $\Sigma 9\{221\}$ interface.

7.4 Discussion

Two potential applications of Type I DNH dynamics can be envisioned. First, Type I DNH dynamics appears better suited for performing isothermal dynamics in systems that are expansive (several hundred nm) along one or more dimensions. In this case, parameters of the dynamics (i.e., thermostat masses, grid-spacing) would have to be chosen so as to

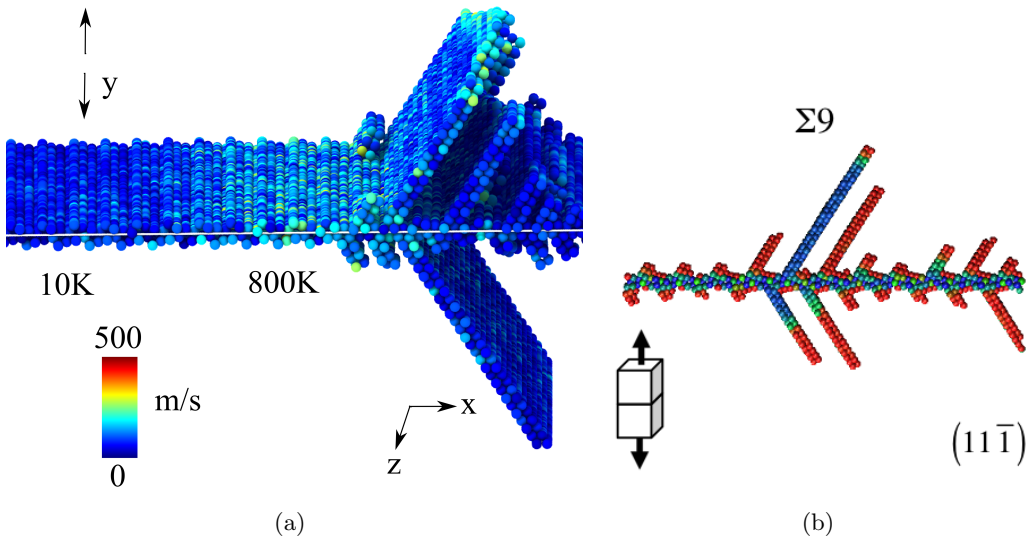

Figure 98: A comparison of dislocation nucleation under uniaxial tension from the Cu $\Sigma 9\{221\}$ interface, under two different dynamical equations of motion. In (a) Type II DNH dynamics has been used with three regions of equal width along the x directions. The temperatures are 10 K in the peripheral regions and 800 K in the middle. Atoms have been colored according to instantaneous speed, and only non-face centered cubic atoms have been shown. In (b), dislocation nucleation behavior is shown for the same interface, deformed along the same loading direction, under pure NPT dynamics at 10 K (image taken from [230]). In contrast with (b), in (a), the dislocation nucleation is clearly localized and the first nucleation event initiates within the high-temperature (800 K) region. However, at the deformation rate applied ($\approx 10^9 \mathrm{s}^{-1}$ in both (a) and (b)), *isolated* dislocation nucleation could not be observed.

be minimally intrusive to the 'natural' dynamics. As an example, an MD simulation with thermostats active only near the edges of the simulation domain boundary (these are the thermostats η_{11}, η_{12}, $\eta_{13}\ldots$ in Figure 92(b)) can be implemented. Such an arrangement would maintain the ensemble temperature over extended time-scales, but would not interfere with the dynamics in the interior. However, besides physically realistic parameterizations of the Type I DNH dynamics, physically unrealistic parameterizations can be useful too. In solids, inertial disturbances, e.g., the nucleation of dislocations, voids, or incremental growth of cracks may produce heating that is both localized and transient. While this heat would be carried outwards from the hot spot via phonons, more aggressive and rapid thermal equilibration may be achieved by using Type I DNH dynamics with a responsive (i.e., low-mass) thermostat. The difference in microkinetic energy between adjacent DNH cells, in that case, would serve as an additional driving force for thermal equilibration. This kind of control might be desirable, e.g., to suppress 'secondary' rearrangement events from getting activated from large-amplitude atomic vibrations that persists in the wake of primary events.

Type II DNH dynamics, on the other hand, can be used to achieve the opposite of thermal homogenization: i.e., to maintain different regions at different temperatures within the same simulation domain. In this context, one must concede that a thermostatting strategy that actively prevents thermal equilibration is clearly aphysical. However, by maintaining *different atomic vibration amplitudes in different regions*, the Type II DNH dynamics effectively increases the probability of activating dislocation sources in the 'hot' regions, while simultaneously suppressing sources in the 'cold' regions. By carefully-delimited regions such that hot regions contain a few dislocation sources at most, Type II DNH dynamics can be used the substantially increase the chance that isolated dislocation nucleation is observed within MD timescales. The atomic trajectories corresponding to the isolated nucleation event can then be interpolated over the simulation time and fed as input to various saddle-point finding methods.

The DNH scheme has an added computational cost depending on the resolution of the thermostat grid, when compared to NH dynamics. However, this cost for ensembles of

multi-million particles is still small compared to the cost of the dynamics itself, as long as each thermostat is assigned a reasonably large number of particles in compliance with the length scales of the dissipative process being studied. A grid resolution that allows for interaction between defects but does not partition the defect structures (e.g., dislocation loops) themselves is likely the most appropriate. For very fine grids, of spacings on the order of the lattice parameter, the NH remote heating/cooling effect is completely removed.

In its current formulation, DNH dynamics is essentially a modification of dynamics in the canonical (NVT) ensemble. Extending this dynamics to the isothermal-isobaric (NPT) ensemble is, as yet, difficult. This is because the NPT equations of motion [133] couple the barostat dynamics with the oscillations of a 'global' thermostat. Since no such thermostat exists in the DNH scheme, it is unclear how an adaptively dilating/warping simulation domain could be consistent with DNH dynamics.

In MD literature [133, 238], it is often emphasized that the dynamics of particles in a system should sample the appropriate phase space distributions expected from the thermodynamic constraints. Indeed, this requirement is necessary in fluid phases where statistical averages of intensive thermodynamic properties or bulk particle correlation functions at equilibrium are important and so sampling the phase space correctly is vital. However, while studying non-equilibrium processes such at elasto-plasticity and/or fracture at finite temperature, the evolution of the phase space is quite rapid and depends instead on the extremes of the particle velocity distribution (at dislocations, flow localization regions and crack tips). The idea of an equilibrium phase space distribution therefore holds little meaning for these processes.

The behavior of both Type I and Type II DNH dynamics can be expected to depend on a delicate interplay of the material's elastic properties and the masses of the thermostats chosen, and further work is warranted in this area. Most importantly, a difference in the relative timescales of propagation of elastic disturbances and thermostat oscillations could lead to different regimes of energy exchange that will determine the 'efficacy' of temperature control. For example, in Type II DNH dynamics, if the inverse of the thermostat mass is small enough, the thermostat will not be able to compensate for the loss of vibrational

energy from the 'hot' regions.

7.5 Computational details

The following codes have been developed in order to create a working implementation of Type I and Type II DNH dynamics for general atomic/molecular systems.

1. A stand-alone C++ program to simulate variants of DNH dynamics using harmonic oscillators in a single dimension.

2. A *compute* class *ke/dnh*, implemented within the MD simulation package LAMMPS [111]. This code separately accumulate the kinetic energy of atoms in different regions of a simulation domain.

3. A *fix* class *dnh* within LAMMPS, which implements Equation sets 51 and 53. The fix class makes minimum modification to the already existing *nh* class which is a part of the standard LAMMPS package.

7.6 Summary

Nosé-Hoover (NH) dynamics is a popular method to simulate isothermal molecular dynamics. In this chapter, two variants of NH equations of motion, called Type I and Type II Discrete Nosé-Hoover (DNH) dynamics are proposed, with the purpose of explicitly controlling the temperature field at different locations within the simulation domain. Potential applications of DNH dynamics could include fine-grained control of the temperature field with tunable thermal exchange between adjacent regions (Type I dynamics), or localized heating at defect nucleation sites in order to induce selective nucleation/propagation of isolated defect structures. The latter could provide a method to generate atomic trajectories to be used as input to optimization algorithms (e.g., nudged elastic band) that compute the energy barrier(s) associated with characteristic deformation mechanisms.

CHAPTER VIII

CONCLUSIONS AND RECOMMENDATIONS

8.1 Contributions

The present research has contributed towards exploring the interface-mediated yield and flow behavior of nanocrystalline metals under combined stress states, and developing methods that could be applied to atomistic simulations to better understand kinetic and kinematic aspects of various deformation unit processes. Simulation frameworks have been developed to enforce simultaneous control of several stress and strain components, thereby providing the capability to simulate material deformation over a wide range of proportional and non-proportional multiaxial deformation paths. In nanostructured materials, such as those with a multilayered, nanocrystalline or nanotwinned microstructure, atomistic simulation can reach length scales close to representative volumes (albeit with time-scale restrictions that are inherent to MD). In these microstructures, complex deformations can be simulated, and the effect of the deformation path the resulting microstructure evolution can be precisely resolved.

Using the thermostat compensation rate $\dot{\eta}$ introduced in Chapter 3, inelastic yield under the combined effect of stress-driven interfacial and intra-granular deformation processes has been resolved for a Cu nanocrystal. In other microstructures/material systems, the evolution of η and its time derivatives can be employed as metric of ensemble-scale criticality, especially in cases where multiple pathways of elastic energy release are present (dislocations, cracks, GB sliding etc.), or where localized 'critical' events exhibit a broad distribution of threshold stresses for activation (e.g., shear shuffling of atoms at the grain boundaries). A metric of criticality derived from atomic dynamics, such as the thermostat η, is less ambiguous than empirical metrics that rely simply on the stress-strain behavior, with no consideration of microstructure evolution. Further, in material systems or microstructures where initial yield is expected to be significantly affected by non-deviatoric

stress components, empirical metrics would require knowledge of the deformation kinetics *a priori*, while no such requirement exists for η.

Schemes for general multiaxial deformation (introduced in Section 2.7.2) have been employed to study shear deformation under an imposed hydrostatic stress in bicrystals (Chapter 5) and nanocrystals (Chapters 4 and 6). The results suggest that the effect of hydrostatic stress on shear deformation is quite significant in nanocrystals and bicrystals. In nanocrystals, such a pressure-effect appears to arise predominantly from pressure-induced changes in elastic stiffness under shear deformation. In bicrystal interfaces, however, shear-stiffening alone cannot explain the observed pressure effect, especially in interfaces that exhibit a decrease in shear strength decreases with imposed compressive pressure ($\Sigma 9\{221\}$ and $\Sigma 5\{210\}$). In microstructures containing an enhanced population of the latter, this anomalous pressure dependence can possibly manifest at the bulk scale, although further work is needed in this direction.

Several aspects of the mechanics of NC metals has been investigated for the first time in this work. First, the direction of the inelastic flow with respect to the deviatoric stress has been assessed for the case of biaxial deformation in nanocrystalline Cu (Section 4.3.2). Second, the role of pre-existing internal atomic stresses towards activating atomic rearrangement in interfacial shear transformation zones has been investigated. Third, pressure-sensitive aspects of shear-driven sliding/migration of Cu interfaces have been explored.

Activation parameters for inelastic deformation in NC Cu have been computed from MD simulations in this work. In particular, these computations have explored—for the first time—the combined effects of temperature, grain size and hydrostatic/normal stress components on the kinetics of elasto-plastic shear deformation. Besides computing activation parameters based on the deformation response of the entire microstructure, modifications to existing MD techniques have been suggested that could permit direct computation of activation parameters for dislocation nucleation from interfacial sources.

Lastly, algorithms have been developed to compute volume-averaged stresses in grain interiors and grain boundaries. These algorithms have been used in conjunction with various existing metrics of interfacial excess volume and non-local continuum metrics of atomic-scale

deformation to resolve the evolution of stress, free volume, and heterogeneous deformation fields in NC microstructures.

Results obtained from the current study— as well as from future studies that utilize the methods developed herein—can potentially serve as guidelines for the design and parameterization of constitutive theories of elasto-plasticity in NC metals.

8.2 Limitations of the present work

The present work inherits the length-scale and time-scale limitations of MD. Given the small characteristic length scales (within a few hundred nanometers) in nanostructured materials, the length-scale restrictions are somewhat less severe; even microstructures approaching representative volumes are sometimes amenable to direct computation. Still, the cost of massively parallel simulations introduces a trade-off between studying the effects of material scaling, and exploring various complex deformation histories. For this reason, atomistic simulations in this work have been limited to grain sizes below 20 nm.

The short time-scales accessible to MD result in effective strain rates routinely in excess of 10^7 s^{-1}. These high rates lead to the suppression of thermally-activated atomic rearrangement pathways that require wait times that are several orders of magnitude longer than nanoseconds. Therefore, in MD simulations, stresses in the simulated material reach very high levels and atomic rearrangement occurs inertially. Depending on rate sensitivity of the material being simulated, the absolute values of yield/nucleation stresses reported in MD simulations are expected to be significantly higher than those obtained at quasi-static experimental strain rates. This difference is clearly an impediment to establishing direct equivalences between the results of experiments and simulations (e.g., in stress-strain curves).

However, despite the high deformation rates, MD can still be expected to predict accurate *deformation kinematics*, provided the deformation mechanisms do not change when the strain rate is reduced to experimental rates of $10^{-5} - 10^{-1}$ s^{-1} (at these rates, thermal assistance and longer timescales for atomic rearrangement become available). In interface-mediated inelasticity, the most likely change in deformation mechanism with decreasing

deformation rate is the onset of diffusive processes, e.g., Coble creep, which is characterized by a small activation volume of $\approx 1b^3$. If creep processes are significant at room temperature and experimental strain rates, MD simulations at high strain-rates might fail to capture them.

In the present research, however, it does not appear that creep processes are expected to be significant, since activation volumes (3-8 b^3) and activation energies ($0.2 - 0.3$ eV) obtained from our simulations are similar to those obtained via experiments [41, 260, 73] in NC metals of similar grain size. Further, the aforementioned studies rule out creep as a prevalent deformation mechanism in their respective experiments and attribute the observed behavior to interfacial shear shuffling [73] and dislocation activity [260], which is similar to what is observed in the MD simulations performed in this work.

In general, care should be taken while extrapolating MD-based studies to predict deformation kinematics at experimental strain rates. To that end, support from experimental evidence, theoretical arguments or accelerated dynamics (e.g., [196, 254]) is preferable. For example, experiments in [260] and [73] used higher melting-point materials than Cu: NC Ni and $Pd_{90}Au_{10}$ (an isomorphous system), respectively. Room-temperature creep in these materials is not very likely. However, for lower-melting fcc metals, such as Al, contribution of creep processes could be more significant at room temperature.

8.3 Recommendations for future work

- At present, deformation mediated by grain boundary *motion* is not very well understood, especially with regards to general grain boundaries of a mixed tilt-twist character. Since mechanical properties of nanomaterials are significantly influenced by the static and dynamic aspects of the interface network, contributions from interface motion should be taken into account. In particular, the results from the current study motivate future efforts directed towards obtaining a kinetic description of stress-driven interface motion, and possibly incorporating influences of interface structure, interfacial non-equilibrium character, and impurity segregation.

- An important aspect of deformation mechanisms in nanocrystals is their stochastic

nature. At the scale of nanograins, stochasticity arises from (a) structural variations in the interfaces, which influences their sliding/migration kinetics, and (b) variations in the dislocation nucleation/propagation kinetics due to an interplay of localized stress concentration, dislocation source geometry, and the energy landscape of subsequent interfacial pinning sites once a dislocation loop has nucleated. One way to estimate the statistical variation is by simulating the deformation of representative volumes of nanocrystals, containing several hundred grains, or, alternatively, performing a careful study of dislocation nucleation from several structurally plausible—but statistically diverse—source geometries, containing both grain boundaries and triple junctions.

- A more accurate estimate of the energy barrier(s) and transition pathway(s) associated with characteristic inelastic rearrangement events may be obtained via saddle point-finding methods, such as Nudged Elastic Band (NEB). NEB-based computations are expected to be particularly useful in the context of shear deformation of bicrystal interfaces since they can potentially reveal the atomistic origins of the interesting pressure-effects reported in the present work.

- A more thorough exploration of the six-component stress space in the context of its effect on atomic rearrangement would be valuable. While the present work has briefly touched upon the role of normal stresses on the kinetics of interface-mediated deformation processes, such a dependence needs to be established more accurately, and preferably in terms of the coupling of non-devatoric stress components with specific inter-granular and interfacial deformation unit processes.

- Given the primary focus of this work, i.e., developing methods to explore and interpret deformation behavior under the influence of complex combined stress states, the mechanical behavior of NC microstructure of fcc metals other than Cu have not been studied in this thesis. That said, simulation methodologies identical to the current work could be used to investigate the behavior of those materials. Such studies are outside the scope of the present work, but are nevertheless important, since the nature of the interatomic interaction influences not only bulk observables, but also the

mechanisms via which inelastic deformation occurs.

APPENDIX A

SINGLE CRYSTAL SHEAR MODULI

The problem concerns computing the elastic modulus of a cubic crystal for shear along a crystallographic direction $\mathbf{s}$, in the plane normal to the direction $\mathbf{n}$, where both $\mathbf{s}$ and $\mathbf{n}$ lie in the plane normal to direction $\mathbf{c}$, such that unit vectors along $\mathbf{s}, \mathbf{n}$, and $\mathbf{c}$ form a right-handed orthonormal triad. We consider a 'reference' fcc single crystal with unit cell basis vectors aligned along the cartesian directions and a shear configuration defined as follows: $\mathbf{s}$ = [100] (x-axis), $\mathbf{n}$ = [010] (y-axis), and $\mathbf{c}$ = [001] (z-axis). In this configuration, the shear modulus is C_{1212} (C_{44} in Voight notation). For a single crystal that has been rotated to align with one half of the bicrystal, following Section 5.2.2, $\mathbf{s}$ is the interface period direction, $\mathbf{n}$ is the interface plane normal, and $\mathbf{c}$ is the tilt axis. For instance, in the case of the $\Sigma 9\{221\}$ interface shown in Figure 45(a), $\mathbf{s} = [11\bar{4}]$, $\mathbf{n} = [221]$ and $\mathbf{n} = [1\bar{1}0]$. The vector triad $(\mathbf{s}, \mathbf{n}, \mathbf{c})$ can be transformed from the reference to the rotated configuration via an orthogonal matrix $\mathbf{R}$. To compute the elastic stiffness for a given combination of $\mathbf{s}, \mathbf{n}$, and $\mathbf{c}$, first, the 4th-rank elasticity matrix C_{ijkl} is constructed in the reference configuration using values of single crystal elastic constants c_{11}, c_{12}, c_{44} and converting them to the full four-index notation. The stiffness tensor in the rotated coordinate system is given by $C'_{ijkl} = R_{im}R_{jn}R_{ko}R_{lp}C_{mnop}$, and the shear modulus in these coordinates is C'_{1212} . Due to the inversion symmetry of the fcc lattice, the elastic properties of the bicrystal containing a symmetric interface can be compared to those of a single crystal. For Cu, the values of three independent elastic constants c_{11}, c_{12}, and c_{44} were taken from [145].

APPENDIX B

ATOMIC MEASURES OF STRESS

While computing stress in atomistic simulations, the role of atomic velocities, i.e., the kinetic term in the atomic stress, is often debated. In the literature, two papers present directly contrasting viewpoints: the work by Zhou [288], which recommends neglecting the kinetic term, and the one by Subramaniyan and Sun [207], where the authors demonstrate that the kinetic part of the stress is essential to compensate for the imbalance in interatomic forces produced as a result of thermal expansion[1] and thus cannot be neglected.

To estimate the extent to which the kinetic term of the virial stress influence the stress measures used in this work, we consider the deformation of Grain 3 in the $g = 10$ nm microstructure. The microstructure was deformed under shear at a constant temperature of 500 K with no imposed hydrostatic pressure. The stress over Grain 3 was computed using three approaches: (i) considering only the interatomic forces, i.e. the virial term, (ii) considering only the atomic velocities, i.e., the kinetic term and (iii) using both the virial and the kinetic terms. The results are shown in Figure 99, using labels 'force','kinetic', and 'full' for aforementioned approaches (i),(ii),and (iii), respectively. From plot (a), the close overlap of the 'full' and 'forces' curves shows that the effect of the kinetic term on the computed stress $\bar{\sigma}$ is negligible. However, the values of the stress computed using only the kinetic term (approach (ii)) in Figure 99(a) are surprisingly low, when considered in view of Subramaniyan and Sun's results [207] that demonstrate a significant contribution of the kinetic term to the atomic stress. This apparent discrepancy is resolved once we realize that $\bar{\sigma}$ in Figure 99 is an invariant of the stress deviator. The contribution of the kinetic term to the total stress, on the other hand, is almost purely hydrostatic, since it originates

[1] This imbalance is a consequence of the fact that most of the commonly-used interatomic potentials are not temperature-dependent. They don't explicitly modify the equilibrium interatomic spacing with temperature. In equilibrium at zero external pressure and finite temperature, therefore, the instantaneous force on each atom is not zero, even though the external stress is clearly zero.

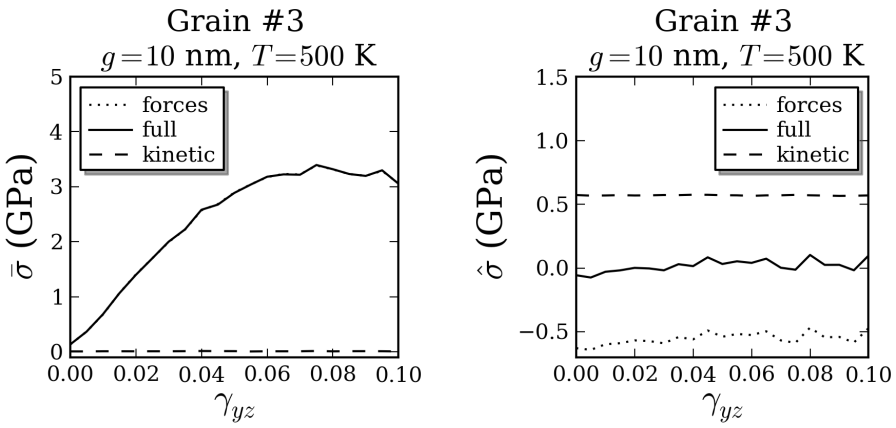

(a) (b)

Figure 99: A comparison of different contributions to the volume-averaged atomic stress. (a) shows the evolution of the von Mises stress ($\bar{\sigma}$) in the interior of grain 3 in the $g = 10$ nm structure during pure shear deformation at 500 K. The 'full' stress includes contribution from both the interatomic forces as well as the atomic velocities. These contributions are separately plotted under the labels 'forces' and 'kinetic', respectively. In (b), the evolution of the hydrostatic stress component $\hat{\sigma}$ has been shown.

from the thermal fluctuation of atoms. Figure 99(b) shows that the hydrostatic component of the 'kinetic' stress is indeed comparable to stress computed based entirely on 'forces', in our simulations. Here, the 'kinetic' and 'forces' contributions are equal in magnitude ($\approx$ 0.6 GPa) but opposite in sign. Clearly, the kinetic contribution to the hydrostatic stress is not negligible.

We conclude that neglecting the kinetic part of the atomic stress in our analysis does not affect the results. However, in general, the kinetic term in the expression of atomic stress is non-negligible at finite temperature, and contributes to the hydrostatic stress. For this reason, the 'full' stress computation has been used for the purpose of ensemble-level stress control (barostatting) throughout this thesis.

REFERENCES

[1] Adams, J., Wolfer, W., and Foiles, S., "Elastic properties of grain boundaries in copper and their relationship to bulk elastic constants," *Physical Review B*, vol. 40, no. 14, pp. 9479–9484, 1989.

[2] Alexander, K. C. and Schuh, C. a., "Exploring grain boundary energy landscapes with the activation-relaxation technique," *Scripta Materialia*, vol. 68, pp. 937–940, June 2013.

[3] Allen, M. P. and Tildesley, D. J., "Computer simulation of liquids," 1987.

[4] Ames, M., Grewer, M., Braun, C., and Birringer, R., "Nanocrystalline metals go ductile under shear deformation," *Materials Science & Engineering A*, vol. 546, pp. 248–257, 2012.

[5] Ames, M., Markmann, J., and Birringer, R., "Mechanical testing via dominant shear deformation of small-sized specimen," *Materials Science and Engineering: A*, vol. 528, no. 1, pp. 526–532, 2010.

[6] Andersen, H. C., "Molecular dynamics simulations at constant pressure and/or temperature," *The Journal of Chemical Physics*, vol. 72, p. 2384, 1980.

[7] Argon, A. S., *Strengthening mechanisms in crystal plasticity*. No. 4, Oxford University Press Oxford, 2008.

[8] Argon, A. and Yip, S., "The strongest size," *Philosophical magazine letters*, vol. 86, no. 11, pp. 713–720, 2006.

[9] Asaro, R. J., "Crystal plasticity," *Journal of applied mechanics*, vol. 50, no. 4b, pp. 921–934, 1983.

[10] Asaro, R. J. and Rice, J., "Strain localization in ductile single crystals," *Journal of the Mechanics and Physics of Solids*, vol. 25, no. 5, pp. 309–338, 1977.

[11] Asaro, R. J. and Suresh, S., "Mechanistic models for the activation volume and rate sensitivity in metals with nanocrystalline grains and nano-scale twins," *Acta Materialia*, vol. 53, no. 12, pp. 3369–3382, 2005.

[12] Ashby, M., *Materials Selection in Mechanical Design*. Elsevier Science, 2004.

[13] Baghbanan, M., Erb, U., and Palumbo, G., "Towards the application of nanocrystalline metals in MEMS," *Physica status solidi (a)*, vol. 203, no. 6, pp. 1259–1264, 2006.

[14] Barai, P. and Weng, G. J., "Mechanics of very fine-grained nanocrystalline materials with contributions from grain interior, GB zone, and grain-boundary sliding," *International Journal of Plasticity*, vol. 25, pp. 2410–2434, Dec. 2009.

[15] Baskes, M., "Modified embedded-atom potentials for cubic materials and impurities," *Physical Review B*, vol. 46, no. 5, p. 2727, 1992.

[16] Baskes, M. and Johnson, R., "Modified embedded atom potentials for hcp metals," *Modelling and Simulation in Materials Science and Engineering*, vol. 2, no. 1, p. 147, 1994.

[17] Baskes, M., Nelson, J., and Wright, A., "Semi-empirical modified embedded-atom potentials for silicon and germanium," *Physical Review B*, vol. 40, no. 9, p. 6085, 1989.

[18] Berendsen, H. J. C., Postma, J. P. M., van Gunsteren, W. F., DiNola, A., and Haak, J. R., "Molecular dynamics with coupling to an external bath," *The Journal of Chemical Physics*, vol. 81, p. 3684, 1984.

[19] Bitzek, E., Derlet, P., Anderson, P., and Van Swygenhoven, H., "The stress–strain response of nanocrystalline metals: a statistical analysis of atomistic simulations," *Acta Materialia*, vol. 56, no. 17, pp. 4846–4857, 2008.

[20] Boyer, R. D., Li, J., Ogata, S., and Yip, S., "Analysis of shear deformations in Al and Cu: empirical potentials versus density functional theory," *Modelling and Simulation in Materials Science and Engineering*, vol. 12, no. 5, p. 1017, 2004.

[21] Brandl, C., Derlet, P. M., and Van Swygenhoven, H., "Strain rates in molecular dynamics simulations of nanocrystalline metals," *Philosophical Magazine*, vol. 89, no. 34, p. 3465, 2009.

[22] Brandl, C., Derlet, P., and Van Swygenhoven, H., "Dislocation mediated plasticity in nanocrystalline Al: the strongest size," *Modelling and Simulation in Materials Science and Engineering*, vol. 19, no. 7, p. 074005, 2011.

[23] Brandl, C., Tiwari, S., Derlet, P. M., and Van Swygenhoven, H., "Athermal critical stresses for dislocation propagation in nanocrystalline aluminium," *Philosophical Magazine*, vol. 90, no. 7, p. 977, 2010.

[24] Brandstetter, S., Budrovic, Z., Van Petegem, S., Schmitt, B., Stergar, E., Derlet, P. M., and Van Swygenhoven, H., "Temperature-dependent residual broadening of x-ray diffraction spectra in nanocrystalline plasticity," *Applied Physics Letters*, vol. 87, no. 23, p. 231910, 2005.

[25] Brandstetter, S., Van Swygenhoven, H., Van Petegem, S., Schmitt, B., Maass, R., and Derlet, P. M., "From Micro- to Macroplasticity," *Advanced Materials*, vol. 18, no. 12, pp. 1545–1548, 2006.

[26] Budrovic, Z., Van Swygenhoven, H., Derlet, P. M., Van Petegem, S., and Schmitt, B., "Plastic deformation with reversible peak broadening in nanocrystalline nickel," *Science*, vol. 304, no. 5668, pp. 273–276, 2004.

[27] Buehler, M. J., *Atomistic modeling of materials failure*. Springer, 2008.

[28] Buehler, M. J., Hartmaier, A., Gao, H., Duchaineau, M., and Abraham, F. F., "Atomic plasticity: description and analysis of a one-billion atom simulation of

ductile materials failure," *Computer Methods In Applied Mechanics And Engineering*, vol. 193, no. 48, pp. 5257–5282, 2004.

[29] Buehler, M., Hartmaier, A., and Gao, H., "Hierarchical multi-scale modelling of plasticity of submicron thin metal films," *Modelling And Simulation In Materials Science And Engineering*, vol. 12, p. S391, 2004.

[30] Bulatov, V. and Cai, W., *Computer simulations of dislocations*, vol. 3. Oxford University Press, 2006.

[31] Bulatov, V., Richmond, O., and Glazov, M., "An atomistic dislocation mechanism of pressure-dependent plastic flow in aluminum," *Acta Materialia*, vol. 47, pp. 3507–3514, Sept. 1999.

[32] Cahn, J. W., Mishin, Y., and Suzuki, a., "Duality of dislocation content of grain boundaries," *Philosophical Magazine*, vol. 86, pp. 3965–3980, Sept. 2006.

[33] Cahn, J. W., Mishin, Y., and Suzuki, A., "Coupling grain boundary motion to shear deformation," *Acta Materialia*, vol. 54, pp. 4953–4975, Nov. 2006.

[34] Caillard, D., Mompiou, F., and Legros, M., "Grain-boundary shear-migration coupling. II. Geometrical model for general boundaries," *Acta Materialia*, vol. 57, pp. 2390–2402, May 2009.

[35] Capolungo, L., Cherkaoui, M., and Qu, J., "On the elastic-viscoplastic behavior of nanocrystalline materials," *International Journal of Plasticity*, vol. 23, pp. 561–591, Apr. 2007.

[36] Capolungo, L., Spearot, D. E., Cherkaoui, M., McDowell, D. L., Qu, J., and Jacob, K. I., "Dislocation nucleation from bicrystal interfaces and grain boundary ledges: Relationship to nanocrystalline deformation," *Journal of the Mechanics and Physics of Solids*, vol. 55, pp. 2300–2327, Nov. 2007.

[37] Carsley, J., Fisher, A., Milligan, W., and Aifantis, E., "Mechanical behavior of a bulk nanostructured iron alloy," *Metallurgical and Materials Transactions A*, vol. 29, no. 9, pp. 2261–2271, 1998.

[38] Champion, Y., Langlois, C., Guérin-Mailly, S., Langlois, P., Bonnentien, J.-L., and Hÿtch, M. J., "Near-perfect elastoplasticity in pure nanocrystalline copper," *Science*, vol. 300, no. 5617, pp. 310–311, 2003.

[39] Chang, J., Cai, W., Bulatov, V. V., and Yip, S., "Dislocation motion in bcc metals by molecular dynamics," *Materials Science and Engineering: A*, vol. 309-310, pp. 160–163, July 2001.

[40] Chang, Y., Lye, M. L., and Zeng, H. C., "Large-scale synthesis of high-quality ultralong copper nanowires," *Langmuir*, vol. 21, no. 9, pp. 3746–3748, 2005.

[41] Chen, J., Lu, L., and Lu, K., "Hardness and strain rate sensitivity of nanocrystalline Cu," *Scripta Materialia*, vol. 54, pp. 1913–1918, June 2006.

[42] Chen, M., Ma, E., Hemker, K. J., Sheng, H., Wang, Y., and Cheng, X., "Deformation twinning in nanocrystalline aluminum," *Science*, vol. 300, pp. 1275–1277, May 2003.

[43] Chen, X., Lu, J., Lu, L., and Lu, K., "Tensile properties of a nanocrystalline 316L austenitic stainless steel," *Scripta Materialia*, vol. 52, pp. 1039–1044, May 2005.

[44] Cheng, S., Spencer, J., and Milligan, W., "Strength and tension/compression asymmetry in nanostructured and ultrafine-grain metals," *Acta Materialia*, vol. 51, pp. 4505–4518, Sept. 2003.

[45] Chokshi, A., Rosen, A., Karch, J., and Gleiter, H., "On the validity of the Hall-Petch relationship in nanocrystalline materials," *Scripta Metallurgica*, vol. 23, pp. 1679–1683, Oct. 1989.

[46] Chookajorn, T., Murdoch, H. A., and Schuh, C. A., "Design of stable nanocrystalline alloys," *Science*, vol. 337, no. 6097, pp. 951–954, 2012.

[47] Clausius, R., "On a mechanical theorem applicable to heat," *The London, Edinburgh, and Dublin Philosophical Magazine and Journal of Science*, vol. 40, no. 265, pp. 122–127, 1870.

[48] Daniels, W. and Smith, C., "Pressure derivatives of the elastic constants of copper, silver, and gold to 10000 bars," *Physical Review*, vol. 111, pp. 713–721, Aug. 1958.

[49] Daw, M. S. and Baskes, M. I., "Semiempirical, quantum mechanical calculation of hydrogen embrittlement in metals," *Physical Review Letters*, vol. 50, p. 1285, Apr. 1983.

[50] Daw, M. S. and Baskes, M. I., "Embedded-atom method: Derivation and application to impurities, surfaces, and other defects in metals," *Physical Review B*, vol. 29, p. 6443, June 1984.

[51] Derlet, P., Gumbsch, P., Hoagland, R., Li, J., McDowell, D., Van Swygenhoven, H., and Wang, J., "Atomistic simulations of dislocations in confined volumes," *MRS bulletin*, vol. 34, no. 03, pp. 184–189, 2009.

[52] Derlet, P. and Van Swygenhoven, H., "Atomic positional disorder in fcc metal nanocrystalline grain boundaries," *Physical Review B*, vol. 67, no. 1, p. 014202, 2003.

[53] Dickenscheid, W., Birringer, R., Gleiter, H., Kanert, O., Michel, B., and Günther, B., "Investigation of self-diffusion in nanocrystalline copper by NMR," *Solid state communications*, vol. 79, no. 8, pp. 683–686, 1991.

[54] Dimiduk, D., Uchic, M., and Parthasarathy, T., "Size-affected single-slip behavior of pure nickel microcrystals," *Acta Materialia*, vol. 53, no. 15, pp. 4065–4077, 2005. cited By (since 1996)293.

[55] Dongare, A., Rajendran, A., Lamattina, B., Brenner, D., and Zikry, M., "Atomic-scale study of plastic yield criterion in nanocrystalline Cu at high strain rates," *Metallurgical and Materials Transactions A*, vol. 41, pp. 523–531, Feb. 2010.

[56] Dongare, A. M., Rajendran, A. M., LaMattina, B., Zikry, M. a., and Brenner, D. W., "Tension–compression asymmetry in nanocrystalline Cu: High strain rate vs. quasi-static deformation," *Computational Materials Science*, vol. 49, pp. 260–265, Aug. 2010.

[57] Donovan, P., "A yield criterion for Pd40Ni40P20 metallic glass," *Acta Metallurgica*, vol. 37, no. 2, pp. 445–456, 1989.

[58] Drucker, D. and Prager, W., "Soil mechanics and plasticity analysis or limit design," *Quart. Appl. Math.*, vol. 10 (2), p. 157165, 1952.

[59] Ebrahimi, F., Bourne, G. R., Kelly, M. S., and Matthews, T. E., "Mechanical properties of nanocrystalline nickel produced by electrodeposition," *Nanostructured Materials*, vol. 11, pp. 343–350, May 1999.

[60] Erb, U., "Electrodeposited nanocrystals: Synthesis, properties and industrial applications," *Nanostructured Materials*, vol. 6, no. 5-8, pp. 533–538, 1995.

[61] Farkas, D., Willemann, M., and Hyde, B., "Atomistic mechanisms of fatigue in nanocrystalline metals," *Physical Review Letters*, vol. 94, p. 165502, Apr. 2005.

[62] Farkas, D., Frø seth, A., and Van Swygenhoven, H., "Grain boundary migration during room temperature deformation of nanocrystalline Ni," *Scripta Materialia*, vol. 55, pp. 695–698, Oct. 2006.

[63] Feynman, R. P., "There's plenty of room at the bottom," *Engineering and science*, vol. 23, no. 5, pp. 22–36, 1960.

[64] Fleck, N. and Hutchinson, J., "Strain gradient plasticity," *Advances in applied mechanics*, vol. 33, pp. 295–361, 1997.

[65] Fleck, N., Muller, G., Ashby, M., and Hutchinson, J., "Strain gradient plasticity: theory and experiment," *Acta Metallurgica et Materialia*, vol. 42, no. 2, pp. 475–487, 1994.

[66] Foiles, S., Baskes, M., and Daw, M., "Embedded atom method functions for the fcc metals Cu, Ag, Au, Ni, Pd, Pt, and their alloys," *Physical Review B*, vol. 33, no. 12, 1986.

[67] Fressengeas, C., Taupin, V., and Capolungo, L., "Continuous modeling of the structure of symmetric tilt boundaries," *International Journal of Solids and Structures*, vol. 51, pp. 1434–1441, Mar. 2014.

[68] Froseth, A., Derlet, P., and Van Swygenhoven, H., "Dislocations emitted from nanocrystalline grain boundaries: nucleation and splitting distance," *Acta Materialia*, vol. 52, pp. 5863–5870, Dec. 2004.

[69] Gao, H., Zhang, L., Nix, W., Thompson, C., and Arzt, E., "Crack-like grain-boundary diffusion wedges in thin metal films," *Acta materialia*, vol. 47, no. 10, pp. 2865–2878, 1999.

[70] Geyang, L., Junhua, X., Liuqiang, Z., Liang, W., and Mingyuan, G., "Growth, microstructure, and microhardness of W/Mo nanostructured multilayers," *Journal of Vacuum Science & Technology B*, vol. 19, no. 1, pp. 94–97, 2001.

[71] Gleiter, H., "Nanocrystalline materials," *Progress in Materials Science*, vol. 33, no. 4, pp. 223–315, 1989.

[72] Gleiter, H., "Nanostructured materials: basic concepts and microstructure," *Acta Materialia*, vol. 48, pp. 1–29, Jan. 2000.

[73] Grewer, M. and Birringer, R., "Shear shuffling governs plastic flow in nanocrystalline metals: An analysis of thermal activation parameters," *Physical Review B*, vol. 89, no. 18, p. 184108, 2014.

[74] Gu, P., Dao, M., Asaro, R. J., and Suresh, S., "A unified mechanistic model for size-dependent deformation in nanocrystalline and nanotwinned metals," *Acta Materialia*, vol. 59, no. 18, pp. 6861–6868, 2011.

[75] Guduru, R. K., Murty, K. L., Youssef, K. M., Scattergood, R. O., and Koch, C. C., "Mechanical behavior of nanocrystalline copper," *Materials Science and Engineering: A*, vol. 463, pp. 14–21, Aug. 2007.

[76] Gullett, P. M., Horstemeyer, M. F., Baskes, M. I., and Fang, H., "A deformation gradient tensor and strain tensors for atomistic simulations," *Modelling and Simulation in Materials Science and Engineering*, vol. 16, p. 015001, Jan. 2008.

[77] Guo, Y.-B., Xu, T., and Li, M., "Atomistic calculation of internal stress in nanoscale polycrystalline materials," *Philosophical Magazine*, vol. 92, pp. 3064–3083, Aug. 2012.

[78] Gurses, E. and El Sayed, T., "On tension-compression asymmetry in ultrafine-grained and nanocrystalline metals," *Computational Materials Science*, vol. 50, pp. 639–644, Dec. 2010.

[79] Haile, J. M., *Molecular dynamics simulation: elementary methods*. John Wiley & Sons, Inc., 1992.

[80] Hall, E., "The deformation and ageing of mild steel III: Discussion of results," *Proceedings of the Physical Society. Section B*, vol. 64, no. 9, p. 747, 1951.

[81] Hanlon, T., Tabachnikova, E., and Suresh, S., "Fatigue behavior of nanocrystalline metals and alloys," *International Journal of Fatigue*, vol. 27, no. 10, pp. 1147–1158, 2005.

[82] Haque, M. A. and Saif, M. T. A., "Deformation mechanisms in free-standing nanoscale thin films: A quantitative in situ transmission electron microscope study," *Proceedings of the National Academy of Sciences of the United States of America*, vol. 101, pp. 6335–6340, Apr. 2004.

[83] Heiligtag, F. J. and Niederberger, M., "The fascinating world of nanoparticle research," *Materials Today*, vol. 16, no. 7, pp. 262–271, 2013.

[84] Henkelman, G., Uberuaga, B. P., and Jónsson, H., "A climbing image nudged elastic band method for finding saddle points and minimum energy paths," *The Journal of Chemical Physics*, vol. 113, no. 22, pp. 9901–9904, 2000.

[85] Hirth, J. P. and Lothe, J., "Theory of dislocations," 1982.

[86] Hodge, A., Wang, Y., and Barbee Jr, T., "Large-scale production of nanotwinned, ultrafine-grained copper," *Materials Science and Engineering: A*, vol. 429, no. 1, pp. 272–276, 2006.

[87] Holmes, M., *Introduction to numerical methods in differential equations*, vol. 52. Springer Verlag, 2007.

[88] Hoover, W. G., "Canonical dynamics: Equilibrium phase-space distributions," *Physical Review A*, vol. 31, no. 3, p. 1695, 1985.

[89] Horvath, J., Birringer, R., and Gleiter, H., "Diffusion in nanocrystalline material," *Solid state communications*, vol. 62, no. 5, pp. 319–322, 1987.

[90] Hu, Q., Li, L., and Ghoniem, N., "Stickslip dynamics of coherent twin boundaries in copper," *Acta Materialia*, vol. 57, pp. 4866–4873, Sept. 2009.

[91] Huang, H. and Spaepen, F., "Tensile testing of free-standing Cu, Ag and Al thin films and Ag/Cu multilayers," *Acta Materialia*, vol. 48, no. 12, pp. 3261–3269, 2000.

[92] Hull, D. and Bacon, D. J., *Introduction to dislocations*, vol. 257. Pergamon Press Oxford, 1984.

[93] Ispánovity, P. D., Groma, I., Györgyi, G., Csikor, F. F., and Weygand, D., "Submicron plasticity: Yield stress, dislocation avalanches, and velocity distribution," *Phys. Rev. Lett.*, vol. 105, p. 085503, Aug 2010.

[94] Ivanov, V. and Mishin, Y., "Dynamics of grain boundary motion coupled to shear deformation: An analytical model and its verification by molecular dynamics," *Physical Review B*, vol. 78, p. 064106, Aug. 2008.

[95] Jones, J. E., "On the determination of molecular fields. ii. from the equation of state of a gas," *Royal Society of London Proceedings Series A*, vol. 106, pp. 463–477, Oct. 1924.

[96] Jung, J., "A note on the influence of hydrostatic pressure on dislocations," *Philosophical Magazine A*, vol. 43, no. 4, pp. 1057–1061, 1981.

[97] Karimpoor, A., Erb, U., Aust, K., and Palumbo, G., "High strength nanocrystalline cobalt with high tensile ductility," *Scripta Materialia*, vol. 49, no. 7, pp. 651–656, 2003.

[98] Karplus, M. and McCammon, J. A., "Molecular dynamics simulations of biomolecules," *Nature Structural & Molecular Biology*, vol. 9, no. 9, pp. 646–652, 2002.

[99] Kelchner, C. L., Plimpton, S. J., and Hamilton, J. C., "Dislocation nucleation and defect structure during surface indentation," *Physical Review B*, vol. 58, p. 11085, Nov. 1998.

[100] Khan, A. S. and Huang, S., *Continuum Theory of Plasticity*. John Wiley & Sons, Inc., 1999.

[101] Khan, A. S., Suh, Y. S., Chen, X., Takacs, L., and Zhang, H., "Nanocrystalline aluminum and iron: Mechanical behavior at quasi-static and high strain rates, and constitutive modeling," *International Journal of Plasticity*, vol. 22, pp. 195–209, Feb. 2006.

[102] Koch, C., "Structural nanocrystalline materials: an overview," *Journal of Materials Science*, vol. 42, pp. 1403–1414, Mar. 2007.

[103] Koch, C. C., "Optimization of strength and ductility in nanocrystalline and ultrafine grained metals," *Scripta Materialia*, vol. 49, pp. 657–662, Oct. 2003.

[104] Koch, C., Morris, D., Lu, K., and Inoue, A., "Ductility of nanostructured materials," *Mrs Bulletin*, vol. 24, no. 02, pp. 54–58, 1999.

[105] Kogure, Y., Kosugi, T., Doyama, M., and Kaburaki, H., "Simulation of mechanical response of point defects in copper," *Materials Science and Engineering: A*, vol. 442, no. 1, pp. 71–74, 2006.

[106] Kohn, W. and Sham, L. J., "Self-consistent equations including exchange and correlation effects," *Physical Review*, vol. 140, no. 4A, p. A1133, 1965.

[107] Kronberg, M. and Wilson, F., "Secondary recrystallization in copper," *AIME TRANS*, vol. 185, pp. 501–514, 1949.

[108] Kulkarni, Y., Knap, J., and Ortiz, M., "A variational approach to coarse graining of equilibrium and non-equilibrium atomistic description at finite temperature," *Journal of the Mechanics and Physics of Solids*, vol. 56, pp. 1417–1449, Apr. 2008.

[109] Kumar, K., Suresh, S., Chisholm, M., Horton, J., and Wang, P., "Deformation of electrodeposited nanocrystalline nickel," *Acta Materialia*, vol. 51, pp. 387–405, Jan. 2003.

[110] Kumar, K., Van Swygenhoven, H., and Suresh, S., "Mechanical behavior of nanocrystalline metals and alloys," *Acta Materialia*, vol. 51, no. 19, pp. 5743 – 5774, 2003. The Golden Jubilee Issue. Selected topics in Materials Science and Engineering: Past, Present and Future.

[111] LAMMPS, "LAMMPS molecular dynamics simulator." http://lammps.sandia.gov/, 2014.

[112] Laplace, P. S., *A philosophical essay on probabilities*. Wiley, 1902.

[113] Larsen, K. P., Rasmussen, A. A., Ravnkilde, J. T., Ginnerup, M., and Hansen, O., "MEMS device for bending test: measurements of fatigue and creep of electroplated nickel," *Sensors and Actuators A: Physical*, vol. 103, no. 1, pp. 156–164, 2003.

[114] Legros, M., Elliott, B. R., Rittner, M. N., Weertman, J. R., and Hemker, K. J., "Microsample tensile testing of nanocrystalline metals," *Philosophical Magazine A*, vol. 80, no. 4, p. 1017, 2000.

[115] Legros, M., Gianola, D. S., and Hemker, K. J., "In situ TEM observations of fast grain-boundary motion in stressed nanocrystalline aluminum films," *Acta Materialia*, vol. 56, no. 14, pp. 3380–3393, 2008.

[116] Li, C. H., Edwards, E. H., Washburn, J., and Parker, E. R., "Stress-induced movement of crystal boundaries," *Acta metallurgica*, vol. 1, no. 2, pp. 223–229, 1953.

[117] Li, J. C., "Petch relation and grain boundary sources," *Transactions of the Metallurgical Society of AIME*, vol. 227, no. 1, p. 239, 1963.

[118] Li, J., "Disclination model of high angle grain boundaries," *Surface Science*, vol. 31, pp. 12–26, 1972.

[119] Li, L., Anderson, P. M., Lee, M.-G., Bitzek, E., Derlet, P., and Swygenhoven, H. V., "The stress–strain response of nanocrystalline metals: a quantized crystal plasticity approach," *Acta Materialia*, vol. 57, no. 3, pp. 812–822, 2009.

[120] Li, X., Wei, Y., Yang, W., and Gao, H., "Competing grain-boundary-and dislocation-mediated mechanisms in plastic strain recovery in nanocrystalline aluminum," *Proceedings of the National Academy of Sciences*, vol. 106, no. 38, pp. 16108–16113, 2009.

[121] Liang, W., Zhou, M., and Ke, F., "Shape memory effect in Cu nanowires," *Nano Letters*, vol. 5, no. 10, pp. 2039–2043, 2005.

[122] Liao, X. Z., Zhou, F., Lavernia, E. J., Srinivasan, S. G., Baskes, M. I., He, D. W., and Zhu, Y. T., "Deformation mechanism in nanocrystalline al: Partial dislocation slip," *Applied Physics Letters*, vol. 83, no. 4, pp. 632–634, 2003.

[123] Lissenden, C. J. and Arnold, S. M., "Theoretical and experimental considerations in representing macroscale flow/damage surfaces for metal matrix composites," *International Journal of Plasticity*, vol. 13, no. 4, pp. 327–358, 1997.

[124] Lu, K., Lu, L., and Suresh, S., "Strengthening materials by engineering coherent internal boundaries at the nanoscale," *Science*, vol. 324, no. 5925, pp. 349–352, 2009.

[125] Lu, L., Chen, X., Huang, X., and Lu, K., "Revealing the maximum strength in nanotwinned copper," *Science*, vol. 323, pp. 607–610, Jan. 2009.

[126] Lu, L., Shen, Y., Chen, X., Qian, L., and Lu, K., "Ultrahigh strength and high electrical conductivity in copper," *Science*, vol. 304, no. 5669, pp. 422–426, 2004.

[127] Lu, L., Sui, M., and Lu, K., "Superplastic extensibility of nanocrystalline copper at room temperature," *Science*, vol. 287, no. 5457, pp. 1463–1466, 2000.

[128] Lund, A. and Schuh, C., "Strength asymmetry in nanocrystalline metals under multiaxial loading," *Acta Materialia*, vol. 53, pp. 3193–3205, June 2005.

[129] Lund, A. C., Nieh, T., and Schuh, C., "Tension/compression strength asymmetry in a simulated nanocrystalline metal," *Physical Review B*, vol. 69, no. 1, p. 012101, 2004.

[130] Ma, E., "Watching the nanograins roll," *Science*, vol. 305, no. 5684, pp. 623–624, 2004.

[131] Mara, N., Sergueeva, A., Mara, T., McFadden, S., and Mukherjee, A., "Superplasticity and cooperative grain boundary sliding in nanocrystalline Ni3Al," *Materials Science and Engineering: A*, vol. 463, no. 1, pp. 238–244, 2007.

[132] Martyna, G. J., Klein, M. L., and Tuckerman, M., "NoseHoover chains: The canonical ensemble via continuous dynamics," *The Journal of Chemical Physics*, vol. 97, no. 4, p. 2635, 1992.

[133] Martyna, G. J., Tobias, D. J., and Klein, M. L., "Constant pressure molecular dynamics algorithms," *The Journal of Chemical Physics*, vol. 101, p. 4177, 1994.

[134] McCammon, J. A., "Dynamics of folded proteins," *Nature*, vol. 267, p. 16, 1977.

[135] McDowell, D. L., "Materials design: a useful research focus for inelastic behavior of structural metals," *Theoretical and Applied Fracture Mechanics*, vol. 37, pp. 245–259, Dec. 2001.

[136] McDowell, D. L., "Viscoplasticity of heterogeneous metallic materials," *Materials Science and Engineering: R: Reports*, vol. 62, pp. 67–123, Aug. 2008.

[137] McDowell, D. L., "A perspective on trends in multiscale plasticity," *International Journal of Plasticity*, vol. 26, pp. 1280–1309, Sept. 2010.

[138] McFadden, S., Mishra, R. S., Valiev, R., Zhilyaev, A., and Mukherjee, A., "Low-temperature superplasticity in nanostructured nickel and metal alloys," *Nature*, vol. 398, no. 6729, pp. 684–686, 1999.

[139] McHenry, M. E., Willard, M. A., and Laughlin, D. E., "Amorphous and nanocrystalline materials for applications as soft magnets," *Progress in Materials Science*, vol. 44, pp. 291–433, Oct. 1999.

[140] Medlin, D. L., Mills, M. J., Stobbs, W. M., Daw, M. S., and Cosandey, F., "HRTEM observations of a sigma 3 112 bicrystal boundary in aluminium," *Materials Research Society Symposium Proceedings*, vol. 295, no. 112, pp. 91–96, 1993.

[141] Melchionna, S., Ciccotti, G., and Holian, B. L., "Hoover NPT dynamics for systems varying in shape and size," *Molecular Physics: An International Journal at the Interface Between Chemistry and Physics*, vol. 78, no. 3, p. 533, 1993.

[142] Meyers, M., Mishra, A., and Benson, D., "Mechanical properties of nanocrystalline materials," *Progress in Materials Science*, vol. 51, pp. 427–556, May 2006.

[143] Miller, R. E. and Tadmor, E. B., "The quasicontinuum method: Overview, applications and current directions," *Journal of Computer-Aided Materials Design*, vol. 9, no. 3, pp. 203–239, 2002.

[144] Mills, M., Daw, M., Thomas, G., and Cosandey, F., "High-resolution transmission electron microscopy of grain boundaries in aluminum and correlation with atomistic calculations," *Ultramicroscopy*, vol. 40, no. 1992, pp. 247–257, 1992.

[145] Mishin, Y., Mehl, M. J., Papaconstantopoulos, D. A., Voter, A. F., and Kress, J. D., "Structural stability and lattice defects in copper: Ab initio, tight-binding, and embedded-atom calculations," *Physical Review B*, vol. 63, p. 224106, May 2001.

[146] Mishin, Y., Suzuki, a., Uberuaga, B., and Voter, a., "Stick-slip behavior of grain boundaries studied by accelerated molecular dynamics," *Physical Review B*, vol. 75, p. 224101, June 2007.

[147] Mody, V. V., Siwale, R., Singh, A., and Mody, H. R., "Introduction to metallic nanoparticles," *Journal of Pharmacy and Bioallied Sciences*, vol. 2, no. 4, p. 282, 2010.

[148] Mohamed, F. A. and Li, Y., "Creep and superplasticity in nanocrystalline materials: current understanding and future prospects," *Materials Science and Engineering: A*, vol. 298, no. 1, pp. 1–15, 2001.

[149] Monk, J. and Farkas, D., "Tension–Compression asymmetry and size effects in nanocrystalline Ni nanowires," *Philosophical Magazine*, vol. 87, no. 14-15, pp. 2233–2244, 2007.

[150] Morse, P. M., "Diatomic molecules according to the wave mechanics. ii. vibrational levels," *Physical Review*, vol. 34, no. 1, p. 57, 1929.

[151] Mousseau, N. and Barkema, G., "Traveling through potential energy landscapes of disordered materials: The activation-relaxation technique," *Physical Review E*, vol. 57, no. 2, p. 2419, 1998.

[152] Mühlbach, J., Pfau, P., Sattler, K., and Recknagel, E., "Inert gas condensation of metal microclusters," *Zeitschrift für Physik B Condensed Matter*, vol. 47, no. 3, pp. 233–237, 1982.

[153] Murdoch, H. A. and Schuh, C. A., "Stability of binary nanocrystalline alloys against grain growth and phase separation," *Acta Materialia*, vol. 61, no. 6, pp. 2121–2132, 2013.

[154] Nieman, G., Weertman, J., and Siegel, R., "Microhardness of nanocrystalline palladium and copper produced by inert-gas condensation," *Scripta metallurgica*, vol. 23, no. 12, pp. 2013–2018, 1989.

[155] Nose, S., "A unified formulation of the constant temperature molecular dynamics methods," *The Journal of Chemical Physics*, vol. 81, no. 1, p. 511, 1984.

[156] Odqvist, F., "Die verfestigung von flusseisenähnlichen körpern. ein beitrag zur plastizitätstheorie," *ZAMM-Journal of Applied Mathematics and Mechanics/Zeitschrift für Angewandte Mathematik und Mechanik*, vol. 13, no. 5, pp. 360–363, 1933.

[157] Olmsted, D. L., Holm, E. a., and Foiles, S. M., "Survey of computed grain boundary properties in face-centered cubic metals-II: Grain boundary mobility," *Acta Materialia*, vol. 57, pp. 3704–3713, Aug. 2009.

[158] Olson, G. B., "Computational design of hierarchically structured materials," *Science*, vol. 277, no. 5330, pp. 1237–1242, 1997.

[159] Olson, G. B., "Designing a new material world," *Science*, vol. 288, no. 5468, pp. 993–998, 2000.

[160] Padilla II, H. and Boyce, B., "A review of fatigue behavior in nanocrystalline metals," *Experimental mechanics*, vol. 50, no. 1, pp. 5–23, 2010.

[161] Parrinello, M. and Rahman, A., "Crystal structure and pair potentials: A molecular-dynamics study," *Physical Review Letters*, vol. 45, p. 1196, Oct. 1980.

[162] Petch, N., "The cleavage strength of polycrstals," *J. Iron Steel Inst.*, vol. 174, 1953.

[163] Plimpton, S., "Fast Parallel Algorithms for Short-Range Molecular Dynamics," *Journal of Computational Physics*, vol. 117, pp. 1–19, Mar. 1995.

[164] Prager, W., "The theory of plasticity: a survey of recent achievements," *Proceedings of the Institution of Mechanical Engineers*, vol. 169, no. 1, pp. 41–57, 1955.

[165] Qin, Q. and Bassani, J. L., "Non-associated plastic flow in single crystals," *Journal of the Mechanics and Physics of Solids*, vol. 40, no. 4, pp. 835–862, 1992.

[166] Quinson, R., Perez, J., Rink, M., and Pavan, A., "Yield criteria for amorphous glassy polymers," *Journal of Materials Science*, vol. 32, no. 5, pp. 1371–1379, 1997.

[167] Rahman, A. and Stillinger, F. H., "Molecular dynamics study of liquid water," *The Journal of Chemical Physics*, vol. 55, no. 7, pp. 3336–3359, 1971.

[168] Rajagopalan, J., Han, J. H., and Saif, M. T. A., "Plastic deformation recovery in freestanding nanocrystalline aluminum and gold thin films," *Science*, vol. 315, pp. 1831–1834, Mar. 2007.

[169] Ramesh, K., *Nanomaterials*. Boston, MA: Springer US, 2009.

[170] Randle, V., "Grain boundary engineering: an overview after 25 years," *Materials Science and Technology*, vol. 26, no. 3, pp. 253–261, 2010.

[171] Randle, V., *The role of the coincidence site lattice in grain boundary engineering*. Institute of Materials London, 1996.

[172] Read, W. and Shockley, W., "Dislocation models of crystal grain boundaries," *Physical Review*, vol. 78, no. 3, p. 275, 1950.

[173] Rice, J., "Inelastic constitutive relations for solids: An internal-variable theory and its application to metal plasticity," *Journal of the Mechanics and Physics of Solids*, vol. 19, pp. 433–455, Nov. 1971.

[174] Rice, J., "Dislocation nucleation from a crack tip: an analysis based on the Peierls concept," *Journal of the Mechanics and Physics of Solids*, vol. 40, no. 2, pp. 239–271, 1992.

[175] Rupert, T. J., Gianola, D. S., Gan, Y., and Hemker, K. J., "Experimental observations of stress-driven grain boundary migration.," *Science (New York, N.Y.)*, vol. 326, pp. 1686–90, Dec. 2009.

[176] Rycroft, C. H., "Voro++: A three-dimensional Voronoi cell library in C++," *Chaos: An Interdisciplinary Journal of Nonlinear Science*, vol. 19, no. 4, p. 041111, 2009.

[177] Sanders, P., Youngdahl, C., and Weertman, J., "The strength of nanocrystalline metals with and without flaws," *Materials Science and Engineering: A*, vol. 234, pp. 77–82, 1997.

[178] Sansoz, F. and Molinari, J. F., "Mechanical behavior of Sigma tilt grain boundaries in nanoscale Cu and Al : A quasicontinuum study," vol. 53, pp. 1931–1944, 2005.

[179] Schaefer, H.-E., Wurschum, R., Gessmann, T., Stöckl, G., Scharwaechter, P., Frank, W., Valiev, R., Fecht, H.-J., and Moelle, C., "Diffusion and free volumes in nanocrystalline Pd," *Nanostructured materials*, vol. 6, no. 5, pp. 869–872, 1995.

[180] Schiotz, J., Vegge, T., Di Tolla, F. D., and Jacobsen, K. W., "Atomic-scale simulations of the mechanical deformation of nanocrystalline metals," *Physical Review B*, vol. 60, p. 11971, Nov. 1999.

[181] Schiotz, J., "Strain-induced coarsening in nanocrystalline metals under cyclic deformation," *Materials Science and Engineering: A*, vol. 375, pp. 975–979, 2004.

[182] Schiotz, J., Di Tolla, F. D., and Jacobsen, K. W., "Softening of nanocrystalline metals at very small grain sizes," *Nature*, vol. 391, no. 6667, pp. 561–563, 1998.

[183] Schiotz, J. and Jacobsen, K. W., "A maximum in the strength of nanocrystalline copper," *Science*, vol. 301, pp. 1357–1359, Sept. 2003.

[184] Schmid, E., "Yield point of crystals, critical shear stress law," in *Proceedings of the First International Congress for Applied Mechanics, Delft*, 1924.

[185] Schuh, C. A., Nieh, T. G., and Yamasaki, T., "Hall-Petch breakdown manifested in abrasive wear resistance of nanocrystalline nickel," *Scripta Materialia*, vol. 46, pp. 735–740, May 2002.

[186] Schuh, C. A. and Lund, A. C., "Atomistic basis for the plastic yield criterion of metallic glass," *Nature Materials*, vol. 2, pp. 449–452, July 2003.

[187] Schuster, B. E., Wei, Q., Zhang, H., and Ramesh, K. T., "Microcompression of nanocrystalline nickel," *Applied Physics Letters*, vol. 88, no. 10, p. 103112, 2006.

[188] Schwaiger, R., Moser, B., Dao, M., Chollacoop, N., and Suresh, S., "Some critical experiments on the strain-rate sensitivity of nanocrystalline nickel," *Acta materialia*, vol. 51, no. 17, pp. 5159–5172, 2003.

[189] Segal, V. M., "Engineering and commercialization of equal channel angular extrusion (ECAE)," *Materials Science and Engineering: A*, vol. 386, no. 1, pp. 269–276, 2004.

[190] Shan, Z. and Mao, S. X., "Direct evidence of a deformation mechanism crossover in nanocrystalline nickel," *Advanced Engineering Materials*, vol. 7, pp. 603–606, July 2005.

[191] Shan, Z., Stach, E. a., Wiezorek, J. M. K., Knapp, J. a., Follstaedt, D. M., and Mao, S. X., "Grain boundary-mediated plasticity in nanocrystalline nickel.," *Science (New York, N.Y.)*, vol. 305, pp. 654–7, July 2004.

[192] Shewchuk, J. R., "An introduction to the conjugate gradient method without the agonizing pain," 1994.

[193] Shiga, M. and Shinoda, W., "Stress-assisted grain boundary sliding and migration at finite temperature: A molecular dynamics study," *Physical Review B*, vol. 70, no. 5, p. 054102, 2004.

[194] Slater, J. C., "A simplification of the Hartree-Fock method," *Physical Review*, vol. 81, no. 3, p. 385, 1951.

[195] Smith, C. S., *A search for structure. Selected essays on science, art and history.* MiT Press, 1981.

[196] Sorensen, M. R. and Voter, A. F., "Temperature-accelerated dynamics for simulation of infrequent events," *The Journal of Chemical Physics*, vol. 112, no. 21, pp. 9599–9606, 2000.

[197] Spearot, D. E., Jacob, K. I., and McDowell, D. L., "Nucleation of dislocations from [0 0 1] bicrystal interfaces in aluminum," *Acta Materialia*, vol. 53, pp. 3579–3589, Aug. 2005.

[198] Spearot, D. E., *Atomistic Calculations of Nanoscale Interface Behavior in FCC Metals.* PhD thesis, Georgia Institute of Technology, 2005.

[199] Spearot, D. E., Jacob, K. I., and McDowell, D. L., "Non-local separation constitutive laws for interfaces and their relation to nanoscale simulations," *Mechanics of Materials*, vol. 36, pp. 825–847, Sept. 2004.

[200] Spearot, D. E., Jacob, K. I., and McDowell, D. L., "Nucleation of dislocations from [0 0 1] bicrystal interfaces in aluminum," *Acta Materialia*, vol. 53, pp. 3579–3589, Aug. 2005.

[201] Spearot, D. E., Tschopp, M. A., Jacob, K. I., and McDowell, D. L., "Tensile strength of 100 and 110 tilt bicrystal copper interfaces," *Acta Materialia*, vol. 55, no. 2, pp. 705–714, 2007.

[202] Spitzig, W. and Richmond, O., "The effect of pressure on the flow stress of metals," *Acta metallurgica*, vol. 32, no. 3, 1984.

[203] Sriraman, K., Ganesh Sundara Raman, S., and Seshadri, S., "Synthesis and evaluation of hardness and sliding wear resistance of electrodeposited nanocrystalline Ni–W alloys," *Materials Science and Engineering: A*, vol. 418, no. 1, pp. 303–311, 2006.

[204] Stukowski, A. and Arsenlis, A., "On the elastic–plastic decomposition of crystal deformation at the atomic scale," *Modelling and Simulation in Materials Science and Engineering*, vol. 20, no. 3, p. 035012, 2012.

[205] Stukowski, A., "Visualization and analysis of atomistic simulation data with ovito–the open visualization tool," *Modelling and Simulation in Materials Science and Engineering*, vol. 18, no. 1, p. 015012, 2010.

[206] Stukowski, A., "Structure identification methods for atomistic simulations of crystalline materials," *Modelling and Simulation in Materials Science and Engineering*, vol. 20, no. 4, p. 045021, 2012.

[207] Subramaniyan, A. K. and Sun, C., "Continuum interpretation of virial stress in molecular simulations," *International Journal of Solids and Structures*, vol. 45, no. 14, pp. 4340–4346, 2008.

[208] Suryanarayana, C., "Nanocrystalline materials," *International Materials Reviews*, vol. 40, pp. 41–64, 1995.

[209] Sutton, A. P. and Vitek, V., "On the Structure of Tilt Grain Boundaries in Cubic Metals I. Symmetrical Tilt Boundaries," *Philosophical Transactions of the Royal Society A: Mathematical, Physical and Engineering Sciences*, vol. 309, pp. 1–36, Mar. 1983.

[210] Takagi, M., Ohta, H., Imura, T., Kawamura, Y., and Inoue, A., "Wear properties of nanocrystalline aluminum alloys and their composites," *Scripta Materialia*, vol. 44, pp. 2145–2148, May 2001.

[211] Tanimoto, H., Sakai, S., and Mizubayashi, H., "Anelasticity of nanocrystalline metals," *Materials Science and Engineering: A*, vol. 370, no. 1, pp. 135–141, 2004.

[212] Tao, S. and Li, D. Y., "Tribological, mechanical and electrochemical properties of nanocrystalline copper deposits produced by pulse electrodeposition," *Nanotechnology*, vol. 17, pp. 65–78, Jan. 2006.

[213] Taupin, V., Capolungo, L., and Fressengeas, C., "Disclination mediated plasticity in shear-coupled boundary migration," *International Journal of Plasticity*, vol. 53, pp. 179–192, Feb. 2014.

[214] Tench, D. and White, J., "Tensile properties of nanostructured Ni-Cu multilayered materials prepared by electrodeposition," *Journal of The Electrochemical Society*, vol. 138, no. 12, pp. 3757–3758, 1991.

[215] Thiebaud, R., Weiss, J., and Louchet, F., "Breakdown of avalanche critical behaviour in polycrystalline plasticity," *Nature Materials*, vol. 4, pp. 465 – 469, 2005.

[216] Thostenson, E. T., Ren, Z., and Chou, T.-W., "Advances in the science and technology of carbon nanotubes and their composites: a review," *Composites science and technology*, vol. 61, no. 13, pp. 1899–1912, 2001.

[217] Tiwari, S., Tucker, G. J., and McDowell, D. L., "Simulated defect growth avalanches during deformation of nanocrystalline copper," *Philosophical Magazine*, vol. 93, no. 5, pp. 478–498, 2013.

[218] Tomar, V. and Zhou, M., "Tension-compression strength asymmetry of nanocrystalline -Fe2O3+fcc-Al ceramic-metal composites," *Applied Physics Letters*, vol. 88, no. 23, p. 233107, 2006.

[219] Trelewicz, J. R. and Schuh, C. A., "The Hall–Petch breakdown in nanocrystalline metals: a crossover to glass-like deformation," *Acta Materialia*, vol. 55, no. 17, pp. 5948–5958, 2007.

[220] Trelewicz, J. R. and Schuh, C. A., "Grain boundary segregation and thermodynamically stable binary nanocrystalline alloys," *Physical Review B*, vol. 79, no. 9, p. 094112, 2009.

[221] Tresca, H. E., *Mémoires sur l'écoulement des corps solides.* Imprimerie impériale, 1869.

[222] Tsai, D., "The virial theorem and stress calculation in molecular dynamics," *The Journal of Chemical Physics*, vol. 70, no. 3, pp. 1375–1382, 1979.

[223] Tschopp, M. A. and Mcdowell, D. L., "Asymmetric tilt grain boundary structure and energy in copper and aluminium," *Philosophical Magazine*, vol. 87, no. 25, p. 3871, 2007.

[224] Tschopp, M. A. and McDowell, D. L., "Tension-compression asymmetry in homogeneous dislocation nucleation in single crystal copper," *Applied Physics Letters*, vol. 90, no. 12, p. 121916, 2007.

[225] Tschopp, M. A. and McDowell, D. L., "Dislocation nucleation in Sigma 3 asymmetric tilt grain boundaries," *International Journal of Plasticity*, vol. 24, pp. 191–217, Feb. 2008.

[226] Tschopp, M. A. and McDowell, D. L., "Influence of single crystal orientation on homogeneous dislocation nucleation under uniaxial loading," *Journal of the Mechanics and Physics of Solids*, vol. 56, pp. 1806–1830, May 2008.

[227] Tschopp, M. A., Spearot, D. E., and McDowell, D. L., "Atomistic simulations of homogeneous dislocation nucleation in single crystal copper," *Modelling and Simulation in Materials Science and Engineering*, vol. 15, pp. 693–709, Oct. 2007.

[228] Tschopp, M. and McDowell, D., "Grain boundary dislocation sources in nanocrystalline copper," *Scripta Materialia*, vol. 58, pp. 299–302, Feb. 2008.

[229] Tschopp, M., Tucker, G., and McDowell, D., "Structure and free volume of 1 1 0 symmetric tilt grain boundaries with the E structural unit," *Acta Materialia*, vol. 55, pp. 3959–3969, June 2007.

[230] Tschopp, M., Tucker, G., and McDowell, D., "Atomistic simulations of tension-compression asymmetry in dislocation nucleation for copper grain boundaries," *Computational Materials Science*, vol. 44, pp. 351–362, Dec. 2008.

[231] Tschopp, M. A., Spearot, D. E., and McDowell, D. L., "Influence of grain boundary structure on dislocation nucleation in fcc metals," in *A Tribute to F.R.N. Nabarro* (Hirth, J., ed.), vol. 14 of *Dislocations in Solids*, pp. 43 – 139, Elsevier, 2008.

[232] Tsuzuki, H., Branicio, P. S., and Rino, J. P., "Structural characterization of deformed crystals by analysis of common atomic neighborhood," *Computer Physics Communications*, vol. 177, pp. 518–523, Sept. 2007.

[233] Tucker, G. J., Tschopp, M. A., and McDowell, D. L., "Evolution of structure and free volume in symmetric tilt grain boundaries during dislocation nucleation," *Acta Materialia*, vol. 58, pp. 6464–6473, Nov. 2010.

[234] Tucker, G. J., Zimmerman, J. A., and McDowell, D. L., "Shear deformation kinematics of bicrystalline grain boundaries in atomistic simulations," *Modelling and Simulation in Materials Science and Engineering*, vol. 18, p. 015002, Jan. 2010.

[235] Tucker, G. J., *Atomistic simulation of defect nucleation and free volume in nanocrystalline materials*. PhD thesis, 2011.

[236] Tucker, G. J. and McDowell, D. L., "Non-equilibrium grain boundary structure and inelastic deformation using atomistic simulations," *International Journal of Plasticity*, vol. 27, no. 6, pp. 841–857, 2011.

[237] Tucker, G. J., Tiwari, S., Zimmerman, J. A., and McDowell, D. L., "Investigating the deformation of nanocrystalline copper with microscale kinematic metrics and molecular dynamics," *Journal of the Mechanics and Physics of Solids*, vol. 60, no. 3, pp. 471–486, 2012.

[238] Tuckerman, M. E., Alejandre, J., Lpez-Rendn, R., Jochim, A. L., and Martyna, G. J., "A liouville-operator derived measure-preserving integrator for molecular dynamics simulations in the isothermalisobaric ensemble," *Journal of Physics A: Mathematical and General*, vol. 39, pp. 5629–5651, May 2006.

[239] Vairavapandian, D., Vichchulada, P., and Lay, M. D., "Preparation and modification of carbon nanotubes: review of recent advances and applications in catalysis and sensing," *Analytica chimica acta*, vol. 626, no. 2, pp. 119–129, 2008.

[240] Valiev, R., "Nanostructuring of metals by severe plastic deformation for advanced properties," *Nature materials*, vol. 3, no. 8, pp. 511–516, 2004.

[241] Valiev, R., Alexandrov, I., Zhu, Y., and Lowe, T., "Paradox of strength and ductility in metals processed by severe plastic deformation," *Journal of Materials Research*, vol. 17, no. 01, pp. 5–8, 2002.

[242] Valiev, R., Korznikov, A., and Mulyukov, R., "Structure and properties of ultrafine-grained materials produced by severe plastic deformation," *Materials Science and Engineering: A*, vol. 168, pp. 141–148, Aug. 1993.

[243] Van Swygenhoven, H. and Derlet, P., "Grain-boundary sliding in nanocrystalline fcc metals," *Physical Review B*, vol. 64, p. 224105, Nov. 2001.

[244] Van Swygenhoven, H., Derlet, P. M., and Froseth, A. G., "Stacking fault energies and slip in nanocrystalline metals," *Nature Materials*, vol. 3, pp. 399–403, June 2004.

[245] Van Swygenhoven, H., Derlet, P., and Froseth, A., "Nucleation and propagation of dislocations in nanocrystalline fcc metals," *Acta Materialia*, vol. 54, pp. 1975–1983, Apr. 2006.

[246] Van Swygenhoven, H., Derlet, P., and Hasnaoui, A., "Atomistic modeling of strength of nanocrystalline metals," *Advanced Engineering Materials*, vol. 5, no. 5, pp. 345–350, 2003.

[247] Velasco, M., Swygenhoven, H. V., and Brandl, C., "Coupled grain boundary motion in a nanocrystalline grain boundary network," *Scripta Materialia*, vol. 65, no. 2, pp. 151 – 154, 2011.

[248] Vinogradov, A. Y., Stolyarov, V., Hashimoto, S., and Valiev, R., "Cyclic behavior of ultrafine-grain titanium produced by severe plastic deformation," *Materials Science and Engineering: A*, vol. 318, no. 1, pp. 163–173, 2001.

[249] Vitek, V., "Structure of dislocation cores in metallic materials and its impact on their plastic behaviour," *Progress in materials science*, vol. 36, pp. 1–27, 1992.

[250] Vitek, V., Mrovec, M., Groger, R., Bassani, J., Racherla, V., and Yin, L., "Effects of non-glide stresses on the plastic flow of single and polycrystals of molybdenum," *Materials Science and Engineering: A*, vol. 387389, no. 0, pp. 138 – 142, 2004. 13th International Conference on the Strength of Materials.

[251] Vo, N., Averback, R., Bellon, P., Odunuga, S., and Caro, A., "Quantitative description of plastic deformation in nanocrystalline Cu: Dislocation glide versus grain boundary sliding," *Physical Review B*, vol. 77, no. 13, p. 134108, 2008.

[252] von Mises, R., "Mechanik der festen Korper im plastisch-deformablen Zustand," *Nachrichten von der Gesellschaft der Wissenschaften zu Gottingen, Mathematisch-Physikalische Klasse*, vol. 1913, pp. 582–592, 1913.

[253] Voronoi, G., "Nouvelles applications des parametres continus la thorie des formes quadratiques. Deuxime mmoire. Recherches sur les parallllodres primitifs," *Journal fr die reine und angewandte Mathematik*, vol. 1908, pp. 198–287, Jan. 1908.

[254] Voter, A. F., "Hyperdynamics: Accelerated molecular dynamics of infrequent events," *Physical Review Letters*, vol. 78, no. 20, p. 3908, 1997.

[255] Voter, A. F., "Parallel replica method for dynamics of infrequent events," *Physical Review B*, vol. 57, no. 22, p. 13985, 1998.

[256] Wang, J., Misra, a., and Hirth, J. P., "Shear response of $\Sigma 3\{112\}$ twin boundaries in face-centered-cubic metals," *Physical Review B*, vol. 83, p. 064106, Feb. 2011.

[257] Wang, N., Wang, Z., Aust, K., and Erb, U., "Room temperature creep behavior of nanocrystalline nickel produced by an electrodeposition technique," *Materials Science and Engineering: A*, vol. 237, no. 2, pp. 150–158, 1997.

[258] Wang, X. and Li, D., "Mechanical, electrochemical and tribological properties of nano-crystalline surface of 304 stainless steel," *Wear*, vol. 255, no. 7, pp. 836–845, 2003.

[259] Wang, Y. M., Wang, K., Pan, D., Lu, K., Hemker, K. J., and Ma, E., "Microsample tensile testing of nanocrystalline copper," *Scripta Materialia*, vol. 48, pp. 1581–1586, June 2003.

[260] Wang, Y., Hamza, A., and Ma, E., "Temperature-dependent strain rate sensitivity and activation volume of nanocrystalline Ni," *Acta Materialia*, vol. 54, pp. 2715–2726, June 2006.

[261] Warner, D. and Molinari, J., "Effect of normal loading on grain boundary migration and sliding in copper," *Modelling and Simulation in Materials Science and Engineering*, vol. 16, no. 7, p. 075007, 2008.

[262] Watanabe, T., "Grain boundary engineering: historical perspective and future prospects," *Journal of materials science*, vol. 46, no. 12, pp. 4095–4115, 2011.

[263] Wei, Q., Zhang, H., Schuster, B., Ramesh, K., Valiev, R., Kecskes, L., Dowding, R., Magness, L., and Cho, K., "Microstructure and mechanical properties of super-strong nanocrystalline tungsten processed by high-pressure torsion," *Acta Materialia*, vol. 54, no. 15, pp. 4079 – 4089, 2006.

[264] Wei, Y., Bower, A. F., and Gao, H., "Recoverable creep deformation due to heterogeneous grain-boundary diffusion and sliding," *Scripta Materialia*, vol. 57, pp. 933–936, Nov. 2007.

[265] Wei, Y., Su, C., and Anand, L., "A computational study of the mechanical behavior of nanocrystalline fcc metals," *Acta Materialia*, vol. 54, pp. 3177–3190, July 2006.

[266] Wei, Y. and Anand, L., "Grain-boundary sliding and separation in polycrystalline metals: application to nanocrystalline fcc metals," *Journal of the Mechanics and Physics of Solids*, vol. 52, no. 11, pp. 2587–2616, 2004.

[267] Wei, Y. and Gao, H., "An elastic-viscoplastic model of deformation in nanocrystalline metals based on coupled mechanisms in grain boundaries and grain interiors," *Materials Science and Engineering: A*, vol. 478, pp. 16–25, Apr. 2008.

[268] Wei, Y., Su, C., and Anand, L., "A computational study of the mechanical behavior of nanocrystalline fcc metals," *Acta Materialia*, vol. 54, pp. 3177–3190, July 2006.

[269] Wendoloski, J., Kimatian, S., Schutt, C., and Salemme, F., "Molecular dynamics simulation of a phospholipid micelle," *Science*, vol. 243, no. 4891, pp. 636–638, 1989.

[270] Winning, M., Gottstein, G., and Shvindlerman, L., "Stress-induced grain boundary motion," *Acta Materialia*, vol. 49, pp. 211–219, Jan. 2001.

[271] Wolf, D., Yamakov, V., Phillpot, S., Mukherjee, A., and Gleiter, H., "Deformation of nanocrystalline materials by molecular-dynamics simulation: relationship to experiments?," *Acta Materialia*, vol. 53, no. 1, pp. 1 – 40, 2005.

[272] Wu, Y., Xiang, J., Yang, C., Lu, W., and Lieber, C. M., "Single-crystal metallic nanowires and metal/semiconductor nanowire heterostructures," *Nature*, vol. 430, no. 6995, pp. 61–65, 2004.

[273] Xiong, L., Tucker, G., and McDowell, D., "Coarse-grained atomistic simulation of dislocations," *Journal of the Mechanics and Physics of Solids*, vol. 59, pp. 160–177, Feb. 2011.

[274] Yamakov, V., Wolf, D., Phillpot, S. R., and Gleiter, H., "Deformation twinning in nanocrystalline Al by molecular-dynamics simulation," *Acta Materialia*, vol. 50, pp. 5005–5020, Dec. 2002.

[275] Yamakov, V., Wolf, D., Phillpot, S. R., Mukherjee, A. K., and Gleiter, H., "Deformation-mechanism map for nanocrystalline metals by molecular-dynamics simulation," *Nature Materials*, vol. 3, pp. 43–47, Jan. 2004.

[276] Yamakov, V., Wolf, D., Phillpot, S., and Gleiter, H., "Grain-boundary diffusion creep in nanocrystalline palladium by molecular-dynamics simulation," *Acta Materialia*, vol. 50, no. 1, pp. 61 – 73, 2002.

[277] Yen, M.-Y., Chiu, C.-W., Hsia, C.-H., Chen, F.-R., Kai, J.-J., Lee, C.-Y., and Chiu, H.-T., "Synthesis of cable-like copper nanowires," *Advanced Materials*, vol. 15, no. 3, pp. 235–237, 2003.

[278] Yin, W., Whang, S., Mirshams, R., and Xiao, C., "Creep behavior of nanocrystalline nickel at 290 and 373 K," *Materials Science and Engineering: A*, vol. 301, no. 1, pp. 18–22, 2001.

[279] Yip, S., "Nanocrystals: the strongest size," *Nature*, vol. 391, no. 6667, pp. 532–533, 1998.

[280] Youssef, K. M., Scattergood, R. O., Murty, K. L., Horton, J. A., and Koch, C. C., "Ultrahigh strength and high ductility of bulk nanocrystalline copper," *Applied Physics Letters*, vol. 87, no. 9, p. 091904, 2005.

[281] Yu, C., Kao, P., and Chang, C., "Transition of tensile deformation behaviors in ultrafine-grained aluminum," *Acta materialia*, vol. 53, no. 15, pp. 4019–4028, 2005.

[282] Zbib, H. M., Rhee, M., and Hirth, J. P., "On plastic deformation and the dynamics of 3D dislocations," *International Journal of Mechanical Sciences*, vol. 40, no. 2, pp. 113–127, 1998.

[283] Zehetbauer, M., Stüwe, H., Vorhauer, a., Schafler, E., and Kohout, J., "The role of hydrostatic pressure in severe plastic deformation," *Advanced Engineering Materials*, vol. 5, pp. 330–337, May 2003.

[284] Zhang, K., Weertman, J., and Eastman, J., "Rapid stress-driven grain coarsening in nanocrystalline Cu at ambient and cryogenic temperatures," *Applied Physics Letters*, vol. 87, no. 6, p. 061921, 2005.

[285] Zhang, Y., Han, Z., and Lu, K., "Fretting wear behavior of nanocrystalline surface layer of copper under dry condition," *Wear*, vol. 265, no. 3, pp. 396–401, 2008.

[286] Zhilyaev, A. P. and Langdon, T. G., "Using high-pressure torsion for metal processing: Fundamentals and applications," *Progress in Materials Science*, vol. 53, no. 6, pp. 893–979, 2008.

[287] Zhong, Y. and Zhu, T., "Simulating nanoindentation and predicting dislocation nucleation using interatomic potential finite element method," *Computer Methods in Applied Mechanics and Engineering*, vol. 197, pp. 3174–3181, July 2008.

[288] Zhou, M., "A new look at the atomic level virial stress–On continuum-molecular system equivalence," *Proceedings of the Royal Society of London A*, vol. 459, pp. 2347–2392, 2003.

[289] Zhu, B., Asaro, R., Krysl, P., and Bailey, R., "Transition of deformation mechanisms and its connection to grain size distribution in nanocrystalline metals," *Acta materialia*, vol. 53, pp. 4825–4838, Oct. 2005.

[290] Zhu, T., Li, J., Samanta, A., Leach, A., and Gall, K., "Temperature and strain-rate dependence of surface dislocation nucleation," *Physical Review Letters*, vol. 100, p. 025502, Jan. 2008.

[291] Zhu, X., Birringer, R., Herr, U., and Gleiter, H., "X-ray diffraction studies of the structure of nanometer-sized crystalline materials," *Phys. Rev. B*, vol. 35, pp. 9085–9090, Jun 1987.

[292] Ziegler, H., "A modification of Prager's hardening rule," *Quarterly of Applied Mechanics*, vol. 17, pp. 55–65, 1959.

[293] Ziegler, H., *An introduction to thermomechanics*. Elsevier, 1983.

[294] Zienkiewicz, O. C., Humpheson, C., and Lewis, R., "Associated and non-associated visco-plasticity and plasticity in soil mechanics," *Geotechnique*, vol. 25, no. 4, pp. 671–689, 1975.

[295] Zimmerman, J. A., Kelchner, C. L., Klein, P. A., Hamilton, J. C., and Foiles, S. M., "Surface step effects on nanoindentation," *Physical Review Letters*, vol. 87, p. 165507, Oct. 2001.

[296] Zimmerman, J., Webb, E., Hoyt, J., Jones, R., Klein, P., and Bammann, D., "Calculation of stress in atomistic simulation," *Modelling and Simulation in Materials Science and Engineering*, vol. 12, no. 4, p. 319, 2004.

[297] Zimmerman, J. A., Bammann, D. J., and Gao, H., "Deformation gradients for continuum mechanical analysis of atomistic simulations," *International Journal of Solids and Structures*, vol. 46, pp. 238–253, Jan. 2009.

[298] Zimmerman, J. A., Gao, H., and Abraham, F. F., "Generalized stacking fault energies for embedded atom fcc metals," *Modelling and Simulation in Materials Science and Engineering*, vol. 8, no. 2, p. 103, 2000.